

University of Alberta

**Behaviour of Cold Bend Pipes Under Combined
Loads**

by

Millan Sen



A thesis submitted to the Faculty of Graduate Studies and Research in
partial fulfillment of the requirements for the degree of Doctor of
Philosophy

in

Structural Engineering

Department of Civil and Environmental Engineering
Edmonton, Alberta

Spring 2006



Library and
Archives Canada

Bibliothèque et
Archives Canada

Published Heritage
Branch

Direction du
Patrimoine de l'édition

395 Wellington Street
Ottawa ON K1A 0N4
Canada

395, rue Wellington
Ottawa ON K1A 0N4
Canada

Your file *Votre référence*
ISBN: 0-494-14039-9
Our file *Notre référence*
ISBN: 0-494-14039-9

NOTICE:

The author has granted a non-exclusive license allowing Library and Archives Canada to reproduce, publish, archive, preserve, conserve, communicate to the public by telecommunication or on the Internet, loan, distribute and sell theses worldwide, for commercial or non-commercial purposes, in microform, paper, electronic and/or any other formats.

The author retains copyright ownership and moral rights in this thesis. Neither the thesis nor substantial extracts from it may be printed or otherwise reproduced without the author's permission.

AVIS:

L'auteur a accordé une licence non exclusive permettant à la Bibliothèque et Archives Canada de reproduire, publier, archiver, sauvegarder, conserver, transmettre au public par télécommunication ou par l'Internet, prêter, distribuer et vendre des thèses partout dans le monde, à des fins commerciales ou autres, sur support microforme, papier, électronique et/ou autres formats.

L'auteur conserve la propriété du droit d'auteur et des droits moraux qui protègent cette thèse. Ni la thèse ni des extraits substantiels de celle-ci ne doivent être imprimés ou autrement reproduits sans son autorisation.

In compliance with the Canadian Privacy Act some supporting forms may have been removed from this thesis.

Conformément à la loi canadienne sur la protection de la vie privée, quelques formulaires secondaires ont été enlevés de cette thèse.

While these forms may be included in the document page count, their removal does not represent any loss of content from the thesis.

Bien que ces formulaires aient inclus dans la pagination, il n'y aura aucun contenu manquant.


Canada

ABSTRACT

Cold bends are frequently required in energy pipelines in order to change the vertical and horizontal orientation of the pipeline route. Deformations caused by ground movement along the pipeline tend to accumulate at the site of cold bends, which often causes local buckling at these locations. Little is currently known about the behavior of cold bend pipes under applied loads, accordingly this research program was conducted to investigate their local and global load-deformation relationships.

Full-scale tests were conducted on seven large diameter cold bend pipes and one straight pipe that were loaded under axial load, bending, and internal pressure. The specimens were tested until local buckling occurred, and the curvature of several of the pipes was increased until they fractured at the wrinkle location. It was demonstrated through these tests that the critical strain of cold bend pipes is lower than that of a straight pipe, and that the central bend angle of the specimens could achieve up to 49 degrees without fracturing,

Several ancillary tests were conducted on the specimens to better understand the effects of cold bending on the pipe properties. The residual strains, initial imperfections, and material stress-strain properties were measured for several of the specimens. It was revealed that cold bending causes a distribution of imperfections that is similar in shape to a sine function. It was also

determined that there is a considerable degree of work hardening that occurs on the material in the region of the cold bend.

A finite element model was also created to validate the behaviour of the test specimens. The model incorporated the geometry, imperfections, and material properties that were measured from the cold bends. The model demonstrated reasonable accuracy in predicting both the global and local load deformation behaviour of the specimens during testing. A parametric study was subsequently conducted to assess the influence of the diameter to thickness ratio, internal pressure, material grade, imperfection magnitude, and bending degree / diameter length on the behavior of cold bend pipes under applied loads.

ACKNOWLEDGMENTS

This research project was conducted with the financial assistance from SNAM Rete Gas Ltd, Tokyo Gas Ltd, and TransCanada Pipelines Ltd. In addition to their valuable financial contributions, several members of the industrial sponsor companies provided greatly appreciated technical guidance and assistance to this project. I would like to thank the industry advisory committee and in particular Dr. J. Zhou of TransCanada Pipelines Ltd. who chaired the industry advisory committee. The industry advisory committee is consisted of M. Como and E. Cerelli from SNAM Rete Gas Ltd., K. Yoshizaki and N. Fukada from Tokyo Gas Ltd., and K. Adams, S. Adeeb, and J. Zhou from TransCanada Pipelines Ltd.

I would also like to thank the technicians at the I. F. Morrison Structural Lab for their extensive help during the experimental testing of the specimens. In particular, the technical brilliance of Richard Helfrich who provided countless hours of his expertise towards this project, and Larry Burden who ensured that the testing program proceeded safely. Additionally, I would like to thank Rob Lindemann from the TransCanada Fabrication Shop who provided considerable assistance with regards to the preparation of the specimens prior to testing.

The experience offered by several previous students of the University of Alberta greatly enhanced this research program. My sincerest gratitude is extended to Dr. Heng Khoo, Dr. Mohammad Behbahanifard, and Dr. Alfred Dorey for their invaluable assistance towards the finite element analysis portion of this research. In addition, I would like to acknowledge Connie Song, Vincent Guo, and Jianmin Zhang for their graciously provided contributions during the testing phase of this project.

TABLE OF CONTENTS

| | | |
|------------|---|-----------|
| 1.0 | INTRODUCTION AND LITERATURE REVIEW..... | 1 |
| 1.1 | <i>Special Concerns with Cold Bends</i>..... | 2 |
| 1.2 | <i>Manufacture of Line Pipe</i>..... | 3 |
| 1.3 | <i>Cold Bending Machine</i>..... | 5 |
| 1.4 | <i>Cold Bending Procedure</i>..... | 7 |
| 1.5 | <i>Code Criteria for Cold Bends</i>..... | 9 |
| | 1.5.1 CSA Standard Z662-2003..... | 9 |
| | 1.5.2 ASME B31.3-1999 Edition..... | 10 |
| | 1.5.3 DNV OS-F101-2000..... | 11 |
| 1.6 | <i>Straight Pipe Research Literature Review</i>... | 11 |
| | 1.6.1 Research by Boukamp and Stephens (1973)..... | 12 |
| | 1.6.2 Research by Gresnigt (1986)..... | 13 |
| | 1.6.3 Research by Mohareb, <i>et al</i> (1994)..... | 15 |
| | 1.6.4 Research by Dorey, <i>et al</i> (2001)..... | 16 |
| 1.7 | <i>Cold Bend Research Literature Review</i>..... | 18 |
| | 1.7.1 Research by Palynchuk (1983)..... | 19 |
| | 1.7.2 Research by Wassermann (1983)..... | 20 |
| | 1.7.3 Research by Shibli (1986)..... | 21 |
| | 1.7.4 Research by Murray and Bilston (1993).... | 22 |

| | | |
|-------------|---|-----------|
| 1.7.5 | Research by Olsen and Clark (1995)..... | 25 |
| 1.7.6 | Research by Rosenfeld <i>et al</i> (2002)..... | 27 |
| 1.7.7 | Research by Fukuda, <i>et al</i> (2002)..... | 28 |
| 1.8 | <i>Problem Statement</i> | 30 |
| 1.9 | <i>Scope and Objectives</i> | 32 |
| 1.10 | <i>Layout of Report</i> | 34 |
| | | |
| 2.0 | EXPERIMENTAL PROGRAM | 39 |
| | | |
| 2.1 | <i>Experimental Parameters</i> | 40 |
| 2.1.1 | Geometric and Material Properties..... | 41 |
| 2.1.2 | Specimen Length..... | 41 |
| 2.1.3 | Internal Pressure..... | 42 |
| 2.1.4 | Bending Method..... | 45 |
| 2.1.5 | Axial Load and Bending Moment | 48 |
| 2.2 | <i>Test Specimen Preparation</i> | 49 |
| 2.2.1 | Prior to Delivery..... | 49 |
| 2.2.2 | Initial Measurements..... | 50 |
| 2.2.3 | Specimen Instrumentation..... | 52 |
| 2.3 | <i>Residual Strain Measurement</i> | 56 |
| 2.3.1 | TG Specimen Residual Strain Measurement..... | 57 |
| 2.3.2 | TCPL Specimen Residual Strain Measurement..... | 57 |

| | | |
|------------|--|-----|
| 2.4 | <i>Imperfection Measurement</i> | 59 |
| 2.4.1 | Creation of Initial Imperfections..... | 59 |
| 2.4.2 | Imperfection Measuring Device..... | 60 |
| 2.4.3 | Imperfection Measuring Procedure..... | 62 |
| 2.5 | <i>Test Setup</i> | 65 |
| 2.5.1 | Self-Equilibrating Frame..... | 65 |
| 2.5.2 | Test Setup Bracing..... | 66 |
| 2.6 | <i>Experimental Testing Procedure</i> | 68 |
| 2.6.1 | Alignment of Test Setup and Specimen..... | 68 |
| 2.6.2 | Prior to Loading..... | 72 |
| 2.6.3 | Application of Load..... | 74 |
| 2.6.4 | Jack Resetting..... | 77 |
| 3.0 | MATERIAL TESTING PROGRAM | 91 |
| 3.1 | <i>Material Coupon Locations</i> | 92 |
| 3.2 | <i>Coupon Testing Procedure</i> | 94 |
| 3.3 | <i>Determination of Material Properties</i> | 96 |
| 3.4 | <i>Virgin Material Coupons</i> | 100 |
| 3.4.1 | Virgin Coupon Results..... | 100 |
| 3.5 | <i>Tested End Material Coupons</i> | 102 |
| 3.5.1 | Background to Increasing of Proportional Limit..... | 102 |
| 3.5.2 | Tested End Coupons Results..... | 103 |

| | | |
|------------|---|-----|
| 3.5.3 | Tested End Coupon Discussion..... | 105 |
| 3.6 | <i>Tension Side Bend Material</i> | 106 |
| 3.6.1 | Background to Work Hardening Effect..... | 106 |
| 3.6.2 | Tension Side Bend Coupon Results..... | 108 |
| 3.6.3 | Tension Side Bend Coupon Discussion..... | 109 |
| 3.7 | <i>Compression Side Bend Material</i> | 110 |
| 3.7.1 | Background to Bauschinger Effect..... | 110 |
| 3.7.2 | Compression Side Bend Coupon Results... | 112 |
| 3.7.3 | Compression Side Bend Coupon Discussion..... | 113 |
| 3.8 | <i>Summary of Material Testing Results</i> | 114 |

4.0 INITIAL MEASUREMENTS AND DATA

| | | |
|------------|---|-----|
| | REDUCTION | 121 |
| 4.1 | <i>Initial Geometric Measurements</i> | 121 |
| 4.1.1 | End Ovalization..... | 122 |
| 4.1.2 | Wall Thinning / Thickening..... | 123 |
| 4.1.3 | Bend Length..... | 124 |
| 4.2 | <i>Residual Strain Measurement Results</i> | 125 |
| 4.2.1 | Specified Residual Strain..... | 126 |
| 4.2.2 | Average Residual Strain..... | 127 |
| 4.2.3 | Residual Strain Measurement Results..... | 127 |
| 4.2.3.1 | TG Residual Strain Results..... | 128 |

| | | |
|------------|---|------------|
| 4.2.3.2 | TCPL Residual Strain Results..... | 129 |
| 4.3 | <i>Initial Imperfection Results</i> | 131 |
| 4.3.1 | Overall Geometry..... | 131 |
| 4.3.1.1 | Bend Angle..... | 131 |
| 4.3.1.2 | Vertical Profile..... | 133 |
| 4.3.2 | Initial Imperfections..... | 134 |
| 4.3.2.1 | Reduction of Initial Imperfection Data..... | 134 |
| 4.3.2.2 | Initial Imperfection Measuring Results..... | 135 |
| 4.3.2.3 | Special Case: TG2 Initial Imperfection Measuring..... | 139 |
| 4.3.2.4 | Ovality Measuring Results..... | 140 |
| 4.4 | <i>Reduction of Experimental Data</i> | 142 |
| 4.4.1 | Determination of Global Moment..... | 145 |
| 4.4.2 | Determination of Local Curvature..... | 149 |
| 4.4.3 | Determination of Global Curvature..... | 151 |
| 4.4.3.1 | Global Curvature from Rotation Meter Measurements..... | 152 |
| 4.4.3.2 | Global Curvature from Strain Measurements..... | 153 |
| 4.4.3.3 | Comparison of Global Curvature Measurements..... | 154 |
| 4.5 | <i>Determination of Critical Buckling Strain</i> | 156 |
| 4.5.1 | Critical Strain using Maximum Moment Method..... | 157 |
| 4.5.2 | Critical Strain using Bilinear Method..... | 158 |
| 5.0 | DISCUSSION OF EXPERIMENTAL RESULTS | 175 |
| 5.1 | <i>Prediction of Test Results</i> | 176 |

| | | |
|------------|---|-----|
| 5.2 | <i>SNAM Test Results</i> | 177 |
| | 5.2.1 Overview of SNAM Specimens Test | |
| | Observations..... | 178 |
| | 5.2.2 Global Behaviour..... | 180 |
| | 5.2.3 Local Behaviour..... | 181 |
| | 5.2.4 Critical Strain..... | 182 |
| | 5.2.5 Discussion of Post-Buckling Response..... | 183 |
| 5.3 | <i>TG Test Results</i> | 184 |
| | 5.3.1 Overview of TG Specimen Test | |
| | Observations..... | 185 |
| | 5.3.2 Global Behaviour..... | 185 |
| | 5.3.3 Local Behaviour..... | 187 |
| | 5.3.4 Critical Strains..... | 187 |
| | 5.3.5 Post Buckling Behaviour..... | 188 |
| | 5.3.6 Discussion of Fracture Mechanism in TG | |
| | Specimens..... | 190 |
| 5.4 | <i>TCPL Test Results</i> | 191 |
| | 5.4.1 Overview of TCPL Specimen Test | |
| | Observations..... | 191 |
| | 5.4.2 Global Behaviour..... | 192 |
| | 5.4.3 Local Behaviour..... | 194 |
| | 5.4.4 Critical Strains..... | 195 |
| | 5.4.5 Post Buckling Behaviour..... | 196 |
| | 5.4.6 Tension Side Fracture of TCPL1..... | 198 |

| | | |
|------------|---|------------|
| 5.4.7 | Wrinkle Behaviour of TCPL3 | 203 |
| 5.4 | <i>Comparison of Behaviour Between Specimen Sets</i> | 204 |
| 5.5.1 | Global Behaviour..... | 204 |
| 5.5.2 | Local Behaviour..... | 205 |
| 5.5.3 | Critical Strain..... | 206 |
| 5.5.4 | Post Buckling Behaviour..... | 209 |
| 5.6 | <i>Summary of Test Results</i> | 211 |
| 6.0 | DEVELOPMENT OF FINITE ELEMENT MODEL.... | 227 |
| 6.1 | <i>Purpose of the Finite Element Analysis</i> | 227 |
| 6.2 | <i>Finite Element Method</i> | 229 |
| 6.3 | <i>Elements</i> | 230 |
| 6.4 | <i>Symmetry</i> | 232 |
| 6.5 | <i>Boundary Conditions</i> | 234 |
| 6.5.1 | End Plates and Collars..... | 234 |
| 6.5.2 | Moment Arms..... | 236 |
| 6.5.3 | Loading and Reaction Pins..... | 237 |
| 6.5.4 | Plane of Symmetry..... | 237 |
| 6.6 | <i>Material Properties</i> | 238 |
| 6.6.1 | Overview of Material Model..... | 238 |
| 6.6.2 | Selection of Material for Model..... | 239 |
| 6.6.3 | Material Model Properties..... | 241 |

| | | |
|-------------|---|-----|
| 6.7 | <i>Loading Procedure</i> | 243 |
| 6.8 | <i>Solution Strategy</i> | 244 |
| 6.9 | <i>Initial Geometry of Model</i> | 246 |
| 6.10 | <i>Initial Imperfections of Model</i> | 248 |
| 6.11 | <i>Initial Imperfection Sensitivity Analysis</i> | 251 |
| | 6.11.1 Imperfection Sensitivity Analysis Results... | 252 |
| 6.12 | <i>Mesh Study</i> | 254 |
| | 6.12.1 Mesh Study Results..... | 256 |
| 7.0 | FEA RESULTS AND PARAMETRIC STUDY | 265 |
| 7.1 | <i>Reduction of FEA Output</i> | 266 |
| | 7.1.1 Model Global Curvature..... | 266 |
| | 7.1.2 Model Maximum Moment..... | 267 |
| | 7.1.3 Model Buckle Strain..... | 268 |
| 7.2 | <i>Comparison of FEM and Test Results</i> | 269 |
| | 7.2.1 SNAM Model Results..... | 270 |
| | 7.2.2 TG Model Results..... | 272 |
| | 7.2.3 TCPL Model Results..... | 273 |
| 7.3 | <i>Discussion of Model Results</i> | 274 |
| 7.4 | <i>Supplementary Straight-Bend Model</i> | 276 |
| | 7.4.1 S-B Model Description..... | 277 |
| | 7.4.2 Preventing Local Buckling During Cold Bending..... | 278 |

| | | |
|------------|--|------------|
| 7.4.3 | Cold Bending of S-B Model..... | 279 |
| 7.4.4 | Loading of Cold Bend S-B Model..... | 280 |
| 7.4.5 | Comparison of S-B and T-B Model | |
| | Results..... | 281 |
| 7.5 | <i>Parametric Study of Test Specimens</i> | 282 |
| 7.5.1 | Investigated Parameters..... | 283 |
| 7.5.2 | Constant Variables..... | 285 |
| 7.5.3 | Standard Model..... | 285 |
| 7.5.4 | Diameter/Thickness Ratio..... | 286 |
| 7.5.5 | Internal Pressure..... | 287 |
| 7.5.6 | Material Grade..... | 289 |
| 7.5.7 | Imperfection Amplitude..... | 290 |
| 7.5.8 | Bending Degree / Diameter Length..... | 292 |
| 7.5 | <i>Summary of FEA Results and Parametric</i> | |
| | <i>Study</i> | 294 |
| 8.0 | SUMMARY, CONCLUSIONS, AND | |
| | RECOMMENDATIONS | 316 |
| 8.1 | <i>Summary</i> | 316 |
| 8.2 | <i>Conclusions</i> | 319 |
| 8.3 | <i>Recommendations</i> | 322 |
| | REFERENCES | 325 |

LIST OF TABLES

Chapter 2

Table 2.1 - Proposed Test Specimen Properties80

Table 2.2 - Measured Test Specimen Properties80

Chapter 3

Table 3.1 – SNAM2 Material Properties Summary.....116

Chapter 4

Table 4.1 – Specimen End Diameter Measurements161

Table 4.2 – Specimen Wall Thickness Measurements161

Table 4.3 – Specimen Length Measurements161

Table 4.4 – Specimen Residual Strain Measurements.....162

Table 4.5 – Specimen Initial Imperfection Results Summary162

Table 4.6 – Specimen Global Geometry Imperfection Measuring Results162

Table 4.4 – Specimen Ovality Imperfection Measuring Results163

Chapter 6

Table 6.1 - Summary of Initial Imperfection Sensitivity Analysis258

Table 6.2 - Summary of Different FEM Meshes Analyzed.....258

Chapter 7

Table 7.1 – Summary of Difference between Model and Test Results297

Table 7.2 – Summary of Difference between T-B and S-B Model Results297

| | |
|---|-----|
| Table 7.3 – Parametric Study Model Matrix | 298 |
| Table 7.4 – Parametric Study Results | 298 |

LIST OF FIGURES

Chapter 1

| | |
|--|----|
| Figure 1.1 - Response of Cold Bend to Slope Movement | 36 |
| Figure 1.2 - Response of Cold Bend to Horizontal Ground Movement | 36 |
| Figure 1.3 - Cold Bending Machine | 37 |
| Figure 1.4 - Typical Cold Bend Design | 37 |
| Figure 1.5 - Schematic of Cold Bending Procedure | 38 |

Chapter 2

| | |
|---|----|
| Figure 2.1 – Schematic of Test Setup | 81 |
| Figure 2.2 – Strain Measurement Instrumentation | 82 |
| Figure 2.3 – Measurement of Residual Strain | 82 |
| Figure 2.4 – Initial Imperfection due to Cold Bending..... | 83 |
| Figure 2.5 – End View of Imperfection Measuring Device..... | 83 |
| Figure 2.6 – Imperfection Measuring Device Carriage | 84 |
| Figure 2.7 – During Initial Imperfection Measuring | 84 |
| Figure 2.8 – Overhead of Test Setup | 85 |
| Figure 2.9 – Test Loading System | 85 |
| Figure 2.10 – Jack Side End of Test Setup | 86 |
| Figure 2.11 – Non-jack Side End of Test Setup | 86 |
| Figure 2.12 – Longitudinal Tension Side View..... | 87 |
| Figure 2.13 – Longitudinal Compression Side View..... | 87 |
| Figure 2.14 – Interior Lateral Bracing | 88 |
| Figure 2.15 – Bracing at Jack Side of Testing Frame..... | 88 |
| Figure 2.16 – Aligning Specimen | 89 |
| Figure 2.17 – Welding of Specimen to End Plate..... | 89 |
| Figure 2.18 – End Collars | 90 |

| | |
|---|----|
| Figure 2.19 – Resetting Jack Stroke | 90 |
|---|----|

Chapter 3

| | |
|---|-----|
| Figure 3.1 - Schematic Tension Specimen | 117 |
| Figure 3.2 - Coupon Testing System | 117 |
| Figure 3.3 - Strain Measurement During Testing | 118 |
| Figure 3.4 - Example Material Property Determination | 118 |
| Figure 3.5 - SNAM2 Static Stress-Strain Curve – Low Strains | 119 |
| Figure 3.6 - SNAM2 Static Stress-Strain Curve | 119 |
| Figure 3.7 – Schematic Example of Work Hardening | 120 |
| Figure 3.8 – Schematic Example of Bauschinger Effect | 120 |

Chapter 4

| | |
|--|-----|
| Figure 4.1 – TG2 Residual Strains..... | 164 |
| Figure 4.2 – TCPL2 Residual Strain of Degree Around Circumference..... | 164 |
| Figure 4.3 – TCPL Circumferential Position vs. Residual Strain..... | 165 |
| Figure 4.4 – SNAM2 Vertical Displacement and Global Rotation | 165 |
| Figure 4.5 – Determination of Imperfection Amplitude and Period..... | 166 |
| Figure 4.6 – SNAM2 Initial Imperfections..... | 167 |
| Figure 4.7 – SNAM2 Ovalization..... | 167 |
| Figure 4.8 – TCPL2 Initial Imperfections..... | 168 |
| Figure 4.9 – TCPL2 Ovalization..... | 168 |
| Figure 4.10 – TG2 Imperfections with Global Vertical Deflection..... | 169 |
| Figure 4.11 – TG2 Imperfections..... | 169 |
| Figure 4.12 – TG2 Imperfection Measuring End View..... | 170 |
| Figure 4.13 – TG2 Imperfection Measuring Rail Inside of Pipe | 170 |
| Figure 4.14 – Ovalization Forces Caused by Bending Moment..... | 171 |
| Figure 4.15 – Imperfection Measuring Cross Section | 171 |
| Figure 4.16 – Schematic of Moment and Curvature Determination..... | 172 |

| | |
|---|-----|
| Figure 4.17 – Strain Distribution used to Determine of Local Curvature | 172 |
| Figure 4.18 – Comparison of Rotation Meter and Strain Based Global Curvatures . | 173 |
| Figure 4.19 –Example of Critical Strain using Maximum Moment Method..... | 173 |
| Figure 4.20 –Example of Determination of Critical Strain using Bilinear Method... | 174 |

Chapter 5

| | |
|---|-----|
| Figure 5.1 – SNAM Specimen Moment-Curvature Responses | 214 |
| Figure 5.2 – SNAM1 End Bulge..... | 214 |
| Figure 5.3 – SNAM1 Wrinkle | 215 |
| Figure 5.4 – SNAM2 Demec Strain Distribution by Increasing Load Step | 215 |
| Figure 5.5 – SNAM2 Final End Rotation | 216 |
| Figure 5.6 – SNAM2 Final Wrinkle Shape | 216 |
| Figure 5.7 –SNAM3 Ripples Before Buckling..... | 217 |
| Figure 5.8 – SNAM3 Diamond Shaped Buckle..... | 217 |
| Figure 5.9 – TG Moment-Curvature Responses | 218 |
| Figure 5.10 – Final Buckled Shape of TG1 | 218 |
| Figure 5.11 – Pipe Fracture of TG1 | 219 |
| Figure 5.12 – TG2 Demec Strain Distribution by Increasing Load Step..... | 219 |
| Figure 5.13 – Wrinkle Shape of TG2..... | 220 |
| Figure 5.14 – Close View of Outside Surface of TG2 Wrinkle..... | 220 |
| Figure 5.15 – TCPL Moment-Curvature Responses..... | 221 |
| Figure 5.16 – Wrinkle and Fracture of TCPL1 | 221 |
| Figure 5.17 – Fracture Surface of TCPL1 | 222 |
| Figure 5.18 – TCPL1 Tension Side Strain Distribution by Centre Moment | 222 |
| Figure 5.19 – TCPL1 Circumferential and Neutral Axis Strains..... | 223 |
| Figure 5.20 – TCPL2 Demec Strain Distribution by Increasing Load Step | 223 |
| Figure 5.21 – Initial Buckling of TCPL2..... | 224 |
| Figure 5.22 – Final Wrinkle of TCPL2..... | 224 |
| Figure 5.23 – Final Wrinkle of TCPL3..... | 225 |
| Figure 5.24 – Final Buckled Shape of TCPL3..... | 225 |

| | |
|---|-----|
| Figure 5.25 – Comparison of Moment – Curvature Responses..... | 226 |
|---|-----|

Chapter 6

| | |
|--|-----|
| Figure 6.1 – S4R Element..... | 259 |
| Figure 6.2 – Boundary Conditions of FEM | 259 |
| Figure 6.3 – Elastic Core Depth after Cold Bending and Testing | 260 |
| Figure 6.4 – Comparison of Coupon Result and Model Stress Strain Curves..... | 260 |
| Figure 6.5 – Comparison of Model and Measured Initial Geometry..... | 261 |
| Figure 6.6 – Comparison of Longitudinal Direction Initial Imperfections..... | 261 |
| Figure 6.7 – Comparison of Circumferential Direction Imperfections..... | 262 |
| Figure 6.8 – SNAM2 Imperfection Amplitude Distribution | 262 |
| Figure 6.9 – Moment Curvature Curves with Varying Imperfection Amplitudes..... | 263 |
| Figure 6.10 – Node Distribution Along Imperfections..... | 263 |
| Figure 6.11 – Mesh Distribution of FEM | 264 |

Chapter 7

| | |
|--|-----|
| Figure 7.1 – Schematic of Model Deformation During Loading..... | 299 |
| Figure 7.2 – Comparison of Pressurized Model and Specimen Buckle Shape..... | 300 |
| Figure 7.3 – Comparison of Unpressurized Model and Specimen Buckle Shape | 300 |
| Figure 7.4 – SNAM1 Model and Test Moment vs. Global Curvature | 301 |
| Figure 7.5 – SNAM1 Model and Test Moment and Curvature vs. Buckle Strain..... | 301 |
| Figure 7.6 – SNAM2 Model and Test Moment vs. Global Curvature | 302 |
| Figure 7.7 – SNAM2 Model and Test Moment and Curvature vs. Buckle Strain..... | 302 |
| Figure 7.8 – SNAM3 Model and Test Moment vs. Global Curvature | 303 |
| Figure 7.9 – SNAM3 Model and Test Moment and Curvature vs. Buckle Strain..... | 303 |
| Figure 7.10 – TG1 Model and Test Moment vs. Global Curvature..... | 304 |
| Figure 7.11 – TG1 Model and Test Moment and Curvature vs. Buckle Strain..... | 304 |
| Figure 7.12 – TG2 Model and Test Moment vs. Global Curvature..... | 305 |
| Figure 7.13 – TG2 Model and Test Moment and Curvature vs. Buckle Strain..... | 305 |

| | |
|--|-----|
| Figure 7.14 – TCPL1 Model and Test Moment vs. Global Curvature | 306 |
| Figure 7.15 – TCPL1 Model and Test Moment and Curvature vs. Buckle Strain | 306 |
| Figure 7.16 – TCPL2 Model and Test Moment vs. Global Curvature | 307 |
| Figure 7.17 – TCPL2 Model and Test Moment and Curvature vs. Buckle Strain | 307 |
| Figure 7.18 – TCPL3 Model and Test Moment vs. Global Curvature | 308 |
| Figure 7.19 – TCPL3 Model and Test Moment and Curvature vs. Buckle Strain | 308 |
| Figure 7.20 – Cold Bending Procedure for S-B Model | 309 |
| Figure 7.21 – Comparison of S-B and T-B Models Global Behaviours..... | 310 |
| Figure 7.22 – Diameter/Thickness Ratio Global Behaviour Comparison | 311 |
| Figure 7.23 – Diameter/Thickness Ratio Moment and Critical Strain Comparison.. | 311 |
| Figure 7.24 – Internal Pressure Global Behaviour Comparison..... | 312 |
| Figure 7.25 – Internal Pressure Moment and Critical Strain Comparison..... | 312 |
| Figure 7.26 – Material Grade Global Behaviour Comparison..... | 313 |
| Figure 7.27 – Material Grade Moment and Critical Strain Comparison | 313 |
| Figure 7.28 – Imperfection Amplitude Global Behaviour Comparison | 314 |
| Figure 7.29 – Imperfection Amplitude Moment and Critical Strain Comparison.... | 314 |
| Figure 7.30 – Bending Degree / Diameter Length Global Behaviour Comparison... | 315 |
| Figure 7.31 – Bending Degree / Diameter Length Moment and Critical Strain Comparison..... | 315 |

LIST OF SYMBOLS

Latin Symbols

| | |
|--------------|--|
| a | Ovalization of a straight pipe |
| A_0 | Average amplitude of specimen imperfections along compression line |
| A_{45} | Average specimen imperfection amplitude 45° from compression line |
| C | Applied axial force |
| C_y | Axial load under zero circumferential stress |
| d | Distance between two points in model located one radius to either side of buckle |
| D | Outside diameter of pipe |
| D_{ave} | Average pipe diameter |
| D_i | Inside diameter of pipe |
| D_{max} | Maximum measured pipe diameter |
| D_{min} | Minimum measured pipe diameter |
| e_0 | Initial vertical distance from jack centre to pipe centreline at end plate |
| e_b | Maximum eccentricity at bend |
| e_e | Eccentricity at end of specimen |
| e_{Model} | Eccentricity provided by model moment arms |
| E | Modulus of Elasticity |
| \mathbf{F} | Internal nodal point force vector |
| F_y | Yield strength |
| \mathbf{K} | Tangent stiffness matrix |
| i | Iteration number |
| imp | Imperfection magnitude as percent of wall thickness |

| | |
|-------------------|---|
| L_0 | Initial calliper measurement |
| L_{0Model} | Model original horizontal length |
| L_{Bend} | Calculated bend centreline length |
| $L_{Centreline}$ | Measured total centreline length of bend |
| $L_{Compression}$ | Measured total compression side length of pipe |
| L_{H0} | Original horizontal length of pipe |
| L_{Hinge} | Horizontal distance between hinge pin centre and pipe side of end plate |
| L_n | Calliper measurement at the n^{th} load step |
| $L_{Straight}$ | Straight segment length at each end of bend |
| $L_{Tensile}$ | Measured total tension side length of pipe |
| L_{V0} | Initial vertical deflection of the pipe |
| $L_{V0Model}$ | Initial vertical deflection of model |
| $L_{VMiddle}$ | Vertical deflection of the middle of model at each time step |
| L_{VTest} | Vertical deflection of the middle of pipe during testing |
| M | Applied bending moment |
| M_b | Maximum moment at bend |
| M_e | Bending moment at end of specimen |
| M_{Max} | Pipe maximum second order moment |
| M_{Model} | Second order moment of model at the middle of its length |
| M_p | Plastic moment capacity |
| n | Exponent to define circumferential imperfection distribution of model |
| p | Internal pressure |
| p_y | Internal pressure that causes pipe wall to yield |
| P | Difference between internal and external pressure in pipe |
| P_a | Axial load |
| P_j | Jack load |
| P_p | Axial load due to internal pressure |
| r | Average pipe radius |
| r_0 | Radius of model at compression line |

| | |
|--------------|---|
| r_{θ} | Model radius at angle θ in circumferential direction from compression line |
| r_{imp} | Radius of the bend compression line of the model including imperfections |
| R | Radius of Curvature of pipe centreline |
| \mathbf{R} | Applied external nodal load vector |
| t | Time |
| t | Pipe wall thickness |
| T | Average period of specimen imperfections |
| \mathbf{U} | Displacement vector |
| x_{model} | Value of model parameter being compared |
| x_{test} | Value of parameter during testing being compared |
| x_1, x_2 | Longitudinal position of points left and right of the model buckle |
| y_1, y_2 | Out-of-plane position of points left and right of the model buckle |
| z_1, z_2 | Vertical position of points left and right of model buckle |
| Z | Plastic Section Modulus |

Greek Symbols

| | |
|--------------------------|--|
| Δ_{Jack} | Jack stroke during each load step |
| Δ_{Pin} | Longitudinal movement of the model pin at each time step |
| Δt | Increment of time |
| Δt | Change in wall thickness |
| ϵ_0 | Yield strain |
| ϵ_a | Axial direction strain |
| ϵ_{buckle} | Strain at the buckle of model over a one diameter gauge length |
| $\epsilon_{Calliper}$ | Strain measured using calliper |
| $\epsilon_{Compressive}$ | Strain on the compression side of the cross-section |
| ϵ_{cr} | Critical buckling strain - Gresnigt |

| | |
|-----------------------|---|
| ϵ_{crit} | Critical buckling strain over a gauge length of one diameter – Dorey |
| ϵ_{ln}^{pl} | Plastic component of true strain |
| ϵ_{nom} | Engineering strain |
| ϵ_r | Radial direction strain |
| $\epsilon_{Residual}$ | Theoretical residual strain at extreme fibres of bend |
| $\epsilon_{Tensile}$ | Strain on the tension side of the cross-section |
| ϵ_t | Transverse direction strain |
| ϕ_{Global} | Global curvature of the specimen during testing |
| ϕ_{Local} | Local curvature at a particular cross-section of pipe |
| ϕ_{Model} | Global curvature of model |
| ν | Poisson's ratio |
| π | Pi (=3.141592) |
| γ_n | Octahedral shear strain |
| λ | Half wavelength of imperfection |
| σ_1 | Longitudinal direction stress |
| σ_2 | Circumferential direction stress |
| σ_a | Axial direction stress |
| σ_{eff} | von Mises condition effective stress |
| σ_h | Hoop stress |
| σ_i | Longitudinal stress caused by internal pressure |
| σ_{nom} | Engineering stress |
| σ_r | Radial direction stress |
| σ_t | Transverse direction stress |
| σ_{true} | True stress |
| σ_y | Yield stress |
| σ_θ | Circumferential stress |
| τ_n | Octahedral shear stress |
| ϑ | Bend angle at each interval length |

| | |
|----------------------------|---|
| θ_0 | Average end angle of pipe at beginning of test |
| θ_{end} | End angle of model |
| θ_L | Rotation of the left end of model |
| θ_{Bend} | Relative angle of position on bend with respect to end of model |
| θ_{Model} | Average angle of ends of model at each time step |
| θ_R | Rotation of right end of model |
| θ_{Test} | Average rotation of ends of pipe during testing |
| ϑ_{Total} | Total bend angle |

GLOSSARY & ABBRIVIATIONS

| | |
|----------------------------------|---|
| Amplitude | Half the radial direction distance between adjacent imperfection local maximum and minimum |
| Bauschinger Effect | Decrease in material strength after it had been previously loaded beyond its yield strength, in the opposite direction |
| Bend increment | Distance between kinks during cold bending |
| Bending degree / diameter | Average bend angle / Nominal pipe diameter in length |
| Bending degree / interval length | Angle of each individual kink during cold bending / Kink spacing |
| Bend length | Length of pipe over which curvature during cold bending is applied |
| Bilinear critical strain | Compression strain at buckle at global curvature corresponding to intersection of elastic and inelastic regression lines, in global curvature vs. buckle strain curve |
| Closing mode deformation | Cold bend deformation where extrados elongates and intrados shortens |
| Critical strain | Compressive strain at onset of buckling |
| DSAW | Double submerged arc weld |
| D / t ratio | Diameter to thickness ratio |
| Die | Bending point for cold bend in cold bending machine |
| Donut | Device used to prevent flattening of ends of pipe during cold bending |
| Extrados | Tension side of cold bend |
| Kink | Individual bend in a cold bend pipe |

| | |
|--------------------------------|--|
| Heat treatment | Formation of new material properties for a cold-worked material that has been heated for a prolonged period |
| IMD | Imperfection measuring device |
| Initial imperfection | A deviation from perfection with regards to identical cross-sectional geometry throughout cold bend length |
| Initial vertical deflection | Bending plane displacement of centre of pipe, immediately after cold bending |
| Intrados | Compression side of cold bend |
| LVDT | Linear variable differential transformer |
| Mandrel | Device used to prevent radial direction distortion of pipe in cold bending machine |
| Maximum moment critical strain | Compression strain at buckle location at maximum moment during loading |
| Opening mode deformation | Cold bend deformation where extrados shortens and intrados elongates |
| Ovalization | Bending and neutral axis diameter difference / Average diameter |
| Overbend | Cold bend situated at the top of a slope |
| Period | Distance between adjacent imperfection local maximums or minimums |
| Pinup shoe | Component that prevents downward movement of pipe, at opposite side of die to stiffback, within cold bending machine |
| Residual strain | Strain that is in a material that is free of external forces |
| Residual stress | Stress that is in a material that is free of external forces |
| Ripple | Local buckles in pipe created during cold bending |

| | |
|----------------------------|--|
| S-B model | Straight-bend model |
| SMYS | Specified Minimum Yield Stress |
| Sagbend | Cold bend situated at the toe of a slope |
| Sleeve element | Elastic element that inhibits permanent deformation during cold bending of straight-bend model |
| Springback | Rebound of pipe after retraction of stiffback during cold bending |
| Standard model | Model with typical test specimen characteristics in parametric study |
| Static stress-strain curve | Material stress-strain curve with loading rate effects removed |
| Stiffback | Component that contacts the pipe at the tilting location of the cold bend machine |
| Straight segment length | Region of pipe joint over which there is no applied curvature during cold bending |
| Strain aging | Transformation of material behaviour over time at temperatures well below its recrystallization temperature |
| T-B model | Test-bend model |
| Total bend angle | Summation of end angles of cold bend |
| Work hardening | Increase of material strength after it had been previously loaded beyond its yield strength, in the same direction |

1.0 INTRODUCTION

Pipelines are used to transport natural gas from the remote regions where the reserves are located to the markets where the gas is to be consumed. The pipelines in North America traverse several thousands of kilometers, and therefore encounter considerable variation in the ground terrain. Increasing exploitation of the existing reserves is encouraging the installation of these pipelines into further remote areas such as the Canadian sub-Arctic, which leads to previously inexperienced design conditions. The various slopes, soil types, and seismic activities that are encountered by the pipelines cause them to become affected by geotechnical movement. This ground movement acts to apply various loading conditions on the pipe, and the magnitude of these loads may become sufficiently severe to induce catastrophic failure. It is for this reason that considerable research towards the capacity of a pipe under applied load is required in order to economically design a pipe to resist the expected loads and applied deformations.

Cold bends are frequently required along pipeline routes where there are severe changes in the slope of the trench, or at locations where an abrupt change in the horizontal orientation of the pipeline is required. When assessing the effects of geotechnical movements on a line in service, traditional engineering practice is partially based on the judgment that the geotechnical movements tend to concentrate pipe deformations in the vicinity of these bends. Additionally it has been observed by the sponsors of this research program that wrinkle formation and fractures are often located at the site of cold bends. Consequently, it is of interest to understand the conditions that contribute to local buckling in cold bends, and the conditions that contribute to the amplification of local buckles in the bends into 'wrinkles' in which significant plastic deformations and cross-sectional distortions accumulate.

1.1 Special Concerns with Cold Bends

When a slope is encountered along a pipeline route, an overbend is required at the crest of the slope, and a sag bend is required at its toe. As these slopes are often relatively unstable, considerable ground movement may occur within the slope, and a component of this motion will be orientated in the longitudinal direction of the pipe as shown in Figure 1.1. This movement will be imposed on to the pipe via the pipe-soil interaction within the trench. This applied deformation creates a significant axial load within the pipe. As the movement is longitudinally restrained by the soil along the pipe that is distant from the slope, the bend that is situated at the crest of the slope will experience tension loads while the bend that is positioned at the toe of the slope will experience compression loads. The soil movement will also produce forces transverse to the pipelines that will induce bending moments, which will serve to open the bend at the crest of the slope and close the bend at the toe of the slope. This applied moment may achieve magnitudes that are sufficient to buckle the pipe at the bend location as demonstrated by the numerous buckles that have been observed in field condition pipes that are situated on unstable slopes.

In regions of the world that are prone to earthquakes, liquefaction of the soil during an earthquake will cause considerable ground movement. This ground movement may induce substantial longitudinal displacement along the pipeline. This longitudinal deformation, as shown in Figure 1.2, may continue along the pipeline until a bend in the pipe is encountered. This restraint in displacement occurs because at a change in direction the movement of the pipe becomes resisted by the lateral resistance of the soil, which is somewhat greater than the longitudinal resistance to movement that is caused by the sliding friction between the soil and the pipe. As the pipe will tend to follow the ground movement at the bend, while being drastically constrained a short distance from the bend by the lateral resistance of the soil, there will be significant curvature induced in the pipe at the bend location. This curvature may achieve adequate severity to buckle the

pipe. In addition to buckling the pipe, during major earthquakes it is possible for the curvature induced at the bends to reach a magnitude sufficient to fracture the pipe, and this would lead to catastrophic failure of the pipeline thus endangering human lives.

The final failure mode that will be discussed is for those pipes that are installed at locations where the ground is weak such as in the muskegs of Northern Alberta. As pipelines are typically installed during the winter when the temperature is approximately -30° Celsius, and the operating temperature of gas pipeline may be considerably greater than zero, there will be a significant temperature differential in the pipe under normal operating conditions. The temperature along a pipe will become high depending on its proximity to a compressor station, and this will result in considerable longitudinal expansion of the pipe. As the resistance to this expansion is relatively small in areas of weak soil, this longitudinal deformation may become large. This deformation will tend to accumulate at cold bend locations, as the change in direction will create an eccentricity to the thermal load at the bend location. The induced curvature at the bend may become severe enough to buckle the pipe, and this phenomenon has been observed in line pipe under actual field conditions.

In order to soundly understand the behaviour of a cold bend pipe when it experiences the above loading conditions, it is important to have some knowledge of the procedures involved during the formation of a cold bend pipe. This will allow a better understanding of the experimental results that will be discussed later in this report. It is for this reason that a description of the manufacturing and cold bending procedure for line pipe is provided below.

1.2 Manufacture of Line Pipe

The line pipes that were considered in this research program were manufactured using the double submerged arc weld (DSAW) process. In this process the pipe is formed by passing an initially flat plate through a series of rolls and presses until a tubular shape is formed, and then the edges of the tubular shaped plate are welded together in order to maintain its shape. The initial steps in producing the pipe after the plate is received from the plate mill are to inspect the surface of the plate for defects, plane the edges of the plate to become parallel with each other, and to plane the ends of the plate to become square with the edges. Then the edges of the plate are initially curved using edge-crimping rolls in order to better facilitate final forming of the pipe. Subsequently to actually produce the circular shape, the sheet is passed through a combination of rolls and presses that will first bend the sheet into a U-shaped trough, and then form it into a full O-shaped tube.

After the plate passes through the rolls and presses, the O-formed plate is fed into a longitudinal seam-welding machine where the abutting edges of the plate are properly aligned, firmly secured together, and the outside edges are welded together using the submerged arc process. Then the inside edges of the plate are welded together, and after this is accomplished the completed welds are inspected both inside and out. The next step in producing the line pipe is expansion and testing of the pipe. In this step the pipe is mechanically and/or hydrostatically expanded to ensure accurate size and straightness of the pipe, as well as to increase the transverse yield strength of the pipe material. During mechanical expanding, a circular shaped expander die is passed through the inside of the pipe, and this die permanently expands the pipe cross-section to achieve the specified diameter and roundness tolerances. During hydrostatic expansion, the ends of the pipe are sealed by mandrels, and semicircular dies that are slightly larger than the pipe OD are closed around the outside of the pipe. Then the pipe is hydraulically expanded against the dies. After this is accomplished the dies are

opened and a specified internal pressure is applied to the pipe to test the weld for seats or leaks. Subsequently, induction heating is often used to reduce the pipe residual stresses at the seam weld locations. After the initially flat plate is transformed into a circular pipe, it is ready to undergo the cold bending process.

1.3 Cold Bending Machine

A cold bending machine is used to generate the permanent curvature in a cold bend pipe. To the author's knowledge most of the cold bending machines, as shown in Figure 1.3, operate in a relatively similar manner. In general, the same machine may be used for pipes with varying wall thicknesses and grades of material, however each machine will have a limited range of pipe diameters that it can accommodate. Cold bending machines generate the bend in a pipe by applying a three-point bending moment to several locations along the pipe.

The bending moment is applied to the pipe by using three components of the cold bending machine: the pinup shoe, die, and stiffback, as shown in Figure 1.5(a). The die is positioned above the pipe at the precise bending location, and acts as the fulcrum about which the pipe is bent. The portion of the die that contacts the pipe has a relatively large convex radius of curvature in order to reduce the local curvature of the bend.

The pinup shoe is positioned a few pipe diameters from the bending point, and is positioned beneath the pipe. It is approximately one pipe diameter long, and it is circular shaped so that it can saddle the bottom half of the pipe cross-section. The increased contact area provided by this circular shape will reduce the bearing stresses caused by the radial direction loading of the pipe by the pinup shoe. The pinup shoe is lifted upwards during cold bending and is used to press the top of the pipe into firm contact with one side of the die. This vertical motion

is provide by a wedge that is positioned beneath the pinup shoe and is moved horizontally by a hydraulic cylinder during bending, and it is the vertical component of the motion of this wedge that lifts the pinup shoe.

The stiffback is positioned on the opposite side of the die, and one end of the stiffback is located near the bending point. The stiffback is several pipe diameters long, and is saddle shaped so that it can have a considerable contact area with the bottom of the pipe. The stiffback is initially positioned horizontally, and it is tilted during bending in order to generate the bend in the pipe. The tilting motion of the stiffback is provided by two vertically orientated hydraulic cylinders that are positioned near each of its ends. The bend angle generated on the pipe is dependant on the distance that these cylinders are lifted during bending.

In order to prevent cross-sectional distortion during cold bending, a mandrel is positioned inside of the pipe at the bending point. The mandrel is approximately 1.5 diameters long, and is cylindrical in shape with a diameter that is slightly less than that of the pipe. It is connected to a pneumatic pump, and this pump is used to increase the diameter of the mandrel to that of the inside of the pipe. The mandrel is also attached to a motor that can move it to any location along the length of the pipe. During cold bending, the diameter of the mandrel is increased so that it comes into firm contact with the inside of the pipe, and the stiffness of the mandrel will resist the inward radial movement of the pipe wall during cold bending. Then after a bend is formed, the diameter of the mandrel is decreased so that it may be moved to the next bend location.

1.4 Cold Bending Procedure

When designing a cold bend, the engineer will specify the total bend angle required and the bending degree per interval length. This will result in a bend length that is equal to the total bend angle divided by the bending degree per interval length. However, the total bend angle is not generated by a single uniform bend over the total bend length of the pipe, it is in fact a series of several smaller bends, each a fraction of the total bend angle as shown in Figure 1.4. This breakdown of the total bend angle is required in order to eliminate excessive cross-sectional distortion that would otherwise occur during cold bending. The summation of the angles of each individual bend will equal the total bend angle, and the summation of the distances between each individual bend will equal the total bend length. The average bending degree per interval length specified by the engineer is equal to the summation of the distances between individual bends divided by the summation of the angles of the individual bends.

The first step when cold bending a pipe is to remove any debris from both the inside and outside of the pipe in order to ensure that all components of the bending machine can have firm contact with the pipe. The pipe is then positioned so that it contacts the stiffback and die, while the end of the pipe is proximate to the pinup shoe as shown in Figure 1.5(a). The pipe is then rotated so that the seam weld is orientated 90 degrees from the die in the circumferential direction in order to ensure that it will be located at the neutral axis of the bend. This is necessary because the seam weld is the least ductile portion of the pipe, and the strains along the neutral axis of the bend are the smallest. The next steps are to insert the mandrel inside of the pipe, and to insert a donut at the end of the pipe near the pinup shoe. The donut is a steel column that has a length equal to the inside diameter of the pipe and is orientated vertically at the end of the pipe. Its purpose is to prevent flattening at the end of the pipes cross-section during cold bending.

Once the pipe is properly positioned, each bend point is marked on the pipe to aid in its positioning for the rest of the bends. This bend interval typically ranges from 0.5 to 1 pipe diameter. The pinup shoe is then raised, as demonstrated by Figure 1.5(b), until the top of the pipe becomes firmly contacted with one side of the die. Then the mandrel is advanced to the center of the die, and its diameter is increased so that it firmly contacts the compression and tension sides of the pipe. Considerable care is required when positioning the mandrel because a close proximity to the precise bending point will reduce the level of cross-sectional distortion that will occur during bending. Subsequently the hydraulic cylinder at the back of the stiffback is moderately raised until the pipe comes into firm contact with the die at the stiffback side. Finally to generate the bend as depicted in Figure 1.5(c), the hydraulic cylinders on the stiffback are lifted until permanent deformation is produced in the pipe.

After an individual bend is created, the stiffback cylinders are retracted as shown in Figure 1.5(d), and the mandrel diameter is reduced. Then the angle of each end of the pipe is measured with respect to the horizontal. The angle of the pipe near the pinup shoe will likely read close to zero degrees, while the angle of the pipe near the stiffback is the approximate total bend angle. The exact total bend angle is the angle of the pipe at the stiffback minus the angle of the pipe near the pinup shoe. The first individual bend in the pipe is typically generated using a trial and error approach. This is because during each individual bend a portion of the bend is caused by elastic deformation, and the other portion is due to permanent plastic deformation. As the elastic deformation will rebound once the stiffback is retracted, for the pipe must be bent the desired bend angle plus the predicted elastic deformation. It is for this reason that for the first bend the stiffback is only slightly lifted and then retracted until there is only a small amount of permanent deformation, then it is lifted again to provide the desired bend increment. The distance that the cylinders will be lifted will then remain relatively constant for the remainder of the bend increments. After the first bend is generated the pipe is advanced using a boom until the next bending point is

beneath the center of the die, as shown in Figure 1.5(e), and the procedure is repeated until the final bend angle is produced.

1.5 Code Criteria for Cold Bends

The various international codes that were researched for this project demonstrated guidelines for the production of a cold bend pipe. These guidelines varied between the different codes, and none of them discussed the determination of the critical compressive strain for a cold bend pipe. The criteria for the production of cold bends in the Canadian, American, and DNV are overviewed in this section.

1.5.1 CSA Standard Z662-2003

In the Canadian Oil and Pipeline Systems Standard, the code specifies that the use of cold bends in a pipeline is allowable so long as they are subjected to some limitations. The first of these limitations is that after the pipe is bent by the cold bending machine, it must be free from buckling, cracks, and any other indications of mechanical damage. The next limitation is that the out-of-roundness of the cross-section within the bend cannot be detrimental to the structural integrity and normal operation of the pipeline system, and that allowances must be made for the installation of liners and use of internal inspection tools and pipeline scrapers within the bend. In order to ensure that these tolerances are met, it specifies that the pipe bends must have a difference between the maximum and minimum diameters not exceeding 5% of the specified outside diameter, unless the mechanical properties of the bend are otherwise determined to be within acceptable limits. The final limitation of the code is that

for field cold bends of large diameter pipes, the pipe may not be bent more than 1.5 degrees per longitudinal length of pipe equal to its outside diameter.

These criteria for cold bends are further discussed in the Commentary on CSA Standard Z662-03. The commentary clarifies that the buckling that is not permitted during cold bending is referring to a severe condition that is caused by mechanical instability, as opposed to a surface wave or wrinkle that may occur during cold bending operations. These surface waves are allowable because studies have shown that the presence of small wrinkles is unlikely to induce any local yielding that could damage the coating or lead to failure of the pipe through bursting. The commentary also discusses that the origin of the 5% limit on ovality was based predominantly upon studies in the US that indicated that ovality up to 8% of the specified outside diameter of the pipe is tolerable. Finally, the deflection limit of 1.5 degree per diameter of pipe length was adopted from US standards dated from 1968 and the origin of this limit is not indicated in the commentary.

1.5.2 ASME B31.8-1999 Edition

The American Process Piping Standard limitations for cold bends in pipelines are generally less conservative than those specified in the Canadian Standard. Similar to the Canadian Standard, it specifies that cold bends may be used in a pipeline so long as the finished surface is free of cracks and substantially free from buckling. In addition, the minimum required thickness of a bend, after bending, must be enough to ensure that the stresses during operation and loading do not exceed the allowable stress in the pipe wall of the bend. The limitation on the allowable flattening of the bend pipe is that the difference between the maximum and minimum diameters at the bend cross-section cannot exceed 8% for a pipe with internal pressure.

The limitation on the deflection of the cold bend is that the bend radius of the pipe centerline must be greater than or equal to ten times the nominal outside diameter. This is somewhat greater than the limitation specified in the Canadian Standard, and this increase was provided because industry has shown that cold bends bent greater than 1.5 degrees per diameter of pipe lengths can be produced without compromising the integrity of the pipe. In addition to the deflection limit, the maximum strain of the material in a cold bend may not exceed either 5%, or 50% of the specified minimum longitudinal elongation for the applicable specification, grade and thickness, whichever is less. This requirement may be waived if the most severely strained material can retain at least 10% elongation after bending.

1.5.3 DNV OS-F101-2000

The Offshore Pipeline Standard Det Norske Veritas Submarine Pipeline Systems addresses the use of cold bends when designing for offshore pipeline construction. In this standard minor buckles are permitted in the bend inside radius profile, subject to several limitations. The height and depth of the buckle must not exceed 1 percent of the pipe nominal inside diameter, the length to depth ratio of the buckles must be greater than 12 to 1, and the spacing between the minor buckles must be greater than one nominal pipe diameter.

1.6 Straight Pipe Research Literature Review

To the author's knowledge, there has been no previous research prior to the publication of this report that discusses the critical compressive strain;

hereafter the critical strain is used, of cold bend pipes. For this reason a review of some research conducted on the critical strain of straight pipe will be presented. This information will permit a later comparison between the critical strains of a cold bend pipe and a straight pipe. Numerous research works discussing the critical strain of straight pipe has been conducted both at the University of Alberta and abroad. A review of this research is provided by Das, *et al.* (2003), Dorey, *et al.* (2001), and Del Col, *et al.* (1998); and a brief review of some of the research conducted will be discussed herein. Particular attention will be focused on the research conducted at the University of Alberta, as this is the information that the topics of this research will predominantly be compared with. This discussion will be valuable when assessing the reduction in critical strain resulting from the cold bending of a pipe.

1.6.1 Research by Boukamp and Stephens (1973)

The research by Boukamp and Stephens (1973) is presented in a classical paper that discusses the full scale testing of seven NPS 48 pipes. The purpose of their research was to gain an understanding of the load deformation response of the test specimens under combined loads. The test specimens had diameter to thickness ratios of either 82 or 104, and the grade of the materials was X60. The pipes were loaded with either high or low internal pressures, compressive axial loads to represent either a 57 or 32 degree Celsius temperature differential, and with bending moments that were increased until buckling of the specimens occurred. For some of the specimens the bending moment was reversed after buckling, and the reverse curvature of these specimens was subsequently increased until fracture took place.

The results of their experiments demonstrated that the test specimens were extremely ductile, with local buckling occurring at strains much greater than the

yield strain. It was found that low diameter to thickness ratio pipes were more ductile than those with high diameter to thickness ratios. Additionally, the highly pressurized specimens demonstrated an outward bulge shaped buckle while the low pressurized specimens demonstrated an inward-outward diamond shaped buckle. The strains in the extreme fibres of the pipes indicated that a shifting of the neutral axis towards the tensile side of the pipe occurred after buckling, and this was further verified by the observation that the bulge buckles extended over more than 2/3 of the pipe circumference. Finally for those specimens that were loaded with reverse curvature, tearing occurred at the fold of the wrinkle, which indicated that the fracture was caused by a shear mode failure.

1.6.2 Research by Gresnigt (1986)

The research completed by Gresnigt (1986) was carried out to address the sizeable loads that are imposed on pipes situated at river crossings due to ground settlement. He developed a closed form solution to determine the theoretical moment curvature response of a pipe loaded with internal pressure, based on its geometric properties and a bilinear von Mises yield condition material. This derivation neglected cracking or buckling, and the equations demonstrated that the moment capacity as well as the yield curvature of a pipe increases with decreasing internal pressure.

He also conducted in plane bending tests on 13 reduced scale pipes with diameter (152.5 and 122 mm) to thickness (1.55 mm) ratios of 100 and 80, and with internal pressures that resulted in pipe wall hoop stresses of a magnitude between 0 to 80% SMYS (specified minimum yield stress). He indicated that so long as the laws of similarity and scaling-down were accounted for, the results obtained from these reduced scale tests would be applicable to full-size pipes. From testing, it was demonstrated that the moment curvature relationship of the

test specimens deviated from the previously derived theoretical curves at relatively low magnitudes of bending moment. These deviations were due to residual stresses due to welding and rolling, the difference between the actual material properties and the assumed bilinear stress strain relationship, and the effect of ovalization during testing. It was also observed that the bending plane diameter of the unpressurized specimens decreased during testing, while that of the pressurized specimens increased during testing.

To generate predictive equations for the critical strain of a pipe, additional reduced-scale tests were conducted on seventy grade X52 steel pipes with scale factors of between 1:4 to 1:8. Limited full-scale tests were conducted to verify the reduced-scale results, and the buckling curvature of these tests was within the scatter of the reduced-scale test results. The specimens were loaded in bending until local buckling occurred, and the buckling curvature during testing was defined as the global curvature of the pipe at the maximum value of bending moment. On the basis of the experimental data Equations 1.1 and 1.2 have been developed to specify the critical strain for low and high diameter to thickness ratio pipes respectively. These equations provide the basis for the critical strain design equations provided in CSA Z662-2003. For verification, the critical strains calculated using these formulae have been compared with the available experimental results from seven other research projects. The equations generally yielded conservative solutions for the critical strains of the tested pipes.

- for $t / r' > 1 / 60$:

$$\epsilon_{cr} = 0.25 \cdot \frac{t}{r'} - 0.0025 + 3000 \cdot \left(\frac{P \cdot r}{E \cdot t} \right)^2 \cdot \frac{|P|}{P} \quad (1.1)$$

- for $t/r' < 1 / 60$:

$$\epsilon_{cr} = 0.10 \cdot \frac{t}{r'} + 3000 \cdot \left(\frac{P \cdot r}{E \cdot t} \right)^2 \cdot \frac{|P|}{P} \quad (1.2)$$

and

$$r' = \frac{r}{1 - \frac{3 \cdot a}{r}} \quad (1.3)$$

where ϵ_{cr} is the critical strain associated with buckling, t is the wall thickness, r is the average radius, P is the difference between the inside and outside pressure, a is the ovalization, and E is the Modulus of Elasticity.

1.6.3 Research by Mohareb, et al. (1994)

Mohareb, *et al.* (1994) conducted considerable experimental and analytical work on the behaviour of seven NPS 12 and NPS 20 straight pipes with diameter to thickness ratios of 64 and 51 respectively. The specimens were tested under internal pressure, axial load, and in plane bending until they buckled. The internal pressures that were considered caused hoop stresses of either 0% or 80% SMYS, and the axial loads in the tests simulated compression loads resulting from either a 0 or 45 degree temperature differential. They also studied the effect of active and reactive end conditions when applying the axial load. The active condition maintained the axial load as a constant force and a reactive condition maintained the length of the specimen constant. The results of the experiments demonstrated that the highest moment capacity is obtained for the unpressurized specimens, while the lowest was from the fully pressurized (80% SMYS) specimens. Additionally, the longest yield plateau is observed for the fully pressurized specimen and the length of the plateau decreases as the internal pressure decreases.

Their analytical work was conducted to predict the moment capacity of the test specimens. A finite element model was developed to simulate the behaviour of the test specimens. This model incorporated the use of shell elements, the measured material properties, and the boundary conditions and loading sequence that were experienced during experimental testing. The model replicated the

behaviour of the experiments with reasonable results. In addition to the finite element model, they developed an equation to predict the fully plastic moment capacity of a pipe under pressure and axial load. The equation assumes an elastic perfectly plastic material, and neglects both local and global instability. The equation is presented in Equation 1.4 and was verified by their test results. This equation will be employed in Chapter 5 to predict the moment capacity of the specimens tested in this research program.

$$M_p = \cos \left\{ \frac{\pi}{2 \cdot \sqrt{1 - \frac{3}{4} \left(\frac{\sigma_\theta}{\sigma_y} \right)^2}} \cdot \left(\frac{C}{C_y} - \frac{1}{2} \cdot \frac{\sigma_\theta}{\sigma_y} \right) \right\} \cdot \sqrt{1 - \frac{3}{4} \left(\frac{\sigma_\theta}{\sigma_y} \right)^2} \cdot Z \cdot \sigma_y \quad (1.4)$$

where M_p is the plastic moment capacity, σ_θ is the circumferential stress, σ_y is the yield stress, C is the applied axial force, C_y is the axial load under zero circumferential stress, and Z is the Plastic Section Modulus.

1.6.4 Research by Dorey, et al. (2001)

Dorey, *et al.* (2001) conducted a substantial research program on the critical strain of a straight pipe at the University of Alberta. His research included full scale testing, the development of a finite element model, and the development of design equations to predict the critical strain of a straight pipe.

The 15 specimens that were tested in the experimental program were NPS 30, grade X70, had a diameter to thickness ratio of 92, and a length of 2700 mm. Some of the specimens contained a girth weld. The initial imperfections for all of the specimens were measured at several locations along the specimens' profiles. During testing the internal pressure for the specimens caused hoop stresses

ranging from 0 to 80% SMYS, and the axial loads that were applied were either compression forces that would correlate to a temperature differential of 45 degrees Celsius, or tensile forces resulting in a longitudinal stress of 20% SMYS. The specimens were tested under monotonically increasing curvature and the strain in each pipe at the onset of buckling was determined. In addition to the full scale testing, tension coupon tests were conducted on the different materials for the specimens in the testing program.

A finite element model was also developed to simulate the experimental behaviour. The model incorporated the use of shell elements to represent the pipe wall, reproduced the boundary and loading conditions experienced during the tests, and the material models were developed from the tension coupon tests that were carried out. The model also included the precise initial imperfection profile of the pipes that were measured from the test specimens. The finite element numerical results compared favorably with the test results.

A parametric study using the finite element model was completed on additional pipe geometries and loading conditions. Based on this study design equations were developed that could predict the critical strain of a straight pipe. The variables that were considered were diameter to thickness ratio, internal pressure, yield stress, Modulus of Elasticity, and initial imperfection magnitude. These equations were validated against the experimental results with a mean test to predicted ratios of 1.03. Equation 1.5 below is the equation that was developed if the material of the pipe demonstrates a rounded stress strain curve; and Equation 1.6 below is the predictive equation for critical strain if the pipe material demonstrates a yield plateau. Both equations were developed for plain pipes. Similar companion equations were also developed for girth welded pipes. Equation 1.5 will be later used in Chapter 5 to assess the critical strain of the test specimens in comparison to the predicted critical strain for a similar straight pipe.

$$\epsilon_{crit} = \left(\frac{2.94}{D/t} \right)^{1.59} \cdot \left(\frac{1}{1 - 0.868 \left(\frac{P}{P_y} \right)} \right) \cdot \left(\frac{E}{F_y} \right)^{0.854} \cdot \left(1.27 - \left(\frac{imp}{100} \right)^{0.150} \right) \quad (1.5)$$

$$\epsilon_{crit} = 40.4 \cdot \left(\frac{t}{D} \right)^2 \cdot \left(\frac{1}{1 - 0.906 \left(\frac{P}{P_y} \right)} \right) \cdot \left(\frac{E}{F_y} \right)^{0.80} \cdot \left(1.12 - \left(\frac{imp}{100} \right)^{0.150} \right) \quad (1.6)$$

Where ϵ_{crit} is the critical strain over a gauge length of one diameter, t is the wall thickness, D is the diameter, E is the Modulus of Elasticity, F_y is the yield strength, imp is the imperfection magnitude expressed as a percent of wall thickness, p is the internal pressure, and p_y is the internal pressure that causes the hoop stress in the pipe wall to achieve the yield stress.

1.7 Cold Bend Pipe Research

There have been several previous researches conducted concerning the effects of cold bending on the mechanical properties of the pipe. Some of the effects that have been addressed are the residual stress, residual strain, ovalization, initial imperfections, and modifications of the material properties that are caused by cold bending. In addition, full-scale testing of some cold bend pipes under internal pressure and bending loads has been accomplished in some of these research programs. A review of these researches is extremely valuable for validation and comparison with the information that will be uncovered in this research project.

1.7.1 Research by Palynchuk (1983)

Palynchuk (1983) conducted research on the strains caused by the field bending of an NPS 42 pipe. His research was carried out because cracks in the coating of cold bend pipes indicated that the tensile strains caused by bending is not constant, and that it may be difficult to predict the magnitude and distribution of these strains. In order to measure the strains, holes were punched into the pipe along the compressive and tensile longitudinal axes while it was straight. The distance between the holes was measured before cold bending of the pipe, during bending after each bend increment, and following the completion of bending.

The strain measurements demonstrated that there was considerable variation in the tension side strain in the pipe upon completion of cold bending. More importantly, the maximum measured tensile strains were greater than the tensile strains that would be calculated when assuming a constant radius of curvature of the pipe centerline. In addition to this, the strain measurements taken during cold bending indicated that after each bend increment there is initially a small amount of strain in a particular area, and that this strain increases following additional incremental bending operations. These strains would overlap for up to four subsequent bend increments.

During the installation of the pipe into a cold bending machine, the longitudinal seam weld is positioned at the initial neutral axis of the pipe in order to minimize the strains in the weld. However, the distribution of the strains along the compression and tension sides of the pipe indicated that there was a shift in the neutral axis towards the intrados of the bend due to cold bending. This shift in the neutral axis will cause an increase in the strains at the seam weld location, and this behaviour explains the observations by Palynchuk where local buckles are often located along the seam weld of some cold bend pipes.

1.7.2 Research by Wassermann (1983)

Wassermann (1983) conducted an experimental testing program on two NPS 6 cold bend pipes with a nominal wall thickness of 14.3 mm, and a bend radius of 533 mm. These pipes had a nominal room temperature design stress of 154 MPa. The wall thickness of the pipes was measured at several locations around the circumference, and it was determined that there was a thickening at the intrados and a thinning at the extrados of the bend. The ovality of the pipes was also measured and the maximum mid-wall radius was 77 mm while the minimum was 71 mm. In addition to this the residual stresses in the pipes due to cold bending were determined to be as high as 224 MPa compressive and 153 MPa tensile.

The pipes were loaded under four testing conditions: internal pressure alone, bending alone, internal pressure with constant bending moment, and bending with constant internal pressure. The purpose of the experiments was to determine the effects of the ovality in a cold bend pipe on the hoop stresses when it is subjected to the test conditions. The stresses in the pipes were compared to the theoretical stresses that would arise from the same loading conditions with a perfectly circular pipe. During the pressure only case it was found that the hoop stress varied around the cross section, with the maximum stresses occurring at the intrados and extrados of the bend, while the minimum stresses occurred at the neutral axis. For the bending only case it was found that the distribution of hoop stresses was the same as in the pressure only case for opening mode deformation, while for closing mode deformation the sign of the stresses was reversed. Finally for the combined loading test conditions, it was found that a constant bending load does not have a significant effect on the hoop stresses due to internal pressure, while constant internal pressure will increase the hoop stresses due to a bending load.

1.7.3 Research by Shibli (1986)

Shibli conducted research concerning the failure of cold bent boiler riser and supply pipes in power plant boilers. These failures were determined to be attributed to slow crack growth mechanisms, and he conducted tests on several small diameter heavy walled boiler feed pipes to determine their behaviour due to cold bending. As the topic of crack growth propagation is beyond the scope of this report, only the initial measurements of the cold bend boiler feed pipe specimens that were carried out will be discussed. The Radius of Curvature to diameter ratios of the bends were between 2 to 5, and the material of the pipes were HFS35 and 490Nb. In addition to the bend pipes, uniaxially pre-strained coupons with the same residual strain as the cold bends were tested to determine the effects of cold work on the material properties. The residual strains on the extrados of the bends ranged from 13 to 28%. In addition to this, tensile strains were observed at the initial neutral axis, which indicates shifting of the neutral axis during cold bending which is similar to the findings of Palynchuk. Circumferential direction residual strains were determined to be relatively low in magnitude and tensile at the neutral axis and extrados of the bends.

The shape of the bend cross-section after cold bending was half-elliptical/half-circular, with the extrados being half elliptical. The ovality of the pipes was measured along the entire length of bend, and it was found to be near zero at the ends and non-uniform over the middle portion. Wall thinning at the extrados of the specimens was measured to be generally less than 12.5%. The relationship between wall thinning at the extrados and bend ovality was also studied, and this relationship demonstrated that thinning at the extrados of the bend decreases both with increase in ovality as well as in the bend radius of curvature to diameter ratio.

The tensile stress properties of the pipe material were studied for both the cold bend pipes and uniaxially prestrained materials. Both the ultimate tensile

strength and the 0.2% offset yield stress were observed to increase significantly with pre-strain up to 10%. Residual stress measurements were taken on four of the bends using either the center hole drilled or cutting of a strain-gauged pipe technique. These measurements revealed a non-systematic residual stress distribution from bend to bend. The measured residual stresses ranged from 108 MPa in compression at the extrados of the bend to 183 MPa in tension at the intrados of the bend.

1.7.4 Research by Murray and Bilston (1993)

Murray and Bilston (1993) accomplished an extensive analytical research program on the behaviour of cold bend pipes. They developed equations to determine: the magnitude of the springback of the pipe that occurs during the cold bending operation, the required moment to cold bend a pipe, and the residual stresses in the pipe upon completion of cold bending. These equations were formulated for both elastic perfectly plastic as well as strain-hardening materials. They also developed equations to determine the height and wavelength of the imperfections that occur during the cold bending of pipes with high diameter to thickness ratios. The equations that they developed were subsequently compared to the results from three NPS 12 grade X42 pipes that were cold bent under field conditions.

In order to determine the angle of the springback of the pipe during cold bending, it was assumed that the curvature of the pipe centerline prior to the release of the stiffback was the same as that of the die. This curvature was used to determine the strain in the extreme fibre of the cross-section immediately after tilting of the stiffback. The extreme fibre strain after springback was then determined by subtracting the strain released during springback from the strain prior to release of the stiffback. The final extreme fibre strain after springback

was subsequently used to determine to the final curvature of the pipe. The difference between the curvature of the die and the final curvature of the pipe was used to determine the angle of springback of the pipe that occurs during cold bending. The results from their calculations were subsequently compared to that observed during three pipe cold bending operations, with reasonable results.

Their research indicated that the required moment to permanently bend a pipe is provided by the cold bending machine through the load in the hydraulic cylinders of the stiffback and the eccentricity of these loads to the bending point on the die. In order to predict this moment for an elastic perfectly plastic material, they assumed that prior to the release of the stiffback during cold bending, the stresses within the central core of the pipe cross-section were elastic, while the stresses outside of this core were at the yield stress. The force in an element in the pipe wall was then determined by multiplying the stress in the element by the pipe wall thickness and its infinitesimal length. The moment capacity due to this element was then determined as this force multiplied by the distance from the element to the neutral axis of the pipe. In order to determine the moment capacity of the entire pipe, the moment capacity of each element on the pipe wall was integrated around the circumference. Accordingly, the applied moment that is required to be generated by the cold bending machine is presented in Equation 1.7, and it was determined through a summation of the moment capacity of the elastic core added to the moment capacity of the yielded sections of the pipe. The predicted bending moment compared favorably with the applied moments on the pipe during their cold bending experiments.

$$M = 2 \cdot r^2 \cdot t \cdot \sigma_y \cdot \left[\cos \left(\sin^{-1} \left(\epsilon_0 \cdot \frac{R}{r} \right) \right) + \left(\frac{\sin^{-1} \left(\epsilon_0 \cdot \frac{R}{r} \right)}{\epsilon_0 \cdot \frac{R}{r}} \right) \right] \quad (1.7)$$

where M is the applied bending moment, r is the pipe mid-thickness radius, t is the wall thickness, σ_y is the yield stress, ϵ_0 is the yield strain, and R is the radius of curvature of the pipe centerline during cold bending.

The residual stresses due to cold bending are caused by the springing back of the pipe upon retraction of the stiffback. The first step in determining the residual stress distribution of the pipe was to locate the limits of the elastic core of the pipe cross-section by relating the yield strain of the material to the Radius of Curvature of the bend. This allowed the determination of the stress distribution in the pipe immediately after the tilting of the stiffback. The next step was to determine the stress distribution the pipe during the release of the applied bending moment, with the material behaving elastically. This is the stress distribution that is released by the pipe during springback. The residual stress in the pipe is the difference between the stress distribution in the pipe immediately after tilting of the stiffback and the stress distribution in the pipe during the spring back. Murray and Bilston found that the residual strains in the extreme compression and tension fibres are tensile and compressive respectively. In addition, they found that the magnitude of residual stresses are a maximum at the limits of the elastic core, and these stresses are compressive on the compression side of the bend and tensile on the tension side of the bend.

During the cold bending of pipes with high D/t ratios, the pipe will likely develop ripples in the pipe wall. These ripples are orientated perpendicular to the longitudinal axis of the pipe and their height decreases with distance from the intrados of the bend. Murray and Bilston developed a closed formed solution to determine the half wavelength of these ripples. To develop these solutions, they considered a longitudinal strip of the pipe that is restrained by the hoop stresses that result from radial direction deflection. The radial deflection of this pipe was determined from the governing equation for a beam on an elastic foundation and a zero surface load. They determined that the distribution of the ripples in the pipe

could be described as a sine wave that is a function of distance along the axis of the pipe. The equation for the half wavelength of the ripples was developed as presented in Equation 1.8. From this equation it is demonstrated that the half wavelength increases with increasing wall thickness, diameter, and Poisson's ratio. The length from the equation of half wavelength that they developed compared favorable with their experimental results.

$$\lambda = \pi \cdot \sqrt[4]{\frac{t^2 \cdot r^2}{12 \cdot (1 - \nu^2)}} \quad (1.8)$$

where λ is the half wavelength, t is the wall thickness, r is the mid-thickness radius of the pipe, and ν is the Poisson's ratio.

Finally, the authors developed an equation to predict the height of the ripples caused by cold bending. This formulation was developed by assuming that the behaviour of the compression surface of a pipe during bending was similar to that of a cylinder during axial compression. The relationship was derived using a ripple of a wavelength described by Equation 1.8, in combination with the calculated longitudinal shortening of a buckle. It is assumed that the ripple shape takes the form of a sine wave, and the relationship was dependant on the pipe diameter, wall thickness, bending degree / diameter, and the buckling strain. The predictive capabilities of this equation demonstrated good correlation with their experimental results.

1.7.5 Research by Olsen and Clark (1995)

Olsen and Clark carried out an experimental and analytical program to evaluate the allowable ripple height criteria for cold bend pipes that were specified in the various pipeline codes. Their research philosophy was that the

structural integrity requirements for a cold bend ripple is that the pipe must be able to pass a hydrostatic test, that normal pressure variations must be tolerable, and that the pipe must be able to withstand alternating longitudinal stresses due to thermal changes or bending loading. Upon completion of their research they suggested substantial increases in the allowable height of field bend ripples.

The main premise for their experimental program was that the structural degradation for a ripple in a bend is from cyclic longitudinal stresses. To evaluate this they applied an unrealistically large number of large fatigue loading cycles to field bends that would be rejected under the current practice. Their test specimens consisted of NPS 30 and 36 pipes with a maximum ripple height of 11.4 and 15.2 mm respectively. The specimens were cyclically loaded during testing under four-point bending until fracture occurred. It was observed that the specimens could be cycled at a stress range of greater than 135 MPa for over 75 000 cycles without fracture. This is equivalent to a full depressurization from 72% SMYS hoop stress, or a temperature cycling of 58° C, every day for 232 years. This demonstrates that large height ripples may not be overly detrimental to the pipeline integrity.

They also developed a predictive model to assess the life of any cold bend pipe under cyclic loads. This model was based on a damage parameter that was a function of the mean stress, stress range, and initial strain at the ripple. The initial strain on the ripple was assessed based on its height and length, assuming a sine wave shaped geometry. This model reasonably predicted the behaviour of their test specimens. A parametric study was subsequently conducted using this damage model, and it demonstrated that lower wave length to height ratio ripples have shorter lives, heavier walled pipe have longer lives, and the life of the pipe significantly increases as its grade increases.

1.7.6 Research by Rosenfeld, et al. (2002)

Rosenfeld *et al.* (2002) conducted some analytical work involving the allowable magnitude and distribution of the initial imperfections that are caused by cold bending. These limits were determined by establishing the stress concentration factors on bends with varying geometries of initial imperfections, and using these factors to evaluate the fatigue life of the pipes. Their work included a literature review on the ripples that are caused by cold bending, the development of a finite element model to ascertain the stresses in a cold bend pipe with initial imperfections when loaded with internal pressure or bending moment, and a parametric study to determine the effects of imperfection geometry on the fatigue life of the pipes.

Their model incorporated an elastic, small-displacement, shell finite element analysis. As the cold bends considered exhibited a bend radius greater than 30 diameters, the pipes were modeled as straight sections with the imperfections incorporated as deviations from a perfectly cylindrical pipe. A quarter-symmetric pipe was modeled, as the pipes were assumed symmetrical about both the longitudinal and out-of-plane directions. The profile of the model was characterized using a cosine function with varying imperfection amplitude, imperfection period, number of imperfections, circumferential distribution, and longitudinal distribution. The loading conditions considered were internal pressure and in-plane bending. The local stresses obtained from these analyses were compared to the stresses in a perfect pipe under the same loading conditions in order to determine the stress concentration factors for the varying imperfection geometries. The model was validated by applying the stress concentration factors from the models to various design equations that are used for estimating fatigue life, and comparing the theoretical fatigue life to experimental results obtained from their literature review. Good agreement was achieved for the majority of the models in comparison with the test results.

A parametric study was conducted to determine the effect of imperfection geometry on the stress concentration factors. They reported that the stress concentration factors are strongly affected by the imperfection circumferential distribution, the imperfection amplitude, and the pipe diameter to thickness ratio. The imperfection period was demonstrated to only weakly affect the stress concentration factor. From the results of the parametric study, design equations were developed based on pipe and imperfection geometry to determine the stress concentration factor for cold bends when loaded with either internal pressure or in plane bending. Based on their parametric study allowable stress concentration factors for pipes were assessed assuming a service life of 100 years, and using their design equations permitted the establishment of criteria pertaining to the allowable magnitude of initial imperfections due to cold bending.

1.7.7 Research by Fukuda, et al (2002)

Fukuda, *et al* (2002) conducted an extensive experimental testing program on cold bend pipes. Their research also included a material testing program to determine the effects of cold bending on the mechanical properties of the pipe material. Strain gauges were mounted on two pipes of different size, grade, and wall thicknesses while they were straight. These pipes were then cold bent, and the residual strains in the pipes due to cold bending were measured. Material from the pipes at the regions with the maximum and minimum residual strains was subsequently tested in tension. Following this, they expanded the material properties database by prestraining material from the straight portions of the pipes to various residual strains, and testing these materials in tension as well. It was concluded that the yield stress of the material increased for materials with positive residual strains due to work hardening, and that the yield stress decreased for material with negative residual strains due to the Bauschinger Effect. The increase in yield to ultimate stress ratio due to work hardening varied from 0.03 to

0.1, and the decrease in yield strength due to the Bauschinger Effect varied from 6 to 27% for their extreme fibre materials. It was also determined that the yield stress of the material with compressive residual strains reduced dramatically for residual strains between -1 to 0%, and beyond this range the reduction in the yield stress became relatively consistent.

In addition to the material testing, a finite element model was created to simulate the effects of cold bending on the material properties of the pipe. The model included the pipe, pinup shoe, die, and stiffback, and the procedure for creating the bend was similar to the cold bending procedure that is implemented under field conditions. The residual strains of the model were subsequently compared to the residual strains of the pipe and prestrained materials, with good correlation. The model was then used to predict the material properties of the cold bend pipes with varying degrees of residual strain. The behaviour of the model material behaviour was similar to that observed during the various coupon tests, thus validating the material test observations.

Their research also included full-scale bending tests on two NPS 24 grade X80 cold bend pipes that were each cold bent to approximately 9 degrees. One of these pipes was tested in closing mode bending while the other was tested in opening mode bending. The test setup consisted of the cold bend pipe, two moment arms that were connected to the ends of the pipe, and a hydraulic jack. During testing the pipes were pressurized to 40% SMYS, the bottom of one of the moment arms was pinned in place, and longitudinal displacement was applied to the bottom of the other moment arm. The curvature of the specimens was increased until central bend angles of 38 and 65 degrees were achieved for the closing and opening mode specimens respectively, at which point fracture occurred in the pipes. The critical strains of the pipes were not reported.

A finite element analytical model was also generated to validate their experimental tests. The pipes were modeled as a curved pipe with a constant

curvature, and an imperfection of 0.1 mm in wall thickness at the half side of the model. The material at the crotch of the bend was the straight portion material, while the intrados and extrados of the pipes had the tension side bend and the compression side bend material for the closing and opening mode tests respectively. The pipes were loaded with internal pressure, compression load, and applied bending until sizeable end angles were achieved. The load deformation behaviour of the model was similar to that observed during the tests. However, as the model was compared to only two tested pipes, the predictive capability of the model is difficult to ascertain.

1.8 Problem Statement

Numerous tests have been conducted on straight pipes under various loading conditions at the University of Alberta and other places. The tested specimens have been considerably diverse with respect to the geometric properties, material properties, internal pressures, and axial loads during testing. The critical strains of the specimens have been reported, and this has led to a relatively complete understanding of the behaviour of a straight pipe under internal pressure, axial load, and bending moment. In addition to the tests, the initial imperfections in the radial direction of several of these pipes have been measured to assist in determining their role in the buckling behaviour of a straight pipe.

In addition to the experimental tests, several numerical models of straight pipes under applied bending have been created in recent years. The use of the finite element modeling technique, allowed the behaviour of a straight pipe under applied loads to be numerically simulated with reasonable results. The addition of initial imperfections into these models has further increased their reliability. These models have been validated with numerous test results, and are confirmed

to be acceptable in determining the critical strain of a straight pipe under various loading conditions.

Cold bends are frequently required in the design of pipelines in order to change either the vertical or horizontal direction of the pipeline route. These bends are generated by permanently deforming a joint of pipe in a cold bending machine, while limiting the pipe wall deflection in the radial direction. This procedure will produce residual stresses, residual strains, initial imperfections, and modifications to the material properties of the pipe. These numerous changes will cause a cold bend pipe to behave significantly different from the way a straight pipe will react under applied loads.

Over the years numerous local buckles have been uncovered in pipelines at cold bend locations. These buckles occurred because deformations tend to accumulate at cold bends due to the change in the soil resistance to pipe movement that results from the changing of direction. Current code criteria specifies limitations on the allowable bend radius, ovality, initial imperfections, and wall thinning of a cold bend pipe, however prediction methods for the determination of critical strain are not discussed. It is necessary to understand the allowable strain that a cold bend can accumulate prior to buckling in order to ensure adequate maintenance of the pipeline.

For a cold bend that is situated in a region of considerable seismic activity, an earthquake may impose large magnitude deformation on the pipeline that tend to concentrate at cold bend locations. This excessive deformation may achieve magnitudes well beyond the critical strain of the bend and subsequently lead to rupture the pipe resulting in a catastrophic failure. In order to design the pipeline to accommodate this deformation using ultimate limit states design, it is necessary to understand the post-buckling behaviour of cold bend pipes

1.9 Scope and Objectives

This research project was designed to study the behaviour of cold bend pipes under combined loading. Specifically, the strain at the onset of local buckling and the post-buckling behaviour of cold bends will be investigated herein. This was primarily accomplished through the full-scale testing under a variety of loading conditions of eight pipes. The bending procedures of the specimens were studied in order to gain an understanding of the effect of the cold bending method on the critical strain of these pipes. These variations in bending procedure involved modifying the bend increment and bend intervals of some of the test specimens when they were bent with the cold bending machine.

The effects of cold bending on the geometric properties of the pipe were determined upon completion of the cold bending of the test specimens. During cold bending the portion of the pipe towards the extrados of the bend will elongate, while that towards the intrados of the bend will shorten. These residual strains were measured in this research program in order to understand their relationship to the various cold bending procedures. Upon completion of cold bending small ripples are often observed at the intrados of the bend because radial deflection of the pipe wall is not completely eliminated during bending by the cold bending machine. As these initial imperfections may have a significant impact on the critical buckling strain of the pipe, the initial imperfections were measured at several locations around the circumference of the specimens prior to their testing.

During testing of the specimens, the pipes were pressurized and then loaded under monotonically increasing curvature. The test setup was designed to accommodate up to 60 degrees of rotation for each end of the pipe in order to assess the post buckling behaviour of the specimens. Consequently, the curvature of several of the pipes was increased during testing well beyond the formation of the initial buckle, until fracture of the specimen occurred.

The cold bending procedure generates considerable transformations to the mechanical properties of the bend material. This is because the extrados of the bend is loaded beyond its yield stress in tension, while the intrados of the bend is loaded beyond its yield stress in compression. This loading history on the pipe material will modify the behaviour of the bend when it is loaded again, which will influence the critical strain of the pipe. Thus the mechanical properties of the bend material must be understood, and it is for this reason that an extensive testing program was conducted on material from several locations along the test specimens.

Upon completion of the experimental program, a finite element model was developed in order to validate the experimental testing program. The geometry of the model was determined using the information obtained from the initial imperfection measurements. The initial imperfections that were measured prior to testing were input into the model, and their effect on the critical strain was thoroughly investigated. Finally the material properties of the bend material were incorporated into the model, and the critical strain of this model was compared to the models when using the virgin material properties. Once the model could adequately predict the behaviour of the tested specimens, this model was implemented to predict the behaviour of different cold bend pipes under various loading conditions.

In summary, the scope of this research program envelopes:

1. Review of previous research on cold bend pipes
2. Measurement of the residual strains due to cold bending
3. Measurement of initial imperfections in a cold bend pipe
4. Experimental testing of specimens to determine the strain at the onset of buckling

5. Understanding of behaviour of test specimens extensively into post buckling range
6. Determination of variation of material properties along the bend
7. Development of a finite element model of a cold bend pipe
8. Comparison of the model to the experimental test results
9. Assessment of parameters that affect the behaviour of cold bend pipes

1.10 Layout of Report

The remainder of this thesis consists of seven additional chapters. Chapter 2 describes the experimental portion of this research program. In this chapter the experimental parameters, specimen preparation procedures, residual strain measurement, imperfection measurement, test setup, and testing procedure are discussed.

Chapter 3 presents the material testing program of this research. The selection of the material coupon locations from the bend pipes is first discussed. The coupon testing procedure and method of data reduction procedure is subsequently described in this chapter. Finally, an extensive discussion of the test results for each of the coupon locations is covered in the remaining portion of this chapter.

Chapter 4 provides a discussion of the initial measurements and data reduction procedures that were applied to the test results. A comprehensive discussion of the results from the initial measurements, residual strains, and initial imperfection measurements is first detailed in this chapter. This will be followed by a presentation of the equations incorporated during the data reduction, and the methods employed to determine the critical strains of the test specimens.

Chapter 5 involves an analysis of the experimental test results. The chapter begins with a presentation of the predicted behaviour of the specimens. This is followed by a comprehensive discussion of results obtained from the test observations. This will include an evaluation of the specimens' global, local, and post buckling load-deformation behaviours, along with their critical strains.

Chapter 6 contains a presentation of the finite element model that was developed for this research. In this chapter an overview of the finite element method will first be discussed. This will be followed by an outline of the features of the finite element model that was created for this research. This chapter will conclude with the details of the sensitivity analyses that were conducted on the model.

Chapter 7 details the validation of the finite element model with respect to the experimental test results. A description of the reduction of the model data, and comparison of behaviours of the finite element model with the test specimens is presented. This will be followed by a comparison of the model of Chapter 6 to a more comprehensive model that was created in a parallel research program at the University of Alberta. Subsequently, a parametric study on the effects of varying the properties of the model is presented.

Chapter 8 is the final chapter of this thesis. In this chapter the information that is presented in the previous chapters is summarized. Conclusions are subsequently discussed from the results of this research program. Finally, recommendations are presented for future research on the topic of cold bend pipes.

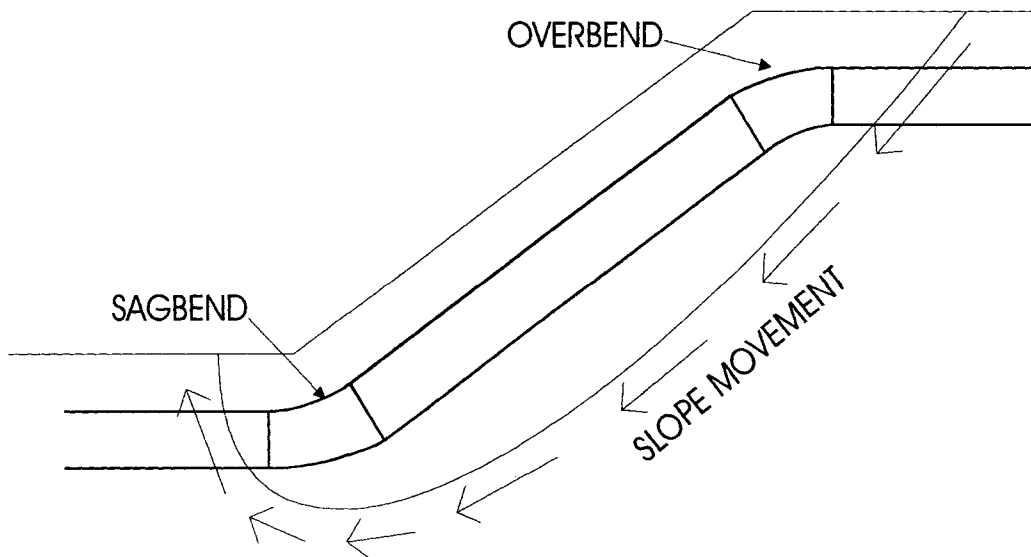


Figure 1.1 – Response of Cold Bend to Slope Movement

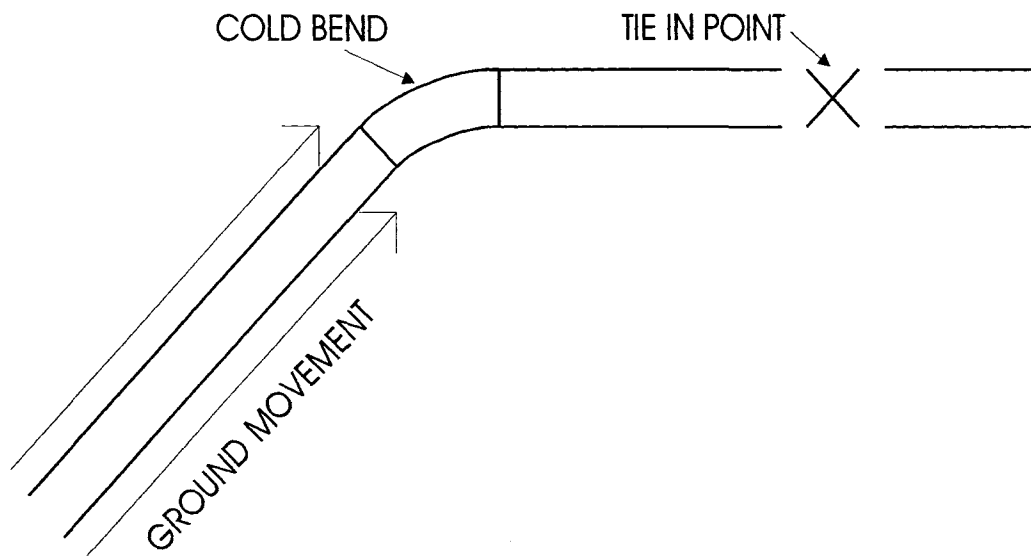


Figure 1.2 – Response of Cold Bend to Horizontal Ground Movement



Figure 1.3 – Cold Bending Machine

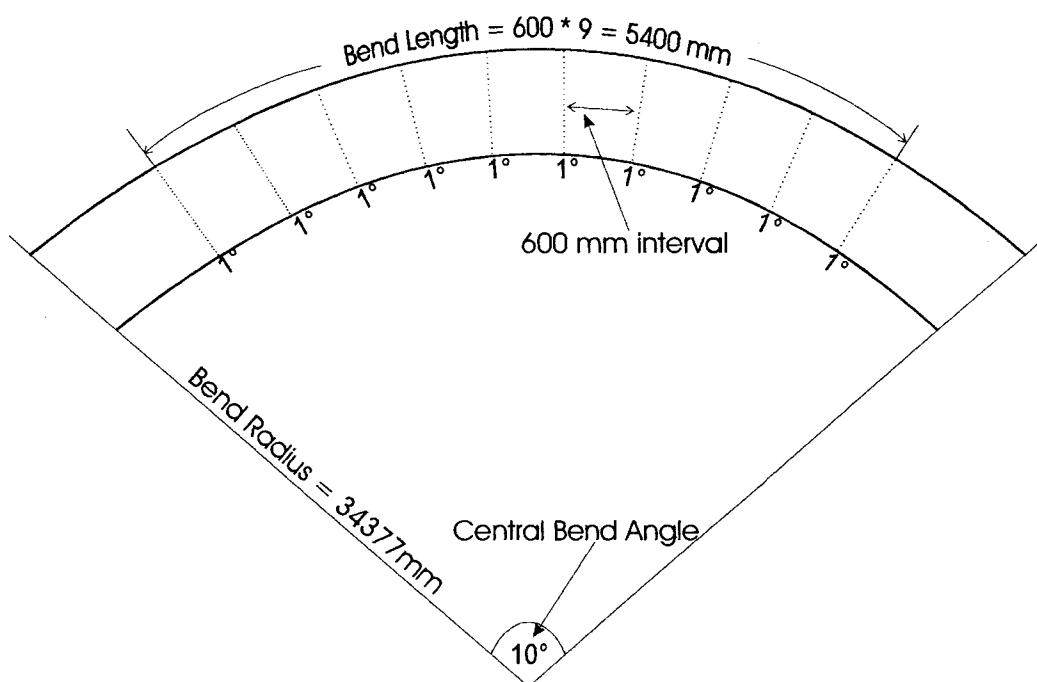


Figure 1.4 – Typical Cold Bend Design

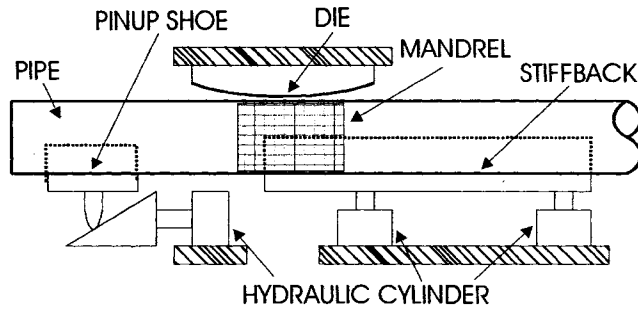


Figure 1.5(a) - Mandrel inserted into pipe at bending location

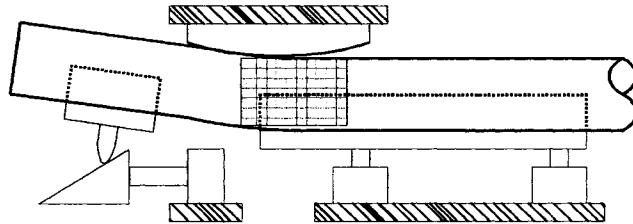


Figure 1.5(b) - Pinup shoe raised

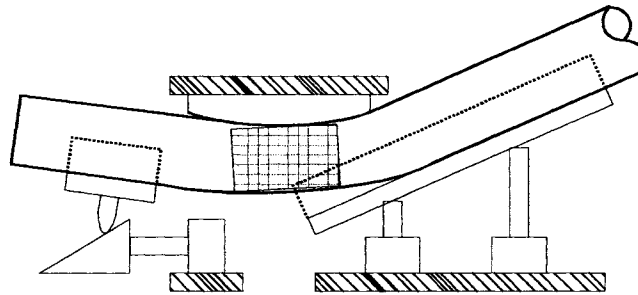


Figure 1.5(c) - Stiffback tilted

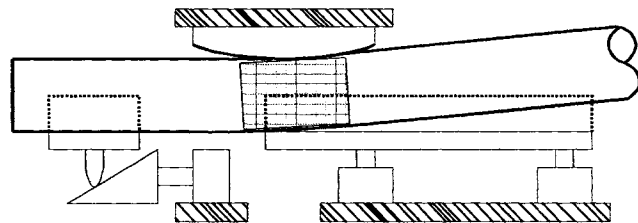


Figure 1.5(d) - Stiffback and pinup shoe retracted

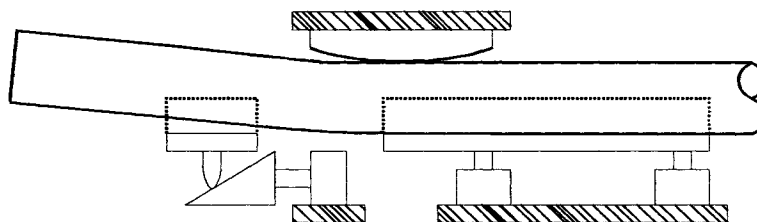


Figure 1.5 (e) - Mandrel removed and pipe advanced

Figure 1.5 – Schematic of Cold Bending Procedures

2.0 EXPERIMENTAL PROGRAM

In order to evaluate the load-deformation behaviour of cold bend pipes, the test specimens for this project were installed into the test setup and loaded under axial load and in-plane bending. Various internal pressures that are similar to pressures used under field conditions were also applied. Sufficient instrumentation was installed onto the specimens and test setup to assess both their local and global behaviours during testing.

For a cold bend pipe exposed to excessive ground movement, the pipe may either experience opening mode or closing mode failure. For the opening mode loading scenario, the intrados of the bend undergoes tension, while the extrados of the bend undergoes compression. This is the case at the overbend for a pipe installed at the crest of a slope, or for the bend section behind the direction of ground movement for a pipe undergoing deformation due to an earthquake. The closing mode condition is where the extrados of the bend undergoes tension, and the intrados of the bend undergoes compression due to the applied load. For the opening mode case, the bend section is axially loaded in tension because on one side of the bend the pipe is longitudinally restrained by the soil, and on the other side the ground deformation is pulling the pipe away from the bend. For the closing mode case the pipe is axially loaded in compression because on one side of the bend the pipe is longitudinally restrained by the soil and on the other side the pipe is loaded towards the direction of the bend by the ground deformation. The latter case is the critical case because the intrados side of the pipe is under axial compression in addition to compression due to bending. It is for this reason that the specimens in this testing program were only tested in closing mode failure.

All testing for this experimental program was conducted at the I.F. Morrison Structures Laboratory at the University of Alberta. A total of 8 specimens were tested each with varying D/t ratios, SMYS (specified minimum yield strength), internal pressures, and bending angle/bend length. The specimens were pressurized, loaded axially, and loaded in bending, within the self-equilibrating frame that is schematically shown in Figure 2.1, in order to establish their load deformation response and critical buckling strain. The curvature was applied to the specimens well beyond the buckling load in order to determine the pipes post buckling behaviour. The applied deformation of some of the specimens was increased until fracture occurred in order to understand the large deformation response of these pipes. Upon completion of the experimental program the results were used to verify the predictive capability of the finite element modeling technique.

2.1 Experimental Parameters

The experimental program was predominantly carried out to determine the moment curvature response and critical buckling strain of cold bend pipes that have various geometrical properties, material properties, bending methods, and circumferential stresses due to internal pressure. These parameters were chosen to best simulate typical pipes that are actually in use for gas transportation. The four specimen parameters studied were: D/t ratio, SMYS, internal pressure, and bending angle / interval length. There were essentially three different sets of specimens tested during the experimental program, with each set having similar geometric and material properties. These specimen sets were labeled after the sponsors of this project as the SNAM, TG, and TCPL specimen sets, after SNAM Rete Gas, Tokyo Gas Ltd., and TransCanada Pipelines Ltd. respectively. The bending properties varied for each specimen in this testing program, as will be discussed in Section 2.1.4.

2.1.1 Geometric and Material Properties

The SNAM set of specimens contained three NPS 30 pipes, which is equivalent to a 762 mm nominal outside diameter. These specimens had a nominal wall thickness of 11.1 mm, which results in a D/t ratio of 69. The grade of these specimens was X60, which is equivalent to having a 414 MPa SMYS.

The TG set of specimens consisted of two NPS 24 pipes, which is equivalent to a 610 mm nominal outside diameter. The nominal wall thickness of these specimens was 14.0 mm, which results in a D/t ratio of 44. The grade of these specimens was X80, which is equivalent to having a 550 MPa SMYS.

The TCPL set of specimens consisted of three NPS 30 pipes. The nominal wall thickness of these specimens was 8.2 mm, and this results in a D/t ratio of 93. The grade of these pipes was X65, which is equivalent to having a 448 MPa SMYS.

2.1.2 Specimen Length

A horizontal length of approximately 7400 mm was used for all of the specimens in this testing program, which is the maximum length of pipe that could be accommodated by the test setup. This specimen length results in a length to diameter ratio of approximately 10 and 12 for the NPS 30 and NPS 24 specimens respectively. The reason that a relatively large length to diameter ratio was required for these specimens is discussed below.

During welding of the endplates to the pipe, residual stresses are created at its ends due to the differential cooling rate of the pipe wall in comparison to that of the thicker weld material. The magnitude of these residual stresses are

significant in comparison with the yield strength of the pipe, and may encourage buckling at the ends of the specimen during testing. This is extremely undesirable because the end buckling failure mode is entirely a result of the test setup, and will not represent the failure mode for a cold bend pipe installed in the field.

The specimens in this testing program have an initial curvature prior to testing; accordingly the eccentricity of the pipe to the jack is greater at the middle of the specimen than at the ends. In addition, the vertical deflection of the pipe during testing is a maximum at the middle of the pipe. For the middle region of the specimen, as the specimen length increases, the initial eccentricity due to cold bending and the vertical deflection during testing will also increase. This will create a larger second-order moment at the middle of the pipe than that at the end of the pipe during testing. The influence of this second-order moment may overcome the effects of the residual stresses at the ends, which will encourage buckling towards the middle of the specimen. This is desirable as the interior of the specimen will have no residual stresses due to the testing setup, and will therefore represent the true behaviour of a cold bend pipe under field conditions.

2.1.3 Internal Pressure

Internal pressure in a pipe causes an outwards radial direction force that presses against the pipe wall uniformly in all directions. For a pipe with a relatively high D/t ratio, the pipe wall will offer little resistance to the bending loads that are caused by this pressure force. For this reason, the forces in the wall due to the internal pressure will predominantly act tangential to the surface of the pipe.

The circumferential stresses that arise from the pressure pushing radially outwards from the inside of the pipe will uniformly increase the pipe radius, thus

introducing tension to the pipe walls in the circumferential direction. Simple statics may be used to evaluate the equation for the stresses in the hoop direction by taking a cut section of a pressurized pipe, and equating the forces in the pipe wall to the applied pressure force inside of the pipe. Solving for the stress in the pipe wall yields the equation for the hoop stress in a pipe due to internal pressure as:

$$\sigma_h = \frac{pD_i}{2t} \quad (2.1)$$

where

σ_h = hoop stress

p = internal pressure

D_i = inside diameter of the pipeline

t = wall thickness

For buried pipelines, the internal pressure also induces stresses in the longitudinal direction. As the pipe expands radially, it will tend to shorten in the longitudinal direction due to the Poisson's effect. However, as a pipe is buried prior to being pressurized, the friction due to the cohesiveness of the soil will restrain the pipe from shortening. This causes tensile stresses in the pipe wall in the longitudinal direction that is described by the equation:

$$\sigma_l = v \frac{pD_i}{2t} \quad (2.2)$$

where σ_l is the resulting longitudinal stress due to the internal pressure, and v is the Poisson's ratio of the pipe wall material.

The internal pressure also acts as a stabilizing force at the inside of the pipe. During loading as the bending strains are increased, the compression side of the pipe will tend to move inwardly during buckling. However, the outward radially acting pressure force will resist the inward collapse of the pipe wall. Thus for a pressurized pipe an outward bulge type buckle is formed, whereas for an unpressurized pipe a diamond shaped buckle is expected to occur.

The internal pressure was applied using water pressure inside the specimens during testing. Water was used to apply the pressure as opposed to the gas that is used under field conditions because in case of a fracture during testing, gas will react with the air to cause a violent explosion while water will simply leak out of the pipe. To apply the internal pressure an inlet hole that was enclosed by the end of the pipe was drilled into one of the end plates. A valve was tapped into this hole to either allow or prevent the flow of water through the endplate. A pneumatic pump was attached to a water line that connected the municipal water supply to the inlet valve. This pump was used to drive the water into the specimen, which generated the internal pressure. For each of the pressurized specimens a hole was flame cut into the specimen near middle of the pipe on the tension side. This hole was required to allow the escape of the air that was contained by the pipe while the specimen was being filled with water. In order to prevent a stress concentration at this location, a thick walled air spout was welded around the hole in order to act as a stiffener. This air spout was grouted so that it could be sealed in order to prevent the flow of water during application of internal pressure, or unsealed to allow the escape of air while the pipe was being filled with water.

Four different internal pressures were used for the eight specimens in the testing program, where each internal pressure was associated with two specimens. These pressures were selected based on limits on allowable circumferential stresses from various international pipeline codes. As a benchmark, two of the specimens were loaded without internal pressure. This condition may occur in a

pipeline in the field during a maintenance operation. For each of the unpressurized specimens, there was an identical specimen tested with internal pressure. This allowed the determination of the effect of internal pressure on the moment curvature response of the pipes. The TG specimens were loaded with an internal pressure resulting in a circumferential stress of 40% SMYS, the SNAM specimens were loaded with an internal pressure resulting in a circumferential stress of 60% SMYS, and the TCPL specimens were loaded with an internal pressure resulting in a circumferential stress 80% of SMYS. These internal pressures are the maximum pressures allowed based on SMYS in a remote location by the Japanese, Italian, and Canadian Pipeline Codes respectively.

2.1.4 Bending Method

The total bend angle and angle/bend length have a significant effect on the response of cold bend pipes under applied curvature. An increase in bending angle results in an increase in the eccentricity of the middle of the bend. The applied moment for a cold bend pipe under field conditions may be described by the equation:

$$M_b = P_a \cdot e_b \quad (2.3)$$

where M_b is the maximum moment at the bend, P_a is the axial load, and e_b is the maximum eccentricity of the bend.

Selection of the overall bend angle used in the testing program involved consideration that the jack load required for the test setup was directly dependant on the eccentricity of the bend. In addition, a sufficient total bend angle was required to ensure that the eccentricity of the middle of the pipe was significantly greater than the eccentricity at the ends of the pipe, in order to discourage end

buckling. Also, to reduce scale effects when comparing the test results to a pipe in the field, it was desired to use bend angles for the specimens that are similar to that of cold bends that are installed in practice. For these reasons the bend angles for the test specimens were between 8 to 14 degrees.

The final bend angle of a cold bend pipe is not achieved by producing a single uniform bend, but is in fact generated by creating a series of multiple kinks. This is necessary to accommodate the limitations of the cold bending machine. After the pipe is aligned in the bending machine, it is bent a fraction of the total bend angle at a point along the pipe. The pipe is then advanced one bend interval, and is bent an additional fraction of the total bend angle. This incremental bending process is repeated until the desired total bend angle is achieved. Once the total bend angle is achieved, the bending degree/diameter is calculated as:

$$\text{Bend Degree / Diameter} = \frac{\text{Diameter} \cdot \text{Total Bend Angle}}{\text{Total Bend Length}} \quad (2.4)$$

The bending degree / diameter may be increased or decreased using either of two methods. The first method is that the bend angle at each bend point may be increased / decreased, and the second method is that the bend spacing may be changed. The bend angle for each individual bend and the spacing of the individual bends depends on the total required bend angle, the available pipe joint length, the bending machine, and economical factors. It is generally more cost efficient to use a larger incremental bend angle with less number of bends. However, this will create higher detrimental stresses to the pipe than if using a smaller incremental bend angle with an increased number of bend intervals. The bending degree / diameter is governed by the various pipeline codes, and the Canadian Pipeline Code CSA Z662-2003 specifies that the maximum degree / diameter for a cold bend pipe is 1.5.

The magnitude of bend angle increment and bending interval may have a significant effect on the critical strain of the pipe. In order to create a permanent bend in the pipe, the pipe must undergo plastic strain at each bending location. This results in residual stresses that exist after the completion of cold bending, and these residual stresses may affect the critical strain. As the magnitude of the bend angle at each bend point is modified, the magnitude and distribution of the residual stresses will also change which may affect the critical strain of the pipe. In addition, because at each bend increment the pipe is bent about a point of relatively small curvature, the strain on the compressive side of the pipe may exceed the critical strain of the pipe at each bending location. This will create permanent ripples at each bending point that serve as initial imperfections in the pipe geometry. Thus the magnitude and distribution of these imperfections will vary as the bending angle per bend point is increased.

The bending degree / diameter for the test specimens ranged from 1.0 to 1.5 degree/diameter. The bending degree / diameter for the SNAM set of pipes was 1.41 for two of the pipes with total bend angles of 11 and 12 degrees. The bend angle increment and bending interval are unknown for these pipes. This set of pipes also contained one straight specimen. The bending degree/diameter for the TG specimens were 1.33 and 1.27 with total bend angles of 10 degrees for both specimens. The first of these specimens was bent approximately 0.75 degrees every 300 mm, while the second specimen was bent approximately 1.5 degrees every 600 mm. The bend angles/diameter for the TCPL pipes were 1.0, 1.5, and 1.5, with total bend angles of 8, 13, and 12 degrees respectively. The first of these pipes was bent 0.5 degrees every 381 mm, while the other two specimens were bent 0.75 degrees every 381 mm.

2.1.5 Axial Load and Bending Moment

There is an axial load on the pipe wall due to the internal pressure because the internal pressure applies a longitudinal direction force against the end plates welded to the specimen. These forces on the endplates produce an axial tension load to the pipe. This tensile load is described by the equation:

$$P_p = p \cdot \frac{\pi \cdot D_i^2}{4} \quad (2.5)$$

where P_p is the axial load due to internal pressure, p is the internal pressure, and D_i is the inside diameter of the pipe.

The axial load in the pipe during testing is a function of the applied jack load and the internal pressure on the specimen. The net axial force during testing is calculated from the subtraction of the axial load caused by the internal pressure acting against the end plates from the value of the axial load supplied by the jack. For those specimens with no internal pressure, the axial load in the pipe is simply equivalent to the applied jack load.

The bending moment in the test specimens is created by applying a compressive axial load on the pipe approximately 600 mm below the centerline, at one end of the specimen. The specimen is restrained from axial direction movement at the same distance below the pipe centerline at the opposite end. This creates a moment at each end of the specimen described by the equation:

$$M_e = P_j \cdot e_e \quad (2.6)$$

where M_e is the bending moment at the ends of the specimen, P_j is the jack load, and e_e is the eccentricity at the ends of the specimen.

This moment is not uniform along the length of the pipe. During testing there exists a moment gradient in the specimen due to the variable vertical profile of the pipe. The first-order eccentricity is the eccentricity at the ends added to the initial vertical deflection of the location of interest along the pipe. The second-order eccentricity is the first-order eccentricity added to the vertical deflection during testing of the location of interest along the pipe. The maximum eccentricity and corresponding maximum moment during testing occurs at the middle of the specimen where there is the largest initial vertical deflection as well as the largest vertical deflection due to loading.

2.2 Test Specimen Preparation

2.2.1 Prior to Delivery

Immediately after cold bending the specimens were approximately 9000 mm long in order to accommodate the cold bending machine, and they were subsequently shortened to a horizontal length of approximately 7400 mm in order to accommodate the testing frame. Preceding cutting of the specimens, considerable care was required to ensure that the center of the bend corresponded to the middle of the specimen. The reason the center of the bend did not initially correspond to the middle of the joint length is because after cold bending each joint consisted of a bend section flanked by two straight segments that were each different in length. To center the bend, the length of each straight segment was cut to become approximately equivalent during the shortening of the specimen. This ensures that the maximum initial vertical deflection will be near the center of the specimen, which will encourage buckling near the middle of the pipe. This was desired because the vertical deflection due to loading is measured at the exact middle of the specimen and at 1016 mm intervals, so if the pipe buckles at the

center interpolation of the vertical deflection at the buckle location may be avoided during determination of the maximum moment of the test.

When the pipe joints were shortened, the ends of the specimen were cut perpendicular to the longitudinal axis of the pipe. This ensured that all axial loads during testing were transferred concentrically through the ends of the pipe. This made certain that there were no additional moments in the pipe wall near the endplates that would occur had the ends been cut differently. The ends of the specimen were also beveled to 60 degrees to facilitate welding of the pipe to the end plates. This was completed to accommodate a full penetration groove weld at the pipe-end plate connection. Using this type of weld ensured that the connection was able to resist the considerable tensile loads that occurred at the ends of the pipe during testing.

Some of the specimens were sandblasted in order to remove the anti-corrosion coating that covered the exterior of the pipes. This simplified the installation of instrumentation as the strain gauges and demec buttons would be mounted directly on the pipe wall. In addition, coating removal was required for those specimens with a relatively thick protective coating in order to facilitate measuring of the initial imperfections.

2.2.2 Initial Measurements

Once the specimen arrived in the structures lab, the first task was to measure the geometry of the pipe. The circumference of the ends of the pipe, and the diameter at four locations around the cross-section, were measured by using a tape measure. The wall thickness at every 45-degree position at the ends of the specimen was measured using a caliper, and the wall thickness at several

locations along the length of the pipe was measured at these same locations by using an infrared thickness-measuring device.

The next step in initial measuring was to determine the locations of the extreme tension and compression fibres of the cold bend specimens. There is no obvious method to determine these locations, and this procedure was important for properly aligning the specimen in the test setup. The first step in accomplishing this task was to position adjustable supports at each end and at the middle of the specimen length. Then with the aid of a surveying level, the elevation of the top of each of the three supports was adjusted so that the top of the pipe was at the same elevation at those three points. This resulted in the direction of the bend of the pipe becoming orientated exactly horizontally with respect to the ground. Then, a hand level was positioned perpendicular to the longitudinal axis at the top of an end of the specimen, and the balanced point of this level was located to determine the neutral axis of the bent specimen. A plum bob was subsequently positioned at this location to determine the opposite neutral axis, and the tension and compression fibres are the points equidistant from the neutral axes around the circumference of the cross-section. This procedure was then repeated at the opposite end of the specimen. Finally, the extreme tension and compression fibres for the entire specimen length were marked by positioning a chalk line at these locations at each end of the specimen.

The length of the tensile and compressive lines, as well as the horizontal lengths was then measured using a tape measure. The neutral axis length was subsequently determined as the length along the seam weld of the specimen. Once all of the length measurements were completed, a square grid was drawn on the compression side of the specimen, along its entire length, for aesthetic enhancement of the buckled specimen. This grid size was 102 mm and 203 mm for the NPS 24 and NPS 30 specimens respectively.

2.2.2 Specimen Instrumentation

Considerable instrumentation was mounted on the specimens in order to understand their deformation response to the applied load during testing. The instrumentation was installed to obtain information during testing about the strains along the pipe, the vertical deflection, the axial shortening, and the rotation of the ends of the specimen during testing. This information was subsequently used to create the graphical plots necessary for comprehending the load-deformation behaviours of the specimens.

Electronic strain gauges were installed at several locations for each specimen in order to determine the strains in the pipe over a gauge length of 5 mm. To measure the tensile strains of the specimen, the strain gauges were spaced at 508 mm for the NPS 30 specimens, and 406 mm for the NPS 24 specimens, on the extreme tension fibre. This is equivalent to a spacing of $2 * D / 3$ for the tension side of the pipe, which is an adequate spacing to capture the relatively smooth strain gradient of the tension side of the pipe during the test. To measure the compressive strains of the specimens, the strain gauges were installed every 254 mm for the NPS 30 specimens, and every 203mm for the NPS 24 specimens, on the extreme compression fibre. This is equivalent to a gauge spacing of $D / 3$ for the compression side of the pipe. Relatively small strain gauge spacing was necessary for the compression side of the pipe in order to ensure that the critical strains near the exact location of the buckle were captured during the test. Strain gauges were mounted at each side of the initial neutral axis near the end of the pipe for both ends. These strain gauges were used to determine the strains that are due to pure axial load, as the bending strains are zero along the neutral axis. Strain gauges were also installed in the circumferential direction at the middle of the pipe. These strain gauges were installed on the compressive line, tension line, and both sides of the initial neutral axis in order to measure the hoop strains due to the internal pressure.

Demec points were installed on the tension and compressive lines of the specimens in order to obtain an analog back up of the strains measured by the strain gauges. Measuring the strains over a longer gauge length is also necessary because after buckling occurs strain gauge readings become very sensitive to their precise location with respect to the buckle location, and may therefore yield unreliable results. The demec gauge length was 254 mm for the NPS 30 specimens and 203 mm for the NPS 24 specimens. Demec points were installed on the extrados of the specimens for the demec strains to be measured every 508 mm for the NPS 30 specimens, and every 406 mm for the NPS 24 specimens. On the intrados of the specimens they were installed for the demec strains to be measured every 254 mm for the NPS 30 specimens and every 203 mm for the NPS 24 specimens. The demec points were positioned so that a strain gauge was located equidistant from each demec point. This was done in order to verify the strain readings of each of the measuring devices. The installation of the strain measuring devices along the compression side of the pipe is shown in Figure 2.2. These demec gauges had a limited range, and this limit was exceeded for those gauges located in the middle portion of the pipe during the tests. For this reason small holes were punched into the pipe adjacent to each demec point. Once a demec gauge reached its limit, the distance between these holes was spanned using a divider. The span of the divider was subsequently measured with a caliper, and this measurement was compared with the initial distance between the holes.

Cable transducers and linear variable differential transformers (LVDT's) were installed to measure the vertical deflection of the pipe during testing. Cable transducers and LVDT's orientated in the vertical direction were spaced every 1016 mm along both the extreme compressive and tension fibres for all specimens. This allowed the vertical profile of the pipe to be measured throughout testing. The cable transducers were aligned so that at each measuring location there was a cable transducer on both the compressive side and tension side in order to verify the deflection results. The two vertical-deflection

measuring locations nearest the nonmoving end were required to be measured by LVDT's, because there were a limited number of cable transducers available in the structures lab. Each cable transducer and LVDT on the compressive line of the pipe was attached to the strong floor of the structures lab, and connected to the pipe via a copper wire to a hook that was tack welded to the bottom of the pipe. The cable transducers and LVDT's on the tension line were attached to a beam located high above the test frame that spanned the length of pipe. These were attached the same way as the vertical deflection instrumentation at the bottom of the specimen. At the center of some of the pipes an additional cable transducer was attached at the bottom of the specimen, a known longitudinal distance away from the cable transducer directly below the center of the pipe. This cable transducer was installed to determine the true vertical deflection at the center of the pipe, as the triangle formed by the two cable transducers could be used to mathematically compensate for any longitudinal deflection that would be measured by these instruments.

The horizontal deflection of the pipe was measured by an LVDT and a series of six cable transducers. The LVDT was installed between the frame at the loading end and the hinge on rollers, in order to measure the stroke of the jack. Cable transducers were mounted at the two top corners and a bottom corner of the end plate that was furthest from the jack. They were connected via copper wires to hooks attached to the jack side end plate that were inline with these cable transducers. These cable transducers were used to measure the summation of the rotation of the two end plates. A mounting bracket independent of the testing frame was installed adjacent to the end plate that was furthest from the jack, and cable transducers were attached to this bracket at locations in line with those on this end plate. These cable transducers were used in order to determine the in-plane and out-of-plane rotation of the end plate furthest from the jack. The rotation of this end plate was subtracted from the summation of the rotations to determine the in-plane and out-of-plane rotation of the jack side end plate.

During testing, considerable tensile loads were applied to the tension members on the testing frame, and large bending loads were applied to the bending beams on the testing frame. For economical purposes, the stresses in the members of the loading frame were designed to approach their yield stress when the jack achieves its load capacity of 4000 kN. As the testing frame is elastic, significant deformation will occur as the jack load increases, with the tension members elongating and the bending members bending during testing. This deformation will create a discrepancy between the measured axial deformation of the pipe and the applied jack stroke, and this difference must be determined. For this reason dial gauges were positioned at the center of the bending beams outside of the loading frame. These gauges were orientated in line with the pipe and were used to measure the longitudinal deformation of the tension members in combination with the bending deformation of the bending beams of the loading frame. These measurements were used to determine the losses in the measured pipe displacements due to the elasticity of the loading frame.

Rotation meters were installed on each of the moment arms of the loading frame. It was assumed that the rotation of the moment arm was equivalent to the rotation of the ends of the pipe. This is acceptable because there was no movement between the moment arms and the pipe, because the pipe was welded to the end plates and the bolts attaching the endplates to the moment arms were pretensioned. These rotation meters were installed to measure the absolute rotation of each end of the pipe.

Pressure transducers were installed in order to measure the jack load and internal pressure of the pipe. The pressure transducer for measuring the internal pressure was located in the line between the water pump and the test specimen. The pressure transducer to measure the jack load was located in the line between the oil pump and the hydraulic jack, and was calibrated using a load cell to convert the measured oil pressure into a force measurement.

2.3 Residual Strain Measurement

During the bending of a pipe in a cold bending machine, the pipe will experience permanent plastic strain. On the extrados of the bend the pipe wall will undergo tensile plastic strain, and on the intrados of the bend the pipe wall will undergo compressive plastic strain. The maximum plastic strains will occur at the extreme fibres of the bend, and there is zero strain along the neutral axis. These residual strains will fluctuate along the length of the bend because the cold bending process does not produce a perfectly uniform curvature in the pipe. Currently little information is known of the magnitude or distribution of these residual strains, and these strains may have an influence on the critical strain of cold bend pipes due to bending. It is for this reason that the residual strains were measured on several of the test specimens in this experimental program.

The residual strains were measured differently for the various sets of specimens tested in this experimental program. For the SNAM specimens they were not measured because the specimens were bent under actual field conditions, where it was not possible to install instrumentation on the pipes prior to bending. For the TG specimens the residual strains were measured using electronic strain gauges, and for the TCPL specimens they were measured using punched holes and a demec gauge, as will be further explained over the following sections. The residual strains were measured in both the longitudinal and circumferential directions of the pipes. They were measured over the middle 2.3 - 2.5 meters of the bend length for all of the specimens for which the residual strains were measured.

2.3.1 TG Specimen Residual Strain Measurement

For the TG specimens, strain gauges were installed on the specimens while the pipes were straight. Uniaxial strain gauges were longitudinally attached to the extreme tension and compression fibres at either 50 mm or 100 mm intervals, over the middle 2.3 m of the pipe. In addition, some biaxial strain gauges were installed in order to determine the residual strains in the circumferential direction. To install the strain gauges the protective coating on the pipes was partially stripped, and the strain gauges were recoated with resin in order to protect them from possible damage inflicted by the cold bending machine. These strain gauges were connected to the data acquisition system while the pipe was straight, and remained connected during the cold bending of the specimens. After the cold bending was completed, the strain recorded by these strain gauges is equivalent to the residual strains of the pipe at the strain gauge locations.

2.3.2 TCPL Specimen Residual Strain Measurement

For the TCPL specimens, holes were punched directly into the specimens while the pipe was straight. These holes were punched at the 0, 11.25, 22.5, 45, 90, 135, 157.5, 168.75, 180, 191.25, 202.5, 225, 270, 315, 337.5, and 348.75 degree circumferential direction positions on the pipe, with zero being the compression line. They were punched at 50 mm intervals over the middle 2.5 meters of the initial straight specimen length. For the determination of the residual strain measuring locations, the tensile and compressive lines were chosen as 90 degrees from either direction of the seam weld, in the circumferential direction.

Punch locations were marked on gridlines along the various circumferential measuring positions that were on the outside of the pipe, and the punches were spaced using a demec standard that was approximately 50 mm long. A marginally longer standard was used for the holes on the interior bend side of the pipe in order to increase the compressive strain measuring range. The holes were punched using a two-step technique, which was necessary in order to obtain repeatable measuring data. A hole was first punched with a relatively blunt conical shaped chisel; then another hole was punched within the first hole with an extremely fine tipped chisel. Using this method allowed the conical shaped demec gauge to fit into the punch, and permitted the tip of the demec to have a very snug fit in the smaller hole. As some blunting of the chisel tips occurred during the hole punching, the chisel tips were continuously sharpened to ensure reliable measuring results. Care was used regarding the depth of these holes in order to minimize the effect of these holes on the load carrying capability of the pipe.

After the holes were punched, the distance between adjacent holes was measured using a 50 mm demec gauge as shown in Figure 2.3. As the fit of the demec gauge into the punched holes was not perfect, it was necessary to measure the distance between adjacent holes repeatedly until two measurements were within ten demec divisions. This error is deemed acceptable, as the distance between adjacent holes will change by hundreds of demec divisions after the pipe is cold bent. The hole punching and measuring was repeated for all 16 circumferential locations for each specimen, and this resulted in approximately 800 residual strain measurements for each pipe. After the pipe underwent cold bending, the distance between the adjacent holes was again at each previously measured location. The difference between the distance between adjacent holes prior to and after bending was used to determine the residual strains in the pipe.

2.4 Imperfection Measurement

2.4.1 Creation of Initial Imperfections

The individual kinks in a cold bend are formed by bending the pipe around the die of the bending machine, until the pipe is permanently deformed. For pipes with large D / t ratios, the pipe wall will local buckle on the intrados of the bend at the bending point during bending, due to the high compressive strains in the pipe that are required for permanent deformation. The extent of this local buckling is reduced by the mandrel that is located on the inside of the pipe during cold bending. The mandrel acts to restrain the pipe wall from deforming in the radial direction towards the centerline of the pipe, however local buckling is not completely eliminated. Thus initial imperfections are created in the pipe during cold bending in the form of small ripples that are created due to the local buckling of the pipe during bending. The magnitude of these imperfections is large enough to be viewed with the unaided eye as shown in Figure 2.4. These ripples occur because the mandrel is not in perfect contact with the pipe wall, and the die is only in contact with the pipe over a relatively short length. The amplitude of these ripples is significantly reduced and distributed over a considerably longer length than if the mandrel was not there.

The imperfections that are formed during cold bending have a significant effect on the moment curvature response of the pipe, and must be measured in order to obtain a reasonable understanding of the pipes behaviour under applied bending. In addition, the magnitude and distribution of the imperfections may vary depending on the pipe geometry, material, and bending method, and the variation of initial imperfections due to these variables is of interest in this project. It is for this reason that considerable effort was made to measure the initial imperfections. The measurements were obtained using an imperfection-measuring device (IMD) that was constructed specifically for this project.

2.4.2 Imperfection Measuring Device

The imperfections on the bent specimens were measured at eight locations in the radial direction on the outside of the pipe surface. They were measured at 0, 22.5, 45, 90, 180, 270, 315, and 337.5 degree locations with zero degree being the compressive line of the pipe. Along with the imperfections, the ovality, global bend angle, and vertical profile were also measured for the entire length of pipe.

The imperfection-measuring device (IMD) consists of a plywood sheet with a circle cut out of it that is large enough for an NPS 30 pipe to fit through it as shown in Figure 2.5. Attached to the inside of the hole at the 135 and 225-degree positions are two 750 mm long steel hollow sections orientated in the longitudinal direction of the pipe. These hollow sections are rigidly attached to the IMD and have rollers that can move in all directions attached at each end. The IMD is supported on the tensile side of the pipe by these rollers. A 750 mm distance between the rollers was selected because this length is sufficient to ensure that the IMD remains perpendicular to the tensile side of the pipe, while not being so long as to be insensitive to the global curvature of the specimen.

The imperfections were measured by LVDT's that are bolted to the plywood sheet at each of the eight measuring locations. These LVDT's are orientated in the radial direction of the pipe, and are each connected to a steel rod with a ball bearing glued to its opposite end. The assembly is bolted to the IMD via a wooden casing that ensures the steel rod and LVDT can only move in the radial direction. It is the ball bearing that makes contact with the pipe, and the steel rod is spring-loaded so that it is in constant contact with the pipe. Thus as the IMD travels along the pipe, the steel rod will move radially as the imperfections are encountered, and the LVDT's will measure the magnitude of these imperfections.

Attached to the bottom of this plywood sheet is a hinge, the bottom of which is perpendicular to the ground and the top of which is perpendicular to the IMD. A rotation meter is mounted to the top of this hinge. This allows the rotation meter to rotate about the hinge pin and measure the global bend angle of the pipe.

Connected to the bottom of this hinge is a sliding rod that only travels in the vertical direction and remains a fixed distance from the pipe tension side. Attached to the bottom of this rod is a cable transducer orientated in the vertical direction. The base of this cable transducer remains a fixed distance from the ground, so therefore as the rod moves up or down, the difference in elevation of the pipe is measured.

The sliding rod is positioned inside of a carriage on rollers that travel along a 4 m long machined rail orientated in the longitudinal direction of the pipe. Attached to the bottom of the carriage is a cable transducer that is orientated in the longitudinal direction and fixed to one end of the rail. This cable transducer measures the horizontal position of the imperfection-measuring device with respect to the pipe. The carriage, rail, and horizontal cable transducer setup are shown in Figure 2.6, and the rotation meter is shown at the top of this figure. The rail is vertically supported by a channel section, and the elevation along the length of the rail was adjusted to accommodate the self-weight of the IMD assembly. The channel section is supported at the two ends by adjustable bolts that were attached to the ground, and were used to level the IMD assembly. The twisting of the channel section was eliminated by a lever arm that extended perpendicular to the rails longitudinal axis, and was supported by the ground.

2.4.3 Imperfection Measuring Procedure

During measuring, the specimen was raised to the required elevation and supported at its ends by the cranes in the U of A structures lab. The elevation of the pipe was chosen so as to maximize the allowable travel of the vertical cable transducer inside of the carriage. The elevation of the ends was carefully adjusted using a level and chain hoists to ensure that the elevation at each end of the pipe was the same. This was necessary in order to accurately measure the maximum initial vertical deflection of the pipe. The pipe was subsequently braced against columns adjacent to each end of the pipe to restrain lateral movement during imperfection measuring.

The rail was positioned so that one end was directly below one end of the pipe, and then the entire length of rail was centered beneath the compressive line of the pipe by using plum bobs at each of its ends. The height of the rail supports was then adjusted so that the elevation of the rail was constant with respect to a surveying level. The twist of the rail was subsequently adjusted by positioning a hand level on the channel section in the out-of-plane direction, and adjusting the elevation of the lever arm attached to the rail until the section was level. Weights were then placed at the end supports of the rail in order to provide stability as well as to resist movement of the rail during measuring.

The imperfection-measuring device was then lifted onto the specimen and connected to the carriage and data acquisition system. The IMD was then pushed to the center of the pipe and the rotation meter was adjusted so as to output a zero reading. This allowed absolute measurement of the initial end angles. The IMD was then pushed to the end of the pipe, and the distance from the LVDT on the neutral axis to the end of the pipe was measured. This measurement was required to determine the vertical deflection of the pipe that the vertical cable transducer did not measure, and was subsequently used to determine the complete vertical

profile of the pipe. The data acquisition system was then set to record one reading every second.

Initial imperfection measurements were obtained by slowly pushing the IMD along the pipe as shown in Figure 2.7. Measurements were recorded approximately every 20 mm in the longitudinal direction of the pipe. Considerable care was taken with respect to the alignment of the IMD in the circumferential direction during the imperfection measuring process. The zero degree LVDT was maintained as near to the compressive line of the pipe as possible, which ensures that all of the other LVDT's were properly aligned. This ensures that the exact location of all of the measurements in the circumferential direction was known during reduction of the data. However, adjustments were necessary to make certain that the LVDT on the neutral axis did not come into contact with the seam weld. This was required because the seam weld would both cover the initial imperfections at the neutral axis and distort ovality measurements. In order to accommodate the process of avoiding the seam weld, one of the LVDT's at the neutral axis was offset 20 mm in the circumferential direction. The effects of this offset on the imperfection results were negligible in comparison with the circumference of the pipe. For those specimens in which the residual strains were measured using the demec gauge, an offset of approximately 10 mm from the proposed circumferential position was required when the punched holes in the pipe used for the residual strain measuring were approached. This was necessary because the residual strain measurements were taken at the same locations in the circumferential direction as the imperfection measurements, and encountering these holes would distort the imperfection measurements.

As the rail for the imperfection measuring apparatus is 4 m long, and the test specimens were approximately 7.4 m long, a longitudinal reset of the rail was required in order to obtain initial imperfection measurements for the entire length of pipe. This was accomplished by first measuring the imperfections over one half of the pipe length, advancing the rail forwards, and then measuring the initial

imperfections over the second half of the pipe. After completion of measuring the first half of the specimen, the resetting process began by pushing the IMD 150 mm past center, and then returning it to center, all the while continuously recording data. This allowed an overlap of measuring data to facilitate the data reduction process. The IMD was then strapped to the pipe using steel bands that were tightened so that the measuring apparatus was locked in place. The rail was subsequently advanced forwards enough so that the carriage could travel to the opposite end of the pipe. Once the rail was advanced, it was positioned beneath the compressive line of the pipe by using plum bobs, and the elevation of each end was adjusted so that the elevation of the rail was the same as prior to the reset. The IMD was then pushed back 150 mm to allow for a further overlap of data. Then measurements were obtained for the second half of the pipe. As the final step, the distance from the neutral axis LVDT to the end of the pipe was measured. Once the measurements were completed, the imperfections over the 300 mm overlap near the center of the pipe are examined to make sure that the results are matching in order to verify that the imperfection measurements were reliable.

After the imperfection measuring was completed, the distance was determined from each LVDT while in the zero position, to the center of the pipe. This was required in order to determine the radius of the pipe at each imperfection location, as well as to use the imperfection measurement results to determine the ovality of the pipe. In order to carry out this procedure, the circle in the IMD was traced onto a plywood sheet and the center of this circle was established. The IMD was then positioned horizontally, and the sheet with the hole outline was laid on top of it. The center of the circle on the plywood sheet was then aligned with the center of the hole of the IMD, and weights were placed on the sheet to secure all components in position. A rod of the same length as the nominal pipe radius was subsequently inserted between the center of the circle and an LVDT. A reading was then taken with the data acquisition system, and process was repeated for the other seven LVDT's. The zero reading distance from centre of the pipe for

each LVDT was then determined by subtracting the LVDT reading during this measuring, from the length of the rod. Once this was accomplished, the measurement of the initial imperfections and curvature of the specimen was completed.

2.5 Test Setup

2.5.1 Self-Equilibrating Frame

A self-equilibrating test setup was constructed for use in this testing program. The loading frame consisted of two tension members that were bolted at each end to a bending beam. The specimens were loaded within this rectangular frame. An overhead view of the as-built frame is shown in Figure 2.8, with the loading jack being situated at the South end of the frame.

A hydraulic jack is positioned at the middle of the South bending beam. During testing this jack was braced against the bending beam on one end, and pushed against a hinge on rollers on its other end as shown in Figure 2.9. This hinge is connected to another hinge by a 125 mm high strength, heat-treated pin. The hinge that does not make direct contact with the jack is then connected to the bottom of a beam that is orientated vertically as shown in Figure 2.10. This beam is used as a moment arm that provides 600 mm of eccentricity to the jack load on the specimen. An end plate is bolted to the top of this moment arm and the pipe is welded to this end plate.

The moment arms in the test setup were required in order to accommodate the 4000 kN load limitation of the hydraulic jack that was used for testing. The eccentricity of 600 mm on the pipe to the load was the minimum eccentricity

required to attain the predicted plastic moment capacity with this jack, for all of the test specimens. This eccentricity was minimized because the applied moment is directly proportional to the jack load and eccentricity, and it is advantageous to maximize the compression load in the test specimens. This is because due to the internal pressure acting against the endplates for those specimens that are pressurized, there was a tensile force in the pipe wall prior to application of the jack load. The magnitude of this tension force may be comparable to the maximum jack load for some of the test specimens. This tensile load on the pipe wall is unrepresentative of a cold bent pipe under field conditions as there are no endplates to resist the pressure forces in the field, thus a pipe under field conditions will actually typically be loaded in compression due to thermal loads. The axial tension in the pressurized specimens is a limitation of the constant moment to axial load ratio loading system used for this test setup, and is for this reason minimized.

At the non-jack side of the test setup as shown in Figure 2.11, the pipe is welded to another endplate. This endplate is bolted to a moment arm that is identical to that on the jack side of the loading frame. Near the bottom of this moment arm is a hinge, and this hinge is connected to another hinge that is welded directly to a deep beam. This beam is the bending beam that is attached to the non-jack side end of the tension members. Longitudinal views of the top and bottom of the specimen while in the test setup are shown in Figures 2.12 and 2.13 respectively.

2.5.2 Test Setup Bracing

Considerable bracing was required on the testing assembly in order to ensure rotation in the specimen was limited to the in-plane direction. Teflon pads were installed at the contact surface with the pipe for all of the braces in order to

minimize friction during testing. Heavy structural steel W-sections was used for all lateral bracing in order to obtain their necessary bending stiffness.

The lateral bracing columns were positioned on each side of the pipes at each of the one-third length locations as shown in Figure 2.14. These columns were employed to restrain the pipe from movement in the out-of-plane direction during testing. Shims were mounted on the columns prior to the start of the test so that there was a close fit between each side of the neutral axis of the pipe and each of the braces. The bottom of these columns was attached to the floor of the structures lab by two pretensioned bolts. These bolts provided the required moment resistance to maintain fixity at the base of each column.

Lateral bracing was installed at each moment arm location in order to restrain the out-of-plane movement of the specimen ends. This bracing was also used to restrain the specimen from twisting about its longitudinal axis. To provide this bracing, columns were bolted to the strong floor of the structures lab near each side of the moment arms. A structural member orientated in the vertical direction was attached to these columns by ready rods as shown in Figure 2.15. These ready rods provided the adjustability required to ensure that the braces could be positioned to establish close contact with the moment arms. This contact was made via two stiffeners on each side of the moment arms, and the vertical distance between the stiffeners provided the eccentricity required to restrain the out-of-plane rotation of the moment arms needed to restrain the pipe from twisting about its longitudinal axis.

During testing, the condition of the moment arm bracing was carefully monitored in order to ensure the ready rods on the braces remained perpendicular to the pipe. This was necessary because the ready rods were applied with large bending loads during axial loading of the specimens due to friction between the moment arms and the brace. In addition, the ready rods were axially loaded from

restraining the lateral movement of the pipe. This loading scenario created a sizeable moment on the ready rods that needed to be considered during testing.

Vertical bracing was provided at the ends of the testing frame in order to resist the upward movement of the frame due to vertical instability of the specimen. This potential movement would occur because of the considerable friction forces that are accumulated in the pin and the hinges during loading. Thus as the pins rotate during testing these friction forces accumulate, and once the forces achieve a sufficient magnitude they will suddenly release. This will induce rotation of the hinges, which will apply considerable vertical forces to the test frame that needs to be resisted. Near the non-jack side of the frame, each tension member was braced from vertical displacement by a structural section that was bolted to the strong floor. At the jack side of the frame, outwards extending steel plates were welded to the hinge on rollers during fabrication of the test frame. A structural section orientated in the longitudinal direction of the pipe was positioned between two columns that were bolted to the strong floor in the proximity of the hinge on rollers. The elevation of this section was adjusted to make contact with the top of the plates on the hinge on rollers, and this section was used to restrain the hinge from vertical movement during testing.

2.6 Experimental Testing Procedure

2.6.1 Alignment of Test Setup and Specimen

Substantial measures were required to properly align the testing frame prior to installation of the test specimens in order to ensure that the load acted through the exact centerline of the pipe during testing. During the initial assembly of the test setup, the tension members were orientated to become

parallel to each other, and the bending members were positioned to become precisely perpendicular to the tension members. This allowed the tension members to be used as a reference plane when aligning the centerline of the specimens. Proper alignment of the specimen centerline in the lateral direction was essential in minimizing the out-of-plane moment applied on the pipe during testing. However, exact alignment was impossible because the hinges were not welded precisely at the center of either the bending beams or moment arms during initial fabrication of the test frame. To compensate for this the slack that existed in the hinges in the lateral location was adjusted to minimize the out of plane eccentricity resulting from initial fabrication of the test setup.

For alignment of the non-jack side, the centre of the hinge and the center of the pipe side of the moment arm were positioned to become equidistant from the tension members in the horizontal direction. Once this was completed hydraulic jacks were positioned beneath the bottom stiffener of the moment arm, towards the pipe side. The height of the jacks was adjusted until the angle of the moment arm was approximately equal to the end angle of the specimen. Wedges were then inserted in the hinge to preserve its position, and the pipe side of the moment arms position was rechecked to confirm that it remained centered between the tension members.

Aligning the jack side of the test frame was considerably more involved because of the additional components of the test setup and the accommodation of the jack stroke. The first step was to position hydraulic jacks at the bottom stiffener of the moment arm towards the pipe side. These jacks were then placed on rollers to accommodate longitudinal movement of the moment arm due to the variability in length of the specimens. The height of the jacks was subsequently adjusted so that the angle of the moment arm was approximately equal to that of the end of the specimen. Following this, the centre of the hinge attached to the moment arm was positioned so that it was equidistant from the tension members. This was then repeated for middle of the pipe side of the moment arm so that the

moment arm became parallel to the tension members. The next step was to position the hinge on rollers to become centered to the jack piston in the lateral direction and install wedges inserted at the hinge to keep everything in place. The final step in aligning the test setup was to recheck the position of all components.

Following aligning of the test frame, the specimen was transferred into the test setup, however aligning of the pipe was a complicated procedure. The first step in accomplishing this was that a circle the size of the nominal pipe diameter was drawn on each endplate. The center of this circle was located in the middle of the endplate in the horizontal direction, and 600 mm from the center of the pin in the vertical direction. These circles become the target locations for the pipe wall at the ends of the specimen. The next step was to support the pipe at its center and the one-quarter length points from each end, by using the crane in the structures lab. Each support consisted of a sling that was attached to a chain hoist that was connected to the crane as shown in Figure 2.16. This support system allowed for the elevation of each support point to be adjusted individually by using the chain hoists, while the crane provided the global vertical and horizontal movement. The end slings were used to adjust the elevation of their respective pipe end, while the middle sling was used to provide longitudinal rotation to the specimen. The specimen was twisted by moving the center chain hoist hook so that it was near the neutral axis of the pipe, tightening the sling, then lifting the chain hoist hook until the pipe rotated the necessary angle.

After the slings were attached, the pipe was transferred to the loading frame. The elevation of the pipe ends was then adjusted using the crane so that they became approximately level to the circles drawn on the endplates. The jack side moment arm was subsequently advanced so that the pipe became contacted with both endplates. The elevation of each pipe end was then adjusted by using the chain hoists, until the pipe walls were aligned with their respective circles. The angle of the moment arms was then adjusted by using the hydraulic jacks on the stiffeners until there was minimal gap between the endplate and the extreme

fibers of the pipe ends. Next, the elevation of each pipe end was readjusted, and the jack side moment arm was again advanced to close any newly formed longitudinal gaps. The next step was to twist the pipe so that the tensile and compressive lines of the pipe were aligned with exact top and bottom of the circles respectively. The final steps were to restrain the pipes longitudinal movement by advancing the jack piston until it contacted the hinge on rollers, and to laterally brace the pipe ends against the end plates so that they were supported in all directions during initial tack welding. It is important to note that due to the cold bending process the ends of the pipe become ovalized, while during alignment of the specimen the ends are to correspond with circles drawn on the endplates. It is for this reason that the location of the ends of the pipe were adjusted so that at the pipe wall was an equal distance outside of the circle at each neutral axis, and was an equal distance inside of the circle at each of the extreme tension and compression positions.

After the pipe was properly aligned, it was prepared for welding to the end plates as shown in Figure 2.17. This was a considerable task as the tensile load at the top of the specimen was approximately equal to that of the jack load, which could achieve a magnitude as high as 4000 kN. To accommodate this load, a full penetration groove weld was used to connect the pipe to the endplates. Using this type of weld ensured that the strength of the connection was greater than the tensile capacity of the pipe wall. In addition, the end plate is grade 50 ksi, while the pipe grades ranged from 60 to 80 ksi. This difference in material grades brought about compatibility difficulties with respect to the bonding of the weld material to the pipe and end plate surfaces. In order to ensure that there was adequate bond between the three contact surfaces, considerable effort was utilized in providing sufficient preheat to both the pipe and the endplates immediately prior to welding. This strengthened the bond strength of the weld material to the pipe and end plate to ensure that this bond was greater than the tension strength of the base metal.

2.6.2 Prior to Loading

After the pipe was welded to the endplates, the specimens that were to be pressurized were filled with water. Then the jack piston was retracted, and the resulting space between the hinge on rollers and jack piston was filled with metal plates. This was accomplished in order to maximize the available jack stroke. During the initial test setup it was discovered that the jack piston would not make uniform contact with the metal plate attached to the hinge on rollers because of warping in the plate that occurred when it was welded to the hinges. This was very consequential as this would lead to eccentric loading on the hinge, which could create a lateral instability on the hinge during loading. For this reason several thin foil shim plates were inserted in the spaces at this contact region until all gaps were filled. After this was completed, the cable transducers, LVDT's, and rotation meters were mounted in the setup, and subsequently connected to the data acquisition system.

The final step prior to testing of the specimen was the installation of the end collars, which were required in order to prevent end buckling as shown in Figure 2.18. These were required because as the pipe is pressurized the diameter will tend to increase due to the radially acting internal pressure, however, as the ends of the pipe were welded to the endplates the diameter was fixed at these locations. This would generate local stresses in the pipe wall at the proximity of the endplates. Thus the combination of residual stresses due to welding and the local stresses at the ends of the specimen may reduce the strength of the cross section sufficiently to bring about end buckling. The installation of the end collars served to stiffen the ends of the pipe so that bending strength of the ends became greater than that of the middle region of the specimen.

The end collars are sections of line pipe of the same diameter as the tested specimen and are 150 mm in length. These sections were cut into two half sections, and the ends were pried apart so that they could more readily be installed

onto a test specimen. Steel flanges were welded to each end of the collars and bolt holes were drilled into these flanges. Once the collars were mounted they function as stiffeners to the ends of the pipe, and prevent any bulge buckling in their vicinity. Due to the relatively long length of the specimens, two collars were used for the NPS 30 specimens in the testing program. This was necessary because the end effects were sufficiently substantial that end buckling would occur if only one collar was installed at each end.

Installation the end collars was a relatively involved process. The first step was to loosely mount the collars to the ends of the pipe, and position the seam weld into the space between the two half collars. Then the bolts on the flanges were tightened so that the space between the two half collar was roughly equivalent at each side. Due to the ovalization of the pipe during the cold bending process, it was discovered that the collars would not become snug around the entire pipe regardless of the tightness of the bolts. Consequently, there was a gap between the bottom of the pipe and the collars, and this gap varied along the length of the collar. This is detrimental to the integrity of the ends of the pipe during testing as the collars stiffen the pipe by resisting radial direction deformation of the pipe wall. To minimize the consequences of the existence of this gap, the tightness of the bolts on the flanges was adjusted so that the space was uniform over the entire length of the collar. Once the collars were in the proper position, the bolts were loosened so the pipe could be pressurized. This was necessary because as the pipe is pressurized the diameter will tend to increase; however, the pipe diameter would be restrained from radial deformation at the collar positions if they were tight. This would generate bearing stresses at the edge of the collars that, in combination with the jack load and residual stresses due to the welding, could encourage buckling at the edge of the collars.

2.6.4 Application of Load

Immediately prior to application of the load, the initial demec, caliper, and electronic readings were recorded. Then the internal pressure was applied to the specimen. Demec and electronic readings were subsequently measured again in order to obtain initial readings for the strains due to bending alone. Following this, the collars were tightened so that all of the bolts on the flange were snug, but in minimal tension. Attention was required to ensure the collars were in minimal tension because if they were excessively tightened, they would induce bearing stresses on the ends of the pipe that would encourage end buckling.

After the collars were tightened, the pipe was loaded with the hydraulic jack. This applied a bending moment to the pipe cross-section equal to the jack load multiplied by the sum of the initial moment arm and the vertical deflection of the specimen. For the unpressurized specimens the jack load also applied axial compression to the pipe. For the pressurized specimens, the jack load reduced the magnitude of the axial tension force in the pipe wall due to the internal pressure acting against the end plates.

The jack load was increased at approximately 100 kN intervals during the elastic phase of testing. After each stoppage in loading, water was drained from the specimen to reduce the internal pressure to the initially prescribed testing pressure. This was necessary because prior to buckling, the overall volume of the pipe decreases because of the axial shortening caused by the applied compressive load. As the volume of the water inside the pipe remains constant during loading, the internal pressure generated from the water inside of the pipe increases as the jack load is increased. Electronic readings were taken at each jack stoppage after the pressure was reduced. Demec readings were measured three times during the elastic phase.

The behaviour of the specimen as yielding began to occur was of substantial interest in this testing program. The vertical deflection of the center of the pipe versus the jack load was monitored during testing. Once this relationship became non-linear, this indicates that the specimen was yielding at some locations. In addition, once any strain gauge measured 2500 microstrain, this indicates that the specimen was no longer elastic throughout. At this time the loading increments were dropped to approximately 50 kN. For the majority of the specimens, yielding initially occurred in the section of pipe immediately adjacent to the end collars. This is because due to the applied bending moment the specimen tends to ovalize as the stresses in the extreme fibers approach the material yield stress. However, as the pipe is welded to the end plate and the collars are installed prior to application of bending loads, the cross section maintains its circular shape at the ends. Therefore, adjacent to the collars there is a transition zone where the pipe cross-section transforms from circular to ovular. This results in a relatively abrupt geometry change that attracts load to this location.

After the strains at the ends approached the yield strain, measures were taken to discourage buckling at the ends of the specimen. The first action was to loosen the end collars until there was minimal tension in the bolts attached to the flanges. This was necessary because the tension in these bolts would build up while the collars restrained the ovalization of the specimen. Once the collars were loosened, the specimen would gradually ovalize over the length of the collars, as opposed to immediately adjacent to the collars where the pipe is not stiffened. This action reduced the likelihood of buckling adjacent to the collars. In addition to loosening the collars, the lateral bracing on interior of the pipe length was removed from one side. This bracing was removed because it serves as a stiffener to the cross section of the pipe as it does not permit the lateral expansion of the specimen that is necessary for ovalization to occur. Since the moment resistance of an ovular cross section is less than that of a circular cross section, buckling in the middle section of the pipe would be encouraged if it were permitted to

ovalize. The bracing was removed from only one side of the specimen because during testing the pipe tends to lean to one side, and it would be unsafe to remove the bracing from that side as the pipe could suddenly shift if it was removed.

As the peak moment was approached, the load resistance of the specimen begins to decrease immediately following the application of the jack load. This is due to the redistribution of strain towards the buckled region from the remainder of the specimen. As the stiffness of the buckled region is less than that of the rest of the pipe, and the jack maintains the deformation of the specimen, the load capacity of the pipe will decrease proportionally to the strain reduction in the non-buckled regions. In order to capture the dynamic as well as static loads in the specimens, electronic readings were taken immediately after the jack loading was stopped, and again after the load stabilized. Demec readings were taken approximately three times during the yielding stage.

Once the peak load was achieved, the loading method was changed to stroke control. That is, the longitudinal movement of the hinge on rollers was monitored, and the specimen was loaded by increasing the jack stroke until the hinge travels a specified distance. This loading method was necessary because as the stroke is increased the specimen's load resistance decreases after the peak moment is achieved, and therefore load control is no longer a suitable parameter for controlling the jack load increment during the test. The stroke was incremented at 1 mm intervals immediately after buckling, and the increments were gradually increased to 20 mm after the load-displacement curve became relatively predictable. After the specimen buckles, the diameter of the pipe at the buckled region increases as the specimen is loaded. This results in a greater overall volume, which results in a decrease of internal pressure. For this reason, at each stoppage in load the internal pressure was increased to the proposed testing pressure after buckling occurred. Demec and caliper readings were measured approximately four times during the unloading stage of the test.

2.6.5 Jack Resetting

One of the objectives of this testing program was to determine the post buckling behaviour of cold bend pipes under applied bending. This would enable the understanding of the response of a buried pipeline very near the proximity of a catastrophic natural occurrence such as a massive slope failure or earthquake, where large scale deformation would be applied to the pipe. This is a major reason why the self-equilibrating frame was constructed for this testing program as compared to utilizing a previous pipe test setup from the U of A. This test setup in this experimental program could accommodate rotations at the hinges of up to 60 degrees, as well as limitless vertical deflection of these specimens.

For the majority of the tests, it was desired to deform the specimens until either the pipe fractured, or the axial deformation limit of the test setup was reached. As the necessary axial deformation to fracture the specimens was greater than the maximum jack stroke of 300 mm, resetting of the jack was required for several of the tests. The jack was reset between two to six times for the TG and TCPL tests, and the axial load was not maintained during the jack resets.

The resetting of the jack involved retracting the jack piston once its stroke limit was achieved, and inserting rigid spacers between the piston head and the hinge on rollers. The resetting process commenced with the shutting off the air supply to the jack once the stroke limit of the jack was achieved, as a safety precaution. The next step was to install screw jacks beneath the metal plates that had previously been installed between the jack piston head and the hinge on rollers. These screw jacks provided vertical support to these metal plates that would be required once the jack was retracted. A slight gap was maintained between the screw jacks and the metal plates to ensure that the screw jacks remained perpendicular to the ground as the hinge displaced during unloading. The jack was subsequently retracted at 50 mm intervals. As the jack load was

reduced, the compressive strains in the pipe decreased accordingly. This caused longitudinal expansion of the pipe and a corresponding increase in internal volume, however the volume of the water remained the same. Thus a decrease in internal pressure was observed during the retracting of the jack. Generally for the first two jack resets of each specimen, the internal pressure was increased to the prescribed testing pressure after each jack retraction step.

Once the jack was fully retracted, steel plates were installed to fill the newly formed space between the piston head and the hinge on rollers. The magnitude of this space was always less than the magnitude of the jack retraction distance. This is because due to the internal pressure of the specimen, there is considerable tensile force acting on the endplates. As the stiffness in the buckled region is extremely low, and the tensile axial load is relatively large, there will be considerable longitudinal deformation in this area that will lead to lengthening of the entire specimen. If a third jack reset was required, it was discovered that distance the pipe was rebounding was greater than 75 percent of the retraction distance if the internal pressure was maintained. However, if considerable rebound occurred the deformation of the specimen would increase only marginally after each reset, and the specimen would eventually fail in low cycle fatigue. This is detrimental to the objective of this portion of the project, which was to understand the level of global curvature that could be applied to the pipe before fracture would occur. It is for this reason that after the second jack reset, the pressure was not maintained as the jack was retracted. That is, as the jack was retracted the internal pressure was not increased to the prescribed testing pressure at each retraction interval. This caused a reduction in the tensile load on the endplates during the resetting, and a corresponding reduction of the rebound distance. Using this resetting method, the axial deformation of the pipe became multiple times the magnitude of the maximum jack stroke for several of the tests. Finally after the jack was completely retracted, metal plates were installed between the jack piston and the hinge on rollers as shown in Figure 2.19.

Shimming material was installed between the metal plates and the hinge on rollers to ensure that the hinge was loaded concentrically.

Once the metal plates were installed, the curvature of the specimen could again be increased. The specimen was loaded to a marginal load and demec readings were measured, then the load on the specimen was increased until the load in the specimen was the same as at the level at which the jack reset was required, and demec readings were measured again. Loading was then continued as prior to the reset until either the jack stroke limit was again exhausted, or failure in the specimen occurs. Once failure in the specimen occurred or the axial deformation limit of the test setup was achieved, testing of the specimen was completed.

Table 2.1 - Proposed Test Specimen Properties

| Test Label | Diameter (mm) | Thickness (mm) | Material Grade | Pressure (MPa) | Bend Angle (°) | Degree/Diameter ¹ | Horizontal Length (mm) |
|------------|---------------|----------------|----------------|----------------|----------------|------------------------------|------------------------|
| SNAM1 | 762 | 11.1 | X60 | 7.2 | - | - | 7480 |
| SNAM2 | 762 | 11.1 | X60 | 7.2 | 12 | 1.41 | 7480 |
| SNAM3 | 762 | 11.1 | X60 | 0 | 12 | 1.41 | 7480 |
| TG1 | 610 | 14.0 | X80 | 10.1 | 10.5 | 1.33 | 7480 |
| TG2 | 610 | 14.0 | X80 | 10.1 | 10.6 | 1.27 | 7480 |
| TCPL1 | 762 | 8.2 | X65 | 7.7 | 9 | 1 | 7480 |
| TCPL2 | 762 | 8.2 | X65 | 0 | 14 | 1.5 | 7480 |
| TCPL3 | 762 | 8.2 | X65 | 7.7 | 14 | 1.5 | 7480 |

Notes:

1. Incremental Bend Angle * Nominal Diameter / Bend Interval Length.
This property was not measured for the test specimens

Table 2.2 - Measured Test Specimen Properties

| Test Label | Diameter (mm) | Thickness (mm) | Material Grade ¹ | Pressure ² (MPa) | Bend Angle (°) | Horizontal Length (mm) |
|------------|---------------|----------------|-----------------------------|-----------------------------|----------------|------------------------|
| SNAM1 | 759.6 | 11.48 | X60 | 7.52 | - | 7390 |
| SNAM2 | 759.7 | 11.55 | X60 | 7.50 | 11.9 | 7356 |
| SNAM3 | 760.5 | 11.36 | X60 | 0 | 12.2 | 7407 |
| TG1 | 607.9 | 14.19 | X80 | 10.00 | 10.1 | 7305 |
| TG2 | 608.2 | 14.17 | X80 | 9.85 | 10.2 | 7490 |
| TCPL1 | 761.5 | 8.29 | X65 | 7.34 | 9.4 | 7391 |
| TCPL2 | 760.2 | 8.34 | X65 | 0 | 13.7 | 7389 |
| TCPL3 | 761.0 | 8.36 | X65 | 7.64 | 13.2 | 7373 |

Notes:

1. Actual material properties have been determined in material testing program of this project.
2. Internal pressure in specimen at time of buckling during test.

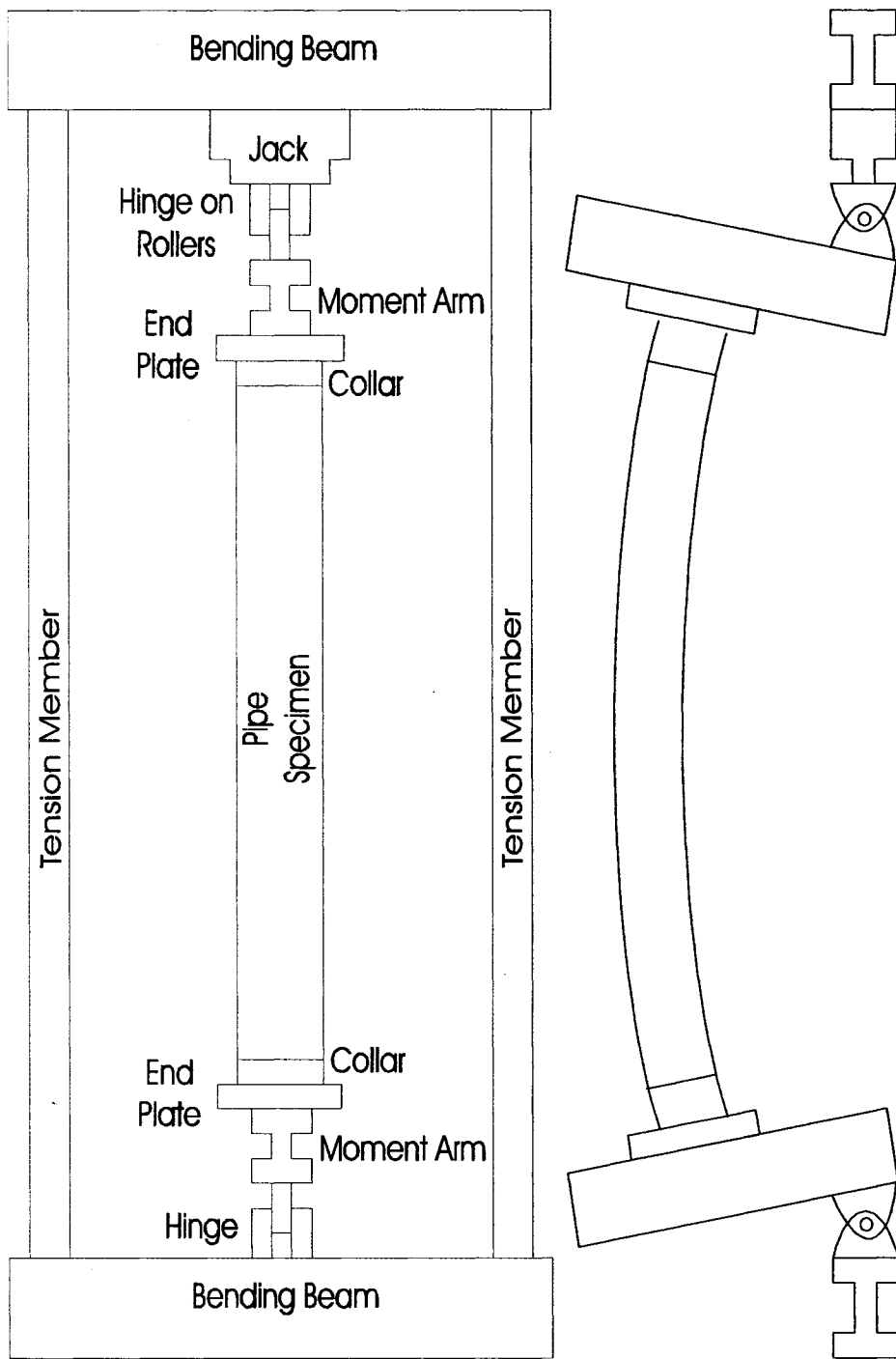


Figure 2.1 – Schematic of Test Setup

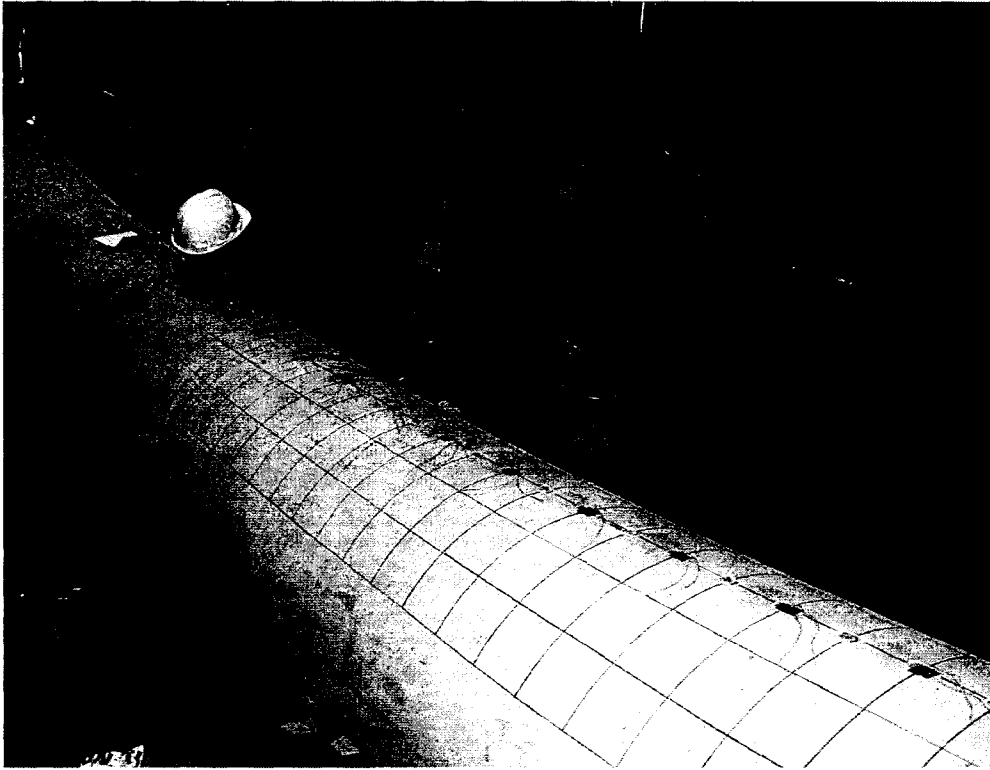


Figure 2.2 – Strain Measurement Instrumentation



Figure 2.3 – Measurement of Residual Strain



Figure 2.4 – Initial Imperfection due to Cold Bending

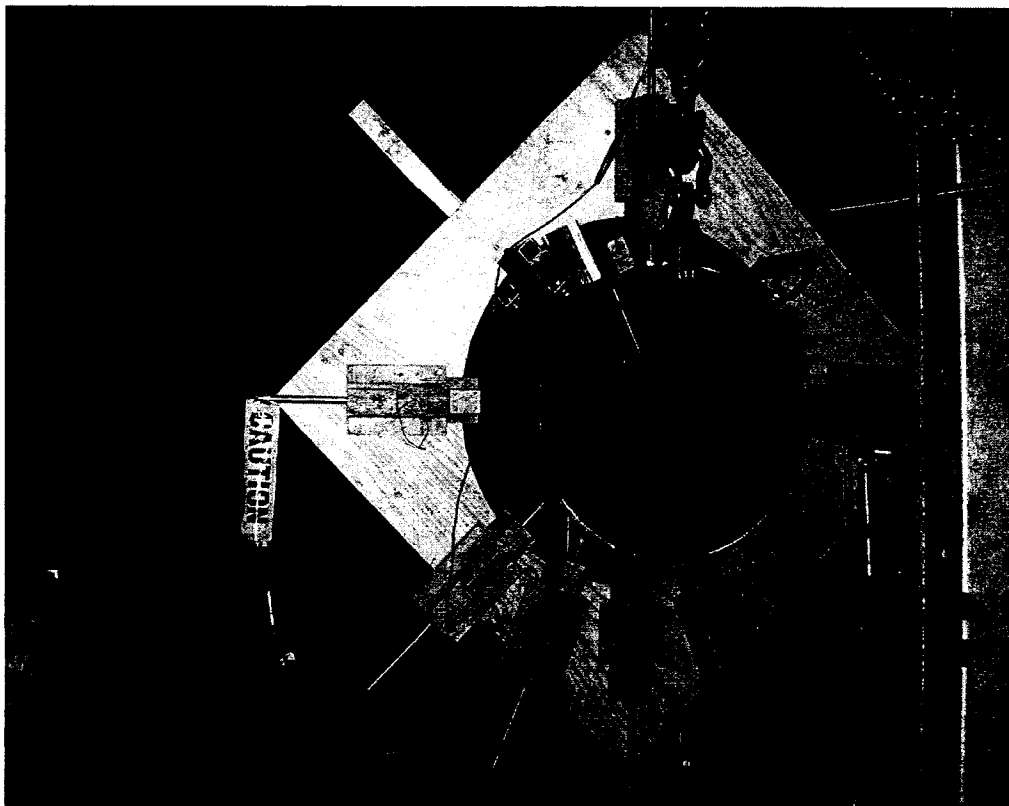


Figure 2.5 – End View of Imperfection Measuring Device

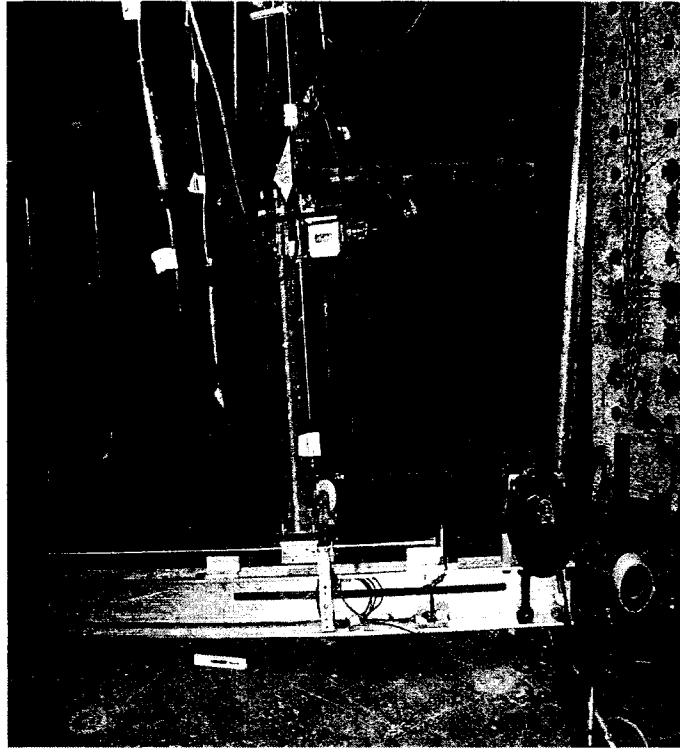


Figure 2.6 – Imperfection Measuring Device Carriage

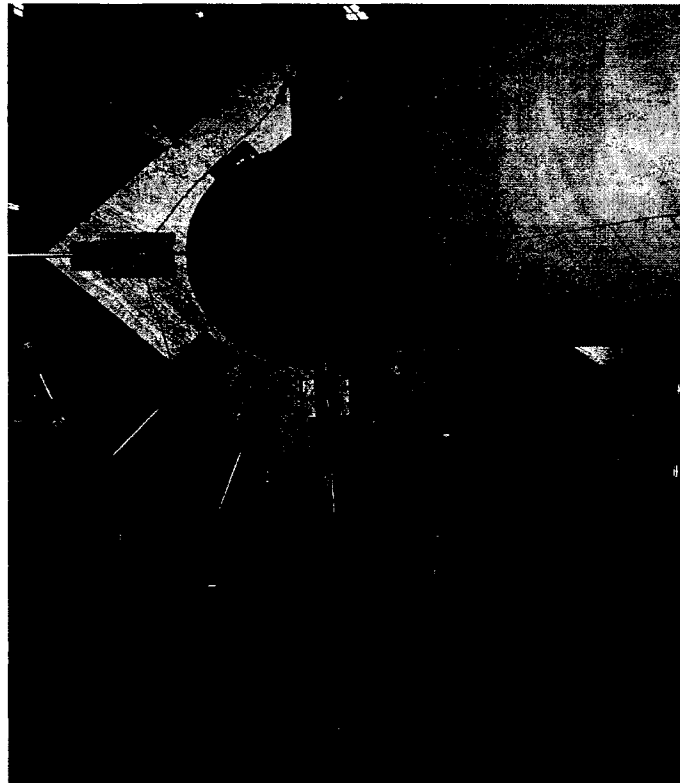


Figure 2.7 – During Initial Imperfection Measuring



Figure 2.8 – Overhead of Test Setup

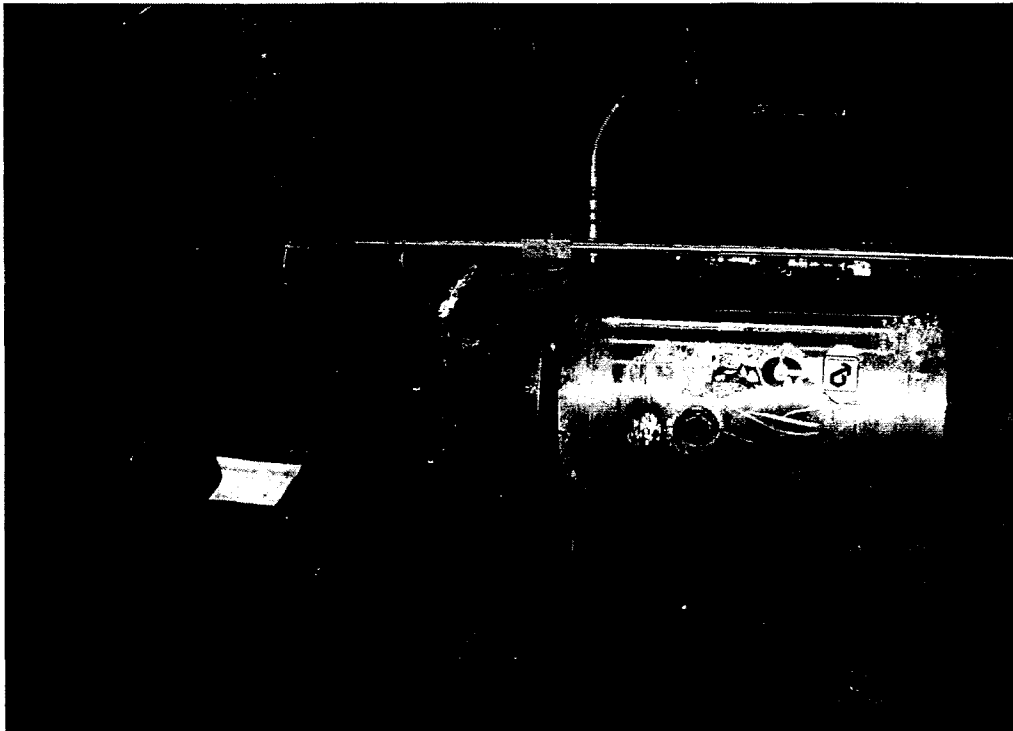


Figure 2.9 – Test Loading System



Figure 2.10 – Jack Side End of Test Setup



Figure 2.11– Non-jack Side End of Test Setup



Figure 2.12 – Longitudinal Tensile Side View

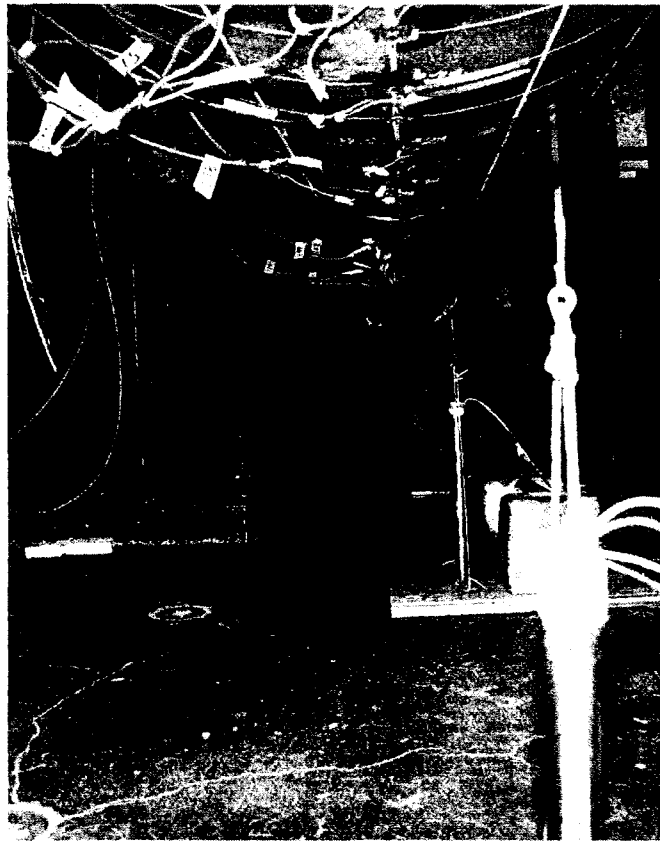


Figure 2.13 – Longitudinal Compression Side View

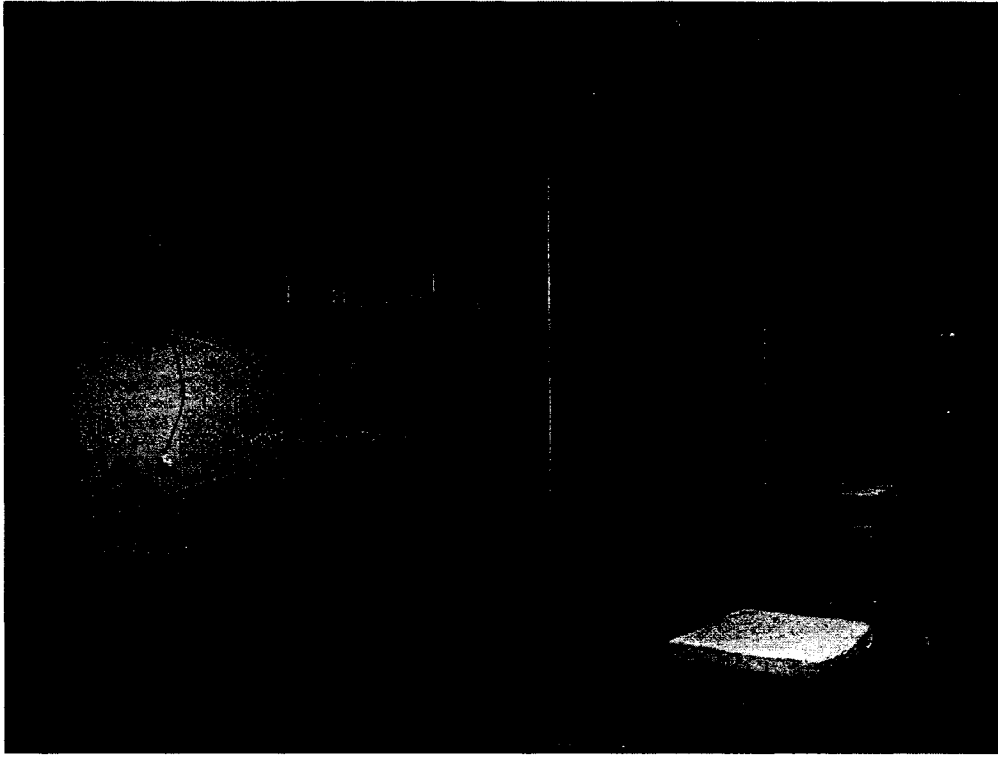


Figure 2.14 – Interior Lateral Bracing



Figure 2.15 – Bracing at Jack Side of Testing Frame

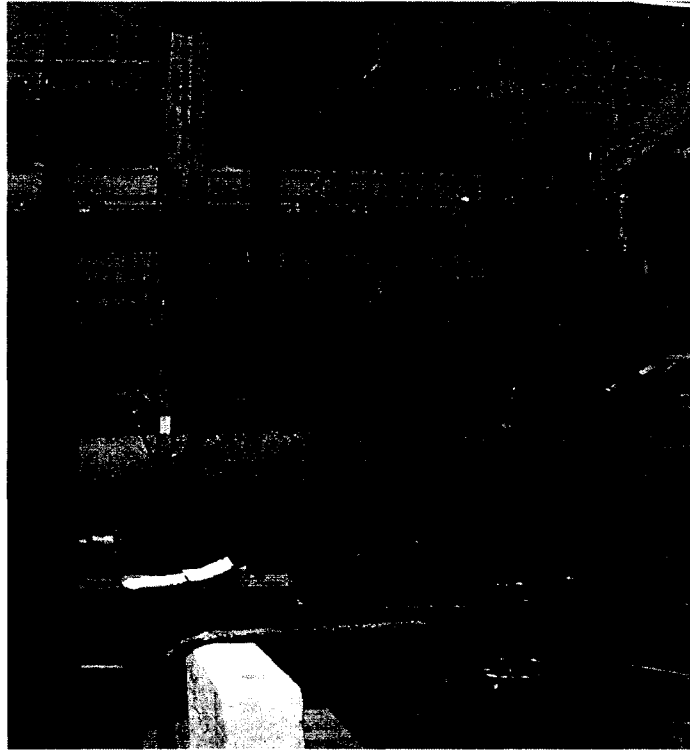


Figure 2.16 – Aligning Specimen

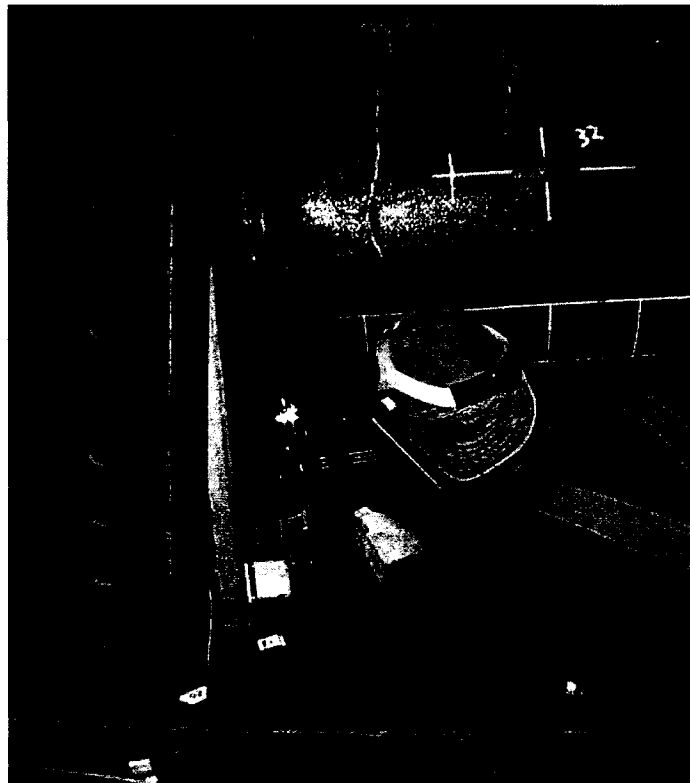


Figure 2.17 – Welding of Specimen to End Plate

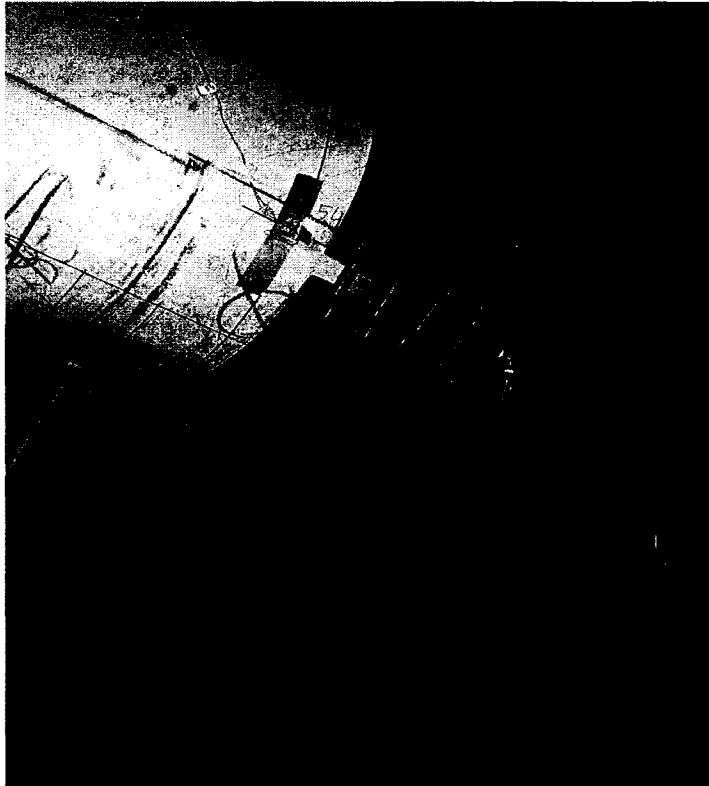


Figure 2.18 – End Collars



Figure 2.19 – Resetting Jack Stroke

3.0 MATERIAL TESTING PROGRAM

The material testing program for this project was conducted in order to determine the effect of cold bending on the material properties of the pipe. In order to create a permanent bend, plastic tensile deformation is induced on the extrados of the bend, and plastic compressive deformation is induced on the intrados of the bend. If closing mode deformation is applied to the cold bend, the tensile side of the pipe undergoes additional tension, and the compression side of the bend undergoes additional compression. This results in changes to the stress-strain behavior of that material due to work hardening if the cold bend is loaded beyond its yield strain. For the case of opening mode deformation on the cold bend, the tensile side of the bend undergoes compression, and the compressive side of the bend undergoes tension. This causes the material to experience the Bauschinger effect if the cold bend is loaded beyond its yield strain. These changes in material properties may have a significant impact on the critical buckling strain of the pipe, and must therefore be investigated.

Throughout this chapter, only the SNAM2 material properties are specifically reported. The variation of this specimens' material behaviour throughout its length, is representative of that of all of the specimens. However, the summary portion of the results sections in this chapter will include conclusions based on the material response of all of the specimens, as a larger number of specimens are necessary to arrive at broad behavioral conclusions. The specific stress-strain curves and discussion for all of the specimens in the material testing portion of this research may be viewed in Pipeline Technology Report No. 2005-1.

3.1 Material Coupon Locations

Material coupons were cut from the pipe wall at four different locations along the length of each of the eight specimens. These locations were: virgin stubs that were removed prior to testing, ends of the tested pipe, tensile side of the bend, and the compression side of bend. The purpose for the selection of these locations was to study the changes that occurred to the stress-strain relationship of the pipe material along the length of pipe due to testing and the cold bending process.

Coupons were cut from stubs removed from the ends of the pipe prior to testing in order to determine the stress-strain relationship of the virgin material. These coupons will establish the reference stress-strain behavior for comparison with those coupons that were cut from locations along the pipe that were affected by testing and cold bending. The steel for the pipes in each of the three sets was taken from two different heats of steel. For the SNAM specimens, a stub from each of the two heats of steel that were used for the pipes was sent to the University of Alberta along with the pipes that were to be tested. Coupons cut from these stubs would demonstrate the stress-strain relationship of the steel without the effects of either cold bending or testing.

Coupons were cut from the straight portion of each of the specimens after the pipe had been tested. The purpose of testing these coupons is to provide the stress-strain relationship of the steel in the pipe that does not include any effects of cold bending. These material properties will include any effects that testing caused on the steel. This information is valuable because the coupons from the bend portion of the pipe have also gone through the in-plane bending test, and any effects of testing from the tested end coupons can be applied to the tested bend coupons. In addition, the tested end coupons will serve as a backup of the virgin material properties. The tested end coupons were cut on the extreme tension fibre of the pipe, approximately one diameter away from the end of the specimen. This

location was chosen to minimize the effects bending due to testing, while remaining adequately distant from the end to keep away from the residual stresses that were introduced to the pipe during welding of the specimen to the endplates. The tested end material will have had some tensile bending stresses applied upon it during testing. This load is caused by the pressure force acting against the endplates of the test setup in addition to the eccentricity of the jack load to the ends of the pipe. These tensile forces are generally between the proportional limit and the yield strength of the steel, and this load level is sufficient in magnitude to alter the stress-strain behavior of the material.

Coupons were also cut from within the bent portion of the pipe from both the extreme compression and tension fibres for each specimen. These coupons were cut after the specimens had been tested. The tension side bend coupons will demonstrate the cold bending effects on the material from the extrados of the specimen. The compression side bend coupons will demonstrate the cold bending effects on the pipe material on the intrados of the specimen, which is the region of the pipe where the buckle will occur. The compression coupons were cut approximately two imperfection periods away from the nearest visible imperfection to the end of the pipe. The tension side coupons were cut at the same longitudinal location as the compression side coupons. These locations were selected in to ensure that the coupons were cut as near to the ends of the pipe as possible while remaining in the bend portion, in order to minimize the effects of bending due to testing on the coupon material.

All of the material coupons were orientated in the longitudinal direction of the pipe although the internal pressure applies stresses to the pipe in the circumferential direction. Circumferential material properties are extremely difficult to obtain because the material would become straightened during coupon testing, and this would result in residual stresses in the coupon material that do not exist in the actual pipe. It was decided that circumferential properties were not necessary for this testing program because the bending stresses that cause

buckling are orientated in the longitudinal direction of the pipe, and in addition prior finite element models of straight pipes at the U of A using only the longitudinal material properties demonstrated a high level of correlation with the behavior of tested pipe results.

3.2 Coupon Testing Procedure

The first step in material testing was that the coupons were cut in order to conform to dimensions specified in the ASTM A370, 1994 standard. The thickness of the coupons was the same as that of the tested pipe, the width of the narrow region of the coupons was 40mm, and the length of the narrow region of the coupon was 200 mm as shown in Figure 3.1. The coupons were cut out of material from the pipe using a power saw, and two coupons were cut from each material location to verify the mechanical properties of each coupon location. In order to allow for measurement of the specimen thickness, the protective coating was removed from three locations along the coupon length. Then the width and thickness of the coupon was measured at these three locations, by using an electronic caliper. The coupons were tested using the MTS 1000 at the U of A structures lab as shown in Figure 3.2. This testing apparatus has a maximum tensile capacity of 1000 kN, and a cartridge with a stroke capacity of 50 mm was used for all of the tests. These limits were both adequate for testing all of the coupons until fracture occurred. The MTS load was measured using a load cell, and the stroke is measured by an LVDT that was installed directly on the MTS 1000.

The first step in conducting the tension coupon tests was to align the specimen in a vertical orientation inside the MTS 1000 and tighten the grips on its ends. These grips are used to transfer the MTS load to the specimen via friction, and this friction is created by wedges located adjacent to the grips that move

vertically and force each of the grips to press against the coupons. The material properties of the coupon are unaffected by these end effects as the coupons are wider at the ends which ensures the plastic deformation would occur in the narrower less stiff region.

The next step was to attach an extensometer to the middle of the specimen. This instrument is used to measure the longitudinal deformation in the coupon over a gauge length of 50 mm. After the extensometer was connected to the coupon as shown in Figure 3.3, the next step was to electronically zero the jack load, jack stroke, and extensometer strain as the coupon was in a stress free condition at the beginning of the test.

The information from the tension coupon tests was acquired by a fluke data acquisition system. Readings were taken approximately every three seconds during testing. This amount of data is suitable to accurately determine the stress-strain behavior of the material while limiting excessive data. During testing, the MTS load vs. stroke relationship was monitored for observation of the behavior of the coupon during testing.

The final procedure was to apply the tensile load to the coupon. In order to conduct the tests in an efficient manner, three different loading rates were used for each coupon. The slowest rate of 0.005 mm/sec was used until a strain of approximately 1000 microstrain in order to obtain a precise value for the Modulus of Elasticity. The loading rate was subsequently increased to 0.017 mm/sec and remained at this rate until the commencement of strain hardening. The final loading rate of 0.12 mm/sec was used for the remainder of the tension tests, during which stage the majority of the strain in the specimen was applied. In order to eliminate the dynamic effects of testing, static points were taken three times immediately after the specimen yielded and once at the ultimate load. In order to obtain these static points, the loading rate of the MTS was reduced to zero, and the stroke was held constant for approximately 30 seconds. At these

static points, a drop in load occurred in the load–MTS stroke relationship for the tension coupon. This drop in load is due to the dynamic effect of loading on the tension coupon. After the ultimate load was achieved the specimen was carefully monitored for necking. Once necking was observed in the coupon, the extensometer was removed in order to protect it from damage. The stroke rate was maintained during necking, and the coupons were tested until fracture occurred in the coupon.

3.3 Determination of Material Properties

A stress-strain curve was created using the testing information obtained from each of the tension coupon tests. The strain at the middle of the coupon was output directly by the extensometer. To determine the stress in the coupon, the MTS load was divided by the cross sectional area of the narrow region of the tension coupon. During the testing of each of the coupons hundreds of stress and strain points were obtained, and this would be cumbersome to apply to the finite element model. For this reason 30-50 points from the stress-strain raw data were selected from each of the coupon tests, and this number of points was adequate to define a smooth representation of the stress-strain behavior of the material.

In order to eliminate the loading rate effects of the coupon tests for the material property determination, a static stress-strain curve was created for each coupon test. This was necessary because the load capacity of a material during loading increases as the rate of strain increases due to dynamic effects, while loading in the finite element model will be applied statically. If the material during coupon testing were held at constant length with the strain rate reduced to zero, then a drop in the tension load on the coupon would occur. This process is called relaxation, and the load during the test while the coupon length is held constant is the static load on the material.

The static stress-strain curve was generated by subtracting the drop in stress observed at the static points from the measured stresses in the dynamic stress-strain curve. The drop in stress at the three static points that were taken immediately after yielding was approximately the same, while the drop in stress from the static point at the ultimate load was somewhat larger due to the increased loading rate that was used during that portion of the test. For this reason the stress subtracted from the dynamic stress-strain curve was different where the loading rates were different, and the two regions were combined so that there was a smooth transition between the portions of the curve with the different loading rates. The static stress-strain curve has the same shape as the dynamic stress-strain curve, but with a vertical shift so that the static points are included in their locust of points. An example of the determination of the static stress-strain curve and the various material properties is shown in Figure 3.4.

Once the static stress-strain curves were created, an average of the two curves for each specimen material location was produced. This was accomplished by first overlaying the static stress-strain curves for the two coupons tested at each specimen measuring location, then manually creating a new stress-strain curve that fell precisely in between these two curves. This average curve was subsequently used for determination of the material mechanical properties.

The Modulus of Elasticity is the initial slope of the stress-strain relationship of the material. This portion of the curve represents the elastic stiffness of the material, and is important for validating the initial geometry of the finite element model. This material property is approximately 200 000 MPa for most steel material. The Modulus of Elasticity was determined by calculating the slope of a best-fit line over the initial linear portion of the stress-strain curve for each of the specimens. As the gauge length of the extensometer was 50 mm, and the elongation over this region at the yield strain of the materials is in the order of

0.1 mm, the reported values for the Modulus of Elasticity in the material testing program will be considered as approximate.

The proportional limit is the value of stress at which the material begins to behave nonlinearly. It is determined by drawing a straight line over the initial linear portion of the stress-strain curve, and determining at what stress the curve diverges from this line. The proportional limit indicates the onset of plastic deformation. From an atomic perspective, the proportional limit is the level of load at which slip of the dislocations within the lattice structure begins to occur. Thus there is the breaking of bonds with original atom neighbors and then reforming bonds with new neighbors, on upon removal of this stress the atoms do not return to their original positions (Timoshenko, 1956). Therefore, after a material is loaded beyond the proportional limit, its load deformation behavior becomes permanently altered. As the reported proportional limit is obtained from the average stress-strain curve from each specimen coupon location, the reported values may be considered the average proportional limit from the two coupon tests.

The yield stress for the material is the stress at which the specimen undergoes a large deformation with a relatively small increase in the applied load. During loading of the material, the overall strain rate applied to the specimen by the MTS has to be matched proportionally by the motion of the dislocations. As the stress on the specimen approaches the yield stress, the individual dislocations begin to move at a high speed. As the dislocations glide within the crystal lattice at these high speeds, rapid multiplication occurs and the mobile dislocation density increases rapidly. This increase in dislocation density leads to the formation of slip bands through a significant volume of the material, which in turn causes yielding of the specimen to occur (Callister, 1994).

The yield stress for the tension coupons was determined based on the both 0.2% offset method and the 0.5% strain methods. The 0.2% offset yield stress is

determined by drawing a line with a slope of the Modulus of Elasticity on the static stress-strain curve, with the origin of this line located at a stress of zero and a strain of 0.2%. The intersection of this line and the static stress-strain curve is the 0.2% offset yield stress. The 0.5% strain yield stress is simply the value of stress at a strain of 0.5% on the static stress-strain curve. The yield stress obtained using the two methods resulted in very similar results for all of the coupons other than the compression side bend coupons. The compression side bend 0.2% offset yield stress was somewhat lower than the 0.5% yield stresses for all of the tests. This is because the 0.2% offset line always intersects the compression side bend stress-strain curve at a strain considerably less than 0.5% because these curves demonstrated a considerably lower proportional limit. Since the 0.5% yield stress is the standard method for determining the yield stress for pipeline design, this method will be used during the discussion on the material properties.

The ultimate stress corresponds to the maximum stress in the static stress-strain curve of the materials. This material property corresponds to the level of stress at which the increase in strength due to work hardening of the material is not enough to counteract the loss in strength due to the reduction in the cross-sectional area of the specimen that occurs during testing. The ultimate stress was relatively constant for all coupons in the testing program that were cut from the same heat of steel.

The percent elongation was determined in order to obtain information on the ductility of the materials along the length of pipe. A 200 mm gauge length was used for all of the coupons. The final percent elongation was determined by adjoining the two fractured pieces of the coupon together after the completion of testing, and measuring the length of the narrow portion of the coupon by using a divider and caliper. This final gauge length was subsequently compared to the initial gauge length. The percent elongation is calculated as:

$$\left(\frac{\textit{Final Length} - \textit{Initial Length}}{\textit{Initial Length}} \right) \cdot 100\%$$

The uniaxial ductility of each specimen is affected by the strain history of the material. That is, one of the material properties of the virgin material is the fracture strain, and this strain will be relatively constant for any material coming from the same heat of steel. Therefore if a material undergoes tensile plastic deformation such as the tension side of cold bend pipes, and this material is subsequently tested in tension until fracture occurs, the ductility of this material will be less than that of the virgin material because some of the ductility has been used up during the initial plastic straining.

3.4 Virgin Material Coupons

The results of the material coupon tests demonstrated several changes in the material properties at the various locations along the pipe. These differences are important in understanding the effect of cold bending on the mechanical properties of the pipe material, and may be used to validate the material properties that were used for the finite element model. The mechanical property results for the SNAM2 material tests in tabular form are shown in Table 1 where SNAM2_V is the virgin coupon, SNAM2_E is the tested end coupon, SNAM2_C is the compression side bend coupon, and SNAM2_T is the tension side bend coupon.

3.4.1 Virgin Coupon Results

The SNAM2 coupon was of X60 material, which has an SMYS of 414 MPa. This value represents the expected 0.5% yield stress of X60 material. It is

expected that all SNAM2 materials will demonstrate a relatively similar stress-strain behavior to the virgin material once the material deforms beyond its residual strain. This is because the virgin material properties for materials from the same heat of steel are essentially the same, and the effects of residual strain will disappear from the stress-strain characteristics of a material once the gradient of the curve becomes relatively low.

The material properties from the virgin stub are used as a benchmark for all of the coupons. The stress-strain relationship for the SNAM2 coupon is shown in Figures 3.5 and 3.6. The Modulus of Elasticity for this coupon was 196 GPa. The Modulus of Elasticity for all of the SNAM coupons was within 15% of these values for their respective heats of steel. The proportional limit for the SNAM2 coupon was 201 MPa, and its 0.5% yield stress was 389 MPa. The yield stress of all of the different SNAM2 coupons will be compared to that of the virgin material in order to determine the effect of cold bending on the yield strength of the pipe material.

The ultimate strength for the SNAM2 virgin coupon was 498 MPa. Thus, the ratio of its yield stress to ultimate stress was 0.78. It is expected that the ultimate stress for all of the SNAM coupons should be relatively similar to that of their respective virgin coupons. This is because the ultimate stress is unaffected by cold working as the residual strains in the material is considerably less than the ultimate strain. The percent elongation of the SNAM2 virgin material at fracture was 22%. It is expected that the percent elongation for the coupons taken from the various locations along the SNAM2 specimen will vary from these values because of the different strain histories that the materials experienced.

3.5 Tested End Material Coupons

The tested end coupons were cut from one of the straight end segments of the pipe after they were tested. These coupons may be used to determine the effect of testing on the pipe material, as the coupons from the bend portion will also have undergone testing. The tensile stresses in these coupons due to testing was caused by the internal pressure acting against the end plates of the test setup, as well as the eccentricity of the jack load to the ends of the pipe. The magnitude of the induced strain was recorded by strain gauges that were installed towards the ends of the pipe. For the majority of the tests the maximum strain at the ends of the specimen was in the order of 0.2%. As this strain is typically between the proportional limit strain and the yield strain of the virgin material, it is expected that there will be some permanent deviations in the stress-strain characteristics of the tested end coupons from its prior-to-test condition. Only the SNAM2 tested end material results are specifically presented herein. The other specimens tested end coupon results and discussion are presented in Pipeline Technology Report No. 2005-1..

3.5.1 Background to Increasing of Proportional Limit

As the tensile load on a material approaches the yield load, slip bands begin to appear on the surface of some of the grains in the material microstructure. These bands demonstrate that there is sliding along the distinct crystallographic planes that are formed by those grains. This occurs because the elastic properties of a single crystal vary in different directions, while the crystals are randomly orientated. Consequently sliding may occur in the most detrimentally orientated individual crystals before the average tensile stress in the material achieves the yield stress. Once this specimen is unloaded, the crystals that underwent sliding are unable to return to their initial shape freely, and

because of this some residual stresses will remain in the specimen after the externally applied load is removed. These residual stresses are compressive in the most weakly orientated crystals of the microstructure for a material with a previously applied tensile force. If after this material is unloaded, and the specimen has a tensile force applied to it for a second time, the grains in which sliding occurred in the first test will not yield until the tensile load reaches the maximum load that was applied during the first loading. Only when the newly applied load exceeds that value will sliding begin again (Timoshenko, 1956). Thus the first tensile load on the material increases the proportional limit in the tensile direction.

3.5.2 Tested End Coupon Results

Testing had a moderate effect on the ends of the pipe for the SNAM2 specimen. The maximum strain experienced by the SNAM2 end material during testing was 0.21%. This strain was between the strain at the proportional limit of its virgin coupon, and the yield strain of 0.5%. It is for this reason that the proportional limit of the tested end coupon was greater than the proportional limit of its virgin coupon, but less than its virgin coupon yield stress as shown in Table 3.1. Additionally, the end coupon behaved slightly nonlinearly after its stress was similar to the stress in the virgin coupon that corresponded to the strain experienced during the test, as shown in Figure 3.5.

The yield stress for the ends of the pipe was greater than that of the virgin material for all of the SNAM specimens. This increase was 47 MPa for the SNAM2 tested end coupon. This yield stress is significantly greater than that of the virgin material, which is not expected because the strain experienced during testing was less than the yield strain. In addition, the stress-strain relationship for the tested end coupon of SNAM2 showed a distinct yield plateau while the

SNAM2 virgin coupon did not. This is contrasting to what may be expected, as a stress history would reduce any signs of a pre-existing yield plateau. There are several possible explanations for this discrepancy. The first explanation is that the stub from which the SNAM2 virgin coupon was cut from was not from the same heat of steel as the SNAM2 pipe. The second explanation may be that the SNAM2 coupon underwent some stress history prior to arrival at the U of A that served to eliminate its yield plateau. The final possibility is that strain aging may have occurred in the SNAM2 end material. As SNAM Rete Gas has confirmed that the specimens were from the same heat of steel and that the materials were not previously loaded, it is believed that it is strain aging that caused the discrepancies observed in the SNAM2 tested end coupon. Accordingly, a description this phenomenon is provided below.

Strain aging is a phenomenon for materials that exhibit a yield plateau, in which the strength of the material is increased after the specimen has been cold worked. This phenomenon will occur if the specimen has been heated at a relatively low temperature for a substantial duration of time. If a material is loaded beyond yield, unloaded, and then reloaded after being stress free for several days at room temperature, the yield point will reappear. In addition, the yield stress will increase due to the aging action. The reappearance of the yield plateau occurs because during the aging period, carbon and nitrogen atoms diffuse to the dislocations within the microstructure of the material that were created during the initial loading. This diffusion serves to create new atmospheres of interstitials that anchor the dislocations, thus increasing the strength of the material (Dieter, 1978). It may be for this reason that the SNAM2 virgin material demonstrates a yield plateau and explains why there is such a major increase in the yield strength of the material.

The tested end ultimate stress to virgin material ultimate stress ratio for the SNAM2 specimen was 1.02, which may be attributed to variations in the material properties along the pipe during the initial forming process, since it is expected

that the ultimate stress will remain constant for all of the coupon tests for each material heat. The percent elongation was 20% for the SNAM2 tested end specimen. This value is somewhat different from the percent elongation of the virgin material although it is expected that these values would be essentially the same, and this discrepancy is likely due to experimental error during percent elongation measurement. To minimize the experimental error when determining the effects of cold bending on the percent elongation of the material, the average percent elongation of the virgin and tested end material will be used. The average of the virgin and tested end percent elongation for the SNAM2 coupons was calculated as 21%.

3.5.3 Tested End Coupon Discussion

The material properties of all of the tested end coupons were generally very similar to those of the virgin coupons. The proportional limit was increased for all of the tested end coupons, because the strain experienced during testing was always between the proportional limit strain and the yield strain of the virgin material. The yield stress of the tested end material was very similar to that of the virgin material for most of the coupons. As the maximum strain experienced at the ends of the pipe during the test was always less than the yield strain, it is expected that the yield stress would not change for the tested end material. The ultimate stress for the tested end material was always within 4% of that of the virgin material, and this is because the ultimate stress of materials from the same heat of steel does not change due to loading. There was a relatively large discrepancy between the percent elongation of the tested end and virgin coupons although it is expected that the ductility would remain the same as relatively low strains are experienced during the tests. These differences may be attributed to experimental error, and to minimize this error the average elongation of the virgin

and tested end coupons will be used for comparison with the tension and compression side bend coupons.

3.6 Tension Side Bend Material

In order to induce permanent deformation in the cold bend pipe, the material on the extrados of the bend must experience tensile stress beyond its yield stress. As the steel for all of the specimens in this experimental program was elasto-plastic, strain hardening will occur in the steel once the strains in the material are greater than the yield strain. Based on the residual strain measurements from the experimental, the strains on the tension side bend were generally between 0.5 and 2%, which is greater than the yield strain. An example of the effect of tensile plastic deformation on the yield strength of the material is shown in Fig 3.7. The changes in material properties due to this permanent deformation will have a considerable effect on the deformation response of the pipes to applied bending, and will therefore affect its critical strain. For this reason substantial effort has been applied to determine the changes in the stress-strain relationship of the tension side bend material of the specimens in comparison to that of the virgin material.

3.6.1 Background to Work Hardening Effect

During elongation of a material beyond the yield strain the material hardens and the stress required to further elongate the material increases beyond its yield stress. This phenomenon is called work hardening or cold working as the temperature at which deformation takes place is “cold” relative to the absolute melting temperature of the metal. Elongation of the material is combined with

uniform reduction of the cross-sectional area so that the volume of the specimen remains essentially constant. The work done during elongation is transformed largely into heat and the specimen becomes hot. However, not all of the mechanical energy is transformed into heat, part of it remains in the specimen in the form of strain energy. Owing to the difference in the orientation of the crystals, the stresses in the specimen due to loading are not uniformly distributed over the cross section, and after unloading some residual stress and a certain amount of strain energy remain in the specimen. This energy is predominantly due to the generation and interaction of dislocations during cold working. If this material is unloaded and then loaded a second time, its yield stress will become increased with respect to the virgin material. The material will behave essentially elastically until it reaches the stress at which the material was unloaded during its first loading cycle. Once it reaches this stress, the stress-strain behavior will be the same as if it had not been unloaded in the first place. With cold working there also is a decrease in ductility of the metal in proportion to the percent cold working for the material.

Work hardening involves dislocations interacting with each other and with barriers that impede their motion through the crystal lattice. As the strain in a material increases beyond yield the dislocation density will increase by several orders of magnitude, and this will accordingly increase the level of interaction between dislocations during loading. The first reason that work hardening occurs is that dislocations accumulate on slip planes at barriers at a crystal within the crystal lattice. These pile-ups produce a residual stress, which opposes the applied stress along the slip plane. This residual stress will serve to hinder dislocation movement along the slip plane upon further loading. The other reason that work hardening occurs in a metal is that glide dislocations on intersecting slip planes may combine with one another to produce a new dislocation that is not orientated in the active slip direction. Thus the dislocations moving along the slip plane must cut through these other dislocations that intersect the active slip plane. These dislocations that intersect the active slip plane serve as a barrier to

dislocation motion that cannot be crossed until the applied stress is increased to a sufficient magnitude required to break down these barriers (Smallman, 1985).

3.6.2 Tension Side Bend Coupon Results

The proportional limit for the SNAM2 tension side bend coupon was 308 MPa. This value is relatively similar to the proportional limit of its tested end coupon. It was observed that the SNAM2 tension side bend coupon demonstrated a yield strength that was 15% greater than that of its virgin material. This increase in yield strength is due to the work hardening that occurs on the tensile side of the bend during the cold bending of the pipe. That is, it is expected that the tension side bend material will remain linear until the maximum stress it experienced during its first stress cycle, and after this level of stress is achieved the stiffness of the specimen will reduce, as shown in Figure 3.7. The calculated residual strain in the tension side bend material for the SNAM2 specimen is 1.2%, and the corresponding stress to this strain for the virgin material is 411 Mpa. It is apparent from Figure 3.5 that the stress-strain relationships for the tension side bend material is relatively linear until a stress near 411 Mpa, and after this stress is achieved the slope of the stress-strain curves begins to considerably decrease.

The ultimate stress was within 1% of the virgin material ultimate stress for the SNAM2 tension side bend coupon, as cold bending does not affect the ultimate stress of the material. The yield to ultimate stress ratio was 0.89 for the SNAM2 tension side bend coupon, compared to the ratio of 0.78 for its virgin material. This occurred because of the roundness in the shape of the initial portion of the stress-strain relationship of the virgin material in Figure 3.5, in comparison to that of the tension side bend material. The SNAM2 tensile bend stress-strain relationship becomes very similar to the tested end coupon stress-strain relationship after a strain of approximately 5%. The percent elongation was

23 % for the SNAM2 tension side bend coupon, and this value is relatively similar to the tested end material percent elongation.

3.6.3 Tension Side Bend Coupon Discussion

The proportional limit of all of the tension side bend coupons was generally similar to the proportional limit of their respective tested end coupons. In addition, the yield stress of the tension side bend material was greater than that of the virgin material for all of the specimens in this material testing program. The cause of this increase in yield stress is from the work hardening that occurs in the steel as the extrados of the bend is loaded beyond its yield stress during the cold bending process.

The increase in yield stress over that of the respective virgin material was greatest for the SNAM coupons, next greatest for the TG coupons, and the increase was smallest for the TCPL coupons. This information suggests that the grade of the material does not have a major effect on the effect of work hardening on the material, as the TG coupons were of the highest grade but did not demonstrate either the greatest or least amount of work hardening. The residual strain was the greatest for the TCPL specimens, next greatest for the SNAM specimens, and was the smallest for the TG specimens. Thus the magnitude of the residual strain does not correlate with the increase in yield stress for the materials tested in the program. The yield to ultimate stress ratio increase of all of the tension side bend materials increased by between 0.03 to 0.13, with an average increase of 0.08, over that of their respective virgin materials for all of the specimens.

The percent elongation of the tension side bend coupons was generally less than the average percent elongation of the respective virgin and tested end

coupons. Also, this decrease in ductility was relatively similar in magnitude to the residual strains in the pipe. Consequently it may be inferred that there is a decrease in ductility corresponding to the magnitude of the residual strain in the material at the tension side of the bend for cold bend pipes.

3.7 Compression Side Bend Material

During cold bending of a pipe, the intrados of the bend undergoes compressive strains beyond the yield strain of the material. This will modify the load-deformation relationship of the material once the pipe is loaded again as shown in Figure 3.8. For the closing mode deformation the specimen will eventually buckle at the intrados of the bend because this region is loaded with compressive bending stresses; consequently the material properties at this location are of considerable interest. For opening mode deformation the intrados of the bend will experience tension stresses during bending, and the influence of this loading sequence on the behavior of the material is also of considerable interest. As the material properties for the specimens in this experimental program were determined by tension coupon testing, and the intrados of the bend experienced compressive stress beyond the yield stress during cold bending, the compression side bend coupons will demonstrate the Bauschinger effect during tension coupon testing as described below.

3.7.1 Background to Bauschinger Effect

The primary feature of the Bauschinger effect is that there is a reduction of the yield strength for a material undergoing reverse loading following prestraining. This is because prestraining a material in one direction will

introduce an anisotropy for further deformation if it is loaded in the opposite direction. In addition, the reduction in yield strength becomes further reduced as the magnitude of the prestrain increases. The Bauschinger effect occurs in a material because of a combination of residual internal stresses as well as dislocations that are introduced during prestraining.

The reduction in the elastic limit after prestraining due to locked in stresses may be explained by considering two neighboring grains within the material, each having the same elastic stiffness, but with different elastic limits. Upon loading each of these grains will undergo the same strain in one direction, and if this strain achieves a sufficient magnitude, plastic deformation will occur in the grain that has the lower elastic limit, while the other grain will continue to behave elastically. When the material is unloaded to the condition where there is no applied load, one grain will be in tension and the other in compression. On reloading in the same direction, to the same stress, both will behave elastically, but on loading in the opposite direction the residual stress in the softer grain will aid the applied stress in causing premature yield. Therefore the behavior is asymmetrical and the system is softer for the reverse stressing than it was in the virgin state.

The effect of dislocations introduced after prestraining on the elastic limit of the material may be explained by considering that dislocations have to maneuver obstacles of various strength and these obstacles are not uniformly distributed within the matrix. Thus, dislocations under applied stress easily advance through regions where the moving resistance of obstacles is lesser, and they are stopped at a region where obstacles are denser and stronger. When the dislocations are blocked, they encounter higher moving resistance in the forward direction than in the reverse direction. Thus when deformation is reversed, it is easier to move the dislocation back until it meets another higher resistance region on the other side of the dislocation. This results in a decrease in resistance to

applied load of the overall material and a corresponding decrease in yield strength (Timoshenko, 1956).

3.7.2 Compression Side Bend Coupon Results

It was observed that the proportional limit of the SNAM2 compression side bend coupon was 18 MPa lower than that of its virgin material. In addition, the SNAM2 compression side bend coupon demonstrated a yield strength that was 12% lower than that of its virgin material. The ultimate stress of all of the SNAM2 compression side bend coupons was within 1% of that of its virgin material coupon.

The yield to ultimate stress ratio for the SNAM2 compression side bend coupon is 0.69. This is somewhat lower than the yield to ultimate stress ratio of 0.78 that was observed in the virgin material test for the specimen. In addition, the slope of the stress-strain curve after the proportional limit is considerably lower than that of the virgin material, as shown in Figure 3.5. While the slope of the virgin material stress-strain curve changes dramatically at the yield stress, the slope of the compression side bend stress-strain curve is relatively rounded between the proportional limit and the location where the compressive side bend and virgin material stress-strain curve essentially coincide. This co-linearity occurs at a strain of approximately 2% for the SNAM2 coupon. The percent elongation for the SNAM2 compression side bend specimen was 26%, which is 5% greater than that of its straight coupon.

3.7.3 Compression Side Bend Coupon Discussion

The proportional limit of all of the compression side bend coupons was always lower than that of the respective virgin coupons. It is observed that for all of the compression side bend coupons, that there was a significant decrease in the yield stress of the compressive side bend material in comparison with that of the virgin material. In addition, the shape of the stress-strain curve became rounder than that of the virgin material between the proportional limit and a strain of approximately 2%. This softening of the initial inelastic portion of the stress-strain behavior and the corresponding decrease in yield stress of the compression side bend material is due to the Bauschinger effect.

The average decrease in yield stress was greatest for the TCPL coupons, next greatest for the TG coupons, and was the least for the SNAM coupons. Therefore the grade of the material does not have a significant effect on the extent of the Bauschinger effect on the material, as the TCPL coupons demonstrated the greatest reduction in yield strength but were of neither the lowest or highest grade of material. The average residual strains were greatest for the TCPL specimens, next greatest for the SNAM specimens, and the least for the TG specimens. Thus the extent of the residual strain does not have a major effect on the decrease in the yield stress of the material as the TG coupons had a relatively low residual strain but demonstrated a relatively significant decrease in yield stress.

The yield to ultimate stress ratio of the compression side bend material decreased by between 0.07 and 0.14, with an average decrease of 0.11, in comparison to that of the respective virgin material for all of the specimens. The percent elongation of the compression side bend coupons was generally greater than the average percent elongation of the virgin and tested end coupons. These increases were relatively similar to the residual strain in the pipes.

3.8 Summary of Material Testing Results

A total of 32 sets of coupons of material from the eight pipes were tested in tension until fracture as per the ASTM A370, 1994 standard and the results have been described in this chapter. The coupon tests were conducted on the virgin material, ends of the pipe after testing, compression side of the bend, and tensile side of the bend for all of the specimens. The proportional limit, 0.2% offset yield strength, 0.5% yield strength, ultimate strength, and percent elongation have been studied for the coupons.

There are several relationships that can be observed through the virgin and tested end specimen testing data that are consistent with most of the coupon results. The proportional limit for the virgin material was generally lower than that of the tested ends because testing of the pipes applied strains at the end of the pipe of approximately 0.2%, which is greater than the proportional limit strain of the virgin material. The average yield stress of the coupons was relatively similar to the respective SMYS for all of the virgin and tested end specimens. The ultimate stress was similar for all of the coupons that came from the same heat of steel. Finally, the average percent elongation of the virgin and tested end specimens was used for comparison with those of the bent specimens in order to reduce experimental error.

The proportional limit of the tension side bend coupons was generally relatively similar to that of their respective tested end coupons. The yield stress of the tested end coupons was always between 1 – 19% greater than that of their respective virgin coupons. This increase is due to the work hardening that occurs in the material during cold bending when the pipe is loaded beyond its yield strain. Based on these material tests this increase in yield appears to be independent of grade and residual strain. The yield to ultimate stress ratio increased by an average 0.08 over that of the virgin coupons for the tension side bend coupons. The ultimate stress of the tension side bend coupons was always

similar to that of the virgin coupons because cold bending does not affect the ultimate stress. The average percent elongation of the specimen sets was between 0.5 – 3% less than that of the respective average straight portion coupons. The value of these decreases is similar to the residual strains in the cold bends.

The proportional limit of the compressive side bend material was always lower than that of the respective virgin materials. The shape of the compression side bend stress-strain curve was always considerably rounder than that of their respective virgin curves between the proportional limit and a strain of approximately 2%. The yield stress of these coupons was always lower than that of the respective virgin coupons by between 10 – 20%. This decrease is due to the Bauschinger effect as this material is loaded beyond yield in compression during cold bending, and then is loaded beyond yield in tension during coupon testing. This decrease in yield strength appears to be independent of grade and residual strain for the specimens tested in this experimental program. The yield to ultimate stress ratio decreased by an average of 0.11 for all of the compression side bend coupons in comparison with that of their respective virgin coupons. The ultimate stress of the compression side bend coupons was consistent to that of all of the other coupons that were from the same heat. Finally, the percent elongation was usually between 1.3 – 2.5% greater than that of their respective virgin coupons, and this increase is similar to the residual strains in the cold bends.

Table 1 – SNAM2 Material Properties Summary

| Coupon Label | Modulus of Elasticity (GPa) | Proportional Limit (MPa) | 0.2% Offset Yield (MPa) | 0.5% Yield Strength (MPa) | Ultimate Strength (MPa) | Elongation (%) |
|--------------|-----------------------------|--------------------------|-------------------------|---------------------------|-------------------------|----------------|
| SNAM2V | 196 | 179 | 377 | 389 | 498 | 22 |
| SNAM2E | 199 | 189 | 435 | 436 | 509 | 20 |
| SNAM2C | 167 | 161 | 316 | 342 | 494 | 26 |
| SNAM2T | 191 | 184 | 444 | 448 | 504 | 23 |

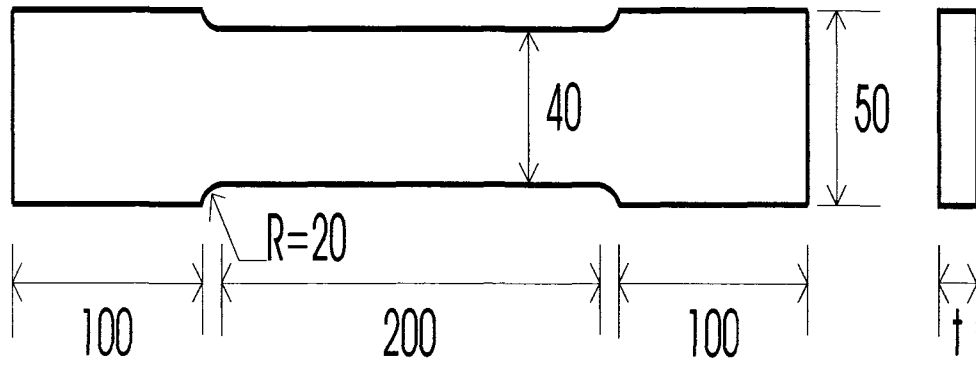


Figure 3.1 - Schematic Tension Specimen (mm)

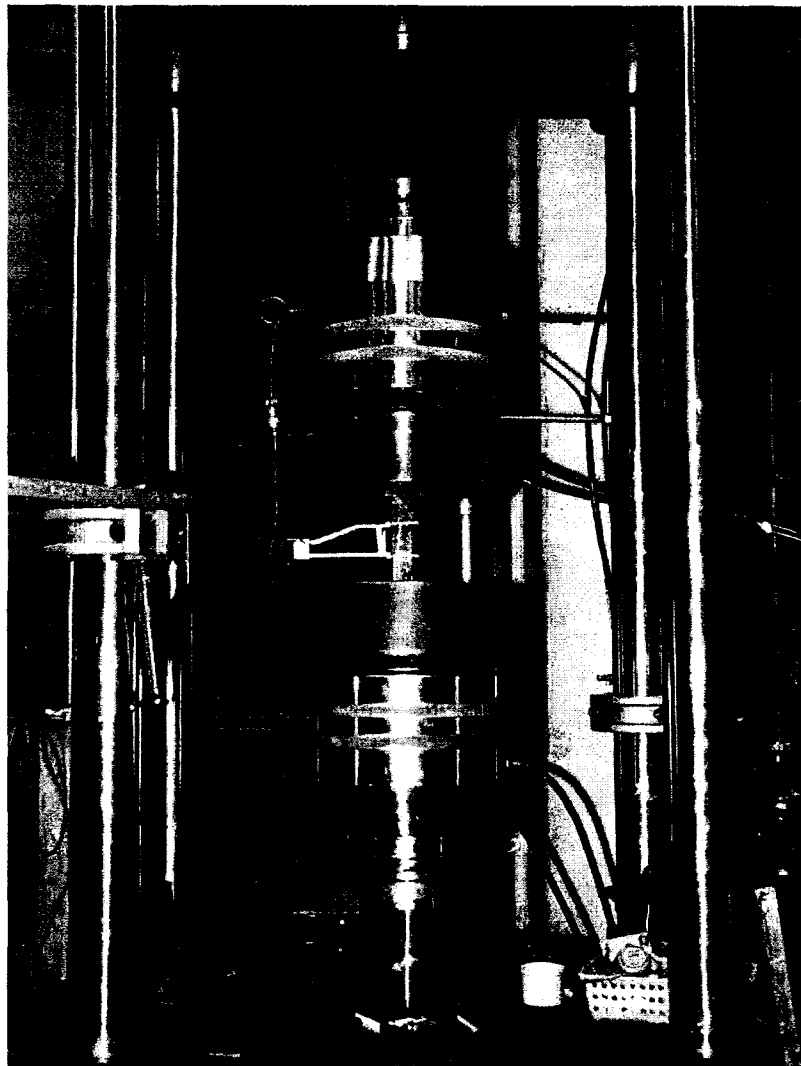


Figure 3.2 - Coupon Testing System

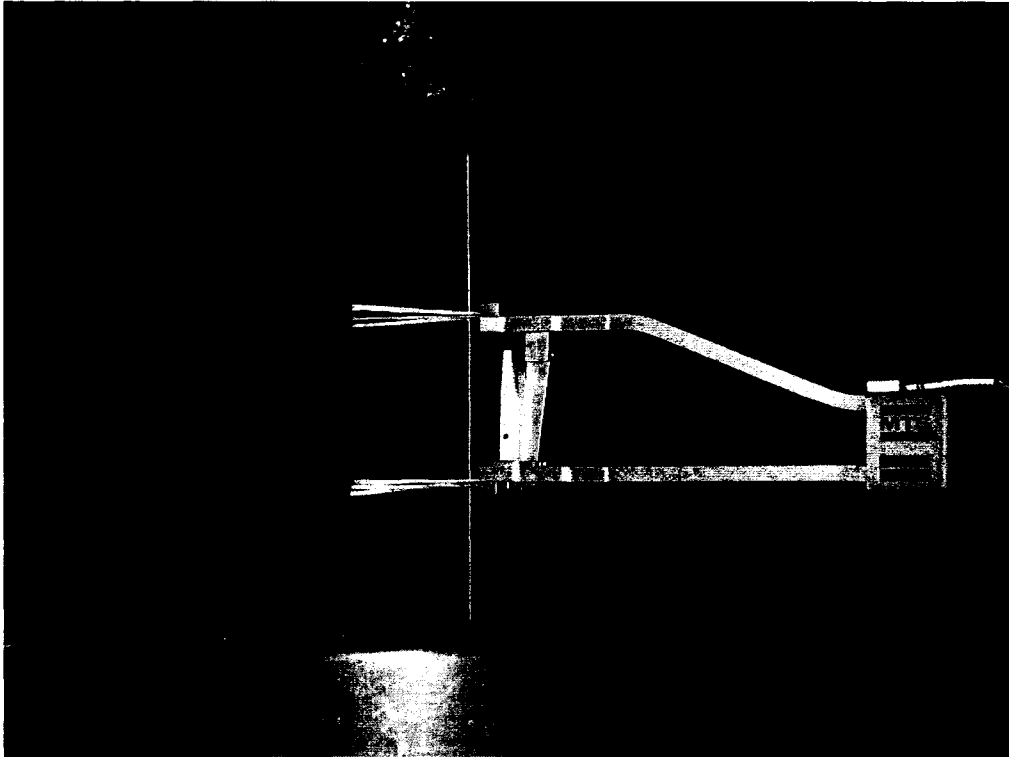


Figure 3.3 – Strain Measurement During Testing

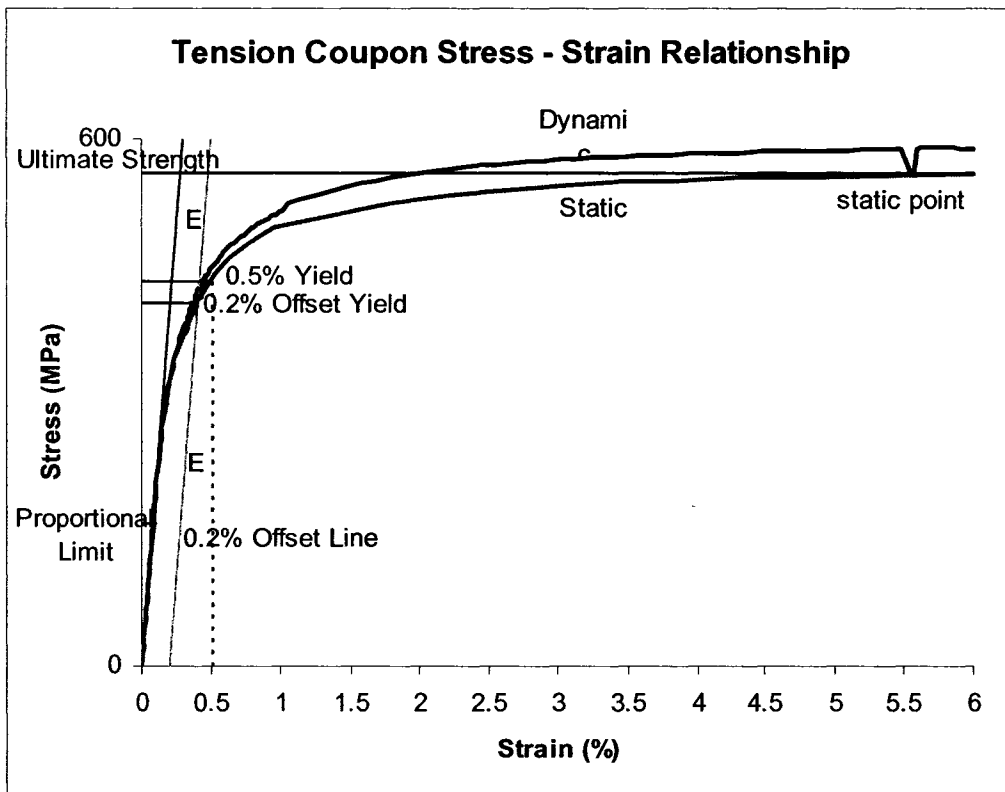


Figure 3.4 - Example Material Property Determination

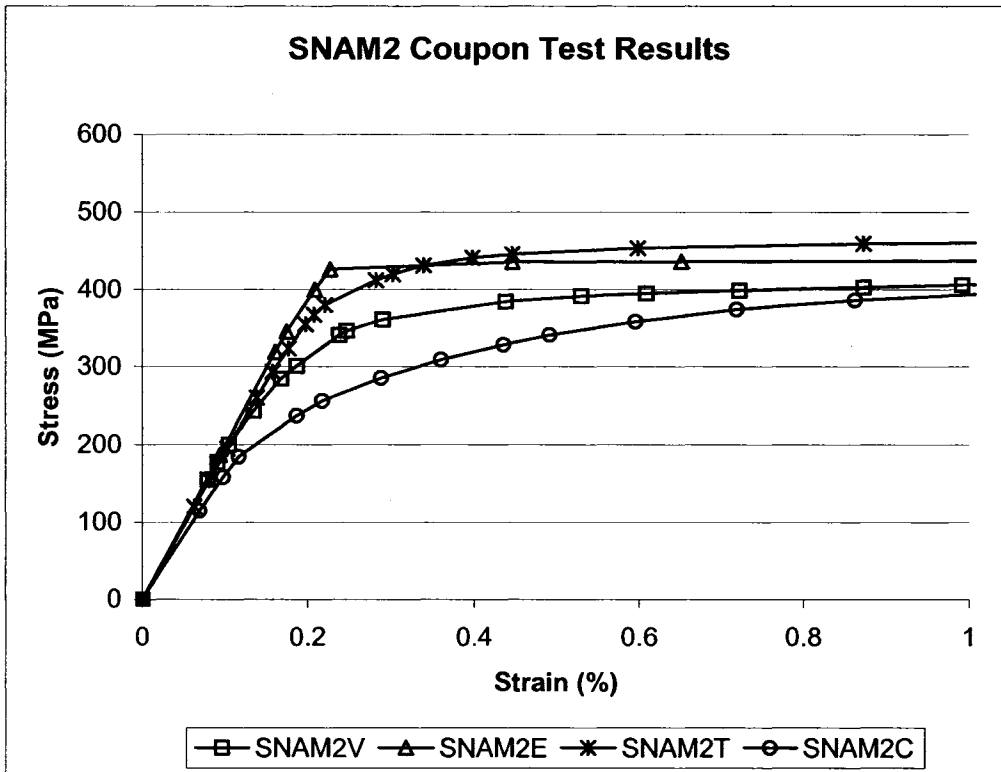


Figure 3.5 - SNAM2 Static Stress-Strain Curve - Low Strains

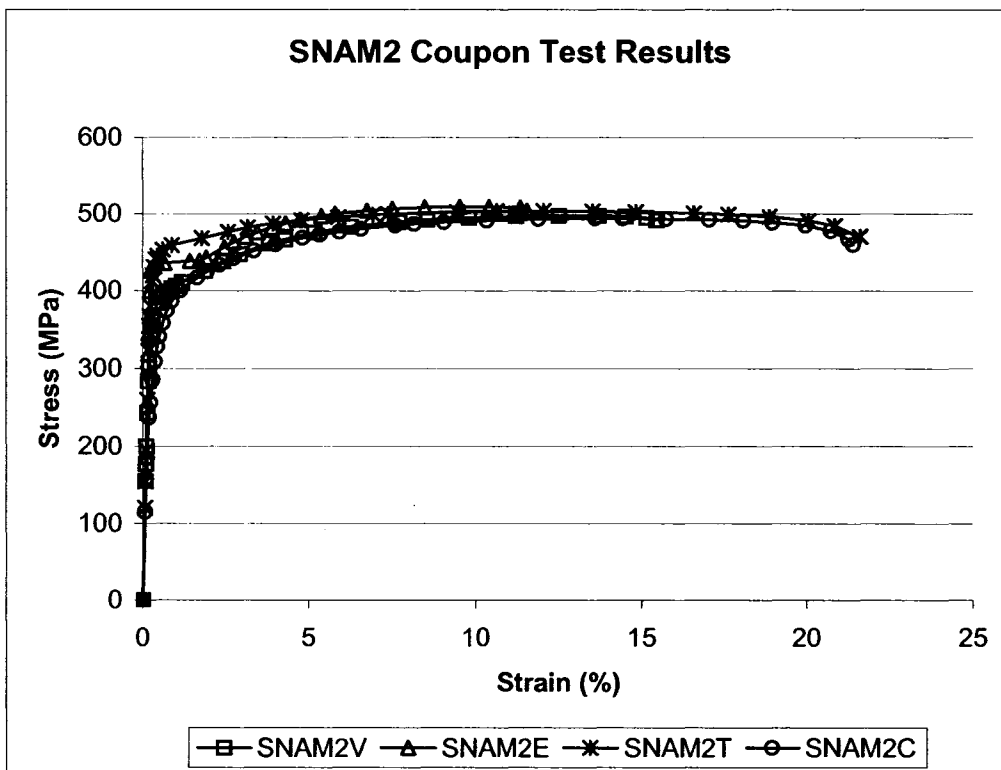


Figure 3.6 - SNAM2 Static Stress-Strain Curve

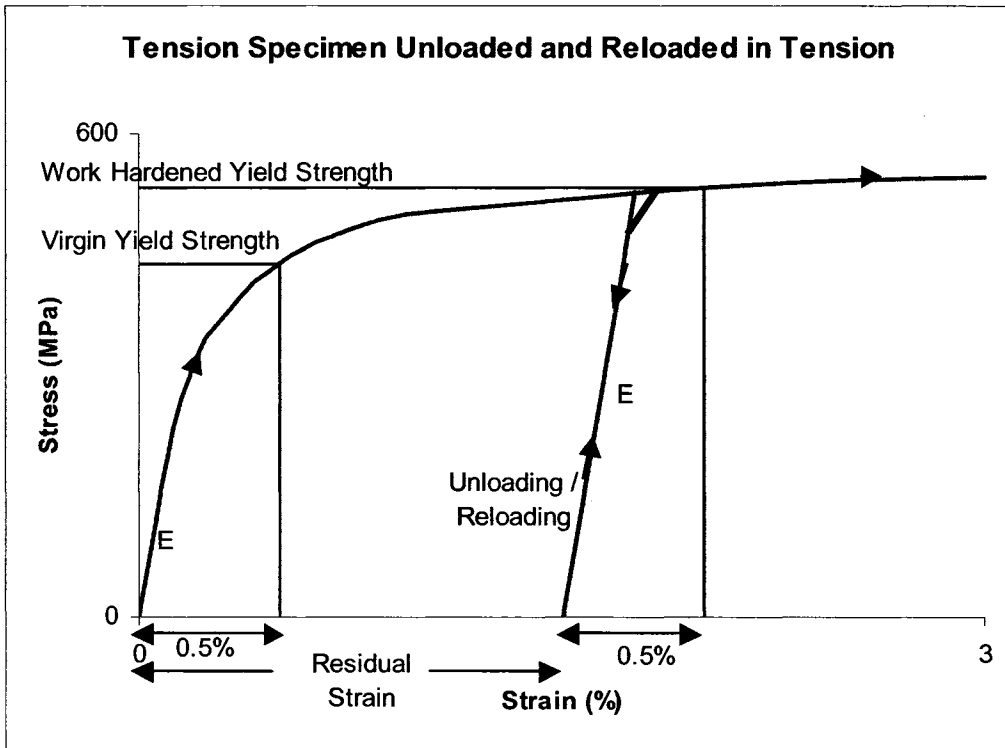


Figure 3.7 – Schematic Example of Work Hardening

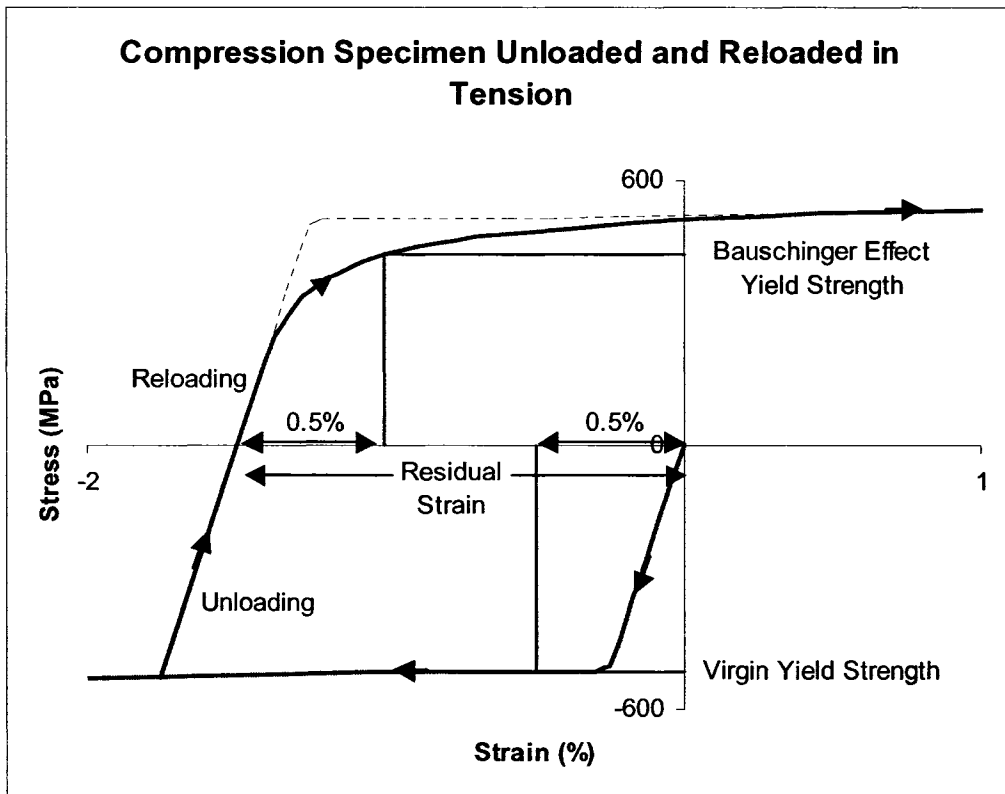


Figure 3.8 – Schematic Example of Bauschinger Effect

4.0 INITIAL MEASUREMENTS AND DATA REDUCTION

This chapter will first present the results of the initial geometry measurements of the specimens. Then a comprehensive discussion of the residual strain and initial imperfection measurements that were measured from the pipes prior to experimental testing will be explained. Subsequently, the methods used for the reduction of the experimental data including the determination of the global moment, global curvature, and local curvature of the test specimens will be presented. Finally, the two methods that were used to determine the critical strain of the test specimens will be established.

The cross-sectional geometry and material properties were alike for each specimen within the three specimen sets. Consequently, the initial measurements were relatively similar for each specimen within each specimen set. Accordingly, the specific initial measurements for only the SNAM2, TG2, and TCPL2 specimens will be presented herein. However in order to study the effect of different methods, this chapter will also contain discussions on the comparison of the initial measurements between the different specimens within each set. The specific initial measurements and discussion for all of the specimens are available in Pipeline Technology Report No. 2005-1.

4.1 Initial Geometric Measurements

Upon arrival of the specimens to the I.F. Morrison Structures Lab at the University of Alberta, several measurements of the specimen geometry were taken. The wall thickness at 8 locations around the circumference and 5 locations

along the pipe length, along with the diameter at four locations at each end of the pipes were measured. Additionally, the tension side length, compression side length, neutral axis length, and horizontal lengths were evaluated. These geometric properties permitted the attainment of information about the effects of cold bending on the pipe geometry. These effects included ovalization, wall thinning and thickening, and residual strains.

4.1.1 End Ovalization

The inside diameter was measured at the 0 – 180, 45 – 225, 90 – 270, and 135 – 315 degree planes at both ends of every specimen in order to determine extent of ovalization of the specimens. They were measured using a measuring tape, and the outside diameters that are presented in Table 4.1 were calculated by adding two times the average wall thickness to the measured inside diameters. The ovalization of the specimens was calculated using Equation 4.1 (Det Norske Veritas, 2000), and the ovalization of the ends of all of the specimens due to the cold bending process varied between 0.1 to 2.8%. In addition, the ovalization of the ends of the test specimens generally increased with increasing diameter to thickness ratio. It is expected that the ovalization at the ends of the pipe will be less than that demonstrated at the bend region, because the straight segments of the bends are not subjected to direct ovalizing forces during cold bending.

$$Ovalization = \frac{D_{max} - D_{min}}{D_{ave}} \quad (4.1)$$

Where D_{max} is the maximum measured diameter, D_{min} is the minimum measured diameter, and D_{ave} is the average diameter of the pipe.

4.1.2 Wall Thinning / Thickening

The wall thickness was measured at the 0, 45, 90, 135, 180, 225, 270, and 315 degree circumferential positions of each specimen. They were measured at each end, the middle, and at the two one-quarter length positions of the specimens. The end measurements were obtained using a manual calliper, and the interior measurements were obtained using an electronic calliper. The average of the 16 wall thicknesses that were measured using the manual calliper is presented as the average specimen wall thickness in Table 4.2. Electronic calliper readings were also taken at the ends of the specimens so that the electronic measurements could be calibrated with the manual measurements, as the manual measurements are more directly attained. This calibration factor was calculated by simply averaging the electronic to manual calliper readings for each location where both measurements were taken. It was observed that the electronic to manual calliper ratios were similar for the specimens with similar wall thicknesses. For this reason three different calibration factors were used on the electronic calliper measurements, one for each specimen set.

While the material at the extrados of the bend elongates and that at the intrados of the bend shortens, the total volume of a unit width of pipe wall will remain constant. This will result in the thinning of the pipe wall at the tension side of the bend, and a thickening of the pipe wall at the compression side. The change in thickness at the extreme fibres of the pipe may be calculated using Equation 4.2.

$$\Delta t = \pm \frac{r}{R} \cdot \frac{t}{2} \quad (4.2)$$

Where r is the pipe radius, R is the radius of curvature of the bend, t is the initial wall thickness, and Δt is the change in wall thickness. When Equation 4.2 was used to predict the change in wall thickness at the extreme fibres of the specimens

in this experimental program, the increase / decrease ranged from 0.036 to 0.082 mm. The magnitude of these values is extremely small, and may be difficult to accurately detect with the instrumentation used in this experimental program.

The electronic calliper readings were used to determine the variation in wall thickness around the pipe circumference over the bend region of the specimens. The wall thickness at the 315, 0, and 45 degree positions were used to calculate the average wall thickness of the intrados of the bend, and the wall thicknesses at the 135, 180, and 225 degree positions were used to calculate the average wall thickness at the extrados of the bends. Based on these measurements it is demonstrated that the wall thickness at the intrados of the bend was greater than that at the extrados for 5 of the 7 bent specimens. The difference in the average intrados and overall wall thickness, and the difference in the average extrados and overall wall thickness of each specimen were averaged together to calculate the average difference in wall thickness for the extreme fibres of the specimens as presented in Table 4.2. The magnitudes of these values are extremely small because of the large radius of curvature of the cold bends, and it may be concluded that the change in wall thickness due to cold bending is negligible for the test specimens.

4.1.3 Bend Length

Several initial length measurements were taken from the test specimens in order to obtain information about the bend geometry and residual strains. The measured horizontal lengths are shown in Table 2.2, and the tension side bend, compression side bend, and centreline lengths for the specimens are presented in Table 4.3. Each bend specimen was comprised of a bend segment flanked by two straight segments, and the length of these segments could not be directly measured. For this reason the measured end angles and specified bending degree

per diameter were used in conjunction with Equation 4.3 to calculate the length of the bend segment. The straight segment length was subsequently calculated using Equation 4.4, and in this equation it is assumed that the straight segment length was the same on both sides of the bent segment. This approximation is reasonable because prior to shipment to the University of Alberta, it was specified that the specimens were to be cut so that the bend region was centred within this length. This geometry was further validated by the initial imperfection measurements where it was observed that the maximum vertical deflection of the specimens was generally positioned near the middle of its length.

$$L_{Bend} = \frac{\vartheta_{Total} \cdot D}{(\vartheta / D)} \quad (4.3)$$

$$L_{Straight} = \frac{L_{Centerline} - L_{Bend}}{2} \quad (4.4)$$

Where L_{Bend} is the calculated bend centreline length, θ_{Total} is the total bend angle, θ / D is the specified bending degree / diameter, D is the diameter, $L_{Straight}$ is the straight segment length at each end of the bend, and $L_{Centerline}$ is the measured total centreline length of the bend.

4.2 Residual Strain Measurement Results

During cold bending, the tension side of the bend undergoes permanent tensile strain, while the compression side of the bend undergoes permanent compressive strain. These residual strains were determined for the test specimens, and are necessary for validation of the finite element model geometry. In order to verify the measurements, simple calculations were used to determine the theoretical residual strains.

4.2.1 Specified Residual Strain

During the design of a cold bend, the engineer generally specifies the bending degree per diameter. This value represents the change in angle for every diameter in pipe length of the cold bend. The specified bending degree per diameter in combination with the pipe radius may be used to calculate the theoretical residual strain in the bend. The first step in calculating this is to determine the radius of curvature of the centreline over a length of one pipe diameter using Equation 4.5. Then Equation 4.6 may be used to calculate the residual strain of the extreme fibres of the pipe. This strain will represent the specified residual strain at the extreme fibres of the bend that are presented in Table 4.4.

$$R = \frac{D}{(\vartheta/D)} \quad (4.5)$$

$$\epsilon_{Residual} = \pm \frac{r}{R} \quad (4.6)$$

Where D is the pipe diameter, ϑ/D is the bending degree per diameter, R is the theoretical radius of curvature of the centreline, r is the pipe radius, and $\epsilon_{Residual}$ is the theoretical residual strain at the extreme fibres of the bend.

4.2.2 Average Residual Strain

The residual strain in the pipe may also be determined through the use of a tape measure. Prior to testing of the specimens, the length of the tension side, compression side, and neutral axis of the bends were measured as presented in Table 4.3. These values may be used in conjunction with Equation 4.7 to calculate the average residual strain at the extreme fibres of the bend. The length of the straight segments at the ends of the pipe are subtracted from the neutral axis length in this equation because the residual strains due to cold bending predominantly occur over the bent region of the pipe. The average tape measure residual strain values presented in Table 4.4 are the average of the tape measure tension and compressive residual strains, and it is demonstrated that these values are similar to, but always larger than the theoretical values calculated using Equation 4.6. This increase in magnitude may be due to errors in calculating the straight segment length, the effects of shifting of the neutral axis, or ovalization during cold bending.

$$\epsilon_{Residual} = \frac{L_{Tensile/Compression} - L_{Centerline}}{L_{Centerline} - 2 \cdot L_{Straight}} \quad (4.7)$$

Where $L_{Tensile/Compressive}$ is the measured total tension or compression side bend length, $L_{Centerline}$ is the measured total centreline length of the pipe, and $L_{Straight}$ is the length of the straight segment of the pipe.

4.2.3 Residual Strain Measurement Results

The residual strains were directly measured for the TG and TCPL specimens. The TG residual strains were measured by installing strain gauges

onto the pipes while they were straight, and maintaining them on the pipes during cold bending. The curve presented in Figure 4.1 demonstrates the strains that are experienced by the strain gauges upon the completion of cold bending, and represent the residual strains in the pipe. In order to measure the TCPL residual strains holes were punched into the specimens while they were straight, and the distance between these holes was measured using a demec gauge. The distance between the holes was then measured again after cold bending was to determine the TCPL specimen residual strains as demonstrated in Figure 4.2. The thicker lines in Figures 4.1 and 4.2 represent the average residual strain at the various measuring locations around the circumference of the specimens.

4.2.3.1 TG Residual Strain Results

For the TG2 specimen, the average strain gauge measured residual strain for the compression side and tension side is presented in Table 4.2. From Figure 4.1, it is demonstrated that the residual strains are distributed non-uniformly along the bend length and that the strains generally fluctuate periodically. This non-uniformity occurs because the total bend angle in a cold bend is comprised of a series of individual kinks as opposed to a single uniform bend.

During cold bending of the TG specimens a single kink was produced at the horizontal position of -3300 mm from centre, while sequential kinks were produced between -1800 to 1900 mm from centre. Comparison of the residual strain at the single kink with those over the bend region of the pipe allow interpretations to be made about the interaction of residual strain between the sequential kinks. As the magnitude of the residual strains in the region of the single kink are generally lower than those in the region of multiple kinks for both of the specimens as demonstrated in Figure 4.1, it may be inferred that there is

interaction between individual bends during the multiple kinking procedure, and this interaction results in the magnifying of the residual strains.

It is also shown in Figure 4.1 that the residual strains on the compression side of the bend experience more extreme magnitudes than what is experienced at the tension side of the bends. This phenomenon occurs because at the extrados of the bend the variation in residual strain is predominantly due to the kinking procedure alone, while the variation in residual strain at the intrados of the bend is due to the kinking procedure as well as the introduction of local buckles into the pipe wall.

In comparing the residual strain distributions for TG1 and TG2, it was observed that the peaks in the residual strains for the TG2 specimen were greater in magnitude than those for the TG1 specimen. This is because of the different cold bending procedures that were used for the specimens, where TG1 was bent approximately 1 degree every 600 mm while TG2 was bent approximately 0.5 degrees every 300 mm. The average extreme fibre residual strains were relatively similar for the two specimens, and this is as expected because they both have the same global radius of curvature. Finally, the average directly measured residual strains were somewhat smaller than both the theoretical and average tape measured residual strains for both specimens. This discrepancy may be due to error in calculating the bend segment length, as these calculations were not confirmed with direct measurements.

4.2.3.2 TCPL Residual Strain Results

The residual strains for the TCPL specimens exhibited a relatively similar distribution to what was observed for the TG2 specimen, as shown in Figure 4.2. It was observed that the directly measured extreme fibre residual strains of

TCPL1 were somewhat less than those experienced by TCPL2. This difference is explained by the varying bending procedures of the TCPL specimens where TCPL1 was bent 1 degree per diameter of length while TCPL2 was bent 1.5 degrees per diameter of length. These varying bending procedures resulted in a lesser global radius of curvature for the TCPL1 specimen, which results in a lower average residual strain.

In addition to the extreme fibre residual strains for the TCPL specimens, information was obtained about their distribution around the circumference. As expected, the residual strains generally demonstrate maximum magnitudes at the extreme fibres and near zero values towards the neutral axis. However as demonstrated in Figure 4.3, the residual strains are not linearly distributed along the pipe cross-section as what would be expected for a perfectly circular cross-section (Timoshenko and Gere, 1958). The strains until 22.5 degrees to either side of the extreme fibres demonstrate a low gradient along the bending axis, and the strains midway between the extreme fibre and neutral axis are significantly greater than half of the extreme fibre strain as what would be necessary to have a linear strain distribution. This non-linearity in strains may be due to the ovalization of the pipe that occurs during bending, where a greater percentage of the area of the pipe material becomes situated towards to the extreme fibres.

For all of the TG and TCPL specimens, it is observed that the average residual strain at the extreme tension fibre was greater than that at the extreme compression fibre. This behaviour is due to the shifting of the neutral axis towards the intrados of the bend during cold bending (Murray and Bilston, 1993). Finally, the TCPL demec measured residual strains were relatively similar the predicted residual strain from Equations 4.3 and 4.4, which validates this residual strain measuring method.

4.3 Initial Imperfection Results

The initial imperfection device (IMD) was used to determine the overall geometry and initial imperfections of the bend specimens as previously discussed in Section 2.4. The rotation and vertical deflection at each longitudinal position were obtained using the rotation meter and cable transducer that were mounted on the carriage of the IMD. The radial direction magnitude and distribution of the initial imperfections were obtained using the LVDT's that were mounted on the plywood sheet that traveled along the test specimens. This information was later used in the finite element model to accurately replicate the pipe geometry.

4.3.1 Overall Geometry

The bend angle and vertical profile for the SNAM2 specimen are presented concurrently in Figure 4.4. This figure is representative the initial geometry measurements for all of the 7 bend specimens. In this figure the horizontal axis represents the horizontal position along the pipe, the left vertical axis represents the initial vertical deflection of the specimen, and the right vertical axis represents the angle of every horizontal position with respect to the angle at the precise middle of the bend.

4.3.1.1 Bend Angle

The measurements obtained from the rotation meter mounted on the carriage of the IMD demonstrated that the curvature of the bend was relatively uniform over the middle portion of the length, as demonstrated by the approximate linearity of the rotation vs. horizontal positions plot shown in Figure

4.4. In this figure, the average rotation is a smooth representation of the rotation meter measurements obtained from the imperfection measuring. The exact measured rotations were generally within 0.5 degrees of this smooth curve, and these fluctuations were motion that was employed during the traversing of the IMD along the specimen. The caused by the jerking rotation towards the ends of the pipes was approximately constant because of the straight segments that flank each side of the bend segments, and the rotation meter readings at the ends of the pipe were added together to calculate the rotation meter total bend angle that is presented in Table 4.6.

The angles at each end of the specimens were never exactly the same, as would be the case if the cold bends had a precisely uniform radius of curvature. This difference is a result of construction tolerances, as each kink in the pipe is not exactly the same angle. The difference in end angles was always less than 4% of the total bend angle. The measured total bend angle was generally less than the specified total bend angle. This measurement error is because the rollers that supported the imperfection-measuring device did not permit measuring until the very ends of the pipe. Measuring began approximately 500 mm from the one end, and finished approximately 350 mm from the opposite end, and these distances are less than the calculated straight segment length for some of the pipes as shown in Table 4.3. The percent error of the specified to measured total bend angle was between 0.3 to 13%. In order to verify the end angles obtained from the rotation meters, the end angles were also calculated using the slope of the pipe over a length of 200 mm from each end, using the vertical profile as presented in the following section. These angles compared favourably with the rotation meter results as shown in Table 4.6, and are the values to be used in the finite element models as they are more representative of the average end angle opposed to the angle of the pipe at a point.

4.3.1.2 Vertical Profile

The vertical cable transducer attached to the carriage of the imperfection-measuring device was used to determine the vertical profile of the bend specimen that is presented in Figure 4.4. This profile is relatively smooth and symmetrical, which suggests that the angle of each kink during cold bending was approximately uniform. The maximum vertical deflection from this plot was required to determine the maximum moment in the pipes during testing. The maximum vertical deflection was generally located near the middle of the specimen length, which verifies that the bend was essentially centred when the pipe was shortened from the original joint length prior to shipment to the University of Alberta.

As measurements were not obtained up until the very ends of the specimens, the cable transducer did not measure a significant proportion of the total vertical displacement. In order to determine the unmeasured vertical displacements, the distance from the end of the pipe to the beginning and end positions of the IMD were measured during the imperfection measuring procedure. These values were used in conjunction with the angles of the ends of the pipes to calculate the vertical and horizontal components of these unmeasured end distances. Thus the end vertical displacements that are shown in Figure 4.4 were indirectly determined. The unmeasured components were assumed to be straight because these distances are generally shorter than the straight segment lengths of the specimens. Because these distances were calculated, a direct measurement of the unmeasured end vertical and horizontal distances were taken for three of the specimens, and these values compared favourably with the calculated distances.

4.3.2 Initial Imperfections

As the specimens in the experimental program demonstrated high diameter to thickness ratios, local buckling occurred at the intrados of the bends during cold bending. The magnitude of these ripples was limited by the radial restraint provided by the mandrel and die within the cold bending machine, and was predominantly a function of operator experience. This is because the position of the mandrel with respect to each kink will affect the pipe wall restraint conditions. These ripples behave as initial imperfections on the pipe, and their magnitude and distribution may have a significant effect on its critical buckling strain. Measurements of the magnitude and distribution of these initial imperfections are imperative for input into the finite element model in order to accurately predict the behaviour of cold bends under combined loads.

4.3.2.1 Reduction of Initial Imperfection Data

In order to interpret the raw data obtained from the imperfection measurements, it was necessary to subtract the initial LVDT measurements from all subsequent readings. This permitted the radial displacements measured by the IMD to be read as the absolute magnitude of the radial deflection with respect to the end of the pipe. Upon completion of imperfection measuring, the reading of each LVDT was recorded when it was positioned one pipe radius from the exact centre of the IMD. This reading added to the pipe radius provided the distance from the LVDT when reading zero to the centre of the IMD. When the LVDT measurements from imperfection measuring are added to this value, the radius of the pipe at each measuring location could be determined. This allowed the radius along the entire length the pipe during imperfection measuring to be obtained.

The first step in determining the horizontal position of the IMD during imperfection measuring was to subtract the initial horizontal cable transducer reading from all subsequent readings. These values were then added to the horizontal component of the unmeasured beginning end portion to determine the position of all IMD readings with respect to the end of the pipe. As the rail of the IMD was shorter than the pipe length, a reset of the rail was required which acted to disrupt the horizontal cable transducer readings of the second half of the pipe. To account for this a horizontal cable transducer reading was recorded when the IMD reached the middle of the specimen after the first half of the test. Then after the rail was reset the IMD was repositioned at the middle of the specimen, and the horizontal cable transducer reading was again recorded. The absolute value of the difference in these readings was added to the horizontal cable transducer readings from the second half of the test to determine the horizontal position of the IMD over the second half of the test with respect to the beginning end of the pipe.

4.3.2.2 Initial Imperfection Measuring Results

The initial imperfection measuring results for the bend specimens are presented in Figures 4.6 to 4.11. These figures feature a fairly regular imperfection distribution over the middle region of the specimens. That is for the specimen compression side measuring locations, the peak-to-peak horizontal distance between imperfections is fairly similar, and the radial direction peak to trough distance of the imperfections is also fairly uniform. The magnitude of the neutral axis imperfections is generally considerably less than the compression side imperfections, and the overall distribution of these imperfections are less regular than the distribution at the other circumferential measuring locations. The tension side imperfections generally have greater magnitudes than the compression side imperfections, and the peak-to-peak distance between adjacent imperfections is somewhat greater than what is observed along the compression side. This is

because the imperfections along the tension side are a result of the kinking procedure during cold bending, while those along the compression side are from a combination of the kinking and local buckling of the pipe wall.

In order to quantify the results from the imperfection measurements, the average amplitude and period of the imperfections were determined for the 0 degree position LVDT for each specimen. The amplitude of an imperfection is defined as one half of the peak to trough radial distance between adjacent imperfections. The period is defined as the horizontal distance between adjacent peaks or troughs of the imperfections. The determination of these parameters is shown pictorially in Figure 4.5. In order to determine the imperfection amplitude and period, the horizontal and radial positions of each peak and trough for the 0 degree position LVDT was tabulated for the entire length of pipe. The horizontal distance between each adjacent peak and trough was calculated and in order to obtain the half wavelength of each imperfection. The average of all of these half wavelengths, multiplied by a factor of two, is the average period of the imperfections in the specimen. The radial direction distance between each adjacent peak and trough was calculated and divided by a factor of two to determine the amplitude of each adjacent imperfection. The average of all of these imperfection amplitudes is the average amplitude of 0 degree position initial imperfections in the specimen.

It is also important to quantify the distribution of the imperfection magnitudes around the circumference of the specimens. It was observed that the horizontal positions of the peaks and troughs of the imperfections at the 315, 337.5, 22.5, and 45 degree positions closely correlated with the horizontal positions of those along the 0 degree position. The magnitude of the imperfection peaks and troughs at these four LVDT locations were tabulated, and the average imperfection amplitudes were determined in the same manner as discussed previously. The average amplitude 22.5 degrees circumferentially from the compression line was calculated as the average of the 22.5 and 337.5 degree

position imperfection amplitudes, and the average amplitude 45 degrees circumferentially from the compression line was calculated as the average of the 45 and 315 degree position imperfection amplitudes. The period of the imperfections was relatively uniform around the compression side of the circumference and was not recalculated for those LVDT locations that were away from the 0 degree position. The average period and amplitudes for the SNAM2, TG2, and TCPL2 specimen imperfections are presented in Table 4.5.

The imperfection measurements for the SNAM2 specimen as shown in Figure 4.6 demonstrated an average amplitude of 0.97 mm, which is considerably greater than the average amplitudes demonstrated by the TG and TCPL specimens. This occurred because the SNAM bend specimens were taken directly from the field, while the other specimens were bent at a bend fabrication yard. Thus the bend operators during the bending of the SNAM specimens may have encountered undesirable time restraints and adverse outdoor conditions which will have affected the quality of the cold bending procedure. The average period of the SNAM2 imperfections was 205 mm, and the period was very similar for both of the SNAM bend specimens. In addition, the period for the majority of the imperfections for both of these specimens was relatively uniform

The average amplitude of initial imperfections for the TG2 specimen was 0.33 mm and the average period was 134 mm, as demonstrated in Figure 4.11. The amplitude and period of the initial imperfections was relatively uniform along the entire length for both of the TG specimens. The relatively small imperfection amplitude and regular imperfection distribution may have been influenced by the nearly ideal field conditions that were experienced during their cold bending.

The average amplitude of the TCPL2 specimen was 0.36 mm, and the average period was 292 mm. Figure 4.8 demonstrates that the amplitude and period of the imperfections for the TCPL2 specimen was not as uniformly distributed as what was observed in the other sets of specimens. In addition, the

compression side radius of the TCPL2 specimen demonstrated a relatively irregular behaviour in comparison with the observations from the other sets of specimens. The erratic amplitude and period of imperfections is possibly due to greater interaction between adjacent kinks that may occur for high diameter to thickness pipes, in comparison to lower diameter to thickness pipes. The non-uniformity in bend radius is due to the increased ovality of high diameter to thickness ratio cold bends, and the corresponding systematic error in radius measurement that is introduced during imperfection measuring as will be discussed in the next section.

The maximum imperfection amplitudes and minimum imperfection periods that were measured for the SNAM2, TG2, and TCPL2 specimens are presented in Table 4.5. These measurements are reported because these values might need to be considered during modeling as a single large imperfection over a short length could trigger local buckling. All of the imperfection measuring numerical results are available in Pipeline Technology Report No. 2005-1.

The period of the imperfections generally increased with increasing diameter to thickness ratio. The amplitude of the imperfections was not significantly affected by diameter to thickness ratio, and was more likely a function of bend operator experience and cold bending conditions. The imperfections of all of the TG specimens and TCPL specimens were similar although different kink spacing and magnitudes were employed within the specimen sets. This behaviour suggests that the cold bending procedure does not have a significant effect on the imperfection magnitude and distribution. The amplitude of the imperfections was generally a maximum at the compression line, and decreased until the neutral axis as demonstrated in Table 4.5.

4.3.2.3 Special Case: TG2 Initial Imperfection Measuring

The initial imperfection measuring setup and procedure for the TG2 specimen was different from the other tests because the strain gauges and thick coating did not permit measuring of the initial imperfections on the outside of the specimen. To accommodate these obstructions, the imperfection measurements were obtained from the inside of the pipe. Only the rail and horizontal cable transducer from the IMD was used during imperfection measuring of this specimen. A 50 mm LVDT was mounted in the vertical orientation on the rail to measure the radial deflection of only the compression line of the specimen.

In order to obtain the imperfection measurements, the pipe was positioned in the concave up position and the rail was inserted inside of the pipe directly beneath the compression line. The rail was supported such that one end of the rail rested on the bottom inside of the end of the pipe, as shown in Figure 4.12, while supports installed inside of the pipe beneath the other end of the rail were elevated to make the rail vertically level. The tilt of the rail was subsequently adjusted so that the LVDT contacted the compression line of the pipe. The LVDT was then connected to the data acquisition system, and pulled along the pipe, as shown in Figure 4.13, to determine the elevation of the pipe compression line with respect to the rail. In order to accommodate the range of the LVDT as well as the global vertical displacement of the pipe, several 50 mm spacers were installed between the LVDT and the rail when it was at the end position. These spacers were removed one-by-one from beneath the LVDT during imperfection measuring each time the stroke of the LVDT became exhausted. This procedure of pulling the LVDT until its stroke was exhausted, removing a spacer, and then pulling it again was repeated until the LVDT reached the end of the rail. As the rail was somewhat shorter than the pipe, three rail advancements were required. During advancement of the rail, the elevation of the rail supports was adjusted such that the elevation of the rail remained the same as prior to the advancement.

As shown in Figure 4.10, the TG2 imperfection measurements include the global vertical displacement of the bend. Figure 4.11 demonstrates the imperfection measurements without the global vertical displacement. In order to obtain the magnitude and distribution of the imperfections without the global vertical displacement, the horizontal and vertical position of each local peak and trough of each imperfection was first tabulated. Then, the global vertical displacement of each of these points was calculated using the average of the vertical displacements from the adjacent imperfections. The amplitude was then calculated as half of the imperfection magnitude minus the vertical displacement magnitude.

4.3.2.4 Ovalization Measuring Results

During the bending of a pipe the extrados of the bend will experience tangential tensile forces, while the intrados of the bend will experience tangential compressive forces. As the curvature of the bend is increased, the direction of these forces will become orientated so that one component will become orientated in the longitudinal direction, while the other component will become orientated in the vertical direction as shown in Figure 4.14. At the extrados of the bend the longitudinal component will be tensile, while the vertical direction component will be orientated towards the pipe centreline. At the intrados of the bend the longitudinal component will be compressive, while the vertical direction force will also become orientated towards the pipe centreline. These vertical forces will cause the in-plane diameter of the pipe to reduce, which will in turn cause the out-of-plane diameter to increase. This flattening of the cross-section will reduce the section modulus of the pipe which will in turn reduce the resistance of the pipe to in-plane bending loads. In addition, if the cold bend is applied with internal pressure the pipe will experience additional bending loads in the circumferential direction because of this ovalization (Boyle and Spence, 1980). Finally when

considering a cold bend under field conditions, if this ovalization becomes excessively large, pipe maintenance equipment may not be able to pass through the bend. It is for these reasons that the ovalization of the cold bends was comprehensively investigated in this experimental program.

The radius at the 90 and 270 degree positions during imperfection measuring were added together to determine the neutral axis diameter, and the radius at the 0 and 180 degree positions were added together to determine the bending axis diameter, for the entire length of the specimens. The difference between the bending axis and neutral axis diameters may be compared to understand the extent of ovalization that occurred in the test specimens due to cold bending.

The average ovalization of the SNAM2 and TCPL2 specimens calculated using Equation 4.1 was 1.2 and 0.9% respectively as shown in Table 4.7, thus the average ovalization was not a function of diameter to thickness ratio. However, it is demonstrated in Figures 4.6 and 4.8 that ovalization of the bends increased considerably as the middle of the specimens was approached for the higher diameter to thickness ratio pipes. This increasing of ovalization towards the middle of the specimen behaviour occurs because the straight segments of the pipe do not experience ovalization forces during cold bending, and act to restrain the ends of the bend segment from ovalizing. Consequently, the maximum ovalization for the SNAM2 and TCPL2 specimens are presented in Table 4.7, and the maximum ovalization measurements from all of the specimens indicate that the maximum ovalization of the specimens generally increased as the diameter to thickness ratio increased.

During imperfection measuring it was found that the neutral axis diameter was slightly underestimated for all of the specimens. This is because the LVDT's used to measure the neutral axis diameter are located at the 90 and 270 degree locations on the imperfection measuring device based on a perfectly circular pipe,

and the imperfection measuring device travels along the pipe on rollers that are supported by the pipes tensile side. As the IMD travels towards the pipe centre, the ovality of the pipe increases. This results in the LVDT's at the 90 and 270-degree positions to move towards the compression line of the pipe because the bending axis diameter of the pipe decreases while the distance from the rollers to the neutral axis LVDT's remains constant. This increases the distance from the LVDT's to the pipe wall, which results in smaller than actual readings for the radius measurement at the neutral axis. This behaviour is demonstrated pictorially in Figure 4.15.

4.4 Reduction of Experimental Data

During the loading of the test specimens, information was collected on the load-deformation response of the pipes by the instrumentation that was installed within the testing apparatus. This information was collected electronically, with the exception of the demec/calliper gauge readings, at numerous load increments during testing. The frequency of the demec/calliper readings was less than that of the electronic readings because of the considerable time required to collect manual measurement of the strains. The data collected through the fluke data acquisition system was initially raw, that is the values obtained from the instrumentation were the exact deformations experienced by the instrumentation with respect to some arbitrary datum that varied for each individual measuring device. This raw information does not permit meaningful interpretations to be conducted on the deformation of the specimens without some data manipulation. In addition, each measuring instrument used in the test setup could only collect information from the loads or deformations in a single direction. For this reason the initial measurements were combined with the measurements that were acquired through the instrumentation to obtain information from the tests that was not directly measured by the instrumentation, such as the applied moment.

Initial electronic and demec measurements were taken at the beginning of each test prior to any significant loading. These measurements will include the effects of the dead weight of the pipe and the water used to pressurize the specimens, as well as the small initial jack load of approximately 20 KN that was used to maintain the pipes position at the start of the test. These loads on the pipe may be considered negligible in comparison to the loads that they experienced during testing. As the response of the pipe relative to its initial position is the information that is required from the tests, the initial readings of the instrumentation were subtracted from all subsequent readings obtained during testing when determining the deformation response of the test specimens.

The range of several of the cable transducers and LVDT's that were used in the test setup was less than the expected deformations during testing that they would be required to measure. In order to accommodate this predicament, measures were taken prior to loading of the specimen. For those instruments whose range would decrease during testing, wires were installed for connecting the measuring device to the pipe, and for those specimens whose range would increase during testing, spacers made of wire hooks with a length similar to the stroke of the instrumentation were produced. During testing the deformation of the instrumentation was closely monitored, and alarms in the data acquisition were set to light up once the stroke of an instrument approached its limit. Every time an alarm went off, the loading of the specimen was immediately stopped and a set of electronic readings were acquired. Then at the alarmed instrument locations, either the wire was shortened for the instruments whose stroke was decreasing, or a spacer was inserted for the instruments whose stroke was elongating. Then to complete the reset of the instrumentation, another set of readings was taken prior to the commencement of reloading of the specimen. During the data reduction of the instrumentation measurements, the difference in the readings immediately before and after the resets was calculated, and added to

all of its subsequent readings. This allowed the sizeable deformations that were experienced by the test specimens to be measured throughout testing.

The reduction of the data from the demec gauge and calliper measurements was conducted differently than for the electronic strain gauge measurements. To determine the demec gauge strains, the initial reading for each demec gauge was first subtracted from all subsequent readings from the test. Then the strain at each loading step was calculated by multiplying this difference by the calibration factor of the demec gauge. To determine the strains obtained from the calliper measurements, the initial reading for each measuring location was subtracted from all subsequent readings at that location, and this difference was divided by the initial calliper reading as demonstrated in Equation 4.8.

Because measurements using the calliper are not as precise as the demec measurements, the first set of calliper readings that was used during the test was calibrated with the demec strain measurements at that load. That is, when it was observed that the stroke of the demec gauge approached the limit of its range during a test, a set of calliper readings was taken. Then during data reduction, the difference between the calliper and demec reading at this load step was calculated, and added to all subsequent the calliper strains that were calculated using Equation 4.8.

$$\epsilon_{Calliper} = \frac{L_n - L_0}{L_0} \quad (4.8)$$

Where $\epsilon_{Calliper}$ is the strain measured using the calliper, L_n is the calliper measurement at the n^{th} load step, and L_0 is the initial calliper measurement of the position along the pipe that is being considered.

4.4.1 Determination of Global Moment

The determination of the global moment in the test specimens was required in order to quantify the load that would cause local buckling of the pipe. The moment experienced by the pipe was caused by the longitudinal force applied by the jack, in combination with the jack eccentricity to the pipe centreline. This parameter is required in order to determine the moment–curvature behaviour of the pipe, which is the relationship that will later be used in Chapter 5 to describe the global behaviour of the test specimen. The global moment will characterize the loading in the pipe as calculated through simple statics, and will neglect any local distortion experienced by the pipes during testing.

The moment that will be determined in this section is the moment that was generated at the middle of the specimen during testing. This will represent the maximum moment of the pipe, and as the buckle for all of the specimens occurred close to the middle of its length, this moment will also represent the moment experienced at the buckle location during testing. In order to verify this assumption, the difference in the moments at the middle and the precise buckle location were compared for the SNAM2 specimen, which buckled further from the middle of the specimen than any of the other pipes. Through the vertical deflection profile obtained from the initial imperfection measurements, the initial vertical deflection at the eventual buckle location was 8mm less than that at the middle of the specimen. Then by interpolating the measurements obtained from the cable transducer at the middle and 1016mm from the middle of the specimen during the test, it was found that vertical displacement at the precise buckle location was 12 mm less than that at the middle of the specimen when the peak moment in the test was achieved. As the total eccentricity of the jack load to the pipe centreline at the middle was 1044mm when the peak moment in the pipe was achieved, and the corresponding total eccentricity the precise buckle location was 1024mm, this resulted in a percent error of 2%. As this error is relatively small, the maximum moment in the pipe may be assumed to be representative of the

moment at the precise buckle location. Therefore, the moment in the pipe during testing was calculated by multiplying the load in the jack with its eccentricity to the pipe centreline at the middle of its length.

As previously discussed in Section 2.2.2, the load in the jack was determined by multiplying a calibration factor with the measurements obtained from the pressure transducer that monitored its hydraulic pressure. Because the orientation of the jack was positioned precisely horizontally, it is the vertical distance from its line of action to the pipe centreline at the middle of its length that provided the eccentricity to the pipe that caused the in-plane moment. To obtain the precise moment experienced at the middle of the pipe, considering the relatively long specimen length and substantial applied curvature, the second-order effects resulting from the vertical deflection of the pipe in combination with the rotation of the moment arms that occurred during the tests needed to be taken into account.

The initial eccentricity of the jack to the pipe centreline at the middle of its length is a summation of the vertical distance from the jack to the pipe centreline at the end plate location, and the initial vertical deflection of the middle of the pipe as previously determined during the initial imperfection measuring. During loading of the test specimens, the jack load was transferred from the jack piston to the hinge on rollers, and then through the pin that connected the hinges to the hinge at the bottom of the moment arm. Because of the angle at the ends of the pipe, and the corresponding initial rotation of the moment arms, the direction of the line of action of the jack at the bottom of the moment arm was different from horizontal.

In addition, there is an initially horizontal distance between the pin and the end of the pipe as pictorially demonstrated in Figure 4.16. Thus, this horizontal distance in combination with the initial rotation of the moment arm, results in an initial vertical distance at the start of the test between the point on the pipe side of

the moment arm that corresponds to the line of action of jack, and the original line of action of the jack at the piston location. Therefore, the vertical distance from the jack to the pipe centreline at the end of the specimen is comprised of two components: the vertical distance from centre of the jack piston to the point of the line of action of the jack at the pipe side of the moment arm, and the vertical distance at the pipe side of the moment arm from the point of the line of action of the jack to the pipe centreline at the end plate location. The magnitude of these dimensions has been presented in Figure 4.16.

At the non-jack side of the testing frame the load at the pin at this location is the same as that provided by the hydraulic jack because the testing frame is in equilibrium. In addition, because of the near symmetry of the test setup, the vertical distance of the pipe at the middle of its length to the pin at the hinges will be similar for both ends of the test frame. It is for these reasons that the moment provided by the non-jack side of the test setup does not require further investigation, as it may be assumed to be the same as that provided at the jack side of the test setup.

In order to determine the second-order moment on the pipe, the vertical displacement of the middle of the specimen during testing was added to the initial vertical distance from the jack piston to the pipe centreline at the middle of its length when computing the total jack eccentricity, as demonstrated in Figure 4.16. This vertical displacement during testing was monitored by two vertically orientated cable transducers that were positioned above and below the specimen. The vertical displacement of the middle of the pipe during testing was calculated as the average of the readings from these two cable transducers when computing the total eccentricity of the jack load. These cable transducers will also account for the vertical deflection of the pipe caused by the rotation of the hinges and moment arms during testing.

Due to the jack stroke during testing, the centre of the pipe experienced some longitudinal deformation that caused an artificial increase in the vertical displacement measurements of the vertical cable transducers at the middle of the pipe. In order to account for this error, an additional cable transducer was installed a known longitudinal distance from the compression side middle cable transducer, and subsequently connected to the same location of the pipe. As the lengths became known for each side of this newly created triangle throughout testing, the true vertical deflection of the pipe could be calculated. This measurement demonstrated to be extremely similar to the vertical deflection using the average of the two vertical cable transducers therefore this measurement was neglected for simplicity.

As the moment gradient along the length of the pipe is relatively low, and the initial angle and rotation of the ends of the pipes during testing is different at each end, the average end angle and rotation of the ends of the pipe were considered when determining the vertical distance from the jack to the centreline of the pipe at the end plate. The equation representing the moment at the pipe centreline at the middle of its length during testing is presented in Equation 4.9. It should be noted that the moment arms were assumed to be rigid in this equation, thus any deformation of the moment arms during testing was neglected.

$$M_{Max} = P_{Jack} \cdot [L_{Hinge} \cdot \sin \vartheta_0 + e_0 \cdot \cos \vartheta_{Test} + L_{v0} + L_{vTest}] \quad (4.9)$$

Where M_{Max} is the second order moment of the pipe at the middle of its length, L_{Hinge} is the initially horizontal distance between the centre of the pin to the pipe side of the end plate, θ_0 is the average angle of the ends of the pipe at the beginning of the test, e_0 is the initial distance from the line of action of the jack to the centreline of the pipe at the end plate, θ_{Test} is the average rotation of the ends of the pipe during testing, L_{v0} is the initial vertical deflection of the pipe as established during initial imperfection measuring, and L_{vTest} is the vertical deflection of the middle of the pipe during the testing.

4.4.2 Determination of Local Curvature

The local curvature is valuable for interpreting the behaviour of the pipe at a particular cross-section along its length, such as at the buckle location. It was calculated by subtracting the strain on the compression side of a particular cross-section along the pipe from that of the corresponding tension side strain, and dividing this result by the original outside diameter of the pipe as demonstrated in Figure 4.17. The strains in Equation 4.10 were measured during testing using the electronic strain gauges, demec gauge, and calliper. In this equation small deformation theory is applied ($\tan \theta \approx \theta$) because the measured strains are relatively small.

$$\phi_{Local} = \frac{\epsilon_{Tensile} - \epsilon_{Compressive}}{D} \quad (4.10)$$

Where ϕ_{Local} is the local curvature at a particular cross-section along the length of the pipe, $\epsilon_{Tensile}$ is the strain on the tension side of the cross-section, $\epsilon_{Compressive}$ is the strain on the compression side of the cross-section, and D is the outside diameter at the end of the pipe.

In Equation 4.10 the diameter from the end of the pipe as opposed to that at the middle of the pipe was used for several reasons. Firstly, the end diameters were directly measured while the interior diameters were calculated from the imperfection measurements, which resulted in measuring error. In addition, based on the measurements presented in section 4.3, the initial end and interior diameters are relatively similar for all of the specimens. Also, the additional ovalization of the specimens during testing was neglected because these measurements were not accurately known when using the instrumentation installed in the test setup.

The specimens experienced an axial load during testing because of the jack load and pressure forces acting against the end plates. This load generated strains at the extreme fibres of the pipes that were reflected in the strain gauge, demec gauge, and calliper measurements. The distribution of the axial strains is uniform along the depth of the cross-section; consequently they do not affect the determination of the local curvature. This is because the compression side strains are subtracted from the tension side strains in this calculation, thus the axial strain component is cancelled resulting in the strain differential representing only the variation in strains due to the bending loads.

Prior to buckling of the specimen, the local curvature is the same as the global curvature at every location along the pipe. For this reason, the local curvature averaged over the entire specimen length may be used to represent the global curvature of the specimen, prior to buckling. Upon the initiation of buckling, the local curvature at the buckle location will become greater than the global curvature because of the concentration of strains. Correspondingly, the local curvature of the pipe cross-section away from the local buckle will become less than the global curvature due to the relaxation of the strains over the majority of the pipe length after local buckling.

The magnitude of the local curvature after buckling is dependant on the gauge length that it is calculated over. That is, the maximum local curvature will occur precisely at the buckle location, and will decrease as the gauge length increases. The gauge lengths selected for the specimens in this specimen were one third of the diameter of the pipe length, one diameter of the pipe length, and the entire pipe length. The one-third-diameter length was selected because the demec and calliper gauge lengths used were one third of the diameter, the one diameter length was used because this is the standard gauge length over which buckle deformations are generally measured, and the entire pipe length was used so that the global curvature calculated using the strain measurements could be compared to those calculated using the rotation meters.

The local curvature over the one-third-diameter gauge length was calculated using the directly measured strains from testing in combination with Equation 4.10. The strain/demec/calliper gauges were spaced at one-third of the diameter intervals on the compression side of the pipes, while they were spaced at two thirds of the diameter intervals along the tension side of the pipe because of the substantial time required to obtain demec measurements in combination with the relatively low strain gradient that would be observed along the tension side of the pipe. Because of this variation in spacing, in order to calculate the local curvature over a gauge length of one pipe diameter, the local curvature from two adjacent pipe cross-sections that are spaced two thirds of a pipe diameter apart was averaged together. Similarly during calculation of the average local curvature over the entire length of pipe, the local curvatures at cross-sections spaced two thirds of a pipe diameter apart over the entire specimen length were averaged together.

4.4.3 Determination of Global Curvature

The global curvature of the specimens was used to assess their global deformation due to the applied moment during testing. It was determined using two different methods in this experimental program. The first method was to divide the rotation between the ends of the specimen by its horizontal length. The second method was to average the local curvatures in the specimen over its entire length. A comparison of the global curvature resulting from these two methods will be discussed in Section 4.4.3.3.

4.4.3.1 Global Curvature from Rotation Meter Measurements

The global curvature may be defined as the rotation between the ends of the specimen divided by its length. The rotation that was used for calculating the curvature was the summation of the angles measured by the rotation meters that were positioned on the moment arms during testing. The specimen length used to determine the curvature refers to the horizontal distance over which the deformation in the pipe occurs.

Previous research based on tests of straight pipes (Dorey, *et al*, 2001) indicated that the end collars on the specimens function to significantly stiffen the ends against bending, resulting in a decrease in the length over which the rotation in the specimen takes place. However, upon completion of the bolting of the collars to the specimens in this experimental program, a small gap was observed between the collar and pipe at the intrados and extrados of the bend for all of the test specimens. This gap occurred because the test specimen cross-section was ovalized while the collar shape was relatively circular. Because of this gap the rotation in the specimens could take place over the entire pipe length, and for this reason the length of the collars was not subtracted from the specimen length during the determination of the global curvature.

The horizontal length of the specimens shortened during testing, which generated a second order effect on the global curvature of the pipes. In order to determine the actual length of the specimens, the stroke of the jack, the rotation of the moment arms, and the rotation of the hinges needed to be accounted for. The jack stroke at each load step was subtracted from the initial horizontal length of the pipes when calculating the horizontal length of the pipes. The rotation of the moment arms acted to increase the horizontal length of the pipe during testing. The horizontal distance from the pin to the end of the pipe, combined with the rotation of the pipe during testing, also increased the length of the specimens during testing. These distances are demonstrated schematically in Figure 4.16. It

was the average rotation of the two moment arms that was used when calculating effect of the rotation of the moment arms and hinges on the global curvature of the pipes, and the equation used to calculate the global curvature of the specimens during testing is presented in Equation 4.11.

$$\phi_{Global} = \frac{\vartheta_{Test}}{L_{H0} + 2 \cdot L_{Hinge} \cdot (1 - \cos \vartheta_{Test}) + 2 \cdot e_0 \cdot \sin \vartheta_{Test} - \Delta_{Jack}} \quad (4.11)$$

Where ϕ_{Global} is the global curvature of the specimen during testing, θ_{Test} is the average rotation of the left and right ends of the pipe during testing, L_{H0} is the original horizontal length of the pipe, L_{Hinge} is the horizontal initial distance from the centre of the pin to the pipe side of the end plate, e_0 is the initial eccentricity provided by the moment arms, and Δ_{Jack} is the stroke of the jack during each load step.

4.4.3.2 Global Curvature from Strain Measurements

As previously discussed in Section 4.4.2, the strain at the extreme fibres may be used to calculate the global curvature of the test specimens. By calculating the local curvature of the specimen using Equation 4.10 at every $2 \cdot D/3$ spaced measuring location, and averaging these values over the entire specimen length, the global curvature of the pipes could be determined. This was accomplished using both the strain gauge and demec/calliper strains. These two strain based global curvatures compared favourably with each other; however, as the demec/calliper gauge measurements are less susceptible to local effects and are a more direct measurement, these measurements will be used to represent the strain based global curvature response of the test specimens.

The global curvature response of the pipes as determined through the strain measurements is only valid prior to buckling. This is because the local curvature calculation based on Equation 4.10 is based on the assumption that plane sections remain plane throughout the bending deformation history, which is not the condition in the pipes after local buckling occurs. Thus the global curvature when determined using the strains in the specimen appear extremely erratic after buckling and do not represent the true global curvature. For this reason only the initial linear portion of the global curvature as determined using the strains in the pipe may be compared with the global curvature using Equation 4.11.

4.4.3.3 Comparison of Global Curvature Measurements

In general, the global curvature response as determined using the rotation meters was relatively similar to the global curvature as determined using the demec gauges prior to buckling of the specimens. However, the demec strain global curvature was typically stiffer than the rotation meter global curvature over the initial region as demonstrated in Figure 4.18. This is contrary to what would be expected, as the global curvature response over the initial portion of the curves should be identical when using either of two methods. Consequently, considerable study was undertaken to investigate this discrepancy.

In order to verify the rotation meter global curvature, the measured angle of each of the North and South end rotation meters were compared with each other at every load step. The linear regions compared favourably for the majority of the specimens, thus verifying the validity of these measurements because it is extremely unlikely that both rotation meters would be incorrect by precisely the same factor. In addition, further investigation of the test setup verified that the angle measured by the rotation meters is exactly the rotation of the ends of the

pipe so long as the moment arms behaved rigidly. Investigation of the horizontal length determination as demonstrated in Figure 4.16 indicated that all of the variables required for determining the horizontal length of the specimen during testing were accounted for. In addition, when comparing the deformed length during testing to the initial length, it was observed that this change is minute during the initial region, thus the denominator in Equation 4.11 is relatively unaffected by the shortening of the specimen during testing. Based on this investigation considering both the numerator and denominator of Equation 4.11, the global curvature when determined using the rotation meters appears to be accurate.

In order to investigate the global curvature as determined using the demec/calliper strains, the average of the demec/calliper and average of strain gauge strains over the entire length of the compression side of the specimens were compared with each other, and the average of the demec/calliper and average of the strain gauge strains over the entire length of the tension side of the specimens were also compared with each other. The demec/calliper strain measurements were thus verified as these measurements compared favourably with the strain gauge strains. The diameters at the ends of the pipes were directly measured using a measuring tape, and they compared favourable at all 8 of the measuring locations for all of the pipes. Investigation of the ovality of the cold bend indicated that ovality over the bend region was always less than 3%, which results in a relatively small error in the local curvature calculation. As several of the specimens were pressurized, it can be assumed that the ovality caused by the applied moment during testing will be relatively minor. Thus it appears that the global curvature as determined using the demec/calliper strain measurements in combination with Equation 4.10 yielded accurate results.

Through this investigation, due diligence has been applied in the determination of the global curvature response of the test specimens, and the discrepancy in the initial stiffness could not be realized. For this reason, the

global curvature of the specimens using both methods will be presented for comparison with the finite element model. As the global curvature using the demec strains is a more direct measurement, it will be assumed that this method represents the true global curvature response of the specimens over the initial portion of the moment-curvature curves. The rotation meter global curvature will represent the global curvature response of the specimens after local buckling because it is the only available measurement of the post buckling global curvature, and the initial regions using the two methods were generally relatively similar.

4.5 Determination of Critical Buckling Strain

The critical strain is defined as the strain experienced by the test specimen when the onset of local buckling occurs. Once the strain in the pipe achieves this value of strain, the moment carrying capability of the pipe will begin to decrease. It is expected that the critical strain of cold bends will be less than that of a straight pipe because of the geometry and material changes introduced during the cold bending process. As discussed in Chapter 1, there are currently several design equations to calculate the critical strain of straight pipes, and after the critical strain of the cold bends is determined the extent of this reduction will become better understood.

Considerable study has been applied in this research to determine the critical strain of the test specimens. This was accomplished because the strains in pipes under field conditions are often monitored at locations in which sizable ground deformation is expected, such as at lines that traverse unstable slopes. In addition, through finite element analysis the strains that would occur along a pipeline during an earthquake may be predicted. If the strains experienced by the pipe are greater than the critical strain, the specimen will buckle, and this will

cause excessive cross-sectional distortion and possible fracture. Values for the critical strain of cold bend pipes is currently unknown, which leads to challenges for the designer when ascertaining the modifications necessary during the initial design phase when considering a pipe that may experience an earthquake, or when determining what level of strain may occur in a pipe prior to the requirement of remediation procedures, such as stress relieving, for a pipe that traverses an unstable slope. In this research program the critical strain of the test specimens was determined using two different approaches.

4.5.1 Critical Strain using Maximum Moment Method

The first method used for determining the critical strain was to determine the strain at the buckle of the pipe when the peak moment is experienced during the test. This is the standard method for critical strain determination that is used in industry. In order to obtain the critical strain using this method, the maximum moment in the pipe as calculated using Equation 4.9 was tabulated for each load step. Then the location of the buckle with respect to the instrumentation was selected as the demec/calliper gauge position that experienced the greatest strains at the end of the test. The strains from this demec/calliper gauge represent the strain at the buckle over a gauge length of one-third of the pipe diameter; however, the strain over a gauge length of one diameter is the standard measure of strain that is used in industry. For this reason, the demec/calliper readings to either side of the demec/calliper position that contained the buckle were also tabulated. Then these three demec/calliper readings were averaged together to calculate the average strain at the buckle over a gauge length of one diameter. Subsequently this strain was plotted against the maximum moment in the pipe. The value of the strain over a gauge length of one diameter corresponding to the maximum moment experienced by the pipe represents the critical strain for the specimen when using the buckle strain at maximum moment method.

The buckle strain at the maximum moment method has some disadvantages that cause inconsistencies during the determination of the critical strain. The first of these complications is that the slope of the moment vs. buckle strain curve may become extremely low at the region where the applied moment is close to the maximum moment as shown in Figure 4.19. This causes the determination of the critical strain to become relatively subjective as only a very minor change in moment may result in a substantial increase or decrease in the strain at the buckle. Thus, the strain at which the pipe buckles may vary depending on the researcher who locates the maximum moment from this curve. In addition, demec readings were taken at only every second or third load step as the maximum load was approached during testing because of the substantial time required to obtain these readings. As the second order moment is unknown during testing, it is possible that demec readings were not obtained at the precise maximum moment experienced by the pipe. As the strains at the buckle are significantly changing when the maximum moment is approached, the strain measured at the largest moment in the pipe at which the demec readings were taken may be quite different from the actual strain at the buckle at the precise maximum moment.

4.5.2 Critical Strain using Bilinear Method

To accommodate the difficulties in determining the critical strain when using the buckle strain at the peak moment method, an alternate method for determining the critical strain of the test specimens was developed in this research program to complement the industry standard method. In this method the global curvature during the test is plotted against the strain at the buckle location over a gauge length of one diameter. The initial region of this curve will demonstrate linearity because the material throughout the pipe behaves elastically during

initial loading of the specimen. In addition, the post-buckling region of this curve will be nearly linear. This behaviour occurs because once the specimen buckles, the majority of the deformation of the specimen will occur at the buckle region. The global deformation of the specimen at this point will become dependant on a number of variables such as the post-yielding material stiffness, buckle shape, cross-section shape, wall thickness, and several other factors. During post-buckling one of these variables will commence to dominate the global curvature response of the specimen, causing a linear global curvature to buckle strain response. The region in between the initial and post-buckling region of the global vs. local curvature plot will not be linear. This non-linearity is a result of the residual stresses, imperfections in the pipe wall, and the non-linearity of the pipe material after the proportional limit is achieved.

In order to determine the critical strain using the global curvature vs. strain at buckle curve, a series of two regression analyses are applied. The slope using points from the initial linear region of the curve is determined using one regression analysis, and then the slope using points from the post-buckling of the curve is determined by using the second regression analysis. The point at the curve at which these straight lines intersect is defined as the global curvature at which local buckling of the pipe is initiated. To obtain the value, the equations of the two lines are equated, and the corresponding global curvature of the test specimen is solved for.

Then the strain at the buckle over a gauge length of one diameter corresponding to this global curvature during the test is assessed. This strain will represent the critical strain of the pipe using the bilinear method. Due to the systematic nature of this method, the critical strains obtained will be very repeatable between different researchers, which will allow for easier comparison of the critical strains obtained from different research projects. It should be noted that the post-buckling regions of the global vs. local curvature plots demonstrated a bilinear relationship for several of the test specimens. This behaviour occurred

because after significant deformation in the pipe occurs, second order effects at the buckle begin to play a substantial role in the deformation behaviour of the specimen. To avoid these complications, the slope of the first portion of the post-buckling curve of the specimens was used when determining the critical strains. An example of the determination of critical strain using the global vs. local curvature curve method is presented in Figure 4.20.

As previously discussed in Section 4.7, the initial linear region of the specimen global curvatures when using the rotation meters did not precisely correspond to the global curvatures when using the demec gauges, and this consequently causes error when using the bilinear global curvature method to determine the critical strain. To address this discrepancy, the global curvature using both the rotation meters and demec strains vs. buckle strain were plotted together for the TG2 specimen, which demonstrated the greatest difference in initial slope. The critical strain was then determined using the initial region of both global curvatures and the post-buckling region of the rotation meter global curvature, as presented in Figure 4.20. It was established that the critical strain when using the demec gauge global curvature was only 0.05% greater than the critical strain when using the rotation meter global curvature. The similarity in these critical strains may be attributed to the relatively low slope of the post-buckling region of the curve. As this difference in critical strain is negligible from a designer's perspective, only the critical strain using the rotation meter global curvature was used for the remainder of the test specimens.

Table 4.1 – Specimen End Diameter Measurements

| Specimen | Average Diameter (mm) | Bending Axis Diameter (mm) | Neutral Axis Diameter (mm) | Average End Ovality (%) |
|----------|-----------------------|----------------------------|----------------------------|-------------------------|
| SNAM2 | 759.7 | 755.8 | 765.1 | 1.2 |
| TG2 | 608.2 | 606.3 | 609.3 | 0.5 |
| TCPL2 | 760.2 | 751.2 | 770.7 | 2.6 |

Table 4.2 – Specimen Wall Thickness Measurements

| Specimen | Average Wall Thickness (mm) | Average Intrados Wall Thickness (mm) | Average Extradados Wall Thickness (mm) | Average Wall Thickness Change (mm) |
|----------|-----------------------------|--------------------------------------|--|------------------------------------|
| SNAM2 | 11.57 | 11.70 | 11.62 | 0.04 |
| TG2 | 14.17 | 14.32 | 14.29 | 0.02 |
| TCPL2 | 8.34 | 8.55 | 8.23 | 0.16 |

Table 4.3 – Specimen Length Measurements

| Specimen | Calculated Bend Segment Length (mm) | Calculated Straight Segment Length (mm) | Measured Neutral Axis Length (mm) | Measured Tension Side Length (mm) | Measured Compression Side Length (mm) |
|----------|-------------------------------------|---|-----------------------------------|-----------------------------------|---------------------------------------|
| SNAM2 | 5679 | 841 | 7360 | 7444 | 7298 |
| TG2 | 4909 | 1284 | 7476 | 7553 | 7426 |
| TCPL2 | 6512 | 446 | 7404 | 7504 | 7316 |

Table 4.4 – Specimen Residual Strain Measurements

| Specimen | Average Tape Measure Residual Strain (%) | Average Demec Measured Residual Strain (%) | Predicted Extreme Fibre Residual Strain (%) |
|----------|--|--|---|
| SNAM2 | 1.29 | - | 1.23 |
| TG2 | 1.29 | 0.89 | 1.11 |
| TCPL2 | 1.44 | 1.35 | 1.31 |

Table 4.5 – Specimen Initial Imperfection Results Summary

| Specimen | Average Period (mm) | Minimum Period (mm) | Average 0° Amplitude (mm) | Average 22.5° Amplitude (mm) | Average 45° Amplitude (mm) | Maximum Amplitude (mm) |
|----------|---------------------|---------------------|---------------------------|------------------------------|----------------------------|------------------------|
| SNAM2 | 205 | 127 | 0.97 | 0.91 | 0.84 | 1.42 |
| TG2 | 134 | 97 | 0.33 | - | - | 0.61 |
| TCPL2 | 292 | 71 | 0.36 | 0.29 | 0.22 | 0.73 |

Table 4.6 – Specimen Global Geometry Imperfection Measuring Results

| Specimen | Maximum Vertical Deflection (mm) | North End Slope Measured Angle (Degree) | South End Slope Measured Angle (Degree) | Total Slope Measured Bend Angle (Degree) | Total Rotation Meter Bend Angle (Degree) |
|----------|----------------------------------|---|---|--|--|
| SNAM2 | 209.5 | 5.21 | 5.32 | 10.54 | 11.72 |
| TG2 | 198.4 | 5.39 | 4.86 | 10.25 | - |
| TCPL2 | 234.3 | 6.65 | 6.20 | 12.85 | 12.37 |

Table 4.7 – Specimen Ovality Imperfection Measuring Results

| Specimen | Average Ovality (%) | Maximum Ovality (%) |
|----------|---------------------|---------------------|
| SNAM2 | 1.18 | 1.79 |
| TG2 | - | - |
| TCPL2 | 0.86 | 1.72 |

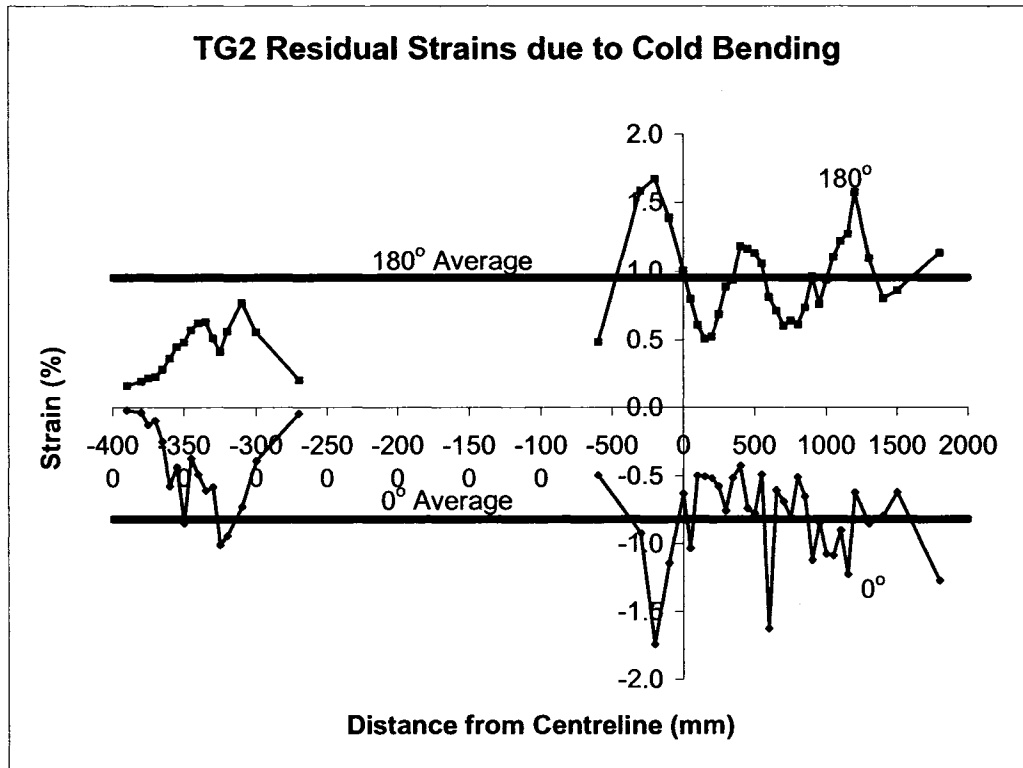


Figure 4.1 – TG2 Residual Strains

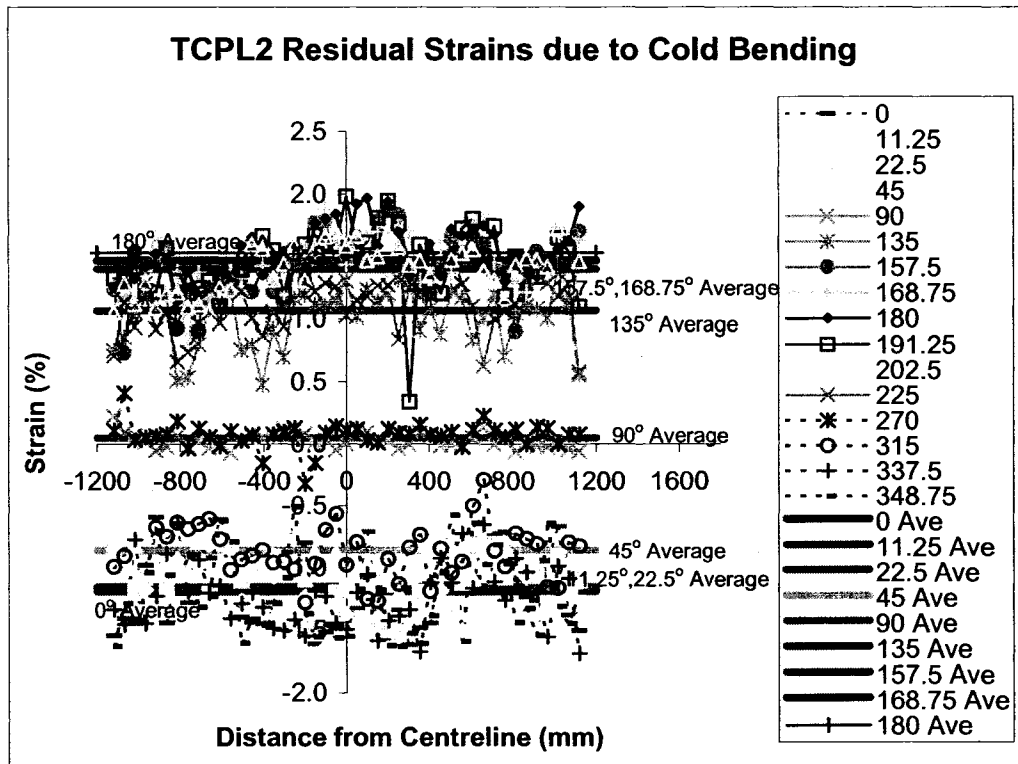


Figure 4.2 – TCPL2 Residual Strain of Degree Around Circumference

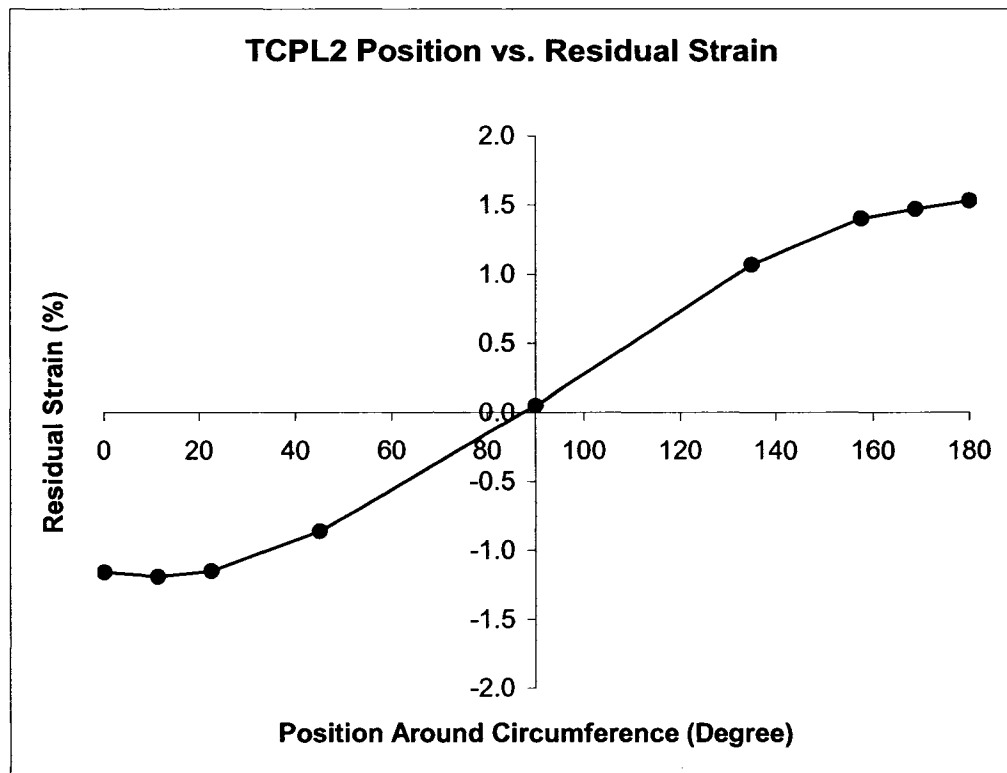


Figure 4.3 – TCPL Circumferential Position vs. Residual Strain

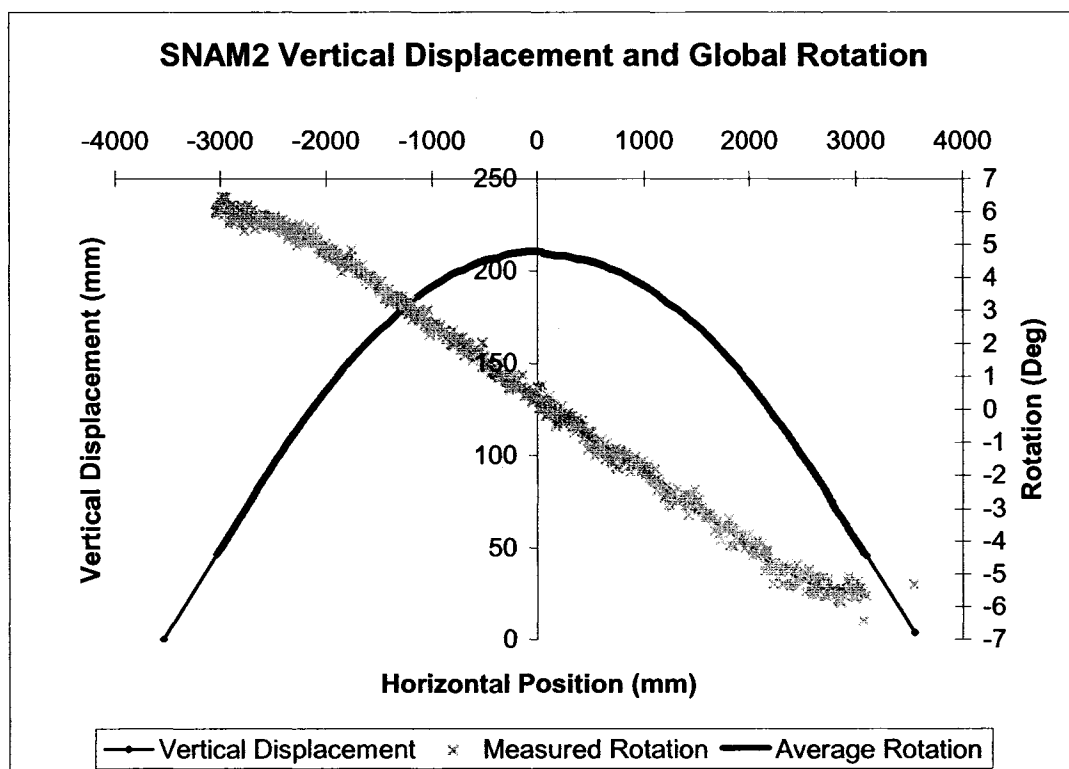


Figure 4.4 – SNAM2 Vertical Displacement and Global Rotation

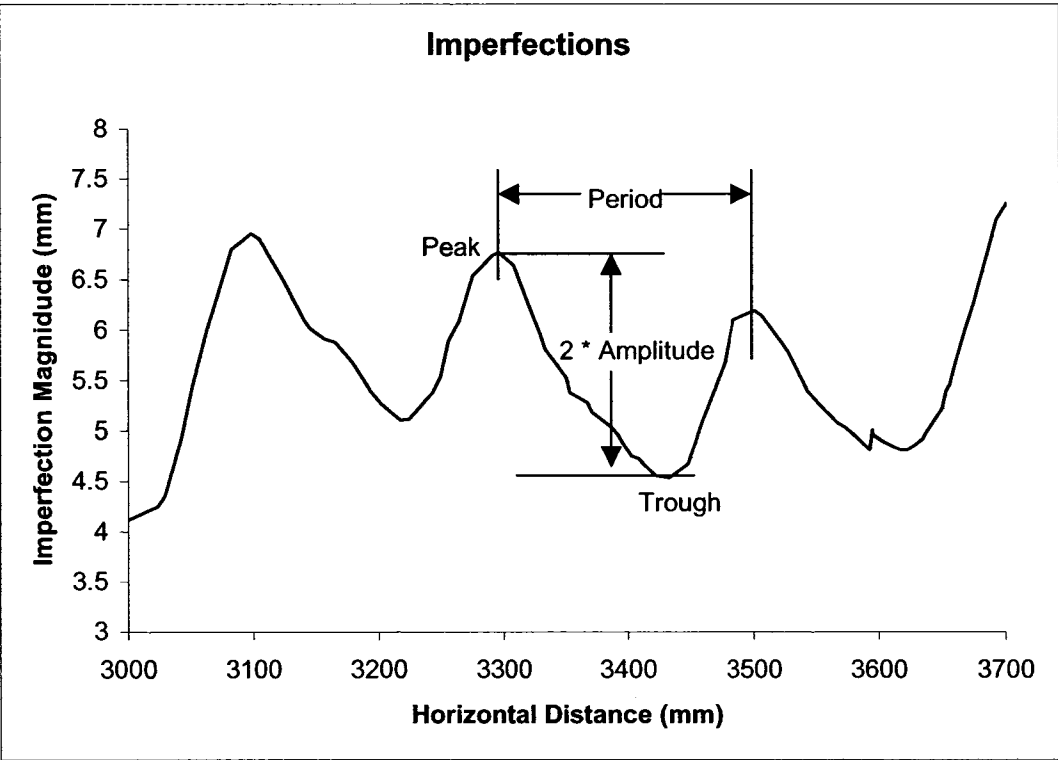


Figure 4.5 – Determination of Imperfection Amplitude and Period

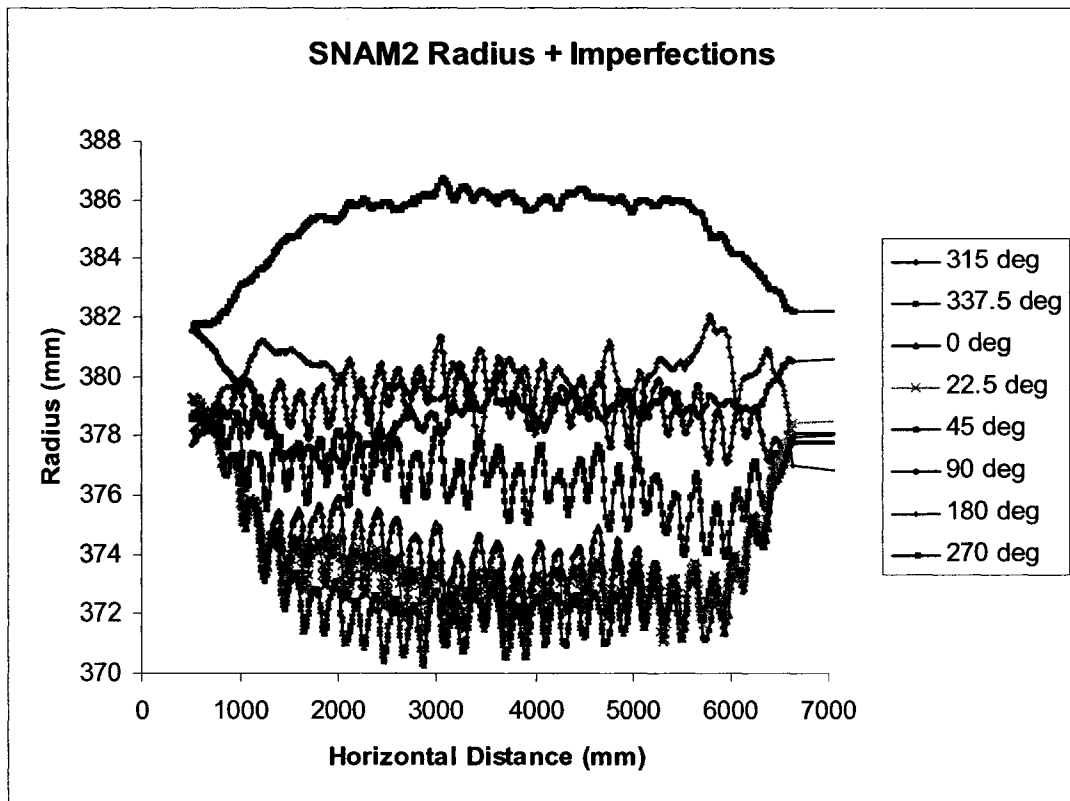


Figure 4.6 – SNAM2 Initial Imperfections

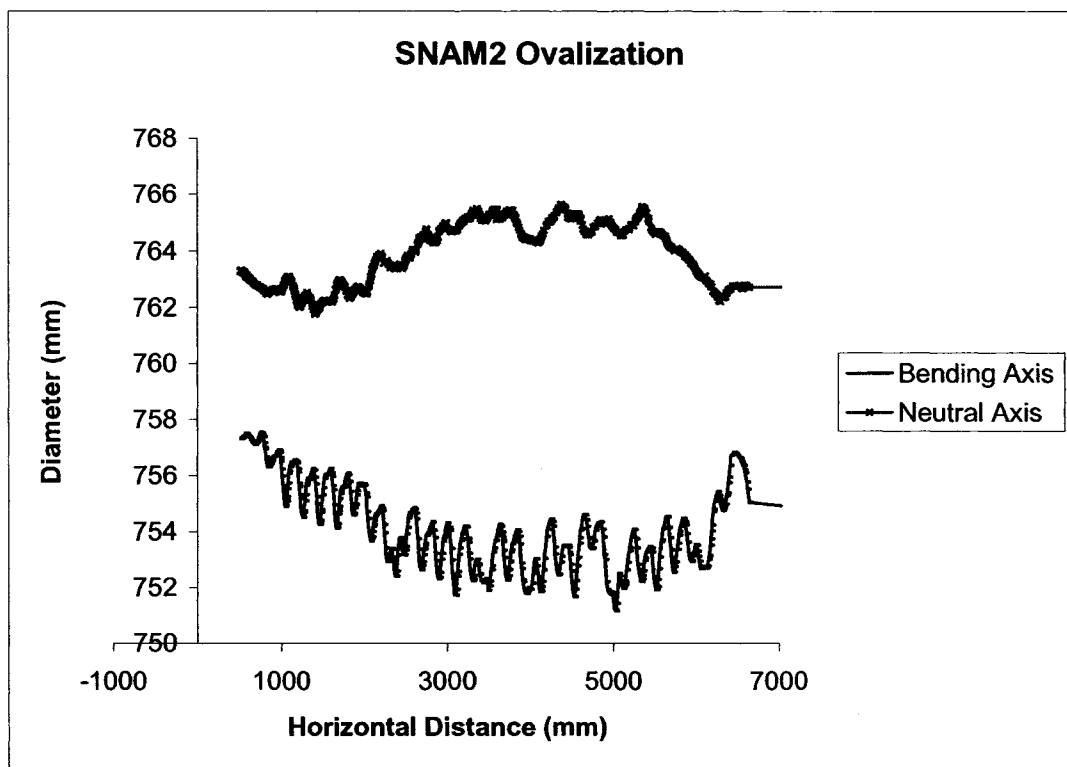


Figure 4.7 – SNAM2 Ovalization

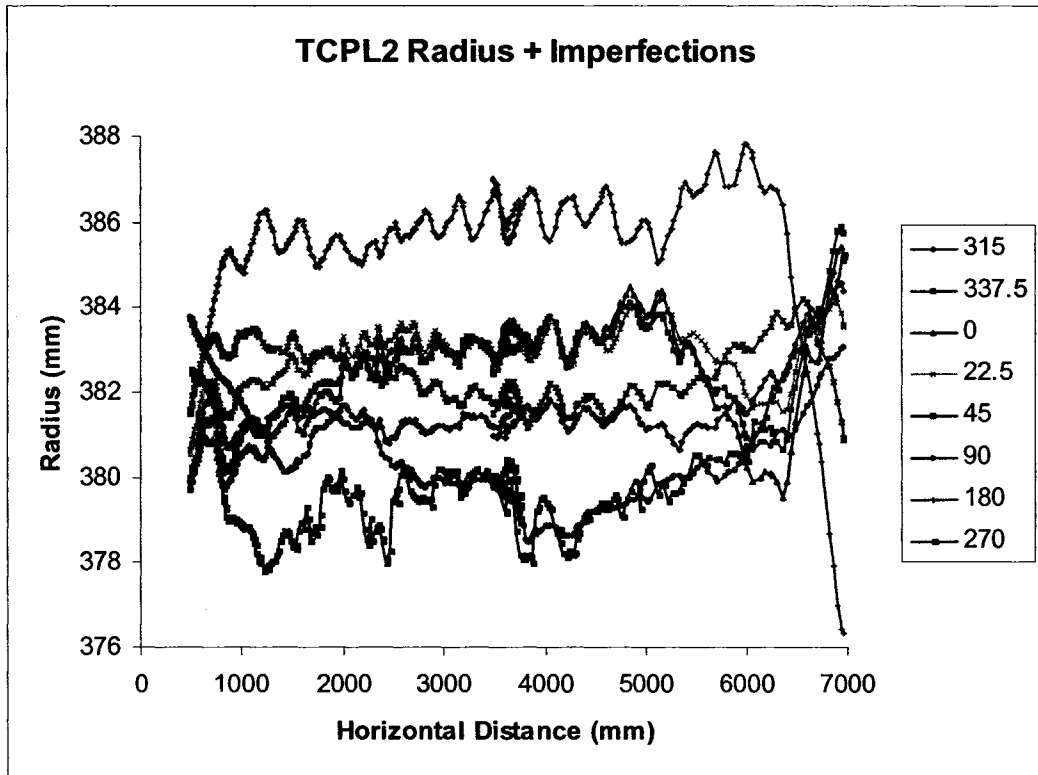


Figure 4.8 – TCPL2 Initial Imperfections

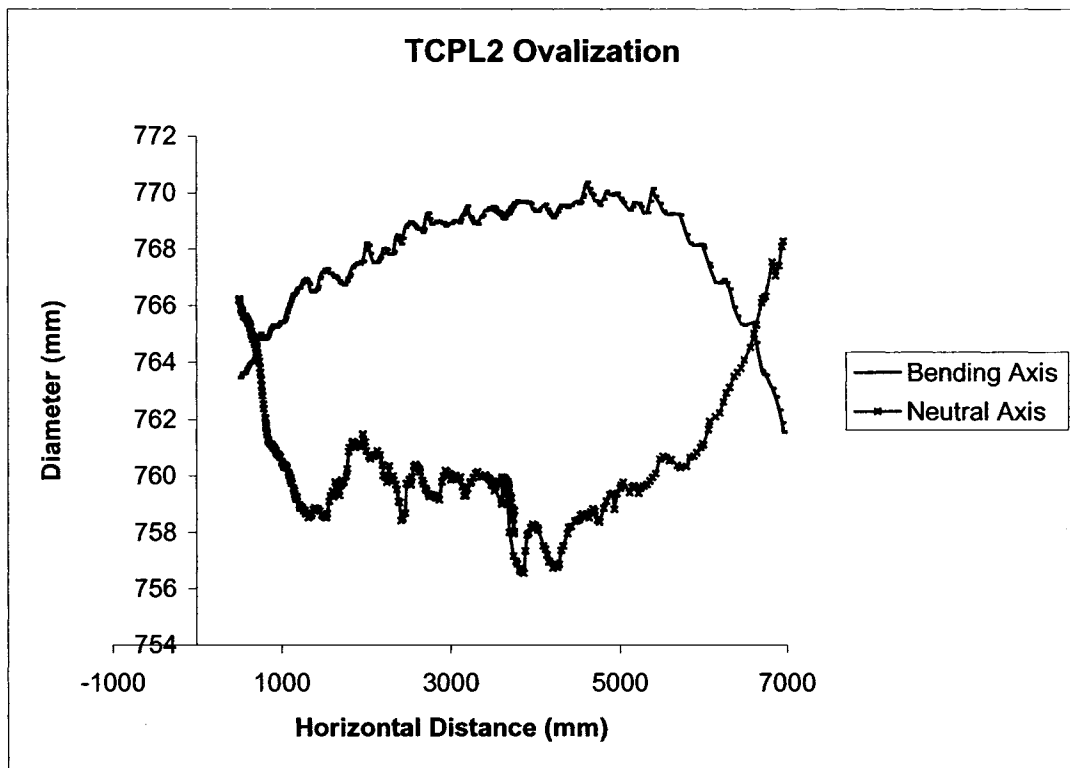


Figure 4.9 – TCPL2 Ovalization

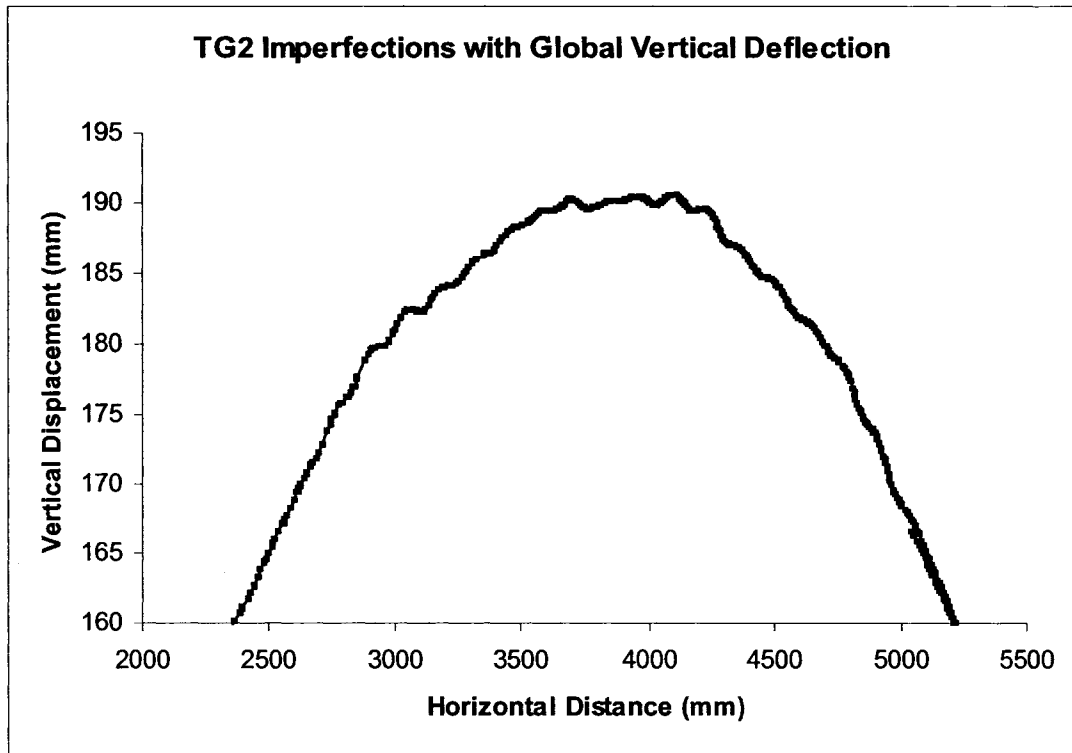


Figure 4.10 – TG2 Imperfections with Global Vertical Deflection

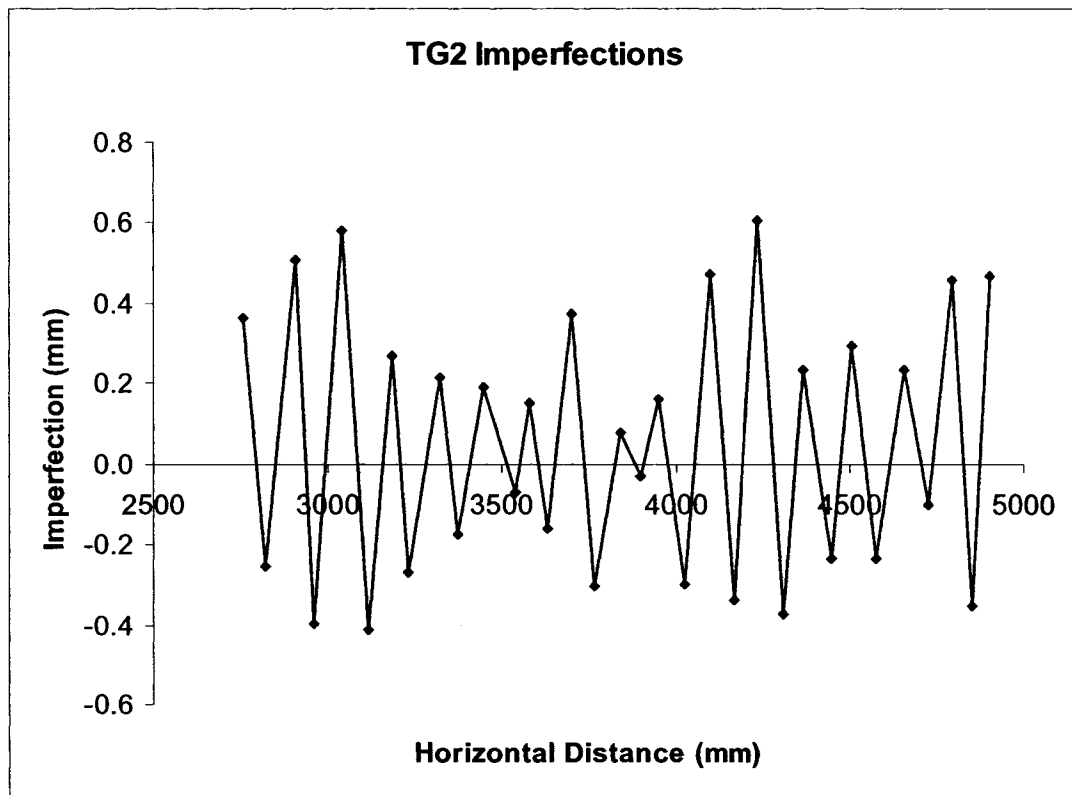


Figure 4.11 – TG2 Imperfections

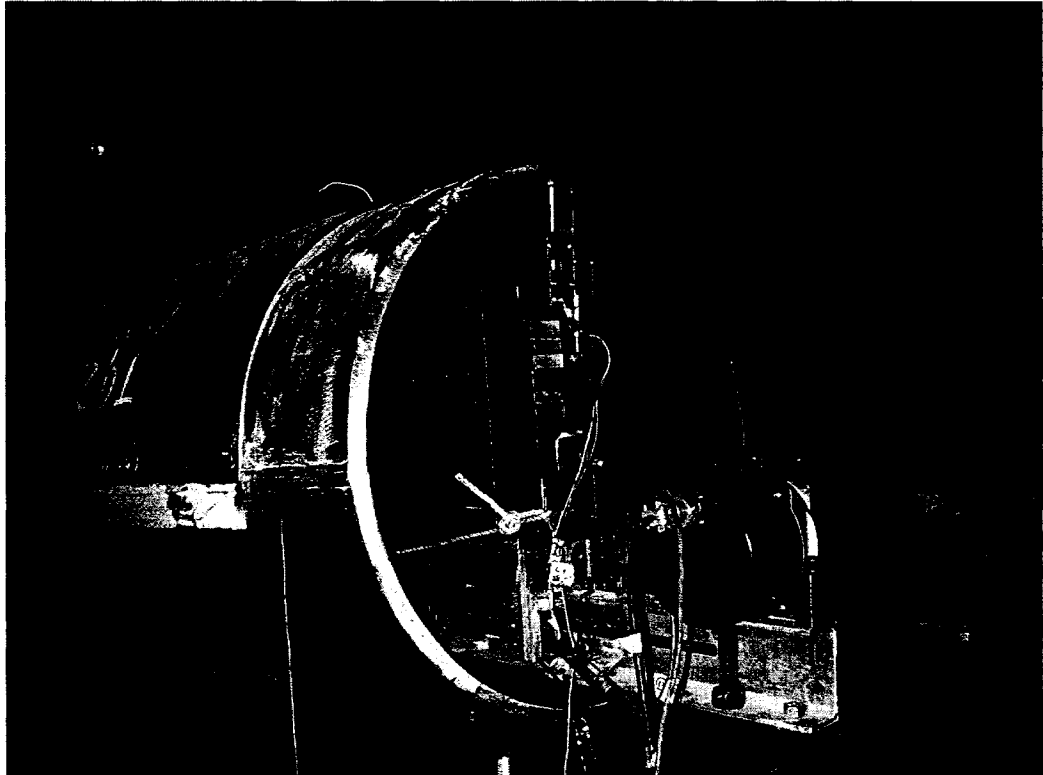


Figure 4.12 – TG2 Imperfection Measuring End View



Figure 4.13 – TG2 Imperfection Measuring Rail Inside of Pipe

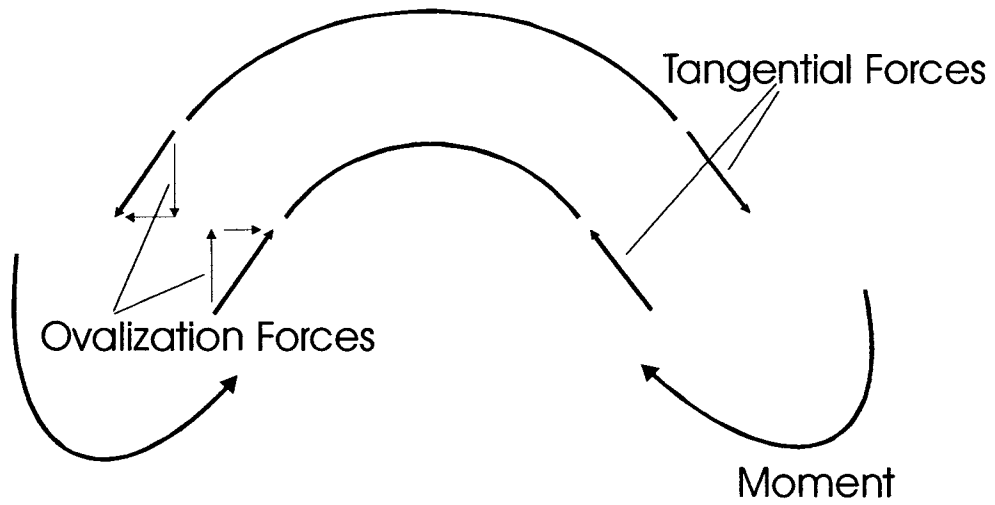


Figure 4.14 – Ovalization Forces Caused by Bending Moment

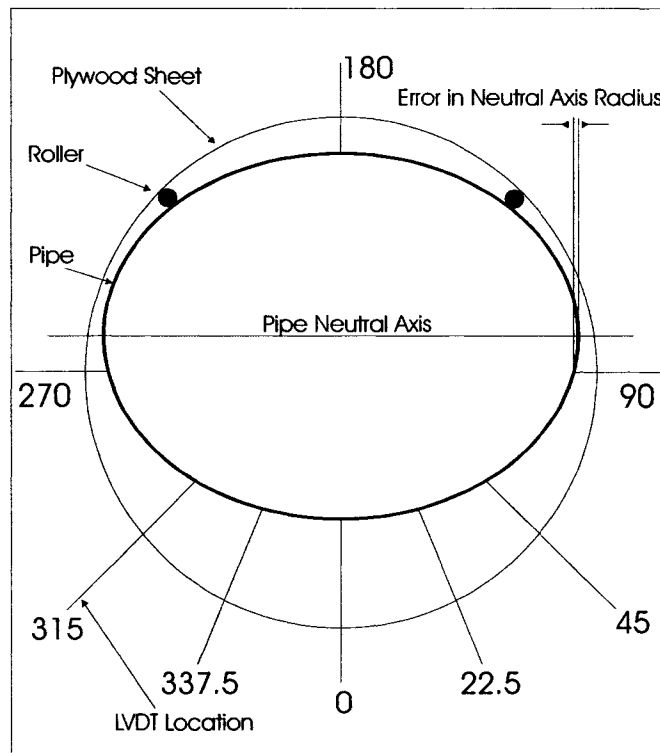


Figure 4.15 – Imperfection Measuring Cross Section

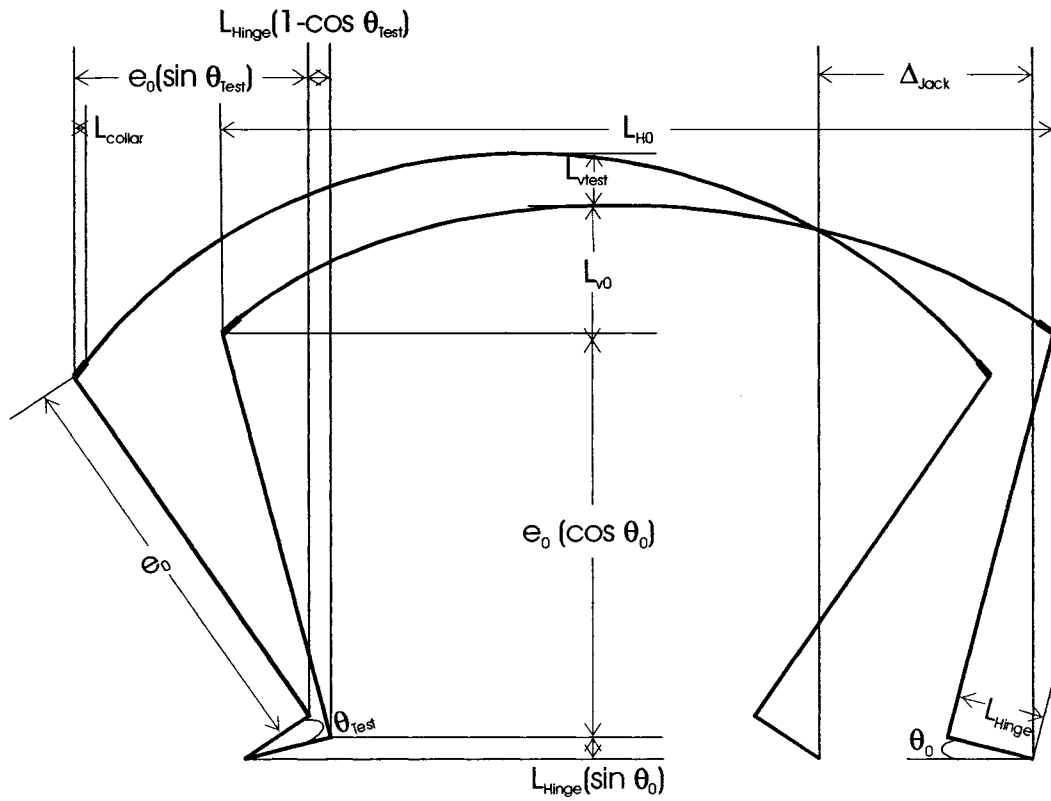


Figure 4.16 – Schematic of Moment and Curvature Determination

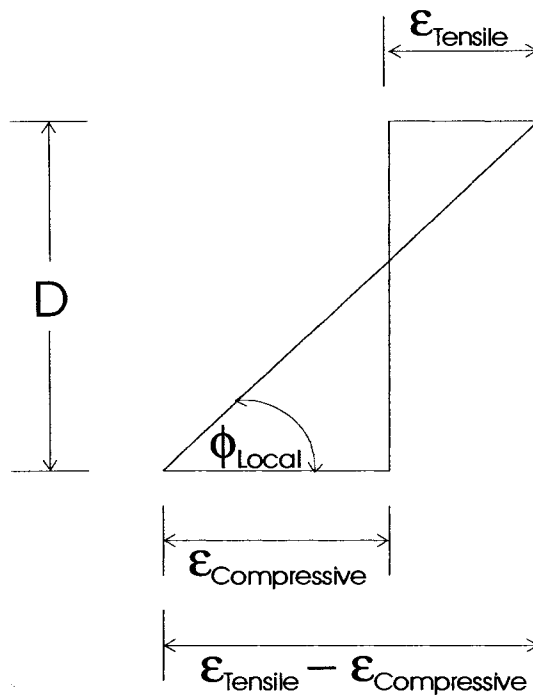


Figure 4.17 – Strain Distribution used to Determine of Local Curvature

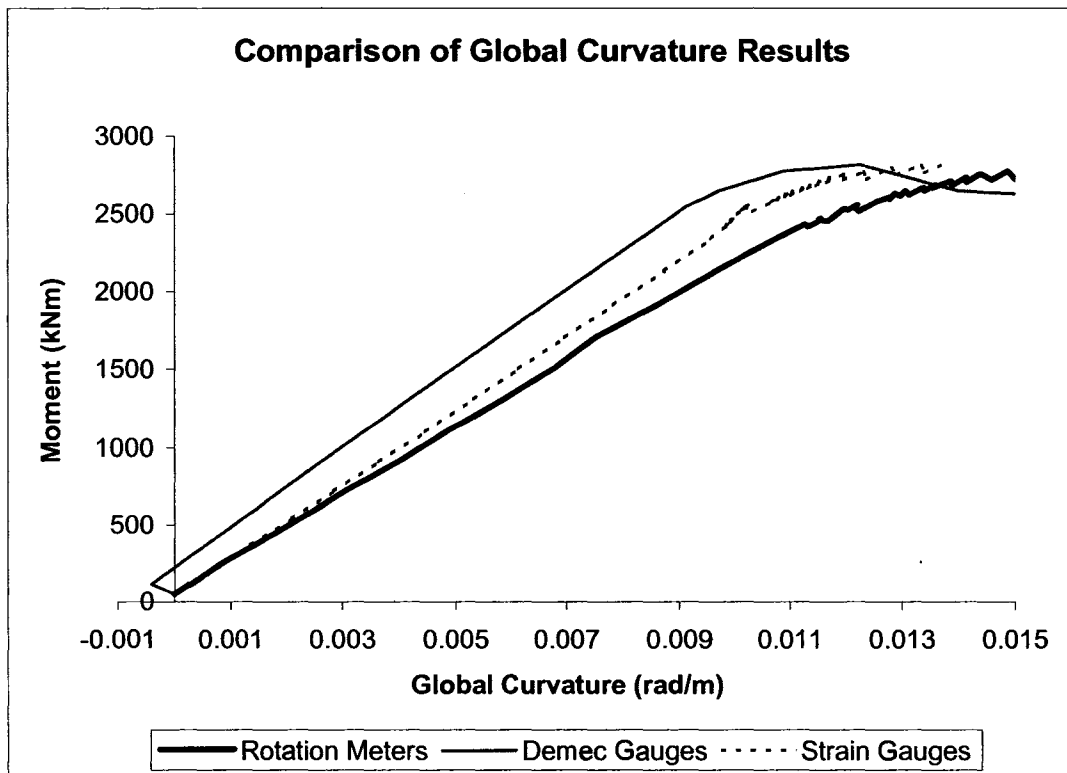


Figure 4.18 – Comparison of Rotation Meter and Strain Based Global Curvatures

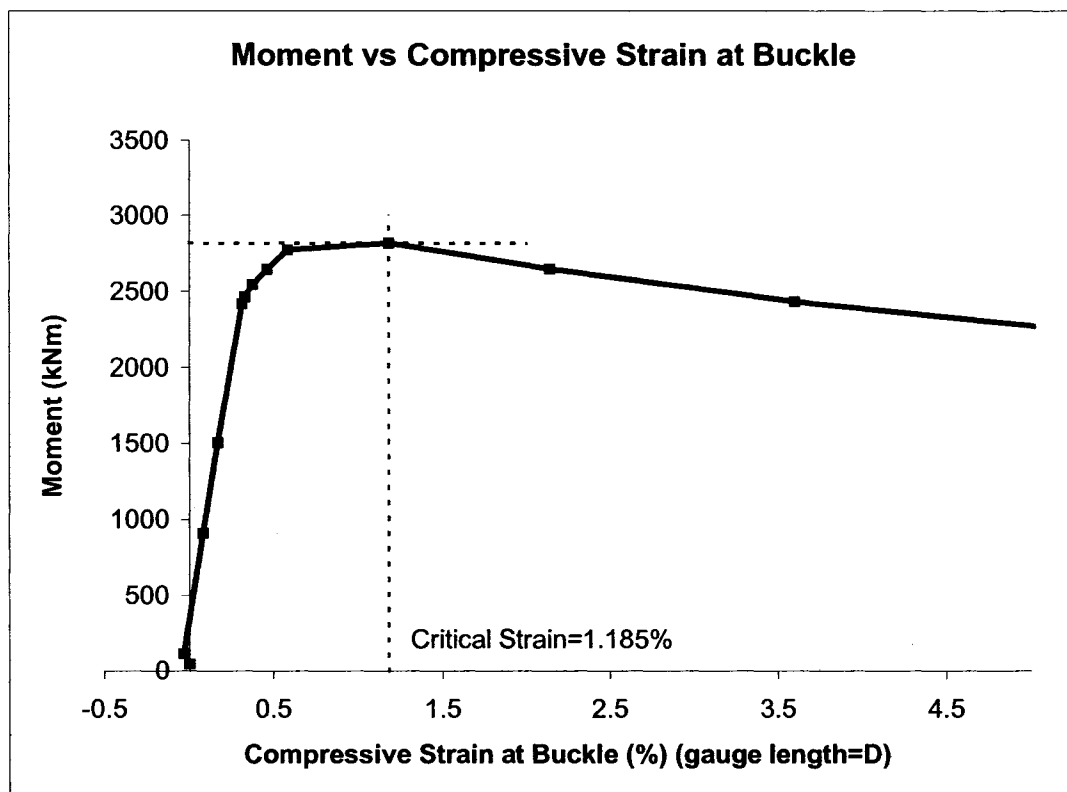


Figure 4.19 – Example of Critical Strain using Maximum Moment Method

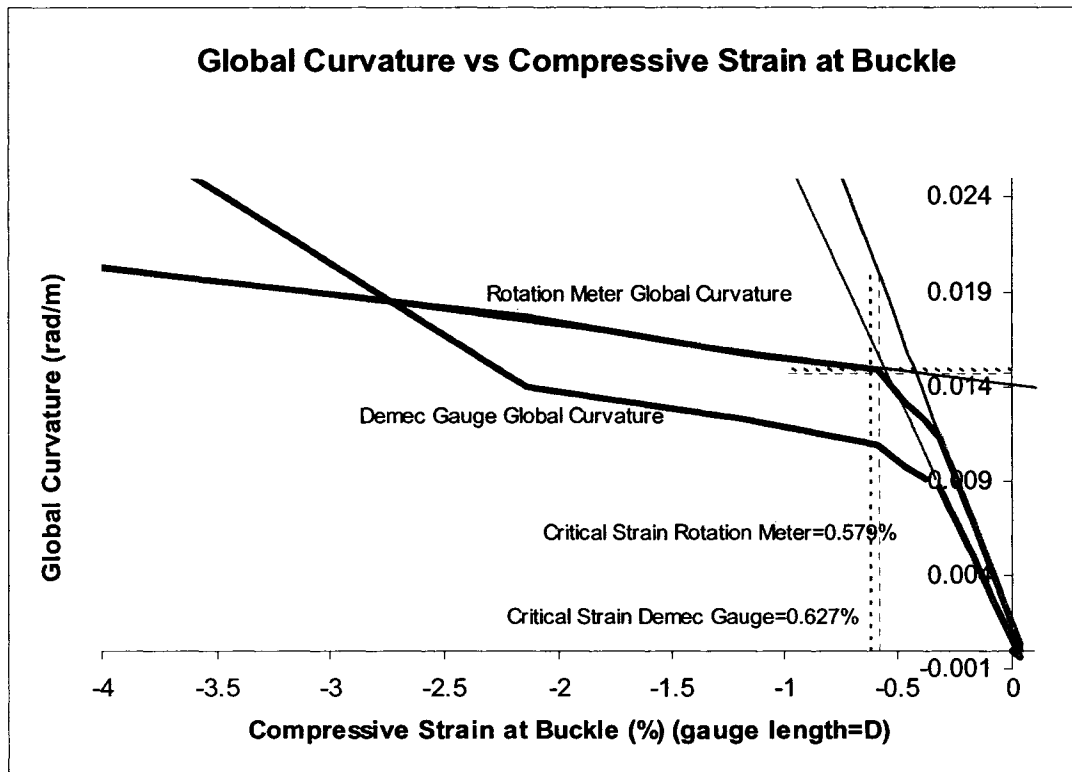


Figure 4.20 – Example of Determination of Critical Strain using Bilinear Method

5.0 DISCUSSION OF EXPERIMENTAL RESULTS

The primary objective when interpreting the results obtained from the experimental program was to gain an understanding of the behaviour of cold bend pipes under combined loads. The critical strain of the test specimens was investigated to gain information about the reduction in the critical strain of a cold bend in comparison to that of a straight pipe. The final goal of the experimental program was to gain an understanding of the post buckling behaviour of the specimens considering the allowable deformation prior to fracture of the specimen.

At the beginning of this chapter some of the equations previously presented in Section 1.6 will be utilized to predict maximum moment and critical strain values for the test specimens. Then, a comprehensive investigation of the results from the SNAM, TG, and TCPL specimens will be presented. Finally, a comparison of the test results between the three sets of specimens will be discussed to demonstrate the effects of all experimental parameters on the behaviour of cold bend pipes. The topics that will be discussed within each test results section include the following:

1. Test Observations
2. Global Deformation based on Moment – Curvature Response
3. Local Deformation based on Strain Distribution
4. Critical Strain Results
5. Post –Buckling Behaviour

All values have been removed from the scales of the moment - curvature figures, and the strain values have been removed from the local deformation figures herein. In addition, the local deformation of only the SNAM2, TG2, and

TCPL2 specimens will be presented herein. Describing the behaviour of only these three specimens during testing without specific values is adequate in understanding the behaviour of cold bend pipes under applied loads. The numerical testing results and local strain distributions with absolute values for all of the specimens are included in Pipeline Technology Report No. 2005-1.

5.1 Prediction of Test Results

During the design of the test setup, it was desired to maximize the compressive load in the specimens during testing in order to better simulate the compressive effects from the thermal expansion that would occur in a pipe under field conditions. As the applied moment and axial load are provided to the specimens by a single jack, and the capacity of this jack was known to be 4000 KN, only the length of the moment arms could be adjusted in order to achieve the required moment to buckle the pipe while at the same time accommodating the capacity of the hydraulic jack. In order to determine this dimension, it was necessary to approximate the level of moment required to buckle the specimens during loading.

As the specimens were loaded with internal pressure, axial load, and bending moment, in order to calculate the plastic moment, the interactive moment equation for a straight pipe that was derived by Mohareb *et al*, 1994 in Equation 1.4, was applied to the eight specimens in this testing program. This equation neglects the effects of strain hardening, local buckling, or any effects of cold bending. Nonetheless, the plastic moment obtained from the use of this equation may be utilized to predict the moment capacity of the test specimens, and may subsequently be compared to the maximum moment in the pipes during the experimental tests in order to validate the results. When utilizing this equation, the pressure force on the end plates was subtracted from the jack load to

determine the axial load in the pipe. In addition, it was necessary to solve the equation iteratively because the applied moment is created by the jack load multiplied by the moment arm length, while the moment capacity of the pipe is also related to the jack load.

It was also desired to predict the critical strain of the test specimens in order to obtain a benchmark for comparison with the test results. The design equation that was developed at the University of Alberta by Dorey *et al*, 2001 in Equation 1.5, was selected for this undertaking due to the reasonable predictive capabilities that this equation demonstrated with the database of pipes studied during the Dorey, *et al* research. This equation does not account for any of the effects from cold bending of the pipes, however, the results will provide some idea of the expected critical strains for the test specimens. It was assumed that the material for all of the test specimens demonstrated a rounded yield plateau because of the load history experienced by the pipe materials during cold bending as previously discussed in Section 3.4. It was also assumed that the initial imperfection magnitude for all of the test specimens was 2% of the wall thickness.

5.2 SNAM Test Results

The three SNAM test specimens were nominally 762 mm in diameter with 11.1 mm wall thickness and Grade X60 material. The differences between the specimens was that SNAM1 was straight and pressurized to 60% SMYS hoop stress, SNAM2 was cold bent at 1.41 degrees per diameter of pipe length and pressurized to 60% SMYS hoop stress, and SNAM3 was bent at 1.41 degrees per diameter of pipe length and unpressurized. The material in SNAM2 and SNAM3 were from the same heat of steel, while the material in SNAM1 was from a different heat.

5.2.1 Overview of SNAM Specimens Test Observations

The overall behaviour of specimens SNAM1 and SNAM2 were relatively similar so may be concurrently discussed. During loading of these specimens, it was observed that the strains began to accumulate towards the ends of the pipes after the yield strain throughout the length became exceeded. Upon further loading an outward shaped bulge buckle formed at one of the ends adjacent to the collar, as shown in Figure 5.2, for both of the specimens. This end buckle was consequential of the applied moment being relatively uniform along the entire length of pipe, while the pipe cross-sectional geometry was homogeneous. Thus, the response of the pipes was very sensitive to disturbances that would cause either an increase in the applied load or a decrease in the moment resistance of a particular cross section. The ends of the pipes contained several disturbances such as residual stresses due to the welding of the pipes to the end plate, and radial stresses resulting from the constraint provided by the end plate that did not permit radial deformation of the pipe wall that was induced by the internal pressure. The combination of these additional stresses caused buckling at the ends of the specimens that was undesirable for this experimental program as this failure mode is a function of the test setup and would not occur under actual field conditions.

In order to encourage buckling towards the middle of the pipes, the specimens were unloaded to two thirds of their maximum load after it became apparent that the failure mode was an end buckle. Subsequently additional collars were installed adjacent to the end collars that were already mounted on the specimens, as shown in Figure 5.5. These additional collars would result in the ends of the pipes being stiffened until a length 300 mm away from each end plate, which was likely beyond the range of the residual stresses caused by the end welds. Additionally, upon reloading of the pipe, the tightness of the collars was continually adjusted to ensure that they were not attached to the pipe too tightly. This permitted a gradual transition for the radial expansion of the pipe wall at the

ends that minimized abrupt deformations in the cross-section. As the pipes were reloaded, the second-order effects from the applied moment in combination with the initial vertical deflection of the middle of the pipe encouraged an outwards bulge shaped buckle to form within the middle third of pipe lengths, as shown in Figure 5.3 where the two columns in the figure are the boundaries of the middle third of the pipe length. After buckling, the stroke of the jack was further increased until the post-buckling behaviours of the specimens were obtained.

The overall behaviour observed in the SNAM3 specimen was generally different from that of the pressurized specimens. Prior to testing of this specimen, two end collars were installed at each of its ends to discourage end buckling. During initial loading, considerable ovalization was observed throughout the pipe due to the ovalization component of the pipe wall forces in combination with the absence of any internal pressure. Thus, after the yield strain throughout the material on the pipe was reached, considerable effort was required to remove the lateral bracing in order to eliminate any artificial stiffening of the pipe cross-section. As the load in the pipe approached the buckling load, it was observed that several of the initial imperfection ripples located towards the middle of the pipe commenced to considerably amplify in magnitude, as shown in Figure 5.7. Once the buckling load was achieved, the specimen demonstrated a sudden collapse resulting from the formation of a buckle near the middle of its length. Following buckling of the specimen, an abrupt reduction in the jack load was observed. This was a result of the sharp decrease in the moment resistance of the pipe cross-section at the buckle location. The specimen was subsequently loaded until the maximum jack stroke of 300 mm was achieved.

5.2.2 Global Behaviour

The moment-curvature curves for the specimens, as shown in Figure 5.1, may be used to describe the load history experienced during testing. The moment-curvature curve for the SNAM1 specimen demonstrates that the specimen underwent three unloading cycles. The first two unloadings were applied for precautionary safety during the nightly closure of the testing facility. The third unloading was applied to facilitate the installation of the second set of end collars. Closer observation of the third unloading cycle of this specimen demonstrates that the slope of the reloading curve was steeper than the slope of the moment curvature curve just prior to this unloading of the specimen. This indicates that the specimen was following different loading path after installation of the second set of end collars. This behaviour occurred because the stiffness of the end buckle was increased by the collar, resulting in the deformations becoming distributed over the entire pipe as opposed to primarily at the end buckle location. The SNAM2 moment curvature curve demonstrates a single unloading cycle, and this reduction in load was required to accommodate the installation of the additional end collars, similar to for the SNAM1 specimen. The SNAM3 specimen experienced monotonic loading during testing.

The initial slope of the moment curvature curves was relatively similar for the three specimens. Closer examination of this region indicates that the moment at which the proportional limit was achieved was also relatively similar for the three specimens. The global curvature corresponding to the peak moment as shown in Figure 5.1, demonstrates that the pressurized straight specimen could undergo approximately 40% more rotation between its ends prior to buckling than the pressurized cold bent specimen, while the pressurized bend specimen could undergo approximately 50% more rotation between its ends prior to buckling than the unpressurized bend specimen.

The predicted plastic moment as determined through the Mohareb-Murray interactive equation were compared to the peak moments during the tests. These calculations resulted in test to predicted ratios of 1.2, 1.3, and 0.8 for the three specimens. One of the reasons the SNAM1 and SNAM2 test moments were greater than the predicted moment is because the actual ultimate to yield stress ratio of the pipe material for the two specimens was greater than one, while the Mohareb-Murray equation assumes a bilinear stress-strain relationship with the yield stress functioning as the ultimate stress of the material. The unpressurized specimen demonstrated a peak moment that was considerably less than the predicted peak moment. This behaviour occurred because the Mohareb-Murray equation neglects any buckling of the specimen, which demonstrates that the unpressurized specimen buckled prior to the full plastification of the pipe cross-section.

5.2.3 Local Behaviour

The compression side strain distribution along the pipe for the moments at which demec strain measurements were recorded is used to describe the local behaviour of the specimens. In Figure 5.4, the solid lines indicate the strain measurements that were taken prior to buckling, the heavy line indicates the strain measurement at the maximum moment, and the dotted lines represent the strain measurements recorded during post-buckling. The minimum strain for the vertical axis has been selected to best demonstrate the strain distribution of the pipe up until the initiation of buckling. The origin of the horizontal axis corresponds to the middle of the specimen length, with the positive direction corresponding to the Southward locations along the specimen. Finally, the series order demonstrated in the legend is organized from the first to the last recording of the demec/calliper gauge measurements, thus the changes in strain distribution with respect to the load history of the tests is also demonstrated in this plot.

The first series in the plot corresponds to the demec strains under the zero pressure load condition. This system is followed for the strain distribution for all of the other specimens in this report.

The strain distribution during testing of the SNAM2 specimen may be used to describe the local behaviour during testing of both the SNAM1 and SNAM2 specimens. The local behaviour of SNAM3 during testing is depicted in Pipeline Technology Report No. 2005-1. In Figure 5.4, the scan with zero moment and internal pressure indicates that the internal pressure acting against the endplates forced the entire bottom of the pipe into tension. After the yield moment was surpassed, until an applied moment of 2159 kN, it is demonstrated that the strains primarily accumulated at the ends of the specimen. As the strain at the -3302 mm location was well beyond the yield strain at this load, it is confirmed that an end buckle had formed at this location. After the specimen was unloaded, had the second set of collars installed, and was reloaded, two bulges began to form at the -1016 and 762 mm positions. The strain subsequently accumulated relatively equally at these two bulges until the maximum moment of 2411 kNm was achieved. After the peak moment the strains primarily accumulated at the buckle positioned at the 762 mm position, and relaxation of the strains occurred away from the bulge locations.

5.2.4 Critical Strain

Interpretations concerning the overall effects of cold bending on the critical strain of a straight pipe are described herein. The critical strain of the straight pipe was 2.0 times that of the bend pipe when using either method of critical strain determination. Based on this comparison it is demonstrated that the change in material properties, initial imperfections, and residual stresses introduced during cold bending have a significant effect on the critical strain of a

pressurized pipe. The critical strain of SNAM2 was approximately 2.3 times that of SNAM3 for both of the critical strain determination methods. This demonstrates that the presence of internal pressure substantially increases the critical strain of a cold bend pipe. This behaviour occurs because the internal pressure resists the inward direction diamond mode buckling that occurs at a lower applied energy level than that of the bulge mode buckle.

5.2.5 Discussion of Post-Buckling Response

The jack stroke during testing of the SNAM1 specimen was increased until the shape of the wrinkle became well defined and a descending branch was clearly evident in the load – deformation curve. As the test setup in this experimental program could accommodate up to 90-degree rotation at the hinges, the stroke of the jack was increased to 300mm during testing of the SNAM2 and SNAM3 specimens. This allowed greater understanding of the level of strain that the specimen could experience prior to fracture, and increased information about the global and local post buckling behaviour.

Observation of the SNAM2 specimen wrinkle in Figure 5.7 demonstrates that the magnitude of the wrinkle in the radial direction increased considerably, as the stroke of the jack was increased during post buckling. The length of the wrinkle remained relatively constant from the point of initiation of buckling until the test was stopped. Upon conclusion of testing, the moment capacity of the specimen had dropped to 70% of its peak capacity.

The general shape of the buckle in the SNAM3 specimen remained relatively consistent throughout testing. This buckle demonstrated a diamond shape, as shown in Figure 5.8, which is the characteristic shape for an unpressurized pipe with a high diameter to thickness ratio (Dorey, *et al*, 2001).

This buckle featured a main inward indentation that was orientated in the out of plane direction and was centred on the compression line of the pipe, with additional depressions located on either side of the main depression in the longitudinal direction. The post-buckling behaviour of this specimen demonstrated an extremely abrupt descending branch. That is, immediately after buckling of this specimen the load dropped by 25%, while the load more gradually decreased after buckling for the SNAM1 and SNAM2 specimens. This slower decrease in moment carrying ability for the pressurized specimens occurred because the internal pressure functions as a stabilizing force inside of the pipe that prevents sudden cross-sectional distortion, thus maintaining the moment capacity of the cross-section at the buckle well after the peak moment was achieved. The moment capacity of the SNAM3 specimen at the completion of the test was 40% of the peak moment. This demonstrates that the post-buckling moment carrying capability at a large global curvature for an unpressurized cold bend pipe is also somewhat less than that of a pressurized cold bend pipe.

5.3 TG Test Results

The two TG test specimens were nominally 610 mm in diameter with 14.1 mm wall thickness and from Grade X80 material. The difference between the specimens was that TG1 was bent at 0.75 degrees every 300 mm of length, while TG2 was bent 1.5 degrees every 600 mm of length. The two specimens had similar total bend angles and were both pressurized to 40% SMYS hoop stress. The materials for the two pipes were rolled from different heats of steel.

5.3.1 Overview of TG Specimens Test Observations

Both the TG1 and TG2 specimens were tested with only one collar at each end due to the limited availability of NPS 24 end collars, nevertheless end buckling did not occur for either pipe. A linear load deformation behaviour was observed during the initial portion of the tests. As the yield moment of the TG2 specimen was achieved, it became revealed that the rotation meters in the test setup were not functioning. As these measurements are crucial in order to understand the global curvature response of the pipe; the rotation meters were repaired, the specimen was completely unloaded, and then the loading was restarted so that the angle measurements would be known over the initial portion of its load history. The specimens were loaded under load control until they buckled within the middle third of their lengths, then after buckling loading was switched to displacement control. After buckling the jack stroke was increased until its stroke limit of 300 mm was exhausted. Then the jack was reset as discussed in Section 2.6.5, and the specimens were subsequently reloaded until the jack stroke became exhausted again. The TG1 specimen underwent three jack resets during testing, while the TG2 specimen experienced five jack resets. This increasing of jack stroke permitted the central bend angle of the specimens to achieve 35 degrees upon completion of testing, as shown in Figure 5.10.

5.3.2 Global Behaviour

The moment curvature curves in Figure 5.9 demonstrate the load history experienced by the TG specimens during testing was dissimilar. The TG1 specimen experienced two unloading-reloading cycles, and testing was stopped during the third unloading cycle. The TG2 specimen experienced five unloading-reloading cycles, and testing was stopped during the sixth unloading cycle. The

first loading cycle for the TG2 specimen was predominantly elastic and was applied because the rotation meters were not functioning.

The initial slopes of the TG moment curvature curves were essentially collinear over the initial region. As the first unloading and reloading lines are not collinear for the TG2 specimen, it is apparent that it experienced some permanent strain prior to unloading, however this deformation is minute so will not significantly impact the critical strain determination for the specimen. The global curvature corresponding to the critical moment during testing was 15% greater for the TG2 specimen in comparison with that of TG1. This is contrary to what would be expected as the TG2 specimen was bent at a greater angle per bend than the TG1 specimen, which would intuitively decrease the pre-buckling deformability of the specimen. As the overall geometries and loading method for the two specimens were the same; the difference in curvature at buckling is likely due to the variation in material properties between the two specimens as they were from different heats of steel and the TG1 specimen material was heated during its coating removal.

The moment capacity of the TG2 specimen was 6% greater than that of the TG1 specimen. This is contrary to what would be expected as TG2 was bent more severely than TG1 specimen. The plastic moment capacity based on the Mohareb-Murray interactive equation in comparison with the peak moment during the tests yielded test to predicted ratios of 1.06 and 1.13 for the TG1 and TG2 specimens respectively. These ratios are within experimental limits, and as they are both greater than one, the difference may be a result of the assumption of the bilinear stress strain relationship assumed during development of the design equation. In addition, these ratios are less than those of the pressurized SNAM specimens, which may be attributed to the fact that the yield to ultimate stress ratios was higher for the TG specimens than for the SNAM specimens.

5.3.3 Local Behaviour

The compression side strain distribution during testing of the TG2 specimen may be used to describe the local behaviour of both of the TG specimens during testing. The initial strain measurements of the TG2 specimen as shown in Figure 5.12 indicates that the internal pressure acting against the end plates resulted in uniform tensile strains throughout its length. The strain accumulation was relatively constant along the specimen until a moment of 1722 kNm. By the moment of 2634 kNm, there was considerable non-uniformity in the strains. At the moment of 2844 kNm it becomes apparent that seven adjacent large magnitude bulges had formed. By the peak moment four of these bulges were accumulating most of the strain. At this moment, the strain at the eventual buckle location of 254 mm had the greatest magnitude and was also accumulating more strain than the other locations. Immediately after the peak moment the bulges that were adjacent to the wrinkle moved away from the middle of the specimen.

5.3.4 Critical Strains

When studying the critical strains of the TG specimen, it became evident that the two critical strain determination methods yielded contradicting results. That is, when using the bilinear global curvature method the TG2 critical strain was 2 times greater than that of TG1, however when using the maximum moment method the TG1 critical strain was 1.2 times greater than that of TG2. Correspondingly, the ratio of the maximum moment method to bilinear method critical strain was 2.0 for TG1, and this high magnitude demonstrates uncertainties in the precise strain at the onset of buckling for this specimen. This behaviour may be because the bilinear method of determining critical strain is sensitive to the shape of the material curve as demonstrated by Dorey, *et al*, 2001,

whereas the TG1 material demonstrated a yield plateau and the TG2 material demonstrated a rounded stress-strain relationship. As the strain at maximum moment method is unaffected by the shape of the material stress-strain curve, these critical strains will be considered when comparing the critical strain of the two specimens. Accordingly, the ratio of the TG1 critical strain to that of TG2 was 1.2. This ratio is relatively small, and the demonstrated increased critical strain of TG1 compared to that of TG2 is because of either the varying bend interval or differing material stress-strain behaviours.

5.3.5 Post Buckling Behaviour

The wrinkle of the TG1 specimen, generally maintained its length of 800 mm throughout testing although its amplitude increased throughout post-buckling. Considerable strain relaxation was observed to either side of the wrinkle during the post buckling response. Upon the conclusion of testing the moment capacity of the specimen prior was 52% of that of the peak moment.

The shape of the wrinkle for the TG2 specimen was similar to that of the TG1 specimen during post-buckling. The strain relaxation was non-uniform during post buckling because of the numerous bulges that had formed prior to buckling of the specimen. The final moment capacity of the specimen was 53% of that of the peak moment, which is similar to that demonstrated by the TG1 specimen. In general, the moment curvature and strain distribution post-buckling response of both TG specimens was very similar.

The unloading locations during jack resetting on the moment curvature curves of Figure 5.9 demonstrate that the specimens initially unloaded elastically, and once the moment decreased to a particular level, the unloading curve became non-linear. Upon reloading the specimens initially behaved elastically, and then

behaved non-linearly after the moment achieved a certain level. For each additional unloading, it is apparent that the curves became inelastic during unloading at higher and higher moments. Correspondingly, it was observed that the reloading response became inelastic at lower and lower moments during each additional reloading. In addition, the slope of the inelastic portion of these loading and unloading cycles significantly decreased with each cycle. This behaviour correlated to an increase in the area of each hysteresis loop during each additional loading cycle. Permanent deformation occurred during the loading cycles as the specimens reloaded at a greater global curvature than they demonstrated prior to unloading. Examination of the fourth and fifth loading cycles for the TG2 specimen demonstrates that the curvature of the specimen did not significantly increase between these load cycles. This behaviour occurred because the pipe rebounded almost the entire jack stroke range during the fourth unloading; thus the jack stroke limit was almost exhausted once the global curvature prior to this unloading was achieved.

The moment capacity of the TG2 specimen began to increase after the third jack reset. This was a result of the closure of the wrinkle during testing. This behaviour will be discussed in Section 5.4.5 as it becomes very important to the post-buckling behaviour of the pressurized TCPL specimens.

During the TG specimen jack resets the internal pressure was applied in the specimens. This resulted in the pipes experiencing tension loads during the unloading of the jack, and compressive loads upon reloading. This series of strain reversals caused the eventual fracture at the crest of the wrinkle in the two specimens, as demonstrated in Figures 5.11 and 5.13. This behaviour is analogous to a pipeline under field conditions failing due to the axial load cycling caused by the temperature fluctuation of its contents. The TG1 specimen abruptly fractured during its third unloading, resulting of the sudden release of its water contents at the wrinkle location. Thorough inspection of the wrinkle in the TG2 specimen upon completion of the sixth unloading revealed that small cracks were

existent at the wrinkle location. As water was observed in the outside of this wrinkle it became recognized that the cracks had penetrated through the thickness of the pipe wall at this point. The precise curvature during testing that this cracking occurred is unknown.

5.3.6 Discussion of Fracture Mechanism in TG Specimens

The final failure mode of the specimens was a fracture at the wrinkle that was induced by low cycle fatigue. As the internal pressure acted against the end plates throughout the majority of the test, there was a mean longitudinal tensile stress in the pipes. In addition, the circumferential directions stresses caused by the internal pressure forced the pipe into biaxial loading, further increasing the mean longitudinal tensile stress as demonstrated in Equation 5.1. The compressive axial stress resulting from the increasing of the jack load behaved as the variable stress resulting in the longitudinal stresses in the pipe alternating between tension and compression.

$$\sigma_{eff} = \sqrt{\sigma_1^2 + \sigma_2^2 + (\sigma_1 - \sigma_2)^2} \quad (5.1)$$

Where σ_{eff} is the von Mises condition effective stress, σ_1 is the longitudinal direction stress, and σ_2 is the circumferential direction stress.

Because of the abrupt change in the pipes cross section at the wrinkle location and the low stiffness of its material, the majority of the strain in the pipe was concentrated at the wrinkle during post buckling. As the material was cyclically loaded, slip bands appeared on the pipe wall at the wrinkle as shown in Figure 5.14. These slip bands were a result of the sliding of dislocations along the weakest crystallographic planes within the material microstructure at the wrinkle. As the cycles were repeated the number of slip bands increased, and some of the

previous slip bands broadened out. This broadening process continued until a crack developed. Once this crack formed, it deepened because of the stress concentration at its end. This deepening continued under the action of the alternating stresses, effectively reducing the pipe wall thickness at the crest of the wrinkle. Eventually the cross section area at this location became so reduced in area that the remaining portion fractured under the tension load that occurred in the pipe during the unloading of the jack.

5.4 TCPL Test Results

The three TCPL specimens were nominally 762 mm in diameter with 8.2 mm wall thickness and Grade X65 material. The difference between the specimens was that TCPL1 was bent at 1 degree per diameter in length and pressurized, TCPL2 was bent at 1.5 degrees per diameter in length and unpressurized, and TCPL3 was bent at 1.5 degrees per diameter in length and pressurized. The internal pressure applied in TCPL1 and TCPL3 during the tests caused 80% SMYS hoop stress. The material for TCPL1 was from one heat of steel, while that of TCPL2 and TCPL3 was from a different heat.

5.4.1 Overview of TCPL Specimens Test Observations

The behaviour of the TCPL1 and TCPL3 specimens during testing was relatively similar so may be jointly discussed. The specimens were tested with two collars at each of their ends in order to reduce the likelihood of end buckling. The load deformation response of the pipes was linear during the initial portion of the tests. As the yield strain in the TCPL3 specimen was approached, there was a failure in the weld at the tensile side of the North end plate. The pipe was

subsequently unloaded, the weld was repaired, and the specimen was then reloaded two days after the failure. The specimens were loaded until a bulge buckle formed within the middle third of their lengths. These buckles were similar to those observed in the TG and pressurized SNAM specimens. After buckling, the stroke of the jack was increased beyond its initial range to determine their post-buckling responses. The jack was then reset three times for the TCPL1 test and five times for the TCPL3 test. The internal pressure was reduced to 10% SMYS hoop stress for the TCPL3 test after the first jack reset.

The behaviour of the TCPL2 specimen was similar to that observed during testing of the SNAM3 specimen. During initial loading considerable ovalization was observed, consequently the lateral bracing was removed when the strains in the pipe approached the yield strain in order to prevent artificial stiffening of the pipe cross-section. The specimen buckled soon after the yield strain was exceeded. This buckle was a diamond shaped buckle that was anti-symmetrical in orientation to the compression line of the pipe. The buckling was accompanied by a sudden reduction in the moment capacity of the specimen. One jack reset was applied during this test.

5.4.2 Global Behaviour

The moment curvature curves of the TCPL specimens shown in Figure 5.15 demonstrate that the three specimens underwent different load histories during testing. The TCPL1 specimen experienced three unloading-reloading cycles during post-buckling. The degree of inelasticity at the wrinkle location of this specimen was significantly increasing with sequential jack resets as demonstrated by the increasing area of the hysteresis loops. The TCPL2 specimen experienced only one jack reset, and a permanent decrease in the moment capacity of the specimen occurred as a result of this unloading-reloading cycle. The dynamic effects of testing are evident in the elastic range where the applied

moment would decrease at a constant global curvature in the specimen. The TCPL3 specimen experienced six load cycles during testing. The first load cycle was necessary because of a failure in the weld on the tension side of the South end plate. This failure occurred because during testing large tension forces are applied to the tension side of the weld from the applied bending loads and tensile force from the pressure pressing against the end plates. For this reason a full penetration weld was used to ensure that the tensile strength of this connection was greater than that of the pipe. Close inspection of this weld after its failure demonstrated that the area of the weld at the failure location was less than that used for the other pipes. This in combination with a possible flaw in the weld material resulted in the tensile capacity of the reduced area weld becoming less than the applied load. The unloading response of the pipe after this failure was non-linear because the specimen was depressurizing while the jack was being unloaded after the weld failure. After the second unloading cycle of the test the applied moment in the pipe significantly dropped because the internal pressure was decreased from 80% to 10% SMYS hoop stress during the first jack reset.

The initial region of the moment curvature curves demonstrates that the specimens behaved linearly with similar slopes at the beginning of the tests. The curvature at the initiation of non-linearity was lower for the pressurized specimens than for TCPL2. The curvature corresponding to the maximum moment shown in Figure 5.15 demonstrates that the global deformation prior to buckling of the zero pressure pipe was 25% less than that for the pressurized pipes, and that the different bend increments of specimens TCPL1 and TCPL3 do not significantly affect their allowable curvature prior to buckling. Following buckling of the TCPL2 specimen the moment capacity immediately dropped to 62% of the peak moment. This occurred because of the considerable cross-sectional distortion and decrease in material stiffness that accompanied buckling of the specimen. The bottom of the first unloading curve for the TCPL3 specimen indicates that a small amount of permanent deformation had occurred prior to the weld failure. The reloading curvature during the load cycles did not coincide with

the unloading curvature for all of the jack resets in the TCPL tests, demonstrating that permanent deformation occurred in the pipes as a result of the jack resets.

The maximum moment capacity for the TCPL3 specimen was 4% larger than that of TCPL1, which is different than what would be expected, as TCPL3 was cold bent more severely than TCPL1. This minor increase in moment capacity is likely attributed to the difference in the material properties of the specimens. The moment capacity of TCPL2 was 15% less than that of TCPL3, while previous testing and finite element modelling (Dorey, *et al*, 2001), has demonstrated that the moment capacity of an unpressurized straight pipe is greater than that of a pressurized straight pipe. Thus based on this test result along with that of the SNAM3 specimen, the cold bending process significantly reduces the moment capacity of a pipe if it is unpressurized. The predicted moment for the pressurized specimens were calculated by multiplying the specified yield stress by the plastic section modulus because the Mohareb-Murray equation would not converge for these specimens because of their large axial tensile loads. As this predicted moment does not consider the effects of axial load or internal pressure their comparison with the test moments will not be discussed. The test to predicted ratio for TCPL2 was 0.86. Therefore similar to for the SNAM3 specimen, it is demonstrated that the TCPL2 specimen buckled prior to full plastification of the pipe cross-section. This is further verified with the large slope of the moment-curvature curve immediately prior to the peak moment that indicates that the material was nearly elastic at the onset of buckling.

5.4.3 Local Behaviour

The local strain during testing for the TCPL2 specimen will be presented herein to describe the behaviour of the unpressurized cold bends under bending and axial load. The local strains during testing for the TCPL1 and TCPL3

specimens are presented in Pipeline Technology Report No. 2005-1. The strain distribution of the TCPL2 specimen shown in Figure 5.20 was relatively uniform until a moment of 1020 kNm. At 1522 kNm four small bulges had formed. At the maximum moment the strains were accumulating with a parabolic distribution between the -1500 to 2300 mm locations, and there was considerable bulge positioned at the middle of the specimen. As the magnitude of the bulges at the maximum moment were of an order of magnitude smaller than those demonstrated by the pressurized specimen, it is shown that there is very little redistribution of strain in the pipe prior to buckling. Immediately after buckling the strains relaxed in a parabolic manner along the length of the specimen. The strains precisely at the wrinkle increased throughout post buckling, while the strains immediately adjacent to the wrinkle demonstrated tension strains. These tensile strains were due to the shape of the wrinkle as demonstrated in Figure 5.22.

5.4.4 Critical Strains

The critical strain of TCPL2 will be compared to that of TCPL3 because these specimens were bent with similar geometries and both materials were from the same heat of steel. The critical strain of the TCPL3 specimen was 3.5 and 4.3 times that of the TCPL2 specimen when using the bilinear and maximum moment methods respectively. This indicates that the stabilizing effect of the internal pressure becomes very dominant in the pre-buckling behaviour of cold bend pipes with high diameter to thickness ratios, which was previously demonstrated with the small magnitude of bulge strains in the TCPL2 specimen at the maximum moment in comparison with those present for the pressurized specimens. The critical strain for TCPL3 was 1.2 and 1.3 times that of TCPL1 when using the bilinear and maximum moment critical strain determination methods respectively. This is intuitively different than what would be expected because the TCPL3

specimen was bent more severely than TCPL1. However, this increase in critical strain is relatively minor and may be explained by the greater yield stress demonstrated by the TCPL3 material in comparison to that of the TCPL1 material.

5.4.5 Post Buckling Behaviour

The length of the wrinkle in the TCPL1 specimen was 1016 mm throughout post buckling, while the magnitude of the wrinkle continuously increased with increasing curvature. The moment at the end of the test was 73% of the peak moment. This is approximately 20% greater than the ratio that was demonstrated by the TG specimens. The bulges that had formed in the specimen prior to buckling remained apparent throughout post-buckling.

It is demonstrated in Figure 5.15 that the slope of the TCPL1 moment curvature curve was constantly near zero after the first jack reset. This indicates that the wrinkle region provided very little stiffness during the latter region of post buckling. Upon examination of the unloading response of the specimen during the jack resets it is demonstrated that the area of the hysteresis loops increased during each unloading-reloading cycle. In addition, the reloading curve demonstrates a somewhat constant slope while the unloading curves are predominantly inelastic for the second and third loading cycles. This behaviour occurs because the tensile force from the internal pressure appreciably increases the stiffness of the pipe, and once this force is overcome the pipe stiffness considerably decreases. This demonstrates that the majority of the deformation associated with the loading and unloading of the specimen is occurring at the wrinkle location where the behaviour associated with its change in shape is extremely non-linear. The concentration of the applied deformations at the wrinkle location of the pipe caused the eventual fracture of the specimen at its

tension side above the wrinkle, as shown in Figure 5.16. This failure mode will be discussed in more detail in Section 5.4.6.

The failure mode of the TCPL2 specimen was a diamond shaped buckle, shown in Figure 5.22, similar to that observed in the SNAM3 specimen. The abrupt drop in moment capacity immediately following buckling was associated with the reduction of moment of inertia at the wrinkled cross-section. The moment at the end of the test was 28% of the peak moment, and the ratio prior to the jack reset was 32%. This latter value is 8% less than the final to peak moment ratio demonstrated by the SNAM3 specimen at a similar global curvature, indicating that a high diameter to thickness ratio pipe decreases in moment capacity more severely than lower diameter to thickness ratio pipe. Close observation of the slope of the post-buckling region of the TCPL2 moment curvature curve demonstrates that, the moment capacity of the pipe did not completely recover after the jack reset, and the stiffness of the pipe appears to increase towards the end of the test. This behaviour indicates that the shape of the wrinkle is evolving during post buckling, with some configurations behaving unstably and other configurations serving to increase the moment capacity of the cross-section.

The longitudinal length of the wrinkle in the TCPL3 specimen was similar to that of the TCPL1 specimen. The moment in the specimen prior to the first jack reset was 80% of the maximum moment. This is similar to the ratio for the TCPL1 specimen at a similar global curvature. This information indicates that the pre and post buckling behaviour of the TCPL1 and TCPL3 specimens were generally relatively similar.

Due to the tension side fracture of the TCPL1 specimen, precautions were necessary in obtaining the post-buckling behaviour of the TCPL3 specimen. As the internal pressure introduced substantial tension loads to the pipe, and previous research (Del Col, *et al*, 1998) has demonstrated that only a small level of internal

pressure is required to maintain the shape of the wrinkle during post buckling, the internal pressure in this specimen was permanently reduced to 10% SMYS hoop stress during the first jack reset. The pressure was decreased in several stages while the jack was being retracted so that sudden compression loads were not introduced to the pipe during the depressurization. A 60% decrease in applied moment accompanied the reduction in internal pressure because of the reduction in longitudinal tension load caused from depressurization. Additionally, the ovalization of the specimen during the loading following depressurization was considerably more than what was observed during post buckling of the TCPL1 specimen. The behaviour of the wrinkle in the TCPL3 specimen during post-buckling will be discussed in detail in Section 5.4.7.

5.4.6 Tension Side Fracture of TCPL1

As discussed in the previous section, the final failure mode for the TCPL1 specimen was a fracture on the tension side of the pipe. The fracture plane was orientated in the circumferential direction, was 960 mm in length, and was located 260 mm from the buckle location in the longitudinal direction that was away from the middle of the pipe. The fracture occurred without warning and resulted in the immediate loss of the containment capability of the pipe. This failure mode is very interesting as it seldom occurs in the testing of pipes subjected to bending loads, however the loading conditions experienced in this test could realistically be experienced by a line pipe that is exposed to extreme ground movements. As there is a great amount of energy released during this type of failure, which could endanger the safety of persons within its blast radius, further study of this failure mode is necessary to prevent this type of fracture from occurring in a high-pressure gas pipeline.

The specimen fractured while the jack stroke was being increased. The tension side demec strain distribution over a gauge length of one-third of the diameter throughout the test is demonstrated in Figure 5.18. The percent elongation from the tension coupon tests of the TCPL1 material, over a gauge length of 200 mm demonstrated that the percent elongation at fracture ranged from 12 – 17% for the pipe material. As the maximum strain in Figure 5.22 was considerably less than that demonstrated during the coupon test of the tension side bend material, it is apparent that the pipe material during the test behaved in a considerably more brittle manner than the level of ductility that it demonstrated during its uniaxial tension coupon test.

During testing of the TCPL specimen, the stresses on an element of the pipe at the fracture location came from four different sources. There was the tensile axial load from the internal pressure acting against the end plates, along with the compressive axial load from the jack force. These axial strains were recorded by the strain gauges located along the neutral axis at each end of the pipe as shown in Figure 5.19. The specimen was also loaded in bending from the eccentricity of the jack to the pipe centreline. The magnitude of the strain at the top of the pipe as measured by the demec gauge at the fracture location is demonstrated in Figure 5.18. Finally, the pipe was pressurized to induce a circumferential direction stress of 80% SMYS. A strain gauge orientated in the circumferential direction at the tension side of the middle of the pipe measured the circumferential strain in the pipe at the time of fracture, however this strain included the circumferential component of the longitudinal strains that were caused by the applied moment, as shown by the variation in circumferential strain with applied moment in Figure 5.19. The internal pressure also induced radial direction stresses in the pipe wall. The magnitude of this stress is calculated as one half of the internal pressure in the specimen. This stress was negligible in comparison with the longitudinal and circumferential direction stresses, and will consequently be neglected for the remainder of this discussion.

Because the neutral axis strains were small in comparison to the extreme fibre strains, the principle loading on the specimen was from the longitudinal bending stresses caused by the jack load and its eccentricity to the pipe, and the circumferential direction stresses caused by the internal pressure. Therefore, the pipe material at the fracture location was in a state of biaxial stress. The magnitude of the circumferential stress caused by the internal pressure as calculated by Equation 2.1 was 358 MPa. Knowing that the longitudinal strain in the pipe was beyond the yield strain, the ratio of the circumferential to longitudinal stress at the fracture location was in the range of 0.62 and 0.66.

Some experimental work has been done by Davis, 1945, to determine the influence of a two-dimension stress state on the strength and ductility of steel. Thin-walled tubes of ordinary medium carbon steel were used to produce the two-dimensional stress conditions in his testing program. The circumferential stress was provided through internal pressure, and a testing machine supplied the axial load. The ratio of circumferential to axial stress was different for each tube, and this ratio was maintained constant throughout testing. The specimens were loaded during testing until they fractured, and the elongation at fracture was used to determine the effects of varying biaxial stress conditions on the ductility of the steel. The diameter, length, gauge length and wall thickness of the tubes was 203, 36.5, 102, and 2.54 mm respectively

The ductility of the specimens with circumferential to axial stress ratios during testing of 0 (axial load only), 0.5, 0.75, 0.762, and 1.00 will be discussed. The axial direction natural strain at rupture for these specimens was 0.780, 0.501, 0.502, 0.469, and 0.098 respectively. Thus based on these tests, it is apparent that as the biaxial stress ratio increases, the ductility of the material decreases. This observed reduction in ductility is substantial, as the rupture strain of the biaxially loaded specimens was less than 64% of the rupture strain of the uniaxially loaded tube.

To increase his test specimen database, another set of specimens was tested under similar loading conditions. These specimens were of SAE 1020 steel tubing, with a diameter and wall thickness of 148 and 4.06 mm respectively. The circumferential to axial stress ratios employed during the tests was 0 (axial stress only), 1 (axial load and internal pressure), and 2 (internal pressure only). The elongation at fracture of these specimens, over a 12.7 mm gauge length, was 102, 37, and 2% respectively. Thus, the observations from the first set of specimens remained consistent with test specimens that demonstrated a different material property and geometry.

For the specimens with a circumferential to axial stress ratio up to 0.762, it was observed that the cracks upon fracture were orientated in the circumferential direction. Those with a ratio higher than this failed in the longitudinal direction. The circumferential fractures occurred along the planes of maximum shear stress, and the true stress at fracture was similar in magnitude to that during tension coupon tests conducted on flat specimens prepared from the same material as the tubes. In all of the tube specimens, the failure occurred once the maximum shear stress in the radial-axial direction was approximately the same value. The equations for the shear stress and shear strain acting on the planes inclined equally to all three principal directions are demonstrated in Equations 5.2 and 5.3 respectively. In these equations it is demonstrated that the octahedral shear stress and strain may increase as the transverse stress increases.

$$\tau_n = \frac{1}{3} \cdot \sqrt{(\sigma_a - \sigma_t)^2 + (\sigma_t - \sigma_r)^2 + (\sigma_r - \sigma_a)^2} \quad (5.2)$$

$$\gamma_n = \frac{2}{3} \cdot \sqrt{(\epsilon_a - \epsilon_t)^2 + (\epsilon_t - \epsilon_r)^2 + (\epsilon_r - \epsilon_a)^2} \quad (5.3)$$

Where τ_n and γ_n are the octahedral shear stress and strains respectively, σ_a , σ_t , and σ_r are the axial, transverse, and radial direction stresses respectively, and ϵ_a , ϵ_t , and ϵ_r are the axial, transverse, and radial direction strains respectively.

Upon completion of these tests, the results from similar tests conducted by MacGregor and Coffin, 1940, were published. These tubes consisted of S.A.E. 1020 steel, with 25.4 mm diameter and 2.54 mm wall thickness. The circumferential to axial stress ratios employed was 0, 0.534, and 1.039. The axial direction true strains at rupture for these specimens, over a gauge length of 102 mm, was 0.696, 0.501, and 0.487 respectively. Thus consistent to the tests conducted by Davis, 1945, the elongation at fracture decreased with increasing transverse to axial strain ratio. Also for these tests, it was observed that once the average shearing stress reached a critical value, the specimens failed by a circumferential rupture.

As demonstrated in Figure 5.17, the TCPL1 specimen demonstrated a shear mode fracture as the fracture plane is inclined nearly 45 degrees to the longitudinal direction, and little necking was observed along the crack. In addition, the shape of this crack is similar to that demonstrated by the specimens with circumferential to axial stress ratios between 0.5 to 0.762. Thus the failure mode of the TCPL1 specimen is the same as that observed during Davis' tests. This failure is a shear mode fracture that was induced by the biaxial loading condition caused from the internal pressure in combination with the applied bending loads. The decrease in ductility over that of the tension coupon was due to the different failure mode of the material during testing in comparison with that experienced during the uniaxial coupon test.

5.4.7 Wrinkle Behaviour of TCPL3

It is demonstrated in Figure 5.15 that the moment capacity of the TCPL3 pipe was decreasing with increasing curvature until the second jack reset, after which its moment capacity commenced to increase. This increase in global stiffness of the pipe occurred because the increasing curvature applied to the pipe caused the ends of the wrinkle to come into contact with each other. The bending stiffness of the pipe increased because closing of the wrinkle resulted in a shifting of the neutral axis towards the tension side of the pipe as well as an increase in the stiffness of the material on the compression side of the pipe that was resisting the applied moment. The moment capacity of the specimen after the closing of the wrinkle was 40% greater than the moment capacity just before the second jack reset. After closing of the wrinkle, its circumference began to increase and it began to span well above the initial neutral axis as shown in Figure 5.23. This indicates that the neutral axis had shifted well above the centreline of the pipe, demonstrating that the stiffness of the wrinkle was very low. The area of the hysteresis loops decreased after closure of the wrinkle, and the their areas were relatively constant for the final two cycles. In addition, the slope of the moment-curvature curve was nearly constant at zero following the third jack reset. This indicates that the behaviour of the wrinkle was relatively stable. The test was finally stopped because it became apparent that the wrinkle would simply continue to fold for a great deal more curvature, while the deformation of the pipe was already substantially greater than what would be expected under even the most severe field conditions.

5.5 Comparison of Behaviour Between Specimen Sets

In this section, a comparison of the behaviour of the specimens between the three specimen sets will be discussed. This will allow conclusions to be made concerning the effects of D/t ratio, internal pressure, material grade, and initial imperfections on the behaviour of cold bend pipes subjected to bending loads. The overall bending geometry of the pipes did not significantly differentiate between the specimen sets so will not be considered a variable during these comparisons. The specimens global behaviour based on the moment curvature relationship, the local behaviour based on the strain distributions, the critical strains, and the post-buckling behaviour based on the global and local behaviours will be compared in this section.

5.5.1 Global Behaviour

Examining the initial region of the moment curvature relationships of the eight specimens, shown in Figure 5.25, demonstrates that the initial slope of the specimens within each of the three sets was similar, but varied between the three different sets. The SNAM specimens demonstrated the largest initial stiffness, with the TCPL specimens demonstrating the next largest, and the TG specimens demonstrating the softest initial stiffness. This is the same order as the moment of inertia magnitudes of the specimens, and the demonstrated order of specimen stiffness is because the initial stiffness is directly dependant on the moment of inertia of the pipe cross-section.

The maximum moment during testing for the pressurized specimens was greatest for the TG pipes, followed by the SNAM specimens, and the peak

moment for the pressurized TCPL specimens was the lowest of the pressurized sets. This is a similar order demonstrated by the plastic moment capacity of the specimens as determined using Equation 1.4, which accounts for D/t ratio, material grade, axial load, and internal pressure of the specimens, where the TCPL plastic moment is an upper bound as it only accounts for the D/t ratio and material yield stress. The peak moment for the unpressurized SNAM3 specimen was greater than that of the TCPL2 specimen, which corresponds to the predicted order when using Equation 1.4.

Considering the pressurized specimens, in general the global curvature corresponding to the peak moment was greatest for the TG specimens, followed by the SNAM pipes, and the TCPL specimens generally demonstrated the lowest global curvature at the peak moment. As previous research, (Del Col, et al, 1998), has demonstrated that increasing internal pressure increased the allowable curvature before local buckling, it may be inferred that increasing D/t ratio decreases the allowable global curvature prior to buckling. The global curvature for the TCPL2 specimen was greater than that of the SNAM3 specimen at the peak moment. This contrasts the behaviour of the pressurized specimens as the TCPL2 specimen demonstrated a higher D/t ratio than the SNAM3 specimen.

5.5.2 Local Behaviour

The pre-buckling behaviour of the pressurized specimens was considerably different from that of the unpressurized specimens. The pressurized specimens developed 4 – 7 bulges prior to buckling, with the bulge at the eventual buckle location always demonstrating the largest magnitude at the maximum moment. The amplitude of the largest bulge away from the buckle location at the maximum moment indicated that increasing the internal pressure magnifies the amplitude of the bulges in the specimens prior to buckling. Because the relatively

high magnitude of these bulges did not trigger local buckling, and considering the proximity of these values to the critical strains of the specimens, the redistribution of the deformations along the pipe becomes very apparent for the pressurized specimens.

The unpressurized specimens developed 3 – 4 small bulges prior to buckling. The length of these bulges was generally 500 mm, which was approximately twice the average imperfection period of the specimens. The amplitude of the largest bulge away from the wrinkle at the maximum moment compared this with the critical strain of the unpressurized pipes indicated that there is very little strain redistribution prior to local buckling for the unpressurized specimens.

5.5.3 Critical Strain

When assessing the critical strains for the test specimens that were obtained using the strain at maximum moment method in comparison with the bilinear global curvature method, it became apparent that the two different critical strains evaluated for each specimen were never precisely equal. The ratio of maximum moment to bilinear global curvature critical strains ranged from 0.9 to 2.1, with seven of the eight specimens demonstrating larger critical strains when using the maximum moment method. This behaviour occurred because the strain corresponding to the maximum moment was generally located directly on the linearly inelastic region of the global curvature vs. strain at buckle plot, while the bilinear global curvature critical strain is always within the non-linear region of this curve. Nonetheless, as the two methods of determining critical strain provided values within 30% for seven of the eight specimens, both methods may be considered reliable when determining the critical strain of the test specimens.

When comparing the critical strains determined from the tests to those predicted using the Equation 1.5, it became apparent that the tested critical strains are somewhat lower than those using the straight pipe predictive equation. The tested bilinear method critical strains will be compared to the predicted critical strains, although the values are generally similar using either of the methods for this testing program, because a similar bilinear critical strain determination method was used during the development of Equation 1.5. The critical strain test to predicted ratio was 0.82 for the straight specimen, and ranged from 0.25 to 0.67 for the bend specimens. The average test to predicted ratio for the bend specimens was 0.47. As Equation 1.5 considerably over predicted the critical strain for the bend specimens, while demonstrated good correlation with the straight pipe and tested specimens in the research by Dorey, it becomes apparent that the effects of cold bending significantly reduces the critical strain of a line pipe.

From these experimental tests comparisons may be made considering the critical strain of cold bend pipes with varying: diameter to thickness ratio for unpressurized pipes, bend angle per bend lengths, and internal pressures. However due to the limited number of test specimens, conclusions could not be made on the critical strain of cold bend pipes with varying: material grades, diameter to thickness ratio for pressurized pipes, or imperfection magnitudes. These variables will be further analyzed from a parametric study using the finite element model discussed in Chapter 7.

Comparing the critical strain of the two unpressurized specimens will reveal the effects of diameter to thickness ratio on the critical strain of an unpressurized cold bend pipe. The critical strain of SNAM2 was 1.1 and 1.3 times that of TCPL2 when using the bilinear and maximum moment methods respectively. Based on this information as well as previous research on straight pipes (Dorey, *et al*, 2001), increasing the diameter to thickness ratio generates an increase in the critical strain of unpressurized cold bend pipes. The magnitude of

this increase is difficult to quantify based on these test specimens because the magnitude of the initial imperfections in SNAM3 were on average 3.4 times that of TCPL2 as shown in Table 4.5, while it is understood that the magnitude of initial imperfections demonstrates a major role in the buckling strain for unpressurized pipes as demonstrated in Equation 1.5 and 1.6. The varying material stress-strain relationships may be neglected when comparing the critical strains of these specimens because they both buckled while the material was predominantly elastic.

The critical strains for TG1 and TG2 were relatively similar, and the critical strains for TCPL1 and TCPL3 were also relatively similar. Furthermore, the critical strain for TCPL3 was greater than that of TCPL1, although TCPL3 was bent more severely than TCPL1. In addition, the magnitude and distribution of the initial imperfections for the TG specimens were relatively similar although their bend intervals were different, and the magnitude and distribution of the TCPL1 and TCPL3 initial imperfections were also relatively similar although the magnitude of each TCPL3 bend was 1.5 times that of the TCPL1 bends. This information combined with the experimental test results demonstrates that different bending intervals and magnitudes do not have a substantial effect on the critical strain of the specimens tested in this experimental program.

Increasing internal pressure generally increased the critical strain of the cold bend specimens, similar to the behaviour for straight pipes as demonstrated in Equation 1.5 and 1.6. The average critical strain of the pressurized TCPL specimens was greater than that of the SNAM and TG specimens, although the TCPL specimens demonstrated the greatest diameter to thickness ratios, had a similar material grade to SNAM2 and a lower material grade than the TG pipes, and demonstrated similar overall bend geometries. The diameter to thickness ratio of the SNAM specimens were 1.5 times that of the TG specimens, the yield stress was only 75% of the yield stress of the TG specimens, and the overall bend geometries were similar. However, the critical strain of the TG specimens was

only 1.08 times that of the SNAM2 specimen. As the SNAM specimens were pressurized to 60% SMYS hoop stress, while the TG specimens were pressurized to 40% hoop stress, this indicates that the internal pressure demonstrates a dominant role in the onset of buckling of these pipes when subjected to bending loads.

5.5.4 Post Buckling Behaviour

In comparing the post buckling behaviour of the pressurized specimens, it is demonstrated that the ratio of the peak moment to moment at a global curvature prior to the first jack reset increases with increasing internal pressure. This ratio was on average 80% for TCPL1 and TCPL3, 73% for SNAM2, and 65% for TG1 and TG2. The internal pressure increases the post buckling moment in the tests because the tension load from the pressure pressing against the end plates considerable acts opposite to the load induced by the hydraulic jack. This is demonstrated in the post-buckling curve of TCPL3 in Figure 5.15 where a severe drop in applied moment accompanied the reduction in internal pressure without significant increase in applied curvature. The ratio of the moment prior to the first jack reset to the peak moment for SNAM3 and TCPL2 were 42 and 29% respectively. This indicates that increasing D/t ratio results in an increase in the post buckling moment capacity of cold bend pipes.

All of the pressurized specimens formed an outwards bulge shaped wrinkle, while the two unpressurized specimens formed an inward diamond shaped wrinkle upon local buckling. The length wrinkle length for the pressurized TCPL specimens and SNAM1 was 1016 mm, while that of the TG specimens and SNAM2 was 762mm. Thus the length of the wrinkle was between one to 1.3 times the diameter in length depending on the D/t ratio or internal pressure of the specimens. The length of the unpressurized wrinkles was between

2.3 to 3 times the diameters in length, with the higher D/t specimen demonstrating a longer wrinkle length. All of the specimens demonstrated strain relaxation along the entire length of the pipe away from the wrinkle location during post-buckling.

Because of the different loading histories of the specimens it is difficult to compare the failure behaviour of the wrinkles, therefore the reasons for discontinuing the testing of the specimens will be summarized below. The curvature of the SNAM2 and SNAM3 specimens was increased until the stroke of the jack was exhausted, and at this point the wrinkles had become very well defined. The curvature of the TG specimens was increased until they demonstrated central bend angles of 35 degrees. At this point the wrinkles fractured at the crest due to the low cycle fatigue caused by the tension-compression load cycling that occurred during the jack resets. The TCPL1 specimen fractured at its tensile side. This occurred because of the substantial tensile strains immediately above the wrinkle location that were caused by the internal pressure, as well as the brittleness of its material that resulted from its bi-axial stress condition. The curvature of the TCPL2 specimen was increased until the twisting of the ends that was caused by the anti-symmetry of the wrinkle forced testing to be stopped. The curvature of the TCPL3 specimens was increased until it demonstrated a central bend angle of 49 degrees. The pressure was decreased to 10% SMYS hoop stress during post-buckling of this specimen, and testing was stopped because it became apparent that the wrinkle would not fracture, but would simply continue to fold for unknown levels of increasing curvature.

5.6 Summary of Test Results

A comprehensive discussion of the results from the experimental testing of the eight test specimens has been presented in this chapter. The test observations, moment curvature response, local strain history, and post buckling behaviour have been discussed for the specimens. In addition, the critical strain using the maximum moment and bilinear global curvature methods has been determined for the specimens in order to understand the allowable strain that a cold bend pipe can undergo prior to the initiation of local buckling. The numerical results and local strain distribution for all of the test specimens may be viewed in Pipeline Technology Report No. 2005-1.

Comparing the tests of SNAM1 and SNAM2 demonstrates that cold bending plays a significant role on the behaviour of a pipe under applied bending. The maximum moment and corresponding curvature at the onset of buckling is decreased for the cold bend pipe. The critical strain of the straight pipe was two times that of the bend pipe using either the maximum moment or bilinear global curvature methods. The critical strain of all of the cold bend specimens ranged from between 25 to 85% of that of a similar straight pipe, as predicted by equation, with an average reduction in critical strain of 48%.

In comparing the effects of varying the degree and interval length of the individual bends created during cold bending, the behaviour of the TG specimens, along with TCPL1 and TCPL3 were investigated. The moment curvature responses were very similar for both specimens, and the strain distribution demonstrated moderately similar behaviours during the tests. The critical strains using the maximum moment method were within 30% for the similar specimens bent using different bending methods. The post-buckling behaviour was essentially the same for the similarly bent specimens.

The unpressurized specimens buckled in a diamond shaped pattern while the pressurized specimens demonstrated a bulge buckle. The moment capacity of the unpressurized specimens decreased by 30% immediately after they buckled. In addition, the absence of internal pressure significantly decreases the peak moment capacity and critical strain of a cold bend pipe in comparison with a similar pipe that is pressurized. The critical strain of the unpressurized specimens was between 23 to 45% of a similar pressurized specimen. The post buckling moment capacity of the unpressurized specimens was also considerably less than that of similar pressurized specimens.

Increasing the D/t ratio and internal pressure of the specimens corresponded to a decrease in peak moment capacity and global curvature at the onset of buckling. Increasing the internal pressure increased the magnitude of the bulges in the specimens prior to buckling. The post buckling moment capacity to peak moment ratio increased with increasing D/t ratio and internal pressure. Comparisons of the critical strains between the specimen sets were not possible due to the numerous variables that were investigated. Finite element modeling may be used to determine the effects of D/t ratio and internal pressure on the critical strain of the test specimens.

The specimens were tested until various failure modes became apparent. The TG specimens fractured at the crest of the wrinkle due to the tension-compression load cycling that occurred during the jack resets. The TCPL1 specimen fractured on its tension side because of its considerable tensile bending strains, in combination with the low ductility that was introduced to the material because of its biaxial stress state. The TCPL2 specimen demonstrated significant twisting at its ends during post buckling because of the anti-symmetry of its diamond shaped buckle. Finally, the TCPL3 specimen that was subjected to a reduced internal pressure of 10% SMYS hoop stress achieved a central bend angle of 49 degrees without fracture. This behaviour occurred because the pipe wall

area at the wrinkle location could continuously fold, thus resisting concentrations of deformations that might induce fracture of the specimen.

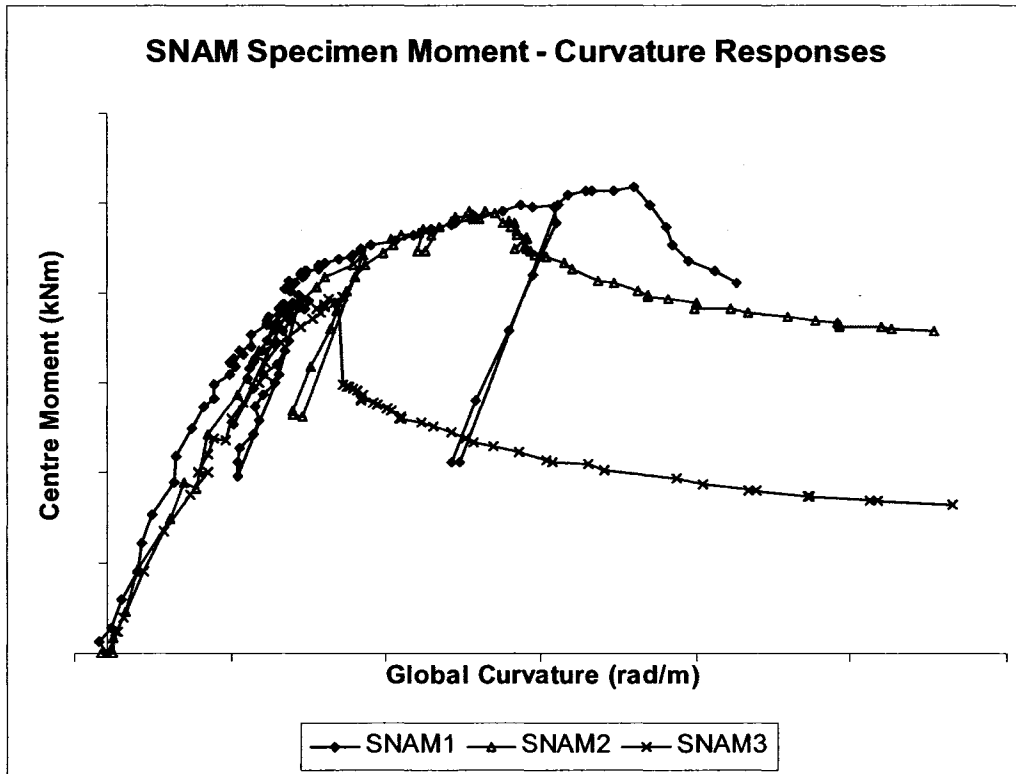


Figure 5.1 – SNAM Specimen Moment-Curvature Responses

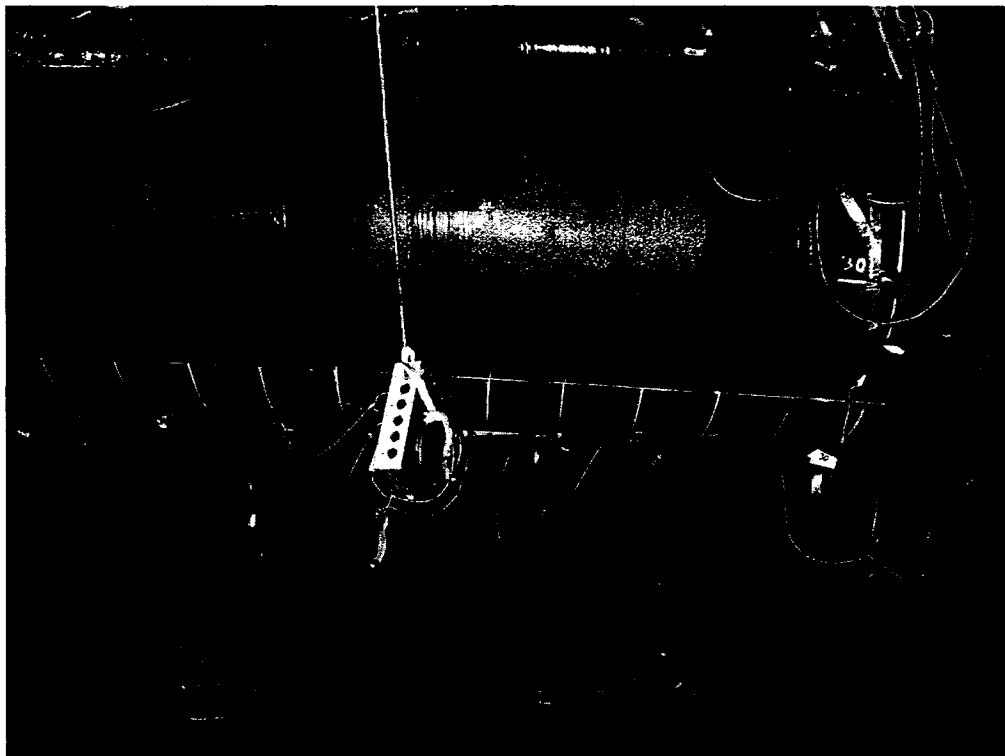


Figure 5.2 – SNAM1 End Bulge

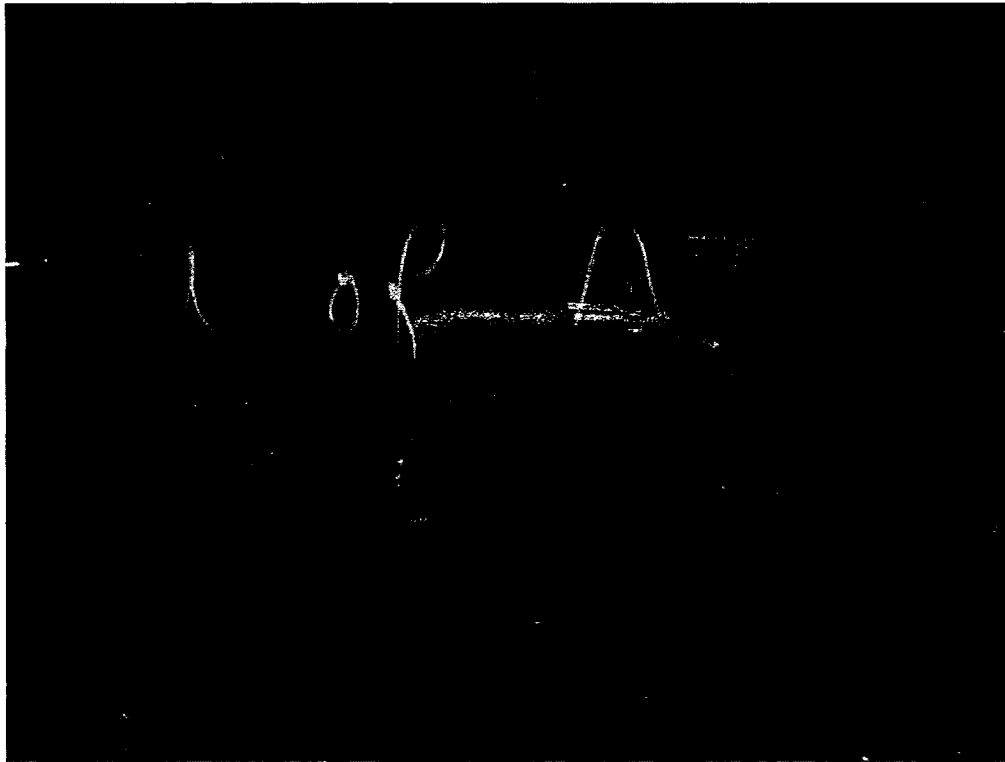


Figure 5.3 – SNAM1 Wrinkle

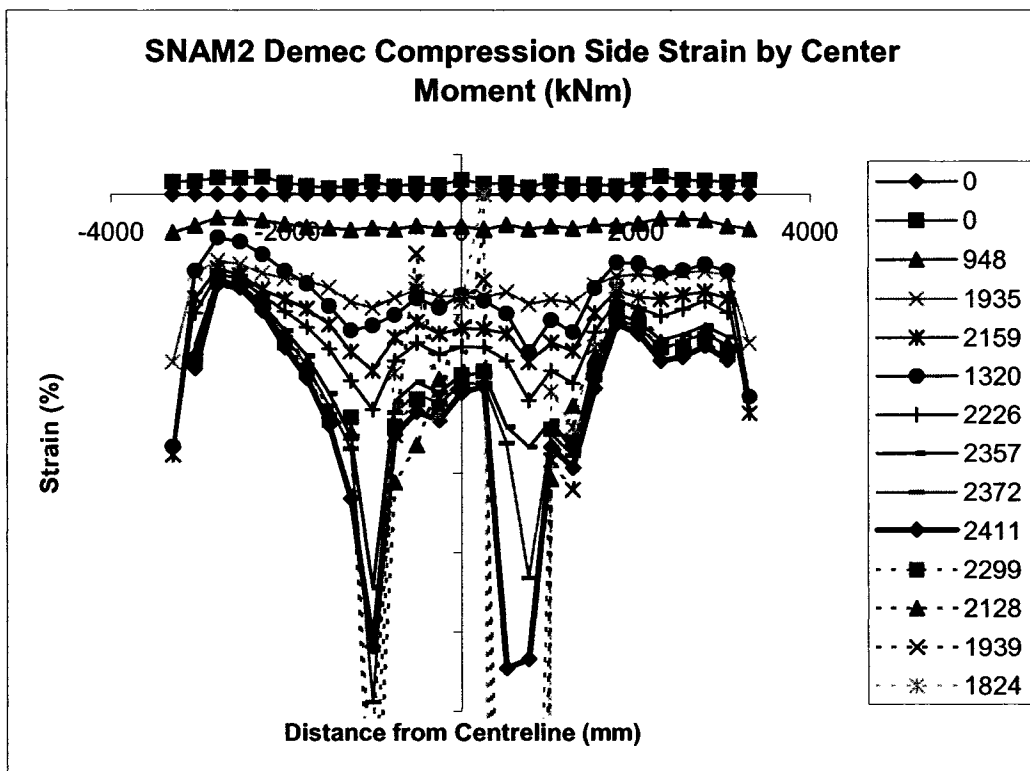


Figure 5.4 – SNAM2 Demec Strain Distribution by Increasing Load Step



Figure 5.5 – SNAM2 Final End Rotation

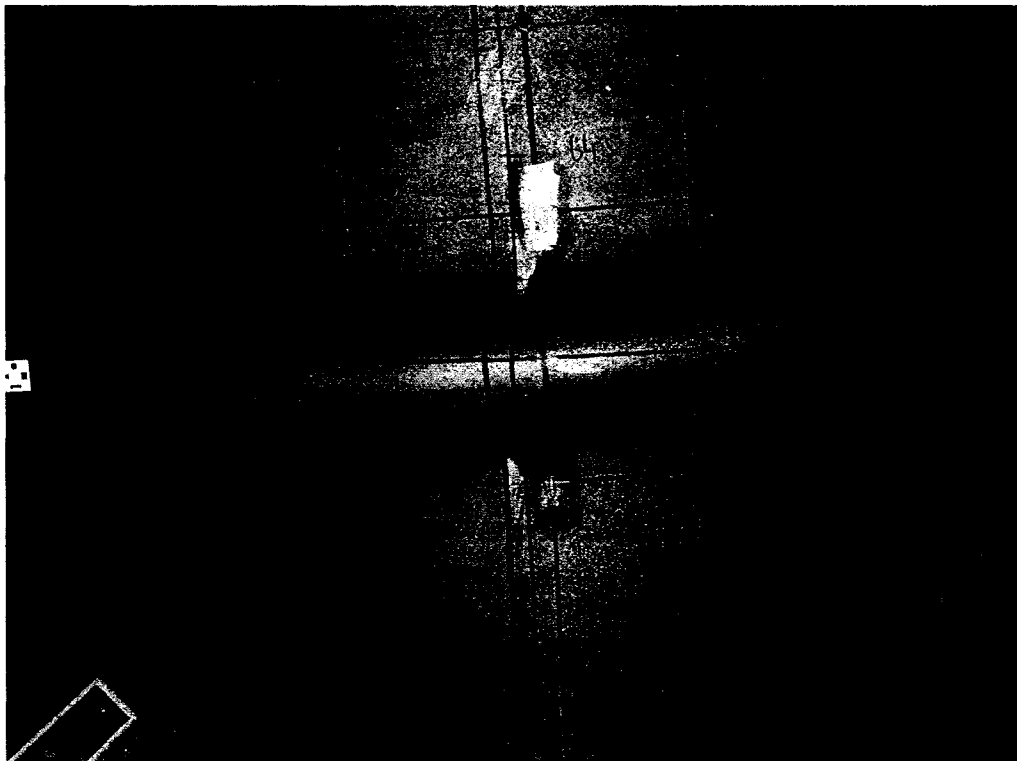


Figure 5.6 – SNAM2 Final Wrinkle Shape

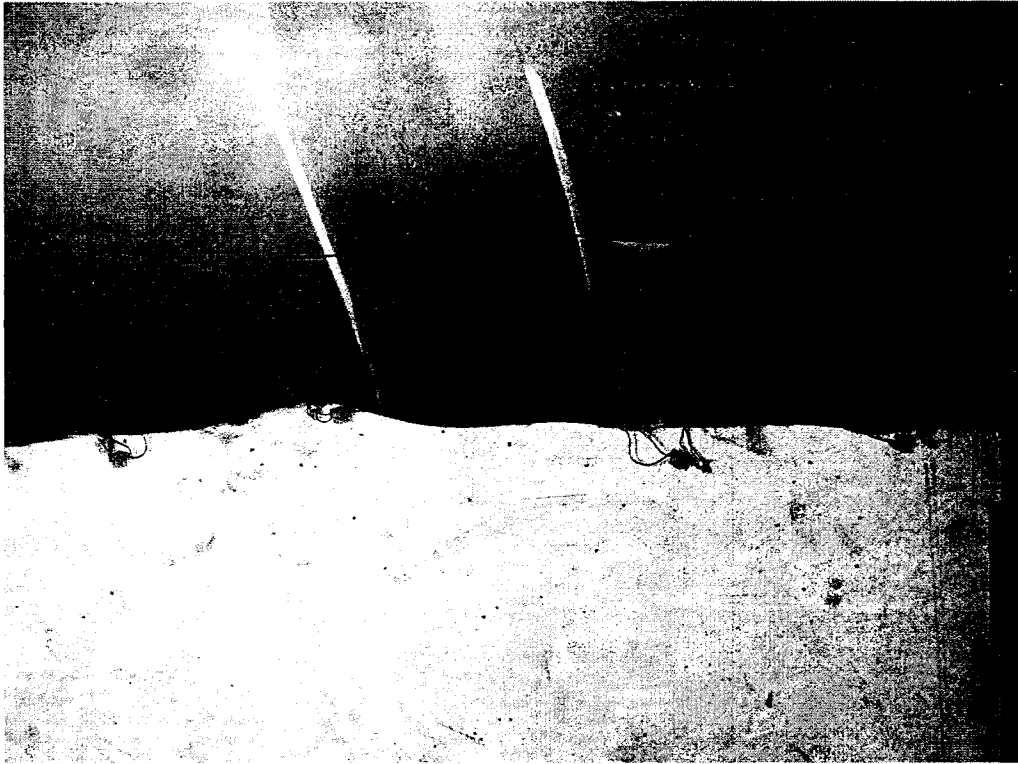


Figure 5.7 –SNAM3 Ripples Before Buckling



Figure 5.8 – SNAM3 Diamond Shaped Buckle

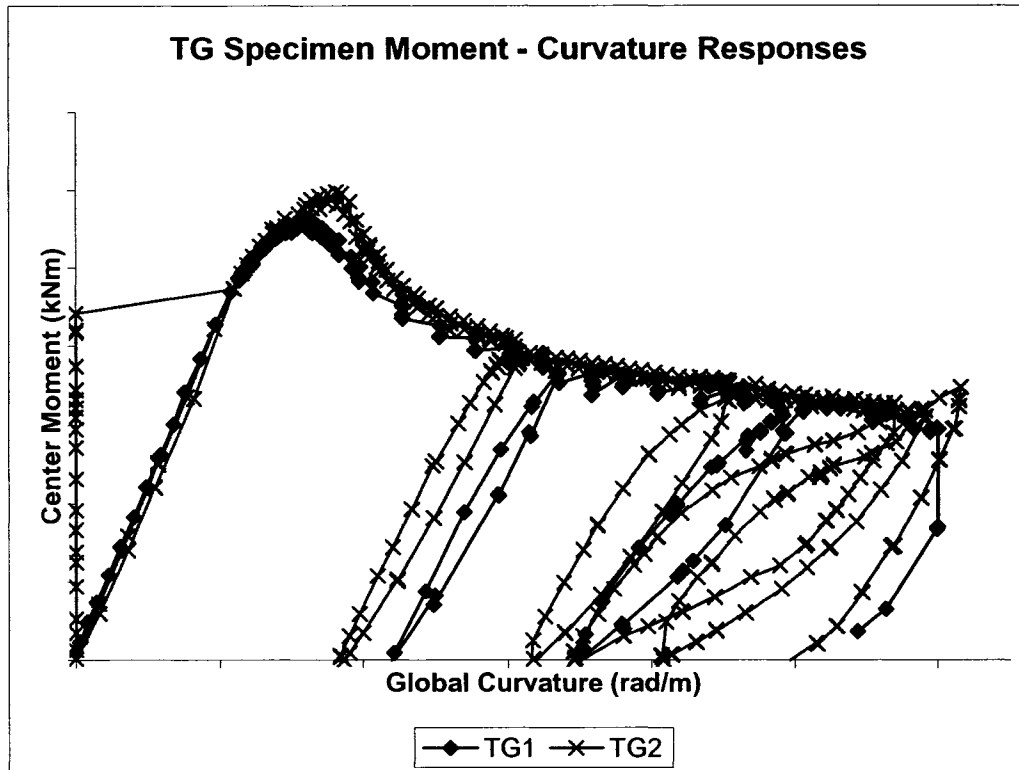


Figure 5.9 – TG Specimen Moment-Curvature Responses

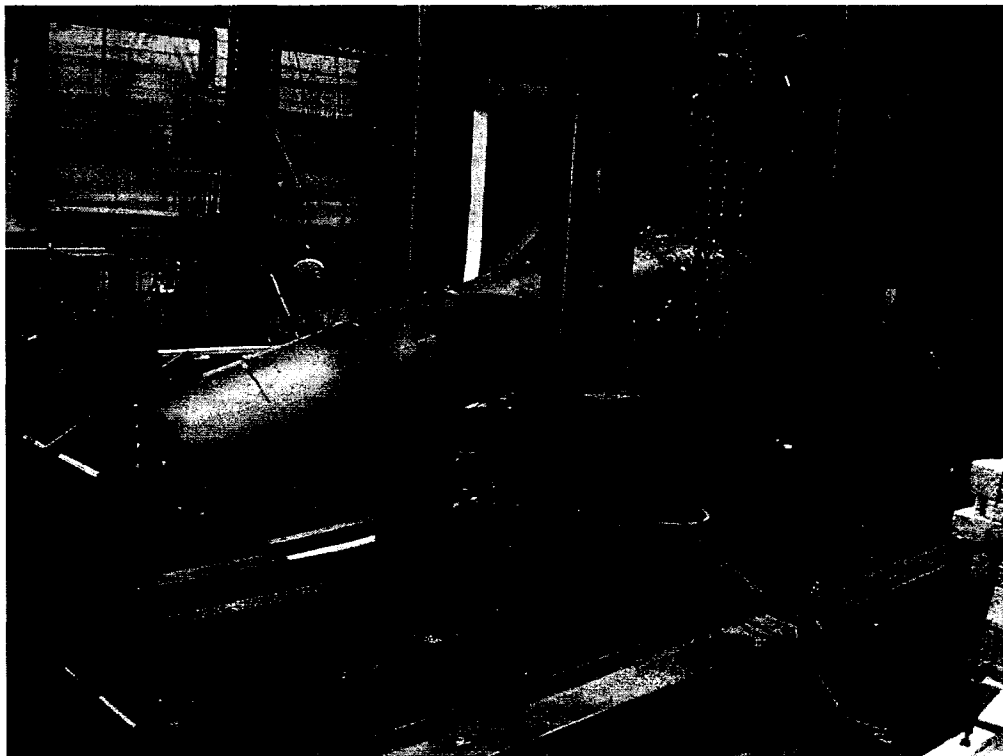


Figure 5.10 – Final Buckled Shape of TG1



Figure 5.11 – Pipe Fracture of TG1

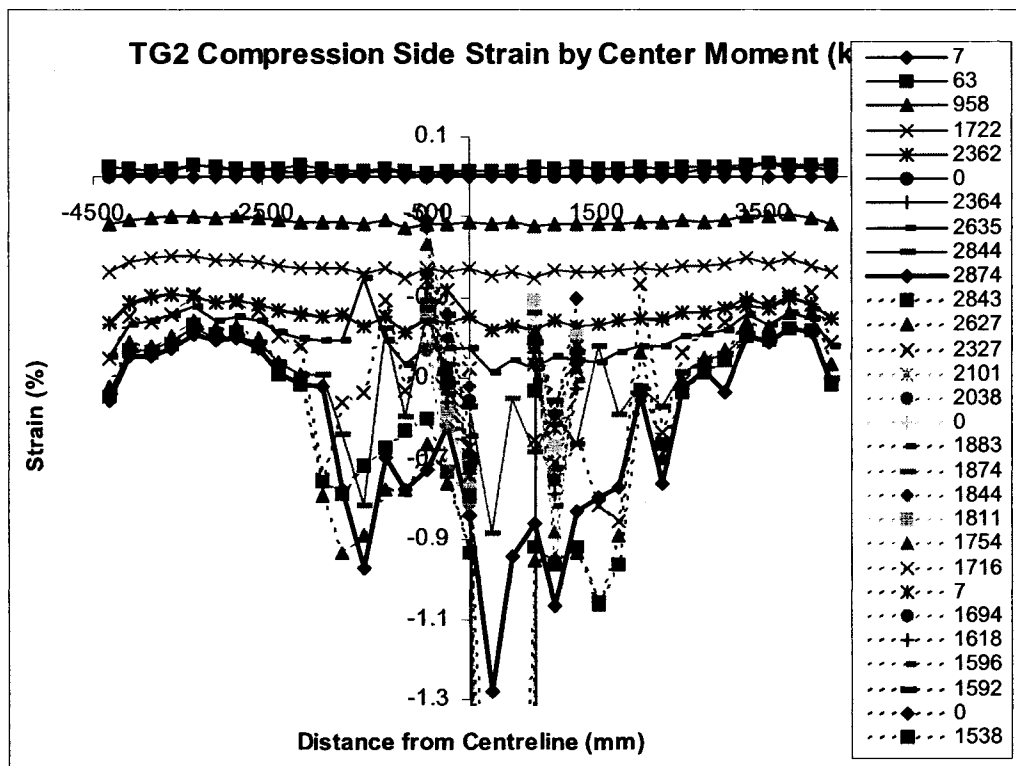


Figure 5.12 – TG2 Demec Strain Distribution by Increasing Load Step

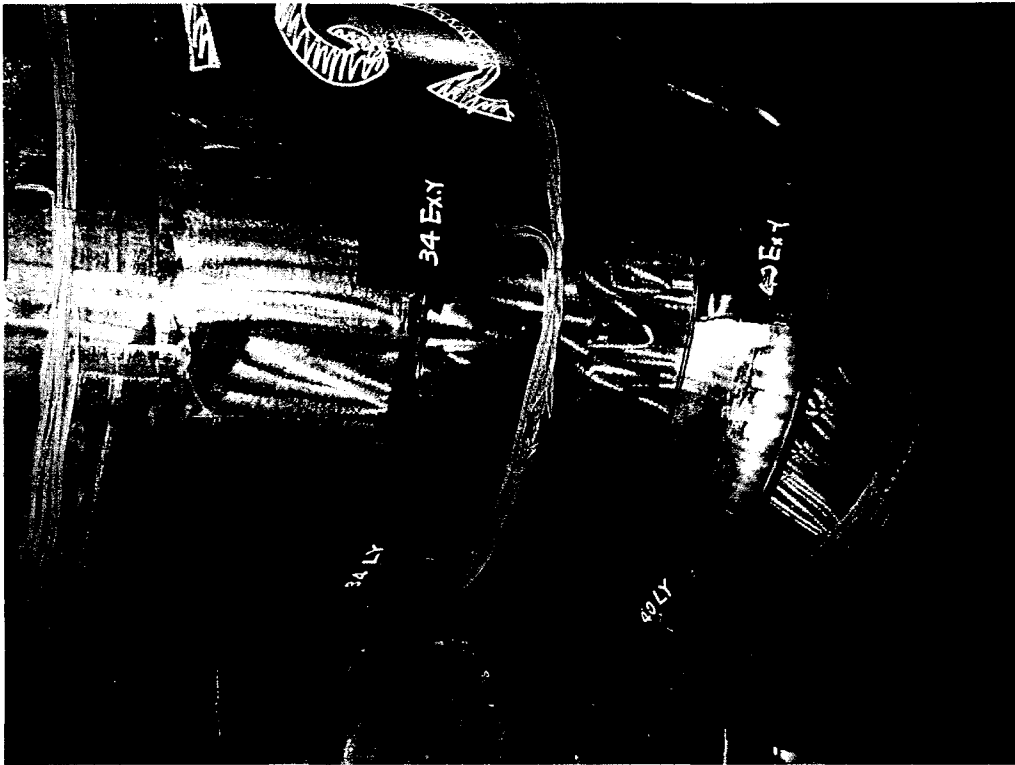


Figure 5.13 – Wrinkle Shape of TG2

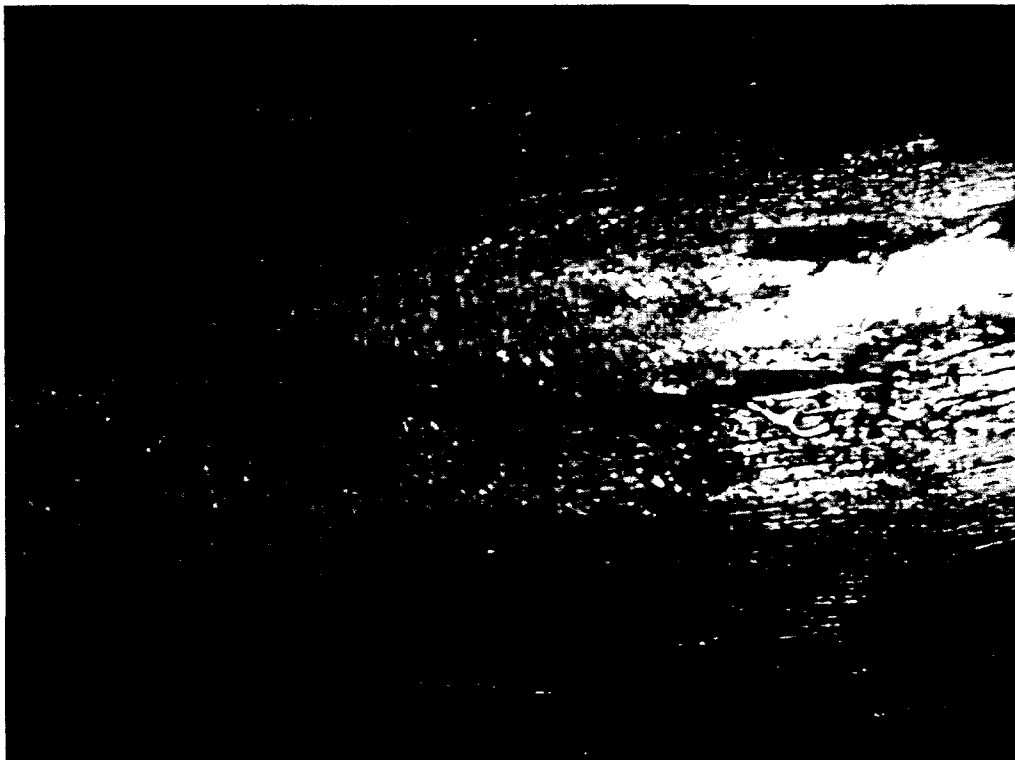


Figure 5.14 – Close View of Outside Surface of TG2 Wrinkle

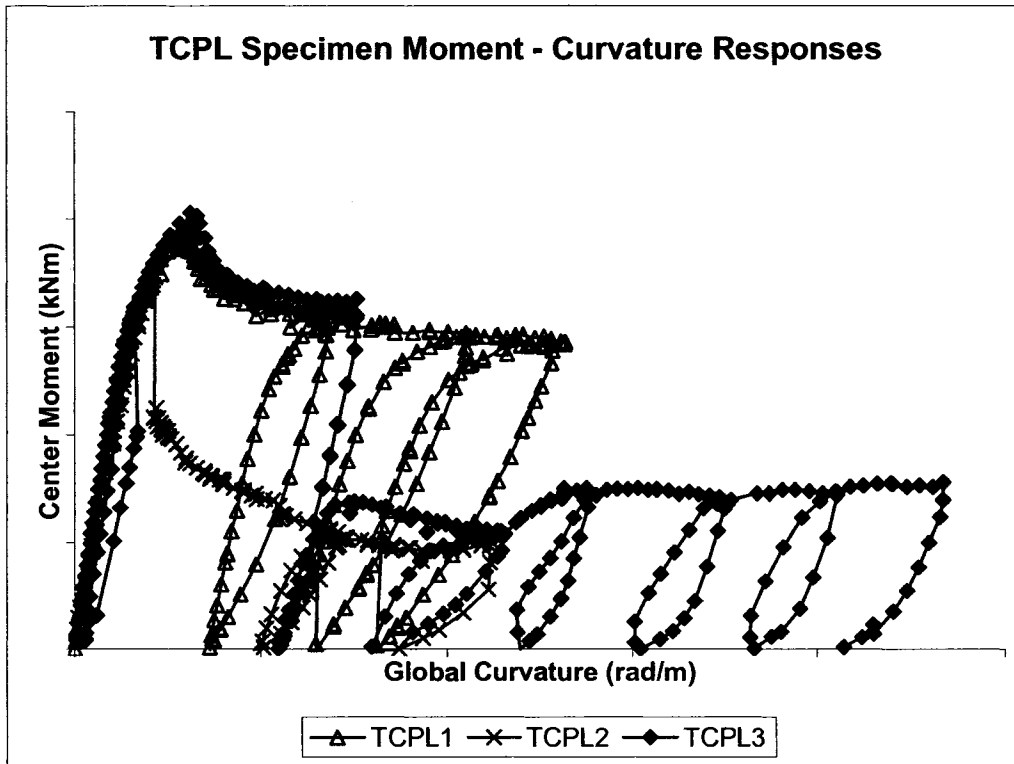


Figure 5.15 – TCPL Moment-Curvature Response



Figure 5.16 – Wrinkle and Fracture of TCPL1

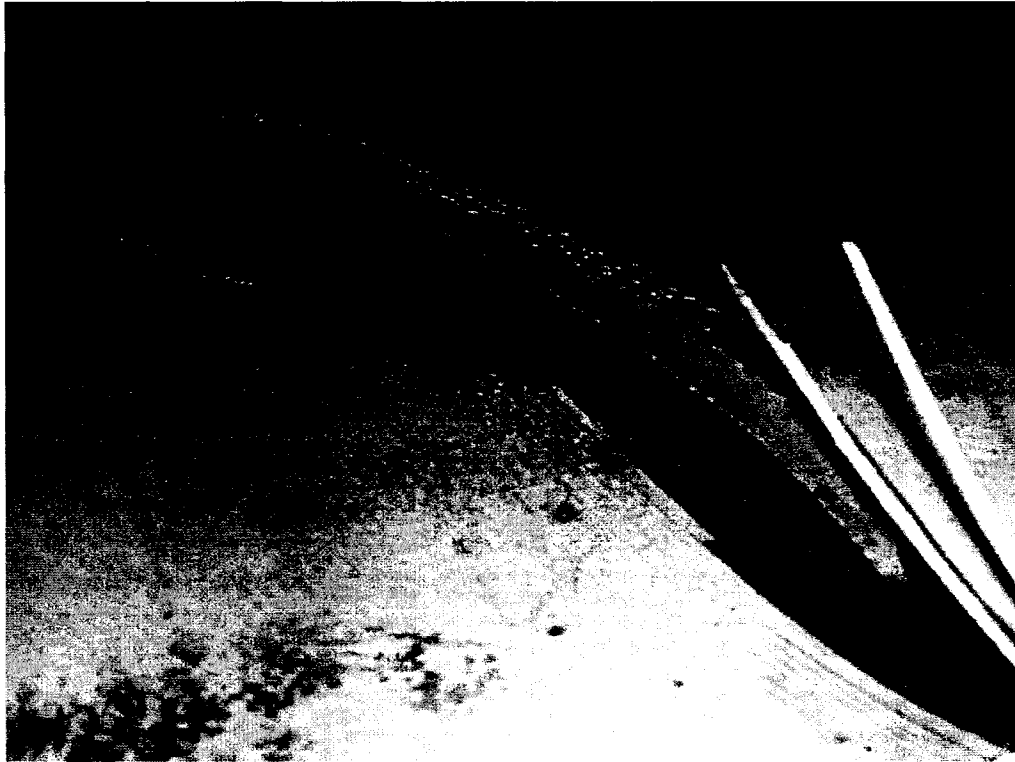


Figure 5.17 – Fracture Surface of TCPL1

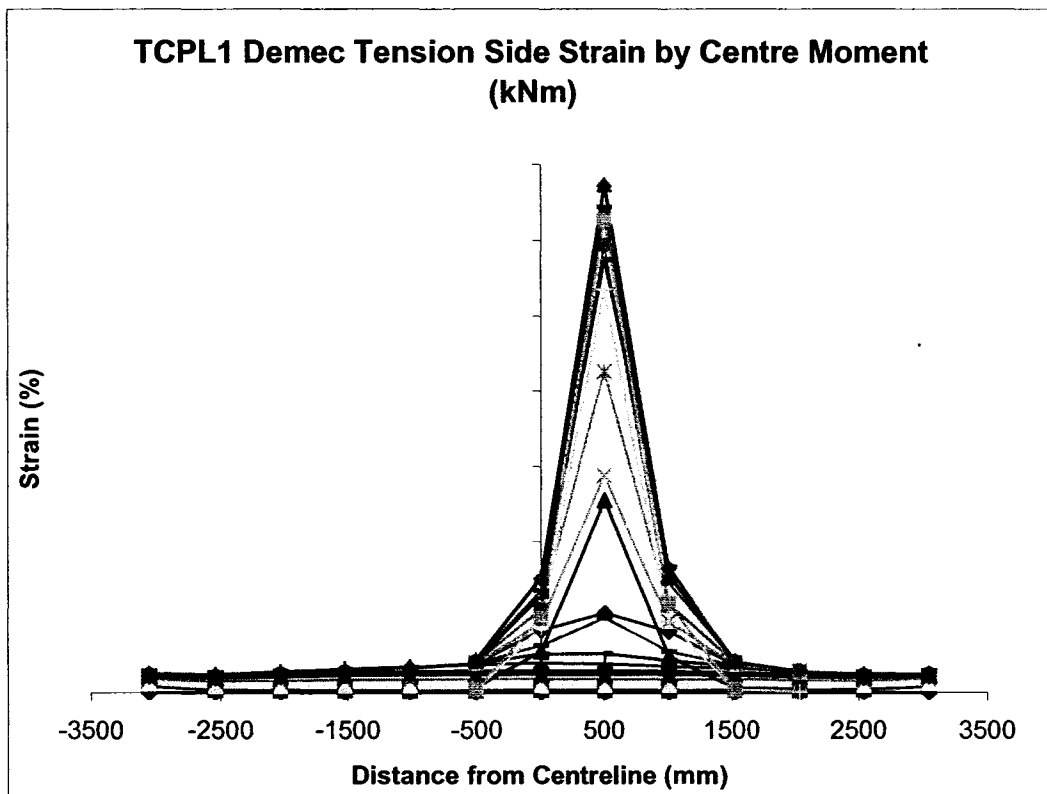


Figure 5.18 – TCPL1 Tension Side Strain Distribution by Centre Moment

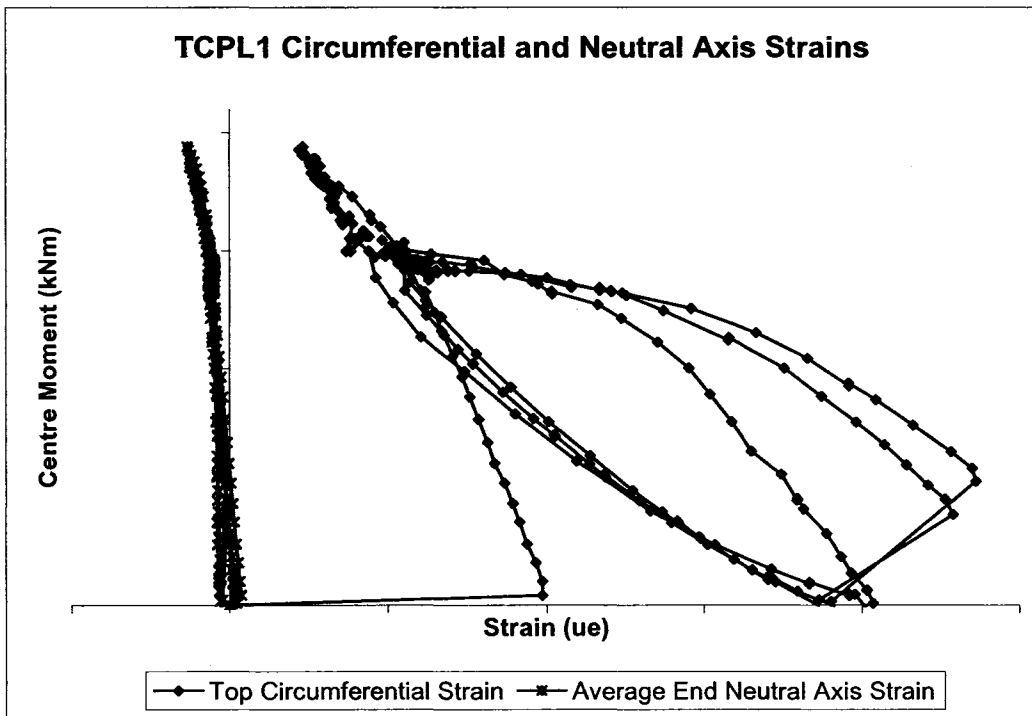


Figure 5.19 – TCPL1 Circumferential and Neutral Axis Strains

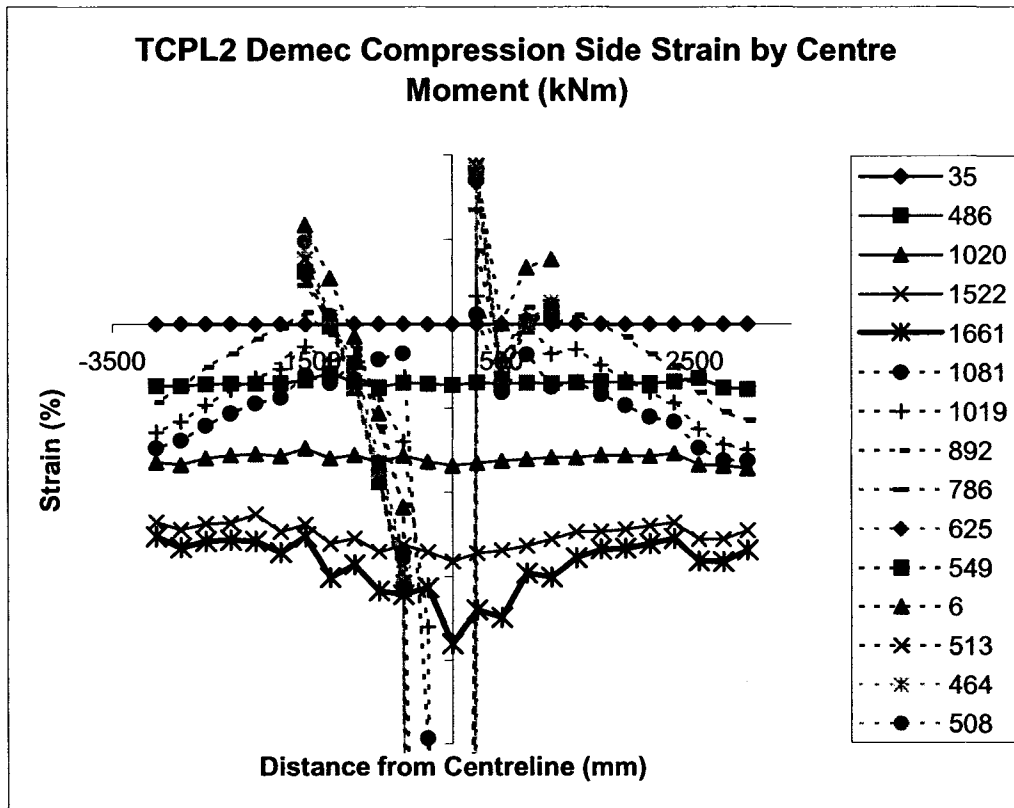


Figure 5.20 – TCPL2 Demec Strain Distribution by Increasing Load Step

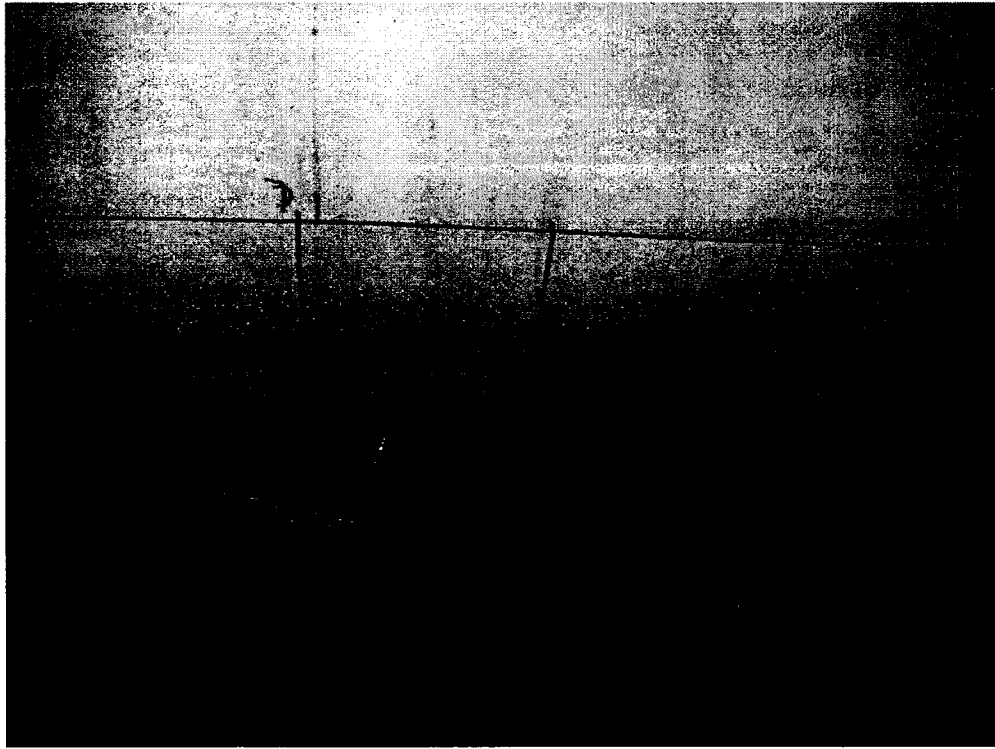


Figure 5.21 – Initial Buckling of TCPL2

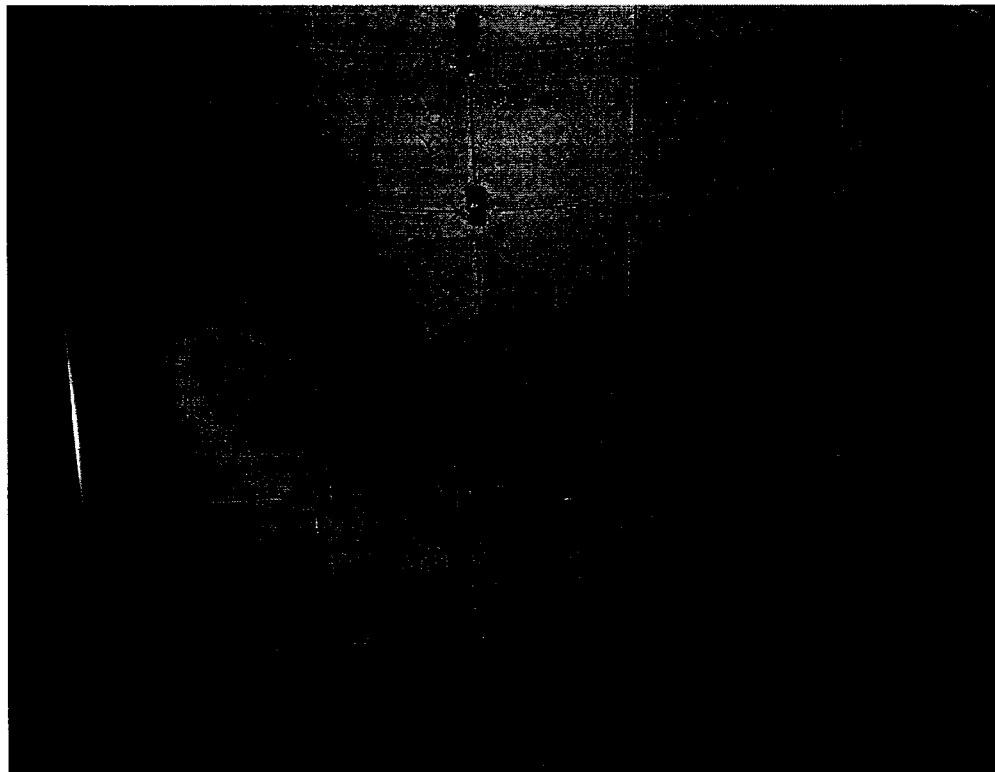


Figure 5.22 – Final Wrinkle of TCPL2

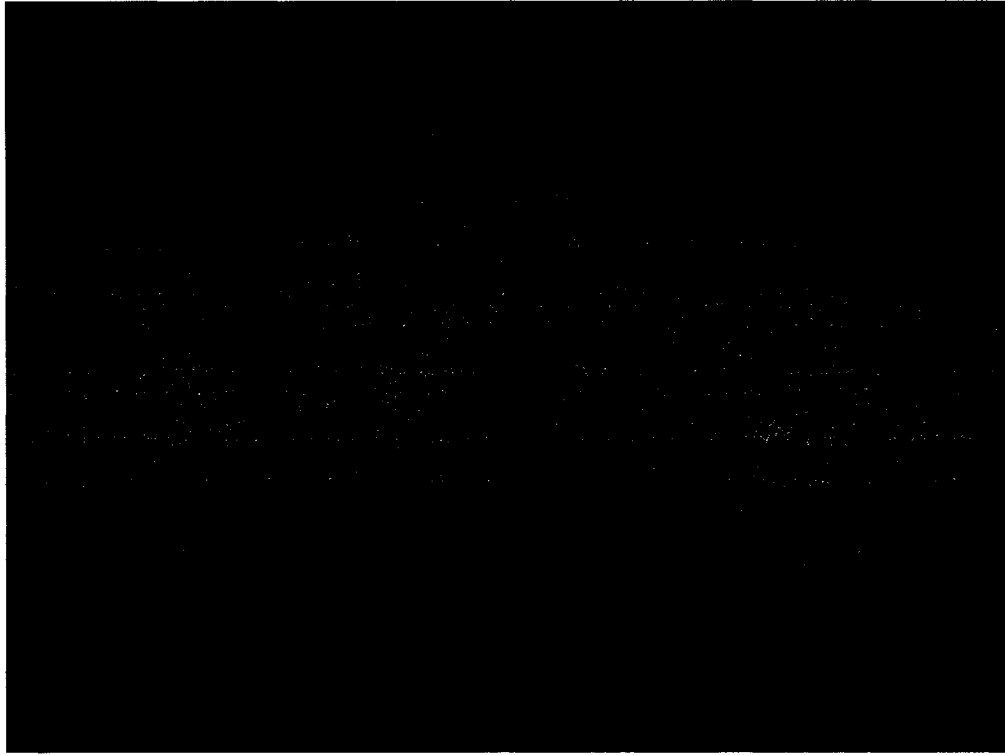


Figure 5.23 – Final Wrinkle of TCPL3



Figure 5.24 – Final Buckled Shape of TCPL3

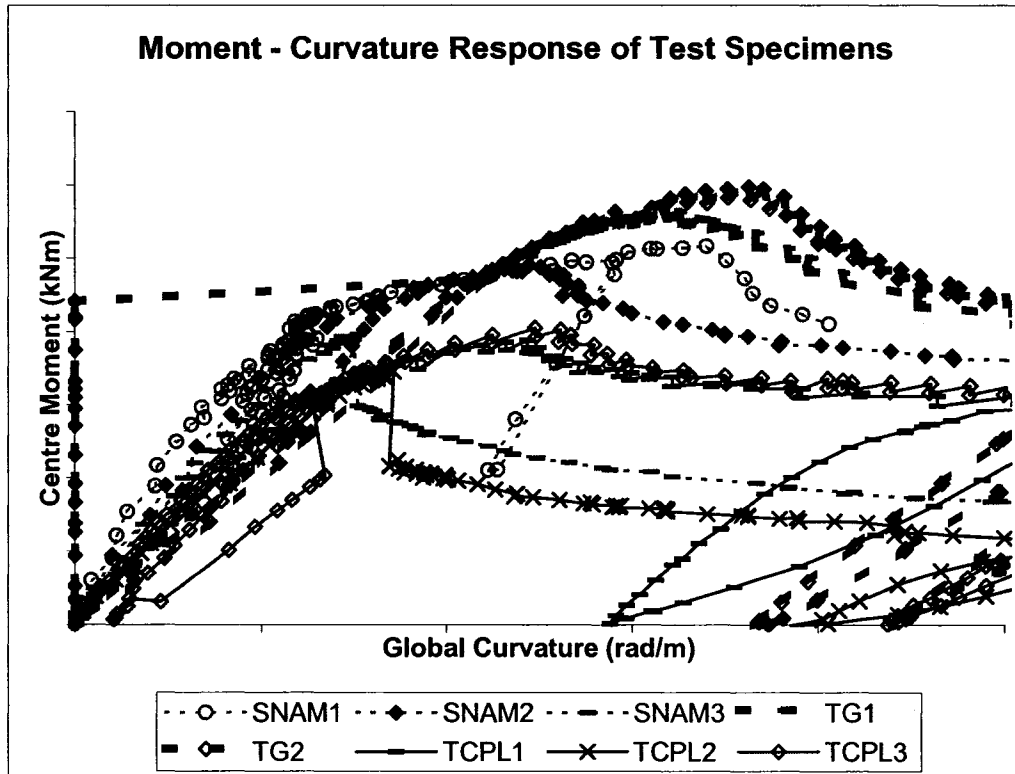


Figure 5.25 – Comparison of Moment - Curvature Responses

6.0 DEVELOPMENT OF FINITE ELEMENT MODEL

This chapter will comprehensively discuss the development of the finite element model that was created to simulate the behaviour of the specimens during testing. A brief overview of the finite element method will be initially presented, followed by an in depth discussion of the main features of the finite element model (FEM). The final two sections of this chapter will review the sensitivity analyses studies that were conducted for the model. In order to demonstrate this information in a concise manner, the SNAM2 model will be implemented to represent all of the models in this chapter.

6.1 Purpose of the Finite Element Analysis

The behaviour of the specimens when subjected to internal pressure, axial load, and bending was directly obtained during the experimental testing program, however, full-scale testing is very expensive and time consuming, thus only a few select parameters could be studied when considering their influence on specimen behaviour. The considerable evolution of the finite analysis method has allowed it to become an effective numerical tool for solving continuum mechanics partial differential equations within engineering tolerances. Consequently, a finite element model for cold bend pipes could be used to predict their behaviour with more diverse geometries, material properties, and load conditions than were demonstrated by the test specimens in this research. This finite element model (FEM) will be validated against the behaviour of the specimens during testing in order to demonstrate its precision in predicting the behaviour of similar pipes when subjected to the same loading conditions.

To perform the numerical analyses, ABAQUS Standard Version 6.3 (ABAQUS) By Hibbitt, Karlsson, & Sorenson, Inc. (HKS, 2002) was employed. The element library of this software package features numerous shell elements that allow for large displacements and finite membrane strains for both thick and thin walled pipes. The material model incorporated in the software permits the constitutive law of the material to be represented as a multi-linear curve with either isotropic or kinematic hardening, thus the results from the tension coupon tests may be directly input into the model. Additionally, the software can accommodate large deformations using non-linear geometry and large strain formulations, thus the behaviour of the pipes may be predicted well beyond yielding of the material. Also, the loading of the model may be applied with either load or displacement control, allowing for the efficient determination of the post-yielding response of the pipes up to a user defined level of deformation. In addition, the software permits control of the convergence criteria, allowing for a user-selected balance between precision and efficiency during solution determination. Finally, previous research at the University of Alberta has demonstrated that ABAQUS has successfully been used to model the behaviour of straight pipe specimen tests within engineering tolerance.

In order to gain assurance of the model predictive capabilities, the moment and global curvature response for the model must be similar to that demonstrated by the specimens during testing. In addition, the model must demonstrate its ability to predict the strain immediately prior to buckling of the specimens during testing. This will provide credibility for the critical strain determination of cold bend pipes that have diverse geometries, material properties, and loading conditions. Subsequently, the sensitivity of the critical strain of the model to these parameters can be determined, which will be valuable information when considering the behaviour of any cold bend pipe under field conditions that is subjected to excessive ground movement.

The validation of the FEM consisted of three stages. The first stage was to compare the initial load-deformation behaviour of each model during loading, with the initial load-deformation behaviour of the specimens during testing. This was necessary to verify that the general geometry of the model is the same as that measured for the specimens. These geometric properties are comprised of the pipe diameter, wall thickness, initial end angle, and vertical deflection due to the cold bending. The initial stiffness also verified that the Modulus of Elasticity from the tension coupon tests was precise, and that the method of load transfer from the loading point to the model was the same as that from the jack to the pipe centreline during the test. The second comparison required for validation was with consideration of the post buckling behaviour of the model. That is, the overall load vs. deformation of the model must compare reasonably with that of the test after the specimens had buckled, while the jack stroke was being increased. This relationship compared favourably for all of the models with little effort. The final stage for the validation of the FEM was to compare the value of the critical buckling strain for the model, with that of the test. This comparison will validate the predictive capabilities of the model so that it may be applied to a design engineering environment.

6.2 Overview of Finite Element Method

In the finite element method, the structure is represented as a series of subdivisions called finite elements, where the joints of these elements are called nodes. When the structure is subjected to applied loads, the variation of displacement inside of the continuum is initially unknown. Thus it is assumed that the variation of the displacement within the elements may be approximated by a shape function, where these functions are defined in terms of the displacements at the nodes. Subsequently, the force-displacement equilibrium equation for every element in the structure is compiled into matrix form, where

the nodal values of the displacements are the unknowns. The next step is to apply the boundary conditions to the nodes of the structure, and this will allow for the solution of the equilibrium equations to be determined. Finally when the nodal values of the displacement are known, the shape functions may be used to define the displacement throughout the assemblage of elements (Rao, 2005).

6.3 Elements

As the thickness of the pipe wall of the test specimens was small in comparison to the diameter, a shell element was selected to represent the pipe wall in the model. The deformations in a shell element are caused by a combination of membrane action and bending action. The membrane strains are constant through the thickness, while the bending strains will vary linearly. If the thickness to diameter ratio of the model is extremely small, the stresses and strains are assumed to be constant through the thickness of the shell. Thus for a thin shell, the strains are only axial, circumferential, and in-plane shear. As the thickness of the shell increases, a stress and strain gradient is introduced in the radial direction. This behaviour may cause numerical conditioning problems when thin shell theory is used to model a thick shell structure (ABAQUS Users Manual, 2002).

A type S4R shell element was selected from the ABAQUS element library to represent the pipe wall of the model. It is a general-purpose shell element that is applicable for both thin and thick shells. It is three-dimensional and its shape is quadrilateral. The deformation of this element is represented by a first order shape function. This is because there are nodes only at the corners of the element, and the displacements between the nodes are linearly interpolated as shown in Figure 6.1. The element has three rotational degrees of freedom, and three displacement degrees of freedom. Six degrees of freedom were necessary to

ensure that the element is applicable for large strain problems, although the rotation about the axis normal to the element is negligible. This element has been applied in previous pipeline models at the University of Alberta, and the results of these models have compared favourably with experimental behaviour.

The S4R element is applicable for moderately thick, as well as thin shell problems because it uses thick shell theory as the shell thickness increases, and thin shell theory as the thickness decreases. Thin shell theory denotes that the transverse shear flexibility is negligible, and the shell normal is always perpendicular to the shell reference surface. As the thickness of the elements was less than 1/15 times the distance between the supports, thin shell theory was used in the elements for this model. First order shear deformation is assumed for this element, and the transverse shear stiffness remains constant during the entire analysis.

The S4R element allows for a change in thickness due to the Poisson's effect when it is subjected to in-plane strain. This makes it applicable for large deformation. A lower-order integration is used to form the element stiffness, which generally leads to more accurate results. Because a reduced order integration rule is used for the stiffness matrix, an hourglass control stiffness parameter is applied to the elements. This stiffness parameter is assigned to the rotational degree of freedom in the element normal direction, and is necessary to eliminate singular modes that may otherwise occur. The hourglass control stiffness is function of the thickness, as well as the initial shear modulus of the material, which is correspondingly a function of the Modulus of Elasticity and the Poisson ratio of the material. The default hourglass stiffness factor was used for this model, and the factor remained constant for each element for the entire analysis. Seven integration points were used through the thickness of the elements so that the post yield stress distribution due to the bending action of the element could be accurately modelled.

A second set of elements was used at the ends of the to establish the boundary conditions in for the model. The characteristics of these elements will be discussed in Section 6.4.

6.4 Symmetry

In order to reduce computer-processing time during the analysis of an FEM, symmetry is often used to decrease the total number of degrees of freedom in a model. For the modelling of the specimens in this project, there are two possible symmetric planes. If the buckling of the pipe occurs perpendicular to applied in plane moment, and there is no out-of-plane movement throughout loading, only half of the pipe in the circumferential direction is required to be modeled. This is possible because the stresses, strains, displacements, and rotations will all be symmetric about the 0 – 180 degree position of the pipe when it is under the aforementioned conditions. The second possible plane of symmetry for the model is at the middle of the pipe in the longitudinal direction. This is because after application of the end moments the maximum moment will be located at the middle of the pipe, as this location has the greatest initial vertical deflection and second-order effects. Thus the specimen would buckle at this location under perfect testing conditions, and this buckle would be symmetric in the longitudinal direction. If this behaviour occurs, all of the degrees of freedom in the model would be symmetrical about the middle of the length of the pipe. Taking advantage of these two possible symmetry conditions would allow for the number of elements in the model to be reduced to 25% of the elements required for a model of the entire pipe.

For this FEM, symmetry in the longitudinal direction was ignored for several reasons. Firstly, the initial end angles of the pipes were not equivalent for any of the specimens. This moved the maximum initial vertical deflection away

from the middle of the pipes, which caused a correspondingly moved the maximum moment during testing from the midpoint. In addition, there was considerable variation in the amplitude and period of the initial imperfections along the length of the pipe, and they were not symmetrical about the middle of its length. As a large imperfection may trigger buckling away from the location of the maximum second order moment, it may be necessary to model one large imperfection that was located only near to the precise middle of the pipe. Finally, the most important reason that the entire length of pipe was modelled was that none of the test specimens actually buckled at precise middle of the length during testing. Therefore it would be undesirable for the all of the models to buckle at this location because the global load-deformation behaviour of the model would then differ from that of the test specimens.

The symmetry condition in the circumferential direction was utilized for this FEM. This resulted in a reduction of the number of elements to half of what would otherwise be required if the entire pipe was modeled. Assuming symmetry in this direction would result in a nearly equivalent response to a full pipe model for several reasons. To begin with, during the testing phase of the program lateral bracing was provided at each side of the pipe at the ends and one-third length locations, as shown in Figure 2.8. This caused the restraint of any out of plane movement of the specimens. In addition to this, all of the specimens buckled perpendicular to the direction of the applied moment, and the wrinkles were either symmetrical or anti-symmetrical about the 0 – 180 position of the pipes. It is noteworthy to discuss that the measured imperfections for the specimens were not symmetrical about the 0 – 180-degree position. This is because the bending process is extremely complicated, and is improbable for the induced ripples in the pipe to become perfectly circular. It was decided that the asymmetry of the imperfections in the circumferential direction would not have a significant effect on the buckling strength of the pipes. This is because the behaviour of the buckle is dominated by the compressive strains at the 0 degree position of the pipe, and

once the buckle is triggered the shape of the initial imperfections is not overly critical.

6.5 Boundary Conditions

In order to simulate the test frame, moment arms, and bracing system of the test setup, it was required to prescribe corresponding boundary conditions to the FEM. When considering the experimental test setup, there are essentially three different boundary conditions on the pipe that need to be considered for the model. The first boundary condition considered was the pin that was used to transfer the load from the jack to the moment arms. The next boundary condition was the moment arm that provided the eccentricity from the jack load to the pipe. The final boundary condition from the test setup was the endplates at the ends of the pipe. In addition to the boundary conditions from the test setup, an additional set of boundary conditions was required to address the plane of symmetry that was used in the model. These four boundary conditions will be discussed in detail below, and are shown pictorially in Figure 6.2.

6.5.1 End Plates and Collars

Beginning with the endplates of the FEM, the endplates were modeled by creating a node at the centre of the pipe at each end, and connecting the adjacent nodes around the pipe wall to this node with several elements. These elements are required in order to transfer the tensile load from the internal pressure acting against the endplates, to the pipe wall. The STRI3 element was selected from the ABAQUS element library for this purpose. This is a 3-node shell element, with 6 degrees of freedom at the nodes. It is flat and triangular faceted, which means

that the initial curvature is ignored (ABAQUS Users Manual, 2002). This is suitable because the endplates in the test setup were flat. This element will predict a thin shell solution, as the transverse shear deformation is ignored, and allows for relatively large rotations. A thin shell solution element is acceptable for the model because the strains in the endplates were below the yield strain throughout the tests. The change in thickness with deformation is neglected for these elements, which is tolerable as they experienced relatively small strains during testing.

The endplate was modeled as elastic, with the same Modulus of Elasticity as that of the pipe. This is acceptable because the end plates in the test setup were made of steel, and there was no plastic deformation observed in them upon completion of the experimental tests. The endplates thickness for the model was 76 mm, in accordance with that used for previous models created at the University of Alberta. This is greater than the 50 mm endplate thickness of the test setup, however, the endplate in the test setup was bolted to a heavy I – section that functioned to significantly increase its bending stiffness. It is not believed that the thickness of the endplate will significantly affect the response of the pipe model, as its sole purpose is to simply transfer the load from the moment arm and internal pressure to the pipe wall.

In order to model the confining collars of the test setup, the wall thickness of the pipe elements was increased by the collar thickness, for 300 mm in length from each end of the pipe. This is not a precise representation of the collars in the test setup, as these collars did not uniformly contact the pipe over its entire circumference. Nonetheless, as end buckling was prevented in the model with these collars, and their length is relatively small in comparison to the overall pipe length, the model collars may be considered adequate for the FEM.

6.5.2 Moment Arms

During the experimental tests, the applied axial load and bending moment were interrelated. The axial load in the specimen was induced by the applied jack load, in combination with the internal pressure acting on the endplates. The applied moment was from the applied jack load in combination with the eccentricity of this load to the pipe centreline. Therefore, the moment arms in the model were utilized to transfer both axial load and moment to the pipe.

As the rotation of the end of the pipe was effectively the same as that of the pin in the test setup, it was necessary to simulate this behaviour in the FEM. This was accomplished in two steps by using multipoint constraints. The first step was to apply a rigid beam constraint to connect each node at the end of the pipe model to the centre of the pipe at the end. This restrained the rotation and displacement of the pipe wall to that of the centre of the pipe, as though connected by a rigid beam. This corresponds to the welding of the pipe to the end plate in the test setup, which is a rigid connection, where the rotation of the entire pipe wall at the end was the same as that of the moment arm. The second step was to connect the node at the centre of the end of the pipe to the loading pin, with another rigid beam constraint. This restrained the rotation and displacement of the centre of the pipe to that of the loading pin, which was located 600mm below this point, as though connected by a rigid beam. This rigid beam correlates to the heavy I – section that was used to provide the eccentricity to the ends of the pipe during the test.

This load transfer system for the model is slightly different from the loading system that was used in the test setup. In the test setup, a hinge was welded to the bottom of the moment arm on its side that is opposite to the pipe. The jack load was transferred to the pipe via the pin that was positioned inside of this hinge. This hinge assembly was not included in the model as it does not affect the loading on the pipe, and would therefore introduce unnecessary

additional elements to the FEM. However, this hinge did increase the initial eccentricity of the jack load to the end of the pipe, and this was previously accounted for during the determination the maximum moment during testing as discussed in Section 4.5.

6.5.3 Loading and Reaction Pins

External boundary conditions were required at the loading and reaction pins of the FEM in order to replicate the bracing system of the test setup. At the loading pin of the model, only the vertical direction displacement degree of freedom was restrained. This restraint modelled the vertical bracing that was installed on the hinge on rollers of the test setup, as shown in Figure 2.11. At the reaction pin of the model, both the vertical and longitudinal degrees of freedom were restrained. This is again the same as for the test setup where the longitudinal displacement of the pin was restrained by the testing frame, and the vertical bracing on the frame restrained the vertical displacement of the hinge.

6.5.4 Plane of Symmetry

Restraints were provided at the nodes positioned on the plane of symmetry of the model in order to ensure that the degrees of freedom in the model were the same as those of a perfectly symmetrical full cross-section pipe. To accomplish this, the displacement in the lateral direction, the out-of-plane rotation, and the rotation in the longitudinal direction were all restrained. In the test setup the columns of the lateral bracing system eliminated any out-of-plane movement of the pipe during testing. Also, since the lateral bracing columns were installed at four locations along the length of the pipe, and were evenly spaced on both sides,

the out-of-plane rotation of the pipe during testing was negligible. At each of the moment arms in the test setup, the lateral bracing was provided to the pipe at two locations that were spaced 600 mm apart in the vertical direction. As this bracing was provided at both sides of the moment arms, the twisting of the specimen was somewhat restricted during loading. Therefore based on this information, the prescribed restraints on the nodes at the plane of symmetry of the model were very similar to those that were provided by the lateral bracing system of the test setup.

6.6 Material Properties

One of the most valuable features of ABAQUS is that the material model may be input as a series of stress-strain points. There is no limit to the number of these points, and the stress-strain behaviour between the input points is linearly interpolated. The material of the model may be elastic-plastic, and different elements may have different material properties. In addition to the input of the stress-strain behaviour, the yield criterion, hardening rule, and dependencies on rate and temperature effects must be specified for each material model.

6.6.1 Overview of Material Model

The von Mises yield condition was selected to define the yield surface of the material. This yield condition assumes that the yield stress is equivalent in all directions, and that the yielding of the material is independent of the equivalent pressure stress. Also, the material behaviour for the model was defined as both temperature and rate independent, as this represents the behaviour of the material during the experimental tests. This is because the specimens were loaded at room

temperature, and after every loading step during the tests time was allotted for the strains in the pipe to stabilize before instrumentation readings were recorded.

The hardening rule that was selected for the material model was isotropic hardening. This signifies that the yield surface changes size uniformly in the three orthogonal principle directions as plastic straining occurs, which results in an increase of the yield stress with plastic strain for the materials in this model. The isotropic hardening rule is only applicable for monotonic loading, as the yield stress for a material is reduced due to the Bauschinger effect during reverse loading beyond the yield stress. As the specimens in the testing program were loaded in closing mode bending, the Bauschinger effect will not affect the material behaviour of either side of the bend.

6.6.2 Selection of Material for Model

Initially, the material properties from the coupons that were cut from the end of the pipe were used to characterize the stress-strain behaviour of the material model. This represents the pipe material in its virgin condition, as the effect of testing on the material at the ends is minor. The behaviour of the model when using this material was satisfactory in comparison with the test results, however the virgin properties are not a true representation of the material behaviour of cold bend pipes.

As extensively discussed in Chapter 3, loading a material beyond the yield strain will cause an increase in the yield stress of the material. This behaviour is due to the work hardening effect, and is applicable to both tension and compression loading for steel. The specimen material on extrados of the bend experienced tensile loads beyond the yield strain during cold bending, and subsequently experienced sizable tension strains again during the experimental

tests. The opposite was the case for the material at the intrados of the bend, where permanent compression strains were experienced during both cold bending and experimental testing. Thus during the experimental tests, the material towards the extreme fibres of the pipes will have demonstrated a higher yield stress than that of the virgin material.

The material behaviour obtained from coupon testing of the compression side bend material does not represent the actual behaviour of the material at the intrados of the model. This is because this coupon was loaded in compression beyond the yield strain during cold bending, then in tension beyond the yield strain during the experimental testing, thus the Bauschinger effect will be exhibited in the material properties obtained during the coupon tests. In contrast, the coupon material from the tension side of the bend experienced tension beyond the yield stress during both cold bending and coupon testing, thus the work hardening effects caused by cold bending will be demonstrated in this materials stress-strain behaviour. Therefore, this material may be considered a true representation of the material behaviour at the extrados of the bend.

Assuming that the pipe material is isotropic, its stress strain behaviour is equivalent in both tension and compression. Also, the magnitudes of the residual strains due to cold bending were similar at both extreme fibres of the bend as demonstrated in Figures 4.1 and 4.2. For these reasons it may be assumed that the stress-strain properties of the tension side bend material will be nearly equivalent to the true stress strain behaviour of the compression side bend material.

For simplicity in the model, the tension side bend material was used to represent the material for the entire pipe in the FEM. This is not the true behaviour of the pipe material as the residual strains due to cold bending decreased from the extreme fibre to the neutral axis, thus the extent of work hardening varied along its depth. The behaviour of the pipe is not overly sensitive to this residual strain gradient because the applied bend angle during the

experimental tests was always greater than the initial bend angle. Consequently, the depth of the elastic region of the specimens during testing was always greater than that during cold bending, and the effects of work hardening are not pertinent in the elastic region of the stress-strain curve. This is demonstrated in Figure 6.3, where the elastic core for the tested pipe is shown to be smaller than that for the pipe after cold bending, thus the material at the limits of the elastic core during testing will likely not have significantly work hardened from the cold bending.

6.6.3 Material Model Properties

To best represent the material behaviour of the test specimens within the FEM, the actual material stress-strain response of the pipes that was obtained from the tension coupon tests was employed for input into the material model. The Modulus of Elasticity for the material model was obtained from the initial linear region of the coupon tests, and a value of 0.3 was selected for the Poisson's ratio. The proportional limit of the specimen stress-strain curves was used to represent the stress corresponding to the onset of plasticity in the material. The determination of these variables was previously discussed in Chapter 3.

During the coupon testing, the dynamic effects of loading were included in the initial stress-strain response of the coupon tests. However, as the pipe was statically loaded in the FEM, the material dynamic response will over predict the strength of the modelled pipe. It is for this reason that the static stress-strain curve of the coupon material, as determined in Chapter 3, was used for input into ABAQUS. During the tension coupon tests, the data acquisition system was programmed to write data every few seconds. This resulted in hundreds of data points that provided unnecessary detail to the stress-strain response. In addition, these points included the minor discontinuities that occur during testing which can cause convergence problems during solving of the model. For these reasons only

select points from the stress-strain output of the coupon tests, that adequately represented the smooth behaviour of the coupon material, was used to define the material model.

The engineering stress during the coupon tests was calculated as the MTS load divided by the original cross-sectional area of the specimen, and the engineering strain was calculated by dividing the elongation of the specimen by the original gauge length. For input into ABAQUS, a true stress – true strain curve is required for the material property definition. A comparison of the engineering stress–strain curve to the true stress–strain curve for the SNAM2 material is presented in Figure 6.4.

During coupon testing, the cross-sectional area of the specimen decreases as the load increases, thus the engineering stress does not represent the actual stress in the specimen. The true stress may be calculated by dividing the load by the cross-sectional area of the deformed specimen, as presented in Equation 6.1. In this equation the cross-sectional area of the deformed specimen was determined by assuming that the volume of the specimen remains constant, and recognizing that, as there is an increase in length due to the applied load there will be a proportional decrease in cross-sectional area. In addition, during tension testing the gauge length of the specimen increases as the strain increases. This successive increase in gauge length with elongation is accounted for when determining the true strain of the specimen as demonstrated in Equation 6.2. To determine the plastic component of the true strain in the pipe material, the elastic strain was subtracted from the true strain when within the plastic region of the stress-strain curve.

$$\sigma_{true} = \sigma_{nom} (1 + \epsilon_{nom}) \quad (6.1)$$

$$\epsilon_{ln}^{pl} = \ln(1 + \epsilon_{nom}) - \frac{\sigma_{true}}{E} \quad (6.2)$$

Where σ_{true} is the true stress, σ_{nom} and ϵ_{nom} are the engineering stress and strain respectively, ϵ_{ln}^{pl} is the plastic component of the true strain, and E is the Modulus of Elasticity of the material.

6.7 Loading Procedure

The first step in loading the pressurized specimens was to apply the internal pressure. The pressure was applied to the pipe, collars, and endplates simultaneously. The magnitude of this applied pressure was the same that was applied to the specimens near the time of buckling during the tests. The application of the internal pressure on the pipe and collars caused tensile membrane stresses on the shell elements in the circumferential direction. The application of the internal pressure on the end plates generated tensile forces on the pipe in the longitudinal direction.

The next loading step was the simultaneous application of the moment and axial load to the model. This was accomplished by applying a longitudinal direction compressive displacement at the bottom of the moment arm that had its longitudinal boundary condition specified as free. As the pin on the opposite end of the specimen had its longitudinal direction degree of freedom specified as fixed, the reaction load at the opposite end of the pipe was equivalent to the resulting load at the loading pin. As the moment arms were specified as the same length at each end, the moments at each end of the model were nearly equivalent throughout loading.

Displacement control was employed to define the longitudinal direction load that was applied at the loading pin. In order to accommodate the large displacements experienced by the specimens during testing, it was necessary to

model the prescribed displacement at the loading pin as a velocity type displacement. Thus the magnitude of the total longitudinal displacement at the loading pin was defined as an angular velocity, and the increment of the prescribed displacement was calculated by ABAQUS as the magnitude of this angular velocity multiplied by the time increment. This displacement was applied as a step function, where the displacement in the model remained constant for the full duration of each time step. The magnitude of the displacement at each time step was increased non-linearly, and the ABAQUS solution scheme automatically optimized the magnitude of each displacement increment. The number of time steps was specified to adequately determine the post buckling response of the specimens. During reduction of the FEM output, it was required to double the magnitude of the applied force and moment in the model for comparison with the behaviour of the experimental tests. This was required because only half of the pipe was modelled in the out of plane direction, thus the load capacity of the model was half of that of a full sized pipe.

6.8 Solution Strategy

In order to solve for the stresses and strains in the model that were induced by the applied loads, it was required to first solve for the nodal displacements. ABAQUS incorporated a full Newton and modified Newton-Raphson solution technique to solve for the nodal displacements of this model. As a full discussion of these solution methods is beyond the scope of this report, they will only be briefly summarized in this section. A full explanation of these solution procedures may be found in several resources such as Bathe, 1996 and Rao, 2005.

The basic equation of equilibrium used to solve for the displacements in a nonlinear analysis at time $t+\Delta t$ is presented in Equation 6.3, where ${}^{t+\Delta t} \mathbf{R}$ is the applied external nodal load vector, and ${}^{t+\Delta t} \mathbf{F}$ is the internal nodal point force

vector. This latter vector is evaluated at time $t+\Delta t$ using the principle of virtual displacements. As the internal forces are nonlinearly dependant on the displacements of the nodes, it is necessary to determine this vector iteratively until the specified convergence criteria is achieved. Equations 6.4 to 6.7 are used to evaluate the internal force vector at iteration $i=1,2,3, \dots$

$${}^{t+\Delta t} \mathbf{R} - {}^{t+\Delta t} \mathbf{F} = 0 \quad (6.3)$$

$$\Delta \mathbf{R}^{(i-1)} = {}^{t+\Delta t} \mathbf{R} - {}^{t+\Delta t} \mathbf{F}^{(i-1)} \quad (6.4)$$

$${}^{t+\Delta t} \mathbf{K}^{(i-1)} \Delta \mathbf{U}^{(i)} = \Delta \mathbf{R}^{(i-1)} \quad (6.5)$$

$${}^{t+\Delta t} \mathbf{U}^{(i)} = {}^{t+\Delta t} \mathbf{U}^{(i-1)} + \Delta \mathbf{U}^{(i)} \quad (6.6)$$

with

$${}^{t+\Delta t} \mathbf{U}^{(0)} = {}^t \mathbf{U}; \quad {}^{t+\Delta t} \mathbf{F}^{(0)} = {}^t \mathbf{F} \quad (6.7)$$

To calculate the solution for the displacements, the response of the FEM is linearized about the conditions at time $t+\Delta t$ and iteration $(i-1)$. In each iteration the out-of-balance load vector is calculated using Equation 6.4, and this vector is then used to determine the increment in displacements by substituting it into Equation 6.5. The iterations are continued until the out-of-balance load vector $\Delta \mathbf{R}^{(i-1)}$ or the displacement increment $\Delta \mathbf{U}^{(i)}$ become sufficiently small (Bathe, 1996).

The difference between the full Newton and modified Newton-Raphson solution strategies lies in the frequency of the calculation of the tangent stiffness matrix ${}^{t+\Delta t} \mathbf{K}^{(i-1)}$. In the full Newton method a new tangent stiffness matrix is calculated at every iteration within a time step, while in the modified Newton-Raphson method the tangent stiffness matrix is updated only at the beginning of the time step. This difference considerably affects the computation time for the model because the calculation of the tangent stiffness matrix is generally the most computationally expensive procedure during a finite element analysis. Thus the modified Newton-Raphson method involves fewer stiffness reformations than the full Newton iteration, where the stiffness matrix update is based on an accepted

equilibrium condition (Rao, 2005). As an insufficiently accurate tangent stiffness matrix will cause a divergence in the solution, ABAQUS incorporates an automatic procedure that selects which solution method to apply to the model in order to optimize its computation time while still satisfying the convergence criteria.

6.9 Initial Geometry of Model

In order to accurately simulate the moment curvature response of the test specimens, the initial overall geometry of the model must be as similar to the actual specimen geometry as possible. These geometric properties are composed of the diameter, wall thickness, end angles, initial vertical deflection, horizontal length, bend segment length, and straight segment length. Verification of the initial geometry of the model is obtained if the initial linear portion of the moment–curvature curve of the model demonstrates a similar slope to that displayed by the test results.

The wall thickness that was used in the model was the average wall thickness that was measured around the circumference of the ends of test specimens. As the specimen wall thinning/thickening effects due to cold bending were relatively minor as demonstrated in Table 4.1, they were consequently ignored in the model. The diameter used in the model was the average of all of the eight diameter measurements taken for each specimen. The ovalization of the specimen due to cold bending was neglected because the ovalization was less than 3% for all of the specimens, and introducing this parameter to the models would unnecessarily complicate the node mapping of the model. The horizontal length of the model was determined using the tape measurements acquired during the initial measurements of the pipe.

The initial end angles of the model were established using the specimen end slopes that were determined during initial imperfection measuring. The average of the two end angles was applied to each end of the model, resulting in the end angle at both ends of the model being equal. The initial vertical deflection profile was determined from the vertical cable transducer measurements obtained during initial imperfection measuring. It was assumed that the maximum initial vertical deflection was positioned at the precise middle of the model length.

In order to ensure that the vertical profile of the model closely correlated with that of the pipe, the straight and bend segment lengths of the model were determined from the horizontal length, maximum vertical deflection, and initial end angle measurements. The first step was to use these three measurements to calculate the horizontal component of the straight portion length at the ends of the model. Once this was determined, the horizontal length of the bend segment could be calculated. It was assumed that the straight segment length was equal at both ends of the model. After this, the Radius of Curvature of the model was calculated using the horizontal length of the bend segment and the initial end angle. This was required to establish the centreline length of the bent segment of the model.

Knowing the radius of curvature and bend segment length allowed for the vertical profile of the model to be established. Attempts were made to replicate the kinks in the pipe that were generated during cold bending, and it was observed that this resulting geometry significantly deviated from that of the actual specimen. Thus the bend segment of the model was generated as a smooth curve that spanned between the two straight segments. It is demonstrated in Figure 6.5 that the vertical profile of the model is extremely similar to that of the test specimens. This comparison validates the simplifications made when assuming that the end angles of the model were equal, and that the maximum vertical deflection occurred at the precise middle of the model.

6.10 Initial Imperfections of Model

The initial imperfections present in a high diameter to thickness ratio pipe cause a considerable reduction to its critical strain limit, and must therefore be included in the FEM in order to accurately replicate its buckling behaviour. During the initial imperfection measurements for the cold bend pipes it became revealed that the initial imperfections follow a fairly regular pattern. That is, the radius of the pipe along the intrados increases and decreases at relatively consistent magnitudes, and the distances between the peaks and valleys of these radius measurements are somewhat even. This behaviour occurs because the cold bend is generated as a series of evenly spaced kinks, and the pipe wall is restrained in the radial direction during cold bending by the mandrel and die of the cold bending machine.

As presented in Section 4.3.2.2, the average amplitude and period of the initial imperfections were determined for every cold bend specimen. The average amplitude of the initial imperfections was determined by calculating the radial direction difference between each local maximum to its adjacent local minimums, determining the average of these differences along the entire length of pipe, and dividing by a factor of two. The average period was determined as the average horizontal distance between adjacent local maximums, and adjacent local minimums, over the entire length of the pipe. The average amplitude and average period of the initial imperfections of the test specimens were employed to define the arrangement of the initial imperfections for the FEM.

Because of the regular configuration of the initial imperfection of the specimens, the initial imperfections distribution over the bend segment of the FEM could be defined as a cosine function. Therefore the radius of the model along its compressive line was varied with the distribution as defined by Equation 6.8. Using this distribution resulted in the magnitude of the initial imperfection varying by the average imperfection amplitude of the specimen, with the local

maximums and minimums being spaced at intervals of the average imperfection period. A local maximum was positioned at the precise middle of the model with this initial imperfection distribution. Figure 6.6 demonstrates the comparison of the initial imperfections along the compression line of the model with the imperfection measurements obtained at the 0 degree position of the IMD.

$$r_{imp} = r + A_0 \cdot \cos\left(\pi \cdot \frac{R \cdot (\theta_{Bend} - \theta_{end})}{T}\right) \quad (6.8)$$

Where r_{imp} is the radius of the bend compression line of the model including imperfections, r is the average radius of the specimen, A_0 is the average amplitude of the imperfections of the specimen, T is the average period of the imperfections of the specimen, R is the Radius of Curvature of the bend segment, θ_{Bend} is the relative angle of the position along the bend with respect to the end of the model, and θ_{end} is the end angle of the model.

It was also necessary to determine the initial imperfection distribution in the circumferential direction of the FEM. The period of the initial imperfections was specified as constant around the circumference of the model, similar to what was demonstrated by the test specimens. It was observed that the magnitude of the imperfections for the majority of the specimens was negligible along the neutral axis, and for this reason the amplitude of the imperfections for the model was input as zero at 90 degrees to either side of the compression line. The average amplitude of the initial imperfections 45 degrees from the compression line were determined for all of the specimens as previously discussed in Section 4.3.2.2, and this value represented the amplitude of the imperfections at this same position for the model. Thus with these two points, in addition to the imperfection magnitude at the compression line, it was possible to model the imperfections around the circumference of the model with a curve.

The sine curve as presented in Equation 6.9 in combination with Equation 6.10 was utilized to establish the imperfection distribution at all nodes around the circumference of the bent segment of the model. In this equation it is demonstrated that the imperfection magnitude is maximum at the compression line, and gradually decreases as the neutral axis is approached. Initial imperfections were not applied to the tension side of the model because the local buckling due to cold bending is predominantly caused by compressive strains. The distribution of the imperfections around the circumference of the model is presented in Figure 6.7.

$$r_{\theta} = r + (r_0 - r) \cdot \sin\left(\frac{\pi}{2} \cdot \left(\frac{90 - \theta}{90}\right)^n\right) \quad (6.9)$$

$$n = \frac{\log\left[\frac{2}{\pi} \cdot \sin^{-1}\left(\frac{A_{45}}{A_0}\right)\right]}{\log\left(\frac{45}{90}\right)} \quad (6.10)$$

Where r_{θ} is the radius of the model at the angle θ in the circumferential direction from the compression line, r is the average radius of the specimen, r_0 is the radius of the model at the compression line, A_0 is the average imperfection amplitude of the specimen at the compression line, and A_{45} is the average imperfection amplitude of the specimen 45 degrees from the compression line.

Up until this point the model has been perfectly symmetrical in the longitudinal direction, which was not the case for the test specimens. Previous research has demonstrated that a longitudinally symmetrical model may demonstrate a different buckling mode from that of an asymmetrical model (Dorey, *et al*, 2001). This was verified in this research program where during the FEA, multiple buckles formed at the peak load for several of the models. This behaviour did not occur for the test specimens where only one buckle developed for all of the pipes. In addition, the formation of multiple buckles considerably

strengthened the post-buckling capacity of the model in comparison to that of the test specimens. There are various methods to discourage multiple buckling in an FEM such as thinning the pipe wall or introducing a transverse load at a specific location of the model. In order to introduce asymmetry to this FEM, the imperfections were modeled over only 75% of the length of the bend portion, beginning from one end. This modelling technique did not appreciably affect the load deformation behaviour of the model because all of the models buckled in the region where the initial imperfections were included.

6.11 Initial Imperfection Sensitivity Analysis

As there was considerable variation in the magnitude of the initial imperfections along the length of the pipes, and the imperfection amplitude was assumed to be constant for the model, a sensitivity analysis was required in order to assess the sensitivity of the model buckling behaviour to the assumed imperfection amplitude. A sensitivity analysis was not completed on the period of the imperfections because the scatter in the period of the imperfections along the specimen lengths was relatively low, and it was decided that the imperfection period would not significantly affect the buckling behaviour of the models.

In order to determine the initial imperfections for the sensitivity analysis, the first step was to tabulate the amplitude of every imperfection along the length of the specimen. Then, the distribution of the imperfection amplitude along the compression line was plotted as shown in Figure 6.8. Subsequently, the magnitudes of the imperfection amplitude corresponding to the 10th and 90th percentile of this distribution were determined. That is, the imperfection amplitude that was at the bottom 10% of the measured amplitudes, and amplitude that was at the top 10% of the measured amplitudes were established. These two values could subsequently be input into the FEM to ascertain the effects of either

small or large magnitude initial imperfections on the buckling behaviour of the model. To determine the circumferential distribution of the imperfections for this sensitivity analysis, the imperfection amplitudes at the 10th and 90th percentiles were tabulated for the 45 and 315-degree locations of the test specimens as well. These values were then used to define the imperfection amplitude around the circumference of the model, for the small and large initial imperfections respectively.

The initial imperfections for the model were then modified from using the average imperfection amplitude at the 0 and 45 deg positions of the specimens, to using the amplitudes at the 10th percentile which demonstrated the effects of having very small imperfections on the pipe, and to using the amplitudes at the 90th percentile which demonstrated the effects of having very large imperfections on the pipe. This process was repeated for each of the models for which imperfection measurements were available. The moment curvature response for the models with imperfections at the 10th, 50th, and 90th percentiles were subsequently compared in order to assess whether incorporating the average imperfection amplitude for the model was an acceptable method of modelling the moment curvature response of a cold bent specimen.

6.11.1 Imperfection Sensitivity Analysis Results

In order to assess the sensitivity of the FEM to the magnitude of the initial imperfections, the variation in both load and deformation at buckling with respect to imperfection amplitude were studied. The moment curvature response of the models was selected for this purpose because the global deformation behaviour is the most descriptive plot to analyse for this parametric study. The results of this study will subsequently be used to assess whether the average imperfection amplitude of the specimens may be used to define the initial imperfection

distribution for the model, or if more complicated method for modeling the imperfections is required.

The imperfection amplitudes at the 10th, 50th, and 90th percentiles for the compression line of all the specimens are presented in Table 6.1. The variation in global curvature at buckling, with respect to global curvature at buckling for the model with 50th percentile imperfections, are also presented in this table for the models with small and big imperfections. The sensitivity of the peak moment to varying imperfection amplitudes is also presented. Figure 6.9 demonstrates the moment curvature comparison with varying imperfection amplitudes for the SNAM2 specimen. From Table 6.1 it is demonstrated that there was considerable range in the amplitude of imperfections throughout the specimen lengths. Moreover, the global moment and curvature at buckling are greater for the models with small imperfections in comparison with the models with average imperfection amplitudes. Accordingly, the critical moment and curvature for the models with large imperfections were always lower than the model with average imperfection amplitudes.

The results of the imperfection amplitude parametric study demonstrate that the moment curvature response of the model is not overly sensitive to the amplitude of the initial imperfections. The average percent difference with varying imperfection amplitudes for the critical global curvature is 5%, with a maximum percent difference of 13%. The average percent difference for the maximum moment is 1.2%, with a maximum percent difference of 4%. As these values may be considered to be within engineering tolerance for a finite element model, assuming the imperfections in the model demonstrate the average amplitude of the test specimens is considered an acceptable assumption for this FEM.

6.12 Mesh Study

In order to understand the effect of the mesh size and distribution on the behaviour of the FEM, a mesh study was completed. Three different meshes were considered for this sensitivity analysis. The first mesh consisted of a coarse mesh for the outside region of the model, a fine mesh for the middle region, and a transition zone between the coarse and fine mesh. The second mesh considered consisted of a fine mesh in the middle region of the model and a coarser mesh for the outside sections. The final mesh considered consisted of a uniform fine mesh. A comparison of the moment curvature response of the models with the three different meshes was compared with the test results in order to achieve a suitable balance between accuracy and computer processing time for the model. A summary of the three different meshes studied, including the length of each region and the corresponding element sizes, is provided in Table 6.2.

Development of the mesh distributions was somewhat complicated due to the different geometries of each of the specimens, as well as the complexities involved with the incorporation of the initial imperfections. All specimens had different bend segment lengths and straight segment lengths, because of the different bend angles and centreline lengths of the pipes. These two different segments were modelled separately in the model to accommodate the node mapping features that are available in ABAQUS. It was extremely desirable to have a single model that could be used for each of the specimens because it would be quite time consuming to repeatedly modify the mesh distributions for each individual specimen. It is for this reason that the number of elements in the straight segment was maintained constant for each model, and the number of elements in the bent segment was also constant for each of the modelled specimens. As the bend and straight segment lengths varied between the different models, but the number of elements was constant for each region, the element lengths in each region varied for each modelled specimen.

When creating the initial model, it was desirable to limit the element length to a reasonable value when considering computer processor time, and it was desired to maintain an aspect ratio of between 1 and 2 in the elements. The circumferential element length was selected to be a comparable magnitude to that implemented in previous pipe models created at the U of A. The longitudinal element length became a subjective and iterative procedure, where the number of elements per zone was first selected, and then the resulting element length and aspect ratio was checked for each of the seven bent pipe models. After each of the models demonstrated a reasonable element length and aspect ratio for each of the zones, the iterations were discontinued. For the collars, it was possible to maintain the same element length for all of the models because they were modelled as 300 mm long for each of the specimens.

The incorporation of the initial imperfections proved to be a very difficult factor during the determination of the FEM mesh. As previously discussed, the initial imperfections followed a cosine function distribution, with a period that was determined from the measured imperfections of the specimen. It is essential to have a peak in the imperfection profile at the very centre of the model, as an imperfection at this position would likely provide the worst-case scenario for the initiation of buckling when determining the critical buckling strain. In addition, in order to capture the peaks of the imperfection cosine distribution, there must be nodes positioned at intervals of exactly one period length away from the middle, as shown in Figure 6.10. This is necessary because the amplitude of the imperfection is a function of distance from the middle of the model, and the imperfection amplitude would be reduced if the nodes were positioned so that the peak amplitudes were not captured. This occurrence would be unrepresentative of the actual imperfection distribution of the cold bend specimens.

In order to implement the peaks and valleys into the imperfection distribution, the node spacing of the fine mesh, transition, and coarse mesh was adjusted so that their respective spacing would be integrally divisible by the

period length. This allowed for the positioning of nodes at the maximum and minimums of the imperfection distribution, for every period over every region. Modifying the zone lengths caused the number of nodes per each cosine wave to vary from model to model because the number of elements was constant for each zone for each model, but the number of periods of imperfections was variable. In order to employ an integral number of periods in the coarse mesh region, the extreme outside of this mesh did not contain initial imperfections. This region was very short for all of the models in comparison with the overall length of the bend segments.

6.12.1 Mesh Study Results

For the first mesh considered the bent segment featured a fine mesh, a coarse mesh, and a transition zone between the fine and coarse meshes. There was a uniform node spacing applied over the straight segments for this mesh distribution. The results of the models with these meshes did not generate very good agreement with the experimental results. This occurred predominantly because at the peak moment, buckling was often initiated at the boundary of the fine and transition mesh zones in the model. This indicates that the abrupt change in element length at this location was triggering local buckling, which does not reflect the true behaviour of the test specimens. For this reason the transition zone was removed from subsequent mesh studies.

The second mesh studied contained a fine mesh, a coarse mesh, and a straight portion mesh, with no a transition zones. The length of the fine mesh was increased for this model in comparison to the model that included a transition zone. The moment curvature response of this model was improved over that of the previously model, predominantly because this model contained considerable more total nodes. However, double buckling at the interface of the fine and

coarse meshes occurred for several of the modelled specimens. As this is not representative of the experimental results, further mesh refinement was required.

Thus the final mesh analysed demonstrated a uniform fine mesh over the bent segment, and a uniform coarser mesh over the straight segment. The element length for both segments in the circumferential direction was 19 mm and 25 mm for the NPS 24 and NPS 30 specimens respectively. The longitudinal node spacing for the bent segment ranged from 28 to 32 mm with an average length of 30 mm for the seven modelled specimens. The longitudinal nodal spacing for the straight portion varied from 15 to 48 mm, with an average length of 31 mm for the different models. Although this mesh contained considerable more nodes than the previously discussed meshes, there was generally good agreement with the behaviour of the test specimens, and all of the models demonstrated a single buckle at the middle third of its length. In addition, the duration of computational time was quite reasonable with this mesh, depending on the level of output requested. It is for these reasons that this mesh distribution, as shown in Figure 6.11, was selected to generate the results from the FEA that will be discussed in Chapter 7.

Table 6.1 Summary of Initial Imperfection Sensitivity Analysis

| Specimen | Amp ¹ 50 th Perc- entile (mm) | Amp 10 th Perc- entile (mm) | Amp 90 th Perc- entile (mm) | ϕ_{crit} 10 th % | ϕ_{crit} 90 th % | Mom _{crit} 10 th % | Mom _{crit} 90 th % |
|----------|---|--|--|--|--|--|--|
| | | | | Diff ² | Diff | Diff ³ | Diff |
| SNAM2 | 0.97 | 0.73 | 1.31 | 1.1 | -0.8 | 0.3 | -0.9 |
| SNAM3 | 1.23 | 0.39 | 1.54 | 12.7 | -0.6 | 3.5 | -0.5 |
| TG1 | 0.360 | 0.155 | 0.635 | 5.3 | -11.9 | 0.8 | -2.8 |
| TG2 | 0.326 | 0.160 | 0.530 | 13.1 | -5.5 | 1.6 | -1.4 |
| TCPL1 | 0.348 | 0.105 | 0.755 | 12.3 | -4.7 | 1.5 | -1.1 |
| TCPL2 | 0.364 | 0.140 | 0.640 | 0.2 | -0.9 | 0.6 | -0.5 |
| TCPL3 | 0.326 | 0.090 | 0.740 | 0.3 | 1.4 | 0.5 | -1.3 |

¹ The amplitudes are the average, 10th percentile, and 90th percentile initial imperfections.

² The ϕ_{crit} % diff is the percent difference of the critical global curvature with respect to the critical curvature using the average imperfection amplitude.

³ The Mom_{crit} % diff is the percent difference of the critical moment with respect to the critical moment using the average imperfection amplitude.

Table 6.2 Summary of Different FEM Meshes Analyzed

| | Segment Length Per Side of Pipe (mm) | Element Length - Longitudinal Direction (mm) | Element Length - Circumferential Direction (mm) |
|------------------|--|---|--|
| Mesh 1 | | | |
| Collar | 300 | 150 | 49 |
| Straight Segment | 574 | 115 | 49 |
| Coarse Bend | 1271 | 51 | 49 |
| Transition | 1027 | 51 | 25 |
| Fine Bend | 514 | 34 | 25 |
| Mesh 2 | | | |
| Collar | 300 | 150 | 49 |
| Straight Segment | 574 | 115 | 49 |
| Coarse Bend | 1579 | 51 | 25 |
| Fine Bend | 1233 | 34 | 25 |
| Mesh 3 | | | |
| Collar | 300 | 38 | 25 |
| Straight Segment | 574 | 48 | 25 |
| Fine Bend | 2812 | 28 | 25 |

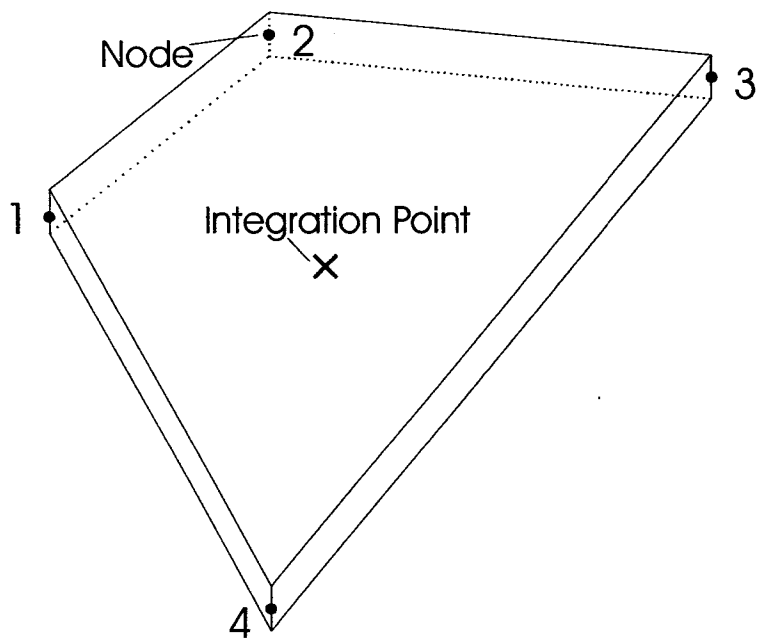


Figure 6.1 – S4R Element

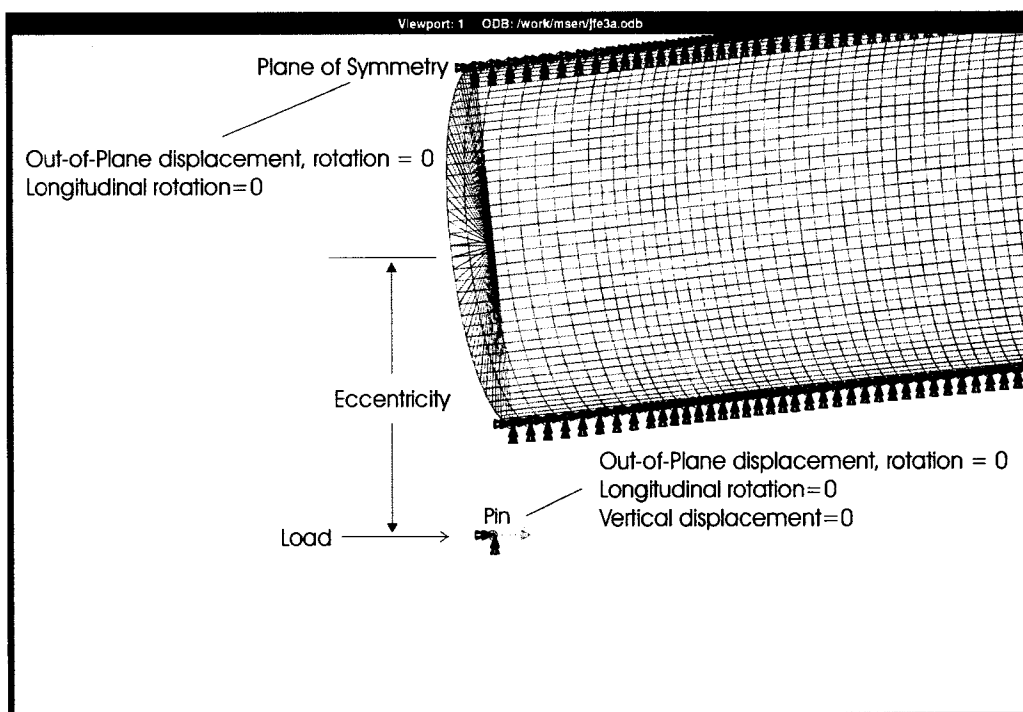


Figure 6.2 – Boundary Conditions of FEM

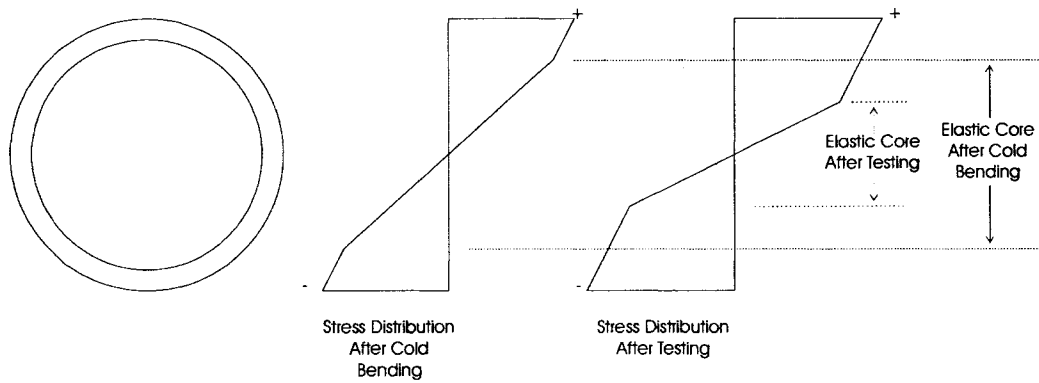


Figure 6.3 – Elastic Core Depth after Cold Bending and Testing

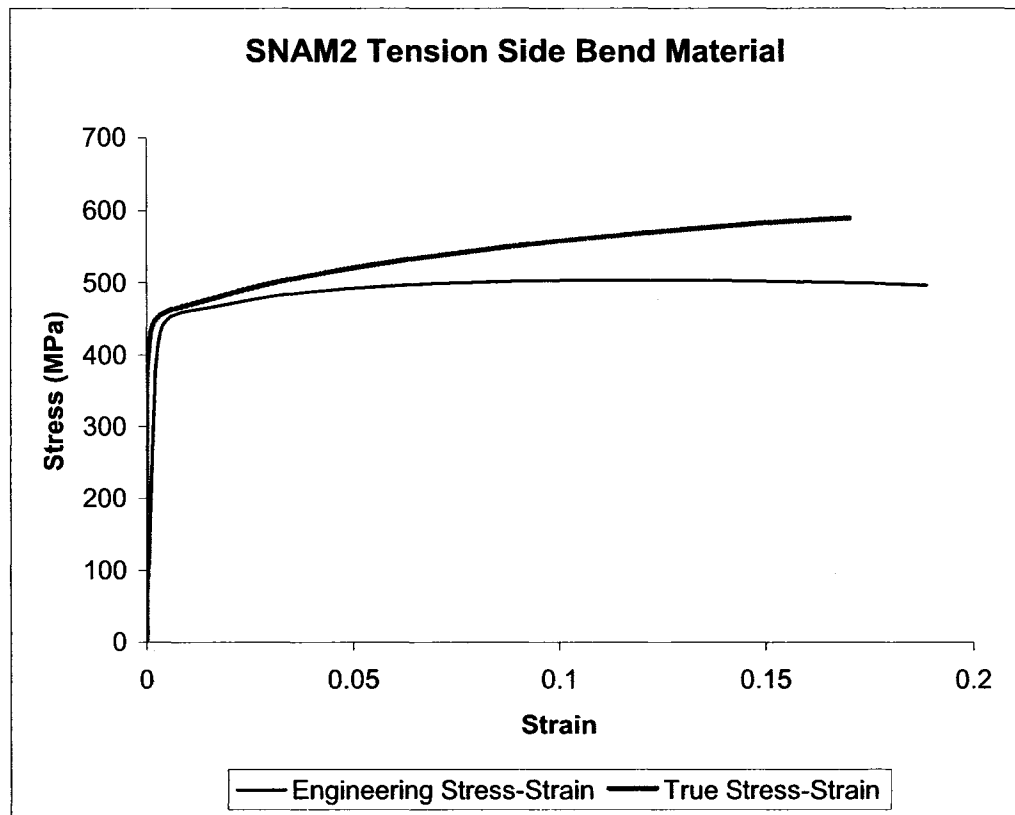


Figure 6.4 – Comparison of Coupon Result and Model Stress Strain Curves

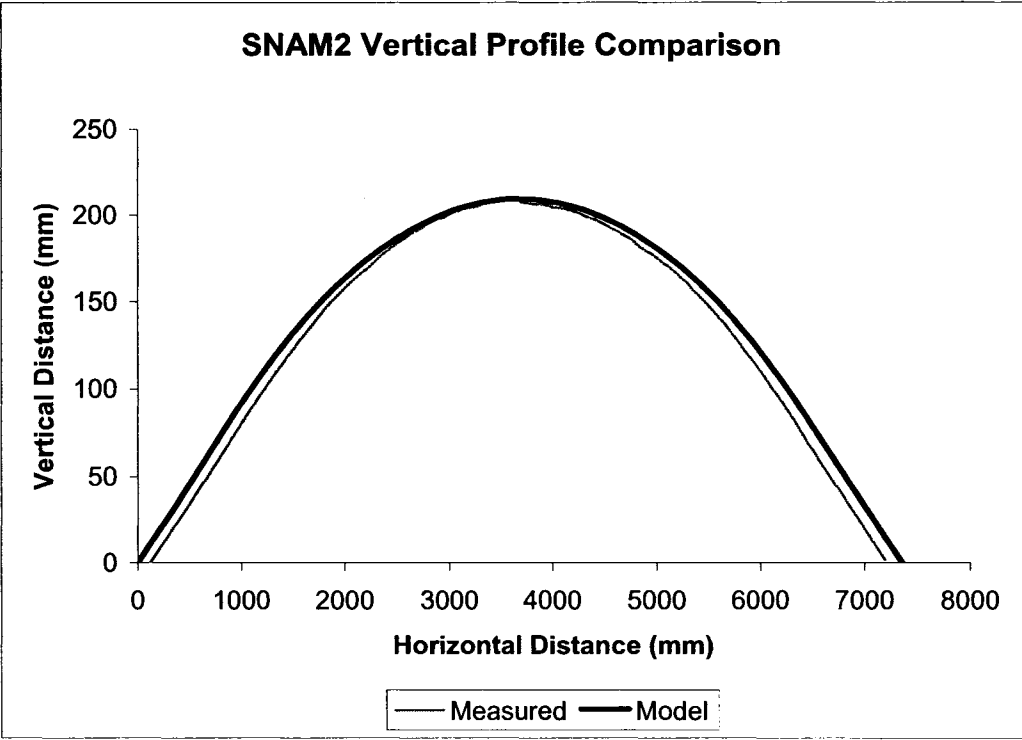


Figure 6.5 – Comparison of Model and Measured Initial Geometry

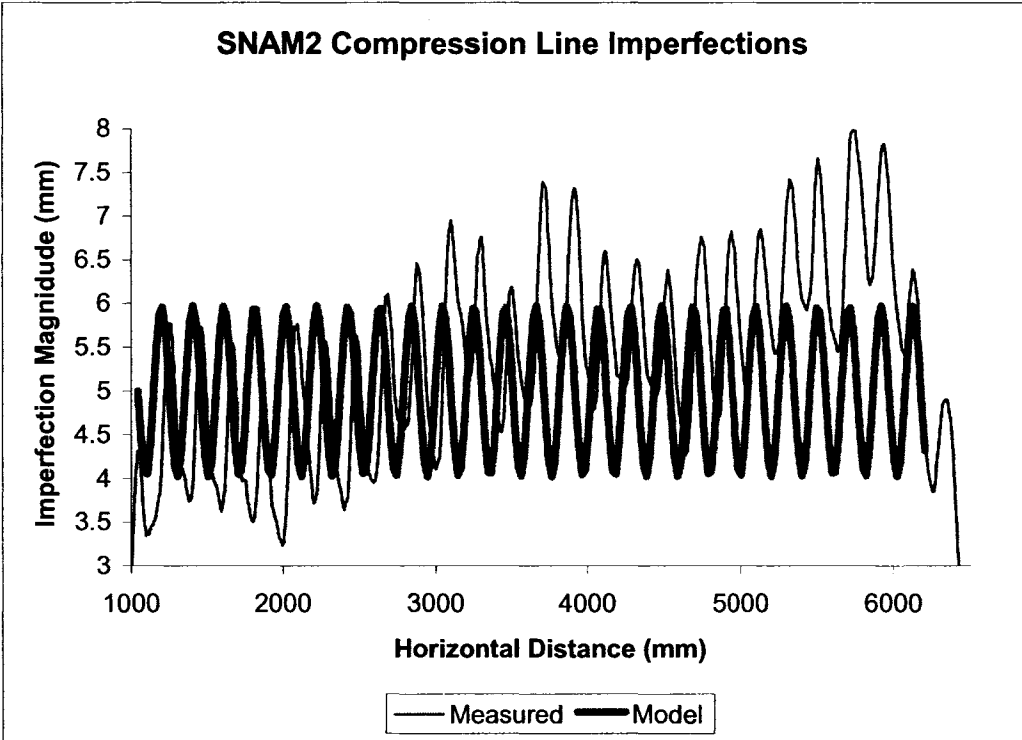


Figure 6.6 – Comparison of Longitudinal Direction Initial Imperfections

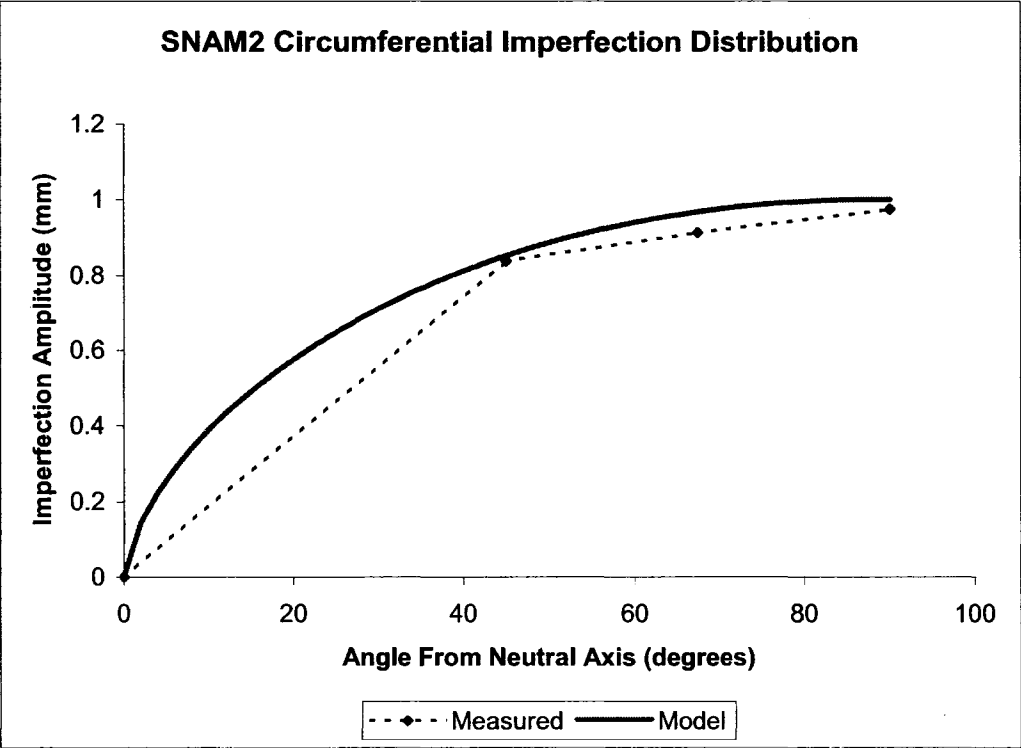


Figure 6.7 – Comparison of Circumferential Direction Imperfections

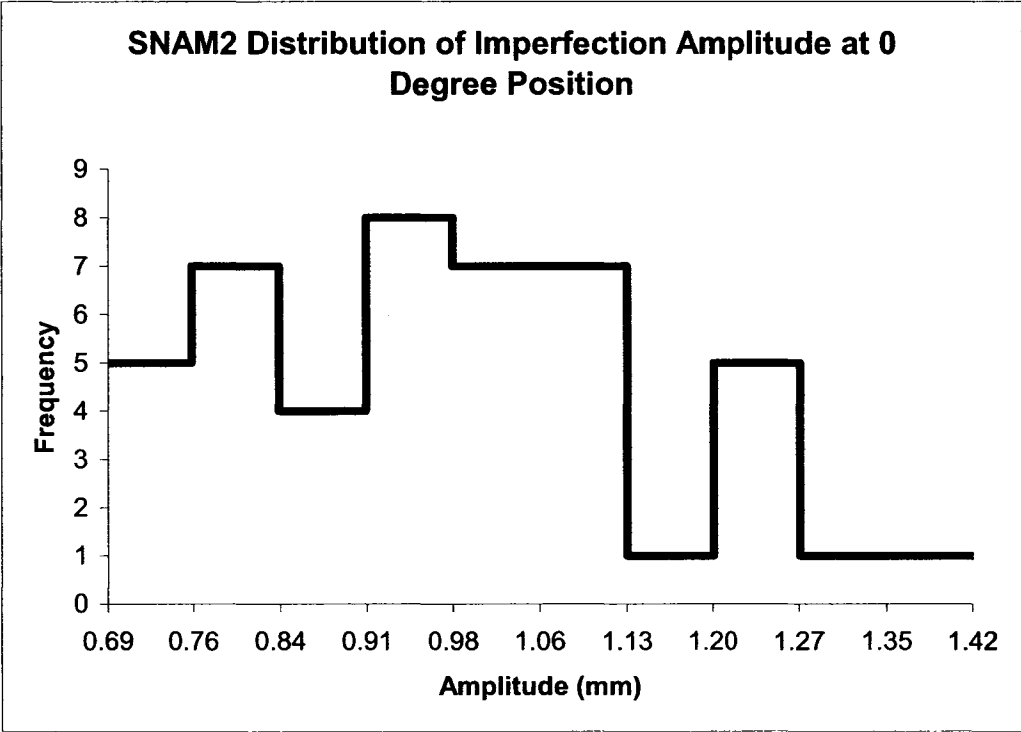


Figure 6.8 – SNAM2 Imperfection Amplitude Distribution

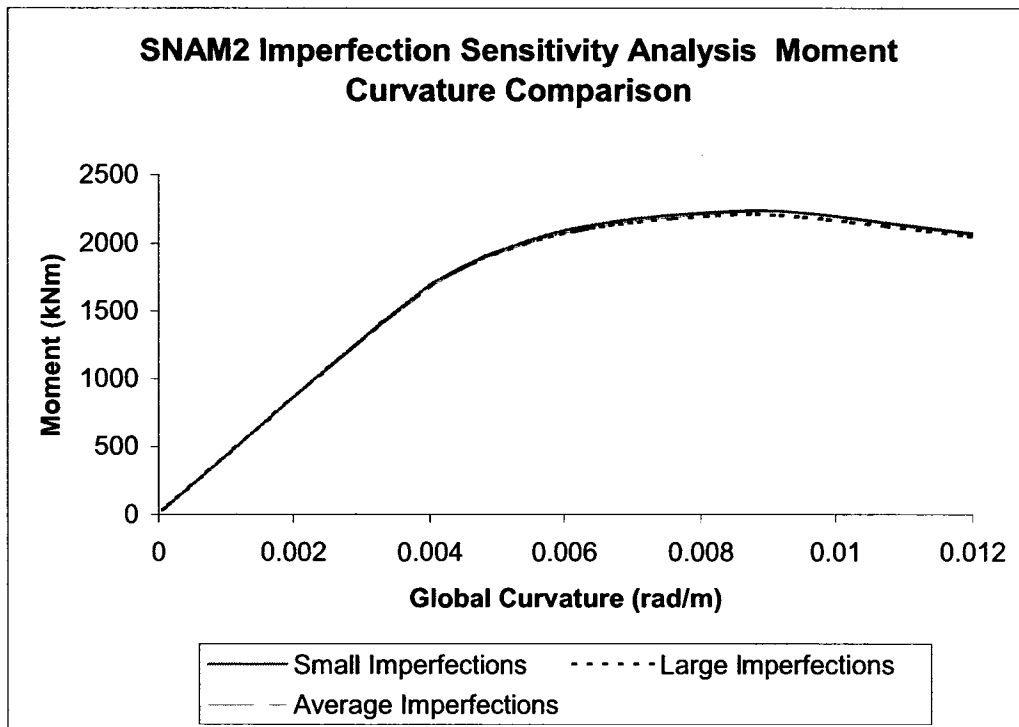


Figure 6.9 – Moment Curvature Curves with Varying Imperfection Amplitudes

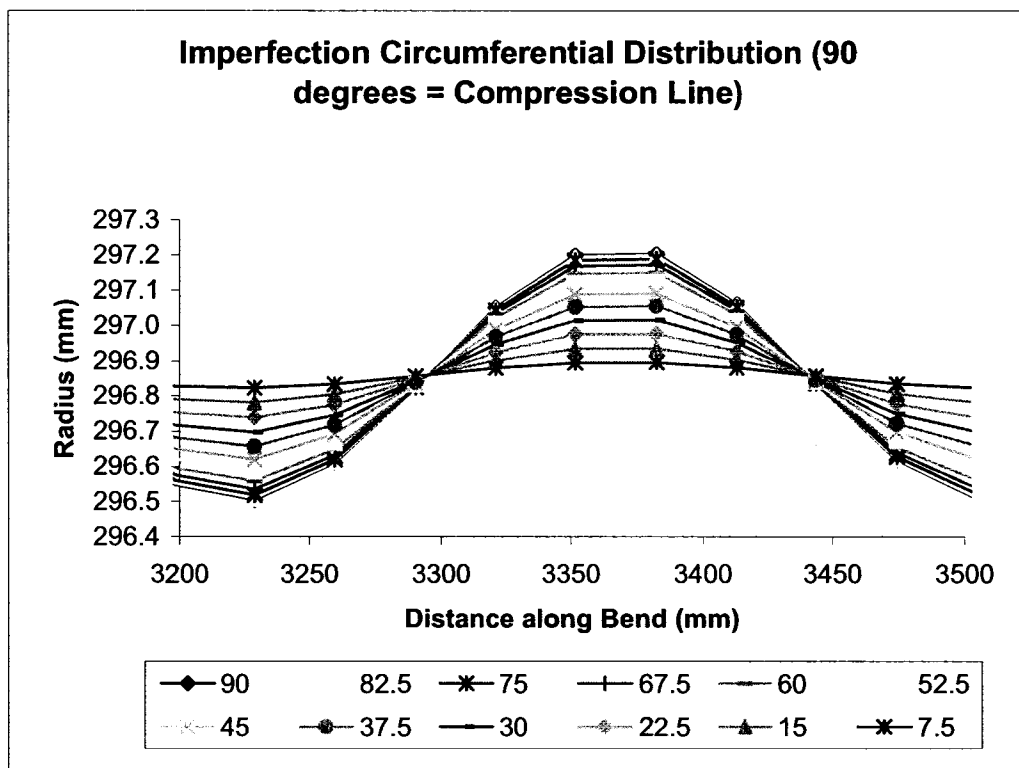


Figure 6.10 – Node Distribution Along Imperfections

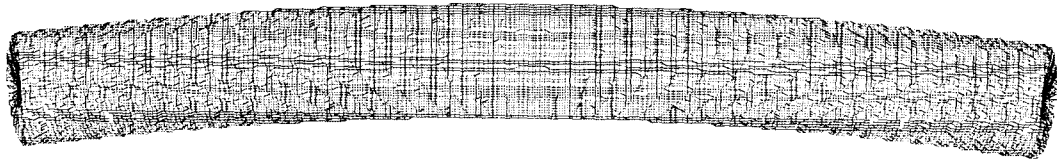


Figure 6.11 – Mesh Distribution of FEM

7.0 FEA RESULTS AND PARAMETRIC STUDY

This first part of this chapter will contain a discussion on the results obtained from the finite element analysis. The moment curvature-behaviour, moment-buckle strain response, curvature-buckle strain response, and critical strain of the models will be compared to the results from the experimental tests in order to verify the predictive capability of the FEM. The validation of the model in this chapter will be subdivided into comparisons of each of the three different specimen set model and test results. Only the percent difference between the models and test results will be presented herein, and the numbers on the scales of the test and model comparison figures have been removed. This will not affect any of the objectives of this research program, as the presentation of absolute values is not necessary in order to validate the FEM. The numerical values for the model results are available in Pipeline Technology Report No. 2005-1. This chapter will begin with a discussion of procedures employed during the reduction of the FEM output.

The second part of this chapter will present the details of an alternative model that was created at the U of A, in parallel to the model that was presented in Chapter 6. This alternate model included the residual stresses that are induced during cold bending. A comparison of the cold bend FEM with the FEM presented in Chapter 6 will be presented in order to discuss the effects of residual stresses on the behaviour of a cold bend pipe. Only the percent difference between this model and the model developed in Chapter 6 will be presented in this report, the absolute values for the results from this alternative model are available in Pipeline Technology Report No. 2005-1.

The final section of this chapter will present a description of the parametric study that was conducted for this research. The variables included in the parametric study were the pipe: diameter to thickness ratio, internal pressure,

material grade, imperfection size, and bending degree per diameter length. A comprehensive discussion of the effects of each of these variables on the global and local response of the model will be studied in order to better understand the behaviour of cold bend pipes under combined loads.

7.1 Reduction of FEA Output

The equations used to calculate the global moment and curvature of the model differed from those for the tests that were previously presented in Section 4.4. This is because the loading conditions of the FEM were slightly different from that of test setup, as shown in Figure 7.1. In addition, the method for determining the strain at the buckle was very different for the model and test. The equations used to determine these three parameters for the model will be presented herein.

7.1.1 Model Global Curvature

The hinges of the test setup were excluded from the FEM in order to reduce unnecessary elements, as unlike for the test setup, they are not required to facilitate the rotation of the moment arms. Thus the equation derived to calculate the global curvature for the model is simpler than that of the test that was previously presented in Equation 4.11, as the horizontal component of the hinge is not applicable to the global curvature of the model. Accordingly, the equation used to calculate the global curvature of the model is presented in Equation 7.1.

$$\phi_{Model} = \frac{\vartheta_r - \vartheta_l}{L_{0Model} + 2 \cdot e_{Model} \cdot \sin \vartheta_{Model} - \Delta_{Pin}} \quad (7.1)$$

Where ϕ_{Model} is the global curvature of the model, θ_L and θ_R is the rotation of the model left and right ends respectively, L_{0Model} is its original horizontal length, e_{Model} is the initial eccentricity provided by its moment arms, and Δ_{Pin} is the longitudinal movement of the model pin at each time step.

7.1.2 Model Maximum Moment

For the purpose of simplicity, the moment arms in the model were precisely vertical, while those in the test setup demonstrated an angle to the vertical that was the same as the specimen. Consequently it is not necessary to determine the vertical component of the moment arm, as was necessary for the testing program, to calculate the eccentricity of the model to the load. In addition, the vertical component of the hinge did not need to be accounted for when determining the initial eccentricity of the load to the model. The equation for calculating the moment in the model is presented in Equation 7.2. In this equation, it is apparent that the load at the pin is multiplied by a factor of two. This is because only half of the pipe was modeled in the circumferential direction, thus the moment capacity of the model would otherwise be one half of that of the test specimen.

$$M_{Model} = 2 \cdot R_{Pin} \cdot [e_{Model} \cdot \cos \vartheta_{Model} + L_{v0Model} + L_{vMiddle}] \quad (7.2)$$

Where M_{Model} is the second order moment of the model at the middle of its length, θ_{Model} is the average angle of the ends of the model at each time step, e_{Model} is the initial distance from the pin to the centreline of the model at the end, $L_{v0Model}$ is the initial vertical deflection of the model, and $L_{vMiddle}$ is the vertical deflection of the middle of the model at each time step.

7.1.3 Model Buckle Strain

It was a relatively complicated procedure to determine the strain at the buckle of the model for comparison with the demec strains measured during the experimental testing. As the demec strains are determined by measuring the distance between two points throughout testing, and comparing them to the initial distance between the points, a similar procedure was required to determine the strains in the model. To facilitate the procedure, the coordinates of the nodes on the compression line of the model, over the middle region, were outputted at every load step. Then during post-processing, the node corresponding to the middle of the buckle was determined. This allowed the determination of the nodes that were positioned at one half of the diameter away from either side of the buckle. The strain at the buckle throughout loading was hence determined by calculating the distance between these two nodes, and comparing it to their initial spacing. This was accomplished by using Equation 7.3 in combination with Equations 7.4 and 7.5 as presented below.

$$\varepsilon_{buckle} = \frac{d_0 - d_t}{d_0} \quad (7.3)$$

$$d^0 = \sqrt{(x_1^0 - x_2^0)^2 + (y_1^0 - y_2^0)^2 + (z_1^0 - z_2^0)^2} \quad (7.4)$$

$$d^t = \sqrt{(x_1^t - x_2^t)^2 + (y_1^t - y_2^t)^2 + (z_1^t - z_2^t)^2} \quad (7.5)$$

Where ε_{buckle} is the strain at the buckle of the model over a gauge length of one diameter, d^0 is the initial distance between two points located one half diameter to each side of the buckle, d^t is the distance at time step t between each of these points, x_1 and x_2 are the longitudinal position of the points that are left and right of the model respectively, y_1 and y_2 are the out-of-plane position of the points that are left and right of the model respectively, z_1 and z_2 are the vertical position of the points that are left and right of the model respectively, the superscript 0 denotes the initial positions, and superscript t denotes the position at time step t .

7.2 Comparison of FEM and Test Results

The results from the FEA output in comparison with the test results will be discussed in this section. The global behaviour of each model will be validated by the moment-curvature curve comparison between the test and model. As previously discussed in Chapter 4, the global curvature of the test specimens was calculated from the demec strains when comparing the linear region of the moment curvature curves, while the global curvature of the test specimens was based on the rotation meters when comparing the inelastic region of these curves. The local behaviour of the models will be verified by both the moment and global curvature vs. buckle strain comparisons with the tests. These curves will be overlaid in the same plots herein in order to save space, where *test_name* curvature represents the global curvature vs. buckle strain results, and *test_name* moment represents the moment vs. buckle strain results. The critical strain of the models was determined using both the maximum moment and bilinear methods for the determination of critical strain. A summary of the model results is provided in Table 7.1

The validation of both the global and local behaviour of the model will be based on the percent difference between the model and test results. The equation to determine this percent difference for the parameter being compared is demonstrated in Equation 7.6.

$$\%Difference = 100 \cdot \frac{(x_{model} - x_{test})}{x_{test}} \quad (7.6)$$

Where the x is the parameter being compared, subscript *test* indicates the value of x as determined from the experimental test, and subscript *model* indicates the value of x as outputted by the model.

All of the models buckled within their middle third, similar to the behaviour demonstrated during the tests. More importantly, the buckling modes observed during testing were captured for both the pressurized and unpressurized models. All of the pressurized models buckled with a bulge shaped buckle, and both unpressurized models buckled with a diamond shaped buckle. A comparison of the pressurized model and test buckles is shown in Figure 7.2, while the unpressurized model and test buckles are compared in Figure 7.3. In addition to the buckling mode, the post-buckling behaviour of the models was very similar to that demonstrated during the tests for the majority of the moment curvature comparisons.

7.2.1 SNAM Model Results

The overall shape of the moment-curvature curves for the three SNAM models compared favourably with the test results. As demonstrated in Figures 7.4, 7.6, and 7.8, the initial slopes of all three model and tests were nearly collinear in these curves. The peak moments for the SNAM1 and SNAM2 models were 7% less than those of the tests, while the peak moment of the unpressurized model was 1% greater than that of the SNAM3 test. The global curvature corresponding to the peak moment (critical curvature) for the SNAM1 model over predicted that of the test by 37%. The models under predicted the critical curvatures of the SNAM2 and SNAM3 tests by 12 and 8% respectively. The large error in the SNAM1 critical curvature may have occurred because it was required to implement an assumed imperfection at the middle of the model, as the initial imperfections were not measured for this specimen.

The post buckling global behaviours of the SNAM1 and SNAM2 models were very similar to those demonstrated during the tests. However, the model of the SNAM3 specimen demonstrated a more gradual decrease in moment capacity

immediately after buckling than was observed during testing. This behaviour occurred because the stabilize function from the ABAQUS loading library was required in the model in order to obtain convergence during the FEA. This function applied an artificial stiffness to the model when it became excessively unstable for convergence, and the ABAQUS default value for this stiffness was implemented to the model. This artificial stiffness functioned to increase the moment capacity of the model immediately after buckling. As shown in Figure 7.8, the moment curvature curves of the SNAM3 model and test eventually converged within the post-buckling region.

The moment vs. buckle strain behavior of the three SNAM models compared reasonably with the test results, as shown in Figures 7.5, 7.7 and 7.9. The initial linear responses of the moment vs. buckle strain curves were nearly collinear with the tests for all three models. All three models over predicted the strain corresponding to the peak moment. The model over predicted the maximum moment critical strain of the tests by 11%, 5%, and 56% for SNAM1, SNAM2, and SNAM3 respectively. The magnitudes of these over predictions were less than 0.3%, which are relatively minor from an engineering tolerance perspective. The post buckling response at the buckle for the SNAM3 model behaved somewhat softer than that of the test specimen primarily because of the artificial stiffness that ABAQUS assigned to the pipe immediately after buckling.

For the pressurized specimens the overall shape of the global curvature vs. buckle strain curves shown in Figures 7.5 and 7.7 was relatively similar, although the magnitude of the curvature over the inelastic region for the test was generally greater than that of the models. For the unpressurized model the shape of this curve in Figure 7.9 compared favourably with the test results, although the unpressurized model demonstrated a parabolic behaviour over the inelastic region, while the test demonstrated a bilinear behaviour. This difference in behaviour is primarily due to the artificial stiffness that was applied to the SNAM3 model immediately after buckling. The critical strain using the bilinear method

compared reasonably with the test results for these models. The percent differences between the model and test bilinear critical strains were 8, 6, and 45% for SNAM1, SNAM2, and SNAM3 respectively. The magnitude of the difference between test and model critical strains was less than 0.2% for the three models, which is relatively small.

7.2.2 TG Model Results

The moment curvature curves of the TG models in comparison to the tests are shown in Figures 7.10 and 7.12. It is demonstrated that the initial slopes in these figures were similar for the model and the test results when the test global curvature was calculated from the demec strains. The peak moments of the models were within 9% of those observed during the tests. The critical curvatures of the models were 11 and 16% lower than those of the tests for TG1 and TG2 respectively. This information demonstrates that the FEM captured the buckling behaviour of these tests. There was also good agreement between the post buckling global responses of these models and tests.

The response of the moment vs. buckle strain compared agreeably for the models in comparison to the test specimens, as shown in Figures 7.13 and 7.15. The slope of this curve was nearly the same as that of the tests for both the initial and post buckling regions, for both of the models. The model over predicted the strain corresponding the peak moment by 2 and 23% for TG1 and TG2 respectively. The behaviour of this curve near the peak moment was extremely flat for both models, which caused a considerable degree of sensitivity when determining the critical strain of these specimens using the maximum moment method.

Similar to the pressurized SNAM model results, the shape of the TG model and test global curvature vs. buckle strain curves were very similar, although the magnitudes of the curvatures over the inelastic regions were greater for the tests than the models. The percent difference of the bilinear method critical strains between the model and tests were 41 and 17% for TG1 and TG2 respectively. The magnitude of the difference in bilinear critical strain between the test and models was less than 0.2% for the TG specimens. The primary reason for the increased percent error from the bilinear critical strain comparisons, to the maximum moment critical strain comparisons, is due to the discrepancy between the initial stiffness of the tests and models when the global curvature was based on the rotation meter measurements.

7.2.3 TCPL Model Results

The initial slopes of the moment curvature curves for the TCPL models closely compared with the test results when the global curvature is based on the demec strains, as shown in Figures 7.14, 7.16, and 7.18. The peak moments of the models were between 2 to 9% lower than the test peak moments. The critical curvatures were between 15 to 30% lower for these models than the tests. This sizeable error suggests that the deformation at buckling becomes difficult for this model to predict as the diameter to thickness ratio of the pipe increases, and this notion will be further discussed in the following section. The models generally reproduced the post buckling global behaviour of the three pipes.

The slope of both the initial and post buckling regions of the moment vs. buckle strain curves shown in Figures 7.15, 7.17, and 7.19 were similar for the TCPL models and test specimens. The model under predicted the strain corresponding to the peak moment by 29% for TCPL1, and over predicted this value by 79 and 37% for TCPL2 and TCPL3 respectively. The magnitude of the

difference in maximum moment critical strain between the models and tests was less than 0.5% for all the TCPL specimens. This information suggests that the model does a fair job of predicting the overall buckle strain behaviour of these specimens, but demonstrates difficulty in predicting the critical strain. One possible source of this error may be from the absence of the residual stresses caused by cold bending for this model. This variable may become more dominant for high diameter to thickness ratio pipes, as the model reasonably predicted the critical strain for the SNAM and TG specimens.

The shape of the global curvature vs. buckle strain response of the TCPL1 and TCPL2 specimens compared favourably with the test results, although the test demonstrated higher global curvatures than the model over the inelastic regions. The unpressurized model was able to capture the bilinear post bucking response observed in this curve for the TCPL2 test. The TCPL3 test and model curves compared favourably at the lower strains, and then the slopes slightly diverged over the larger strains. The bilinear method critical strain percent difference for the test the models were 46, 80, and 60% for TCPL1, TCPL2, and TCPL3 respectively. The magnitude of these differences was always less than 0.7%.

7.3 Discussion of Model Results

The comparison of the model and test moment curvature responses has demonstrated that the model is adequate in simulating the global behaviour of a cold bend pipe. The slope of the initial region of the moment curvature curves was similar to that of the test specimens for all of the models when the test global curvature was based on the demec strains. This behaviour validates the cross-sectional geometry, vertical profile, and loading system that were incorporated in the models. When the buckling modes of the models were examined, a bulge buckle was generated for all of the pressurized models, and the unpressurized

models demonstrated a diamond mode buckle. These failure modes were the same as those observed during testing. The average percent difference between the peak moment of the eight model and tests results was 7%. The average percent difference between the model and test critical global curvatures was 19%. This information establishes that the model may be used to predict the global behaviour of the test specimens to within engineering tolerance.

The model was also able to reasonably simulate the local behaviour of the test specimens. The linear response of the moment vs. buckle strain curves was nearly collinear for all of the models and tests. Also, the slope of the post-buckling regions of these curves demonstrated excellent correlation. This indicates that the overall behaviour of the local deformation of the buckle has been reproduced by the FEM. The average percent difference between the test and model maximum moment critical strains were 18% and 66% for the pressurized and unpressurized specimens respectively. This demonstrates that the model is sufficiently capable of predicting the critical strain of pressurized cold bend pipes, but exhibits difficulty when predicting the critical strain of unpressurized cold bend pipes. Conversely, it must be noted that the magnitude of the difference in critical strain for the unpressurized tests and their respective models was always less than 0.3%. As this magnitude is relatively small and difficult to measure under field conditions, the predictive capabilities of the local behaviour for the model may be considered satisfactory for design purposes.

The global curvature vs. buckle strain relationship of the model exhibited limited correlation to that from the test results. The initial slope of these curves for the model and test were similar for all of the models, although the strain at the onset of inelasticity of the model was somewhat lower than that of the test for the majority of the specimens. In addition, the global curvature at similar values of strain over the inelastic region was greater for the test than the model for nearly all of the specimens. The average percent difference between the model and test bilinear critical strains was 30 and 63% for the pressurized and unpressurized

models respectively. As the magnitude of the difference between the unpressurized test and model critical strains was always less than 0.3% for both unpressurized specimens, the model may be considered fair in predicting the bilinear critical strain of cold bend pipes.

As summarized in Table 7.1, the model demonstrated difficulties in predicting the deformation at buckling for the unpressurized specimens, and to a lesser extent that for the high diameter to thickness ratio specimens. As presented in Chapter 6, the majority of the parameters affecting the critical strain of cold bend pipes have been reasonably incorporated in to this model, herein called the Test-Bend (T-B) Model. These variables include the residual strains, initial imperfections, and changes in the material properties of the pipe that are generated by the cold bending machine. The factors caused by cold bending that have not been included in the model are the ovalization, wall thinning, and residual stresses. The measurement results that were previously presented in Chapter 4 revealed that the extent of ovalization and wall thinning are relatively minor for the test specimens studied in this research program. Therefore it may be that the absence of residual stresses in this FEM is a major source of the errors exhibited in the local deformation of the more sensitive specimens. To address this condition, another FEM was created in parallel to this model at the University of Alberta in order to determine the effects of residual stresses on the behavior of the cold bend pipe model.

7.4 Supplementary Straight-Bend Model

A straight-bend model was created in parallel to the test bend model that was previously presented in Chapter 4. The straight bend model pipe (S-B model) was developed as initially straight, was next cold bent, and subsequently loaded under the conditions provided by the test setup of this research program.

Substantial effort was required to model the cold bending of the pipe, as the bending procedure the pipe experiences in the cold bending machine is unnecessarily complicated and exceedingly computationally expensive to simulate in an FEA. For this reason innovative measures were employed to allow for the major effects of cold bending to become incorporated into the S-B model, while preventing the local buckling of the pipe wall. The details of the development of this model are discussed in the 7th International Pipeline Conference Proceedings, September 29-October 3, 2005, Calgary, Alberta, Canada. The main features of final configuration of this model will be presented herein. A comparison of the behaviour of the S-B model in comparison to the T-B model will be presented in Section 7.4.4.

7.4.1 S-B Model Description

In order to conserve computer-processing time, only half of the pipe in the circumferential direction was modelled. The entire length of the specimen was modelled, and this length was divided into three segments: the collars, straight segments, and bend segment. A uniform node spacing that generated a fine mesh over the entire length of pipe was applied to the model. The longitudinal length of the elements was the diameter / 30 and the circumferential length was the circumference / 100. Consequentially, the aspect ratio of the elements was nearly one.

Type S4R elements were used to define the pipe elements, and STRI3 elements simulated the endplates of the test setup. The test specimen wall thickness represented the thickness of the pipe elements, while the collars and endplates were modelled as 18 and 75 mm thick respectively. All of the material in the model was specified as isotropic with a Poisson's ratio of 0.3. The collar and end plate material was defined as perfectly elastic. The stress-strain

behaviour for the pipe model was based on the specimen tested end coupons elasto-plastic response. This material represented the virgin material properties of the test specimen.

In order to replicate the moment arms of the test setup, loading and reaction pins were implemented 600 mm below the centreline of the model, at each of the ends. The boundary conditions applied to the nodes along the tension and compression lines of the model, along with the loading and reaction pins, enforced out-of-plane symmetry to those nodes. Additionally, the loading pin was restrained from vertical direction movement, while the reaction pin was restrained from moment in both the vertical and longitudinal directions. The nodes at the each end of the pipe were connected to their respective pins with rigid beams elements.

7.4.2 Preventing Local Buckling During Cold Bending

Two different techniques were employed to prevent local buckling during cold bending of the model. The first of these measures was to provide radial direction links to connect all of the elements at each cross-section in the model. This restrained the radial displacement of the nodes along the compression line of the model to that of the nodes along the tension line. The second measure employed to prevent local buckling was to provide a thick elastic sleeve to the entire length of pipe. This significantly increased the stiffness of the pipe wall in all directions. The implementation of these strengthening elements simulated the effects of the mandrel and die within the cold bending machine.

To strengthen the pipe wall against radial direction displacement, a node was first created at the centre of the pipe at each nodal cross-section. The nodes at each model cross-section were subsequently connected to their respective

centre node with type B31 beam elements from the ABAQUS element library. This is a two-node linear beam element that demonstrates six degrees of freedom. These radial links were specified as circular with a radius of 20 mm, exhibited a Modulus of Elasticity of 210 GPa, and a Modulus of Rigidity of 80 GPa. The function of these links was to strengthen the pipe wall located near the compression line against the radial displacement that occurs during local buckling, by connecting them to the elements near the neutral axis and tension side of the pipe.

To further strengthen the pipe wall against local buckling during cold bending, additional nodes were created at the same positions of those nodes originally along the pipe wall. These additional nodes were connected with elements that were isotropic and only behaved elastically, and their movements were constrained to that of their corresponding original nodes along the pipe. These additional sleeve elements demonstrated the same Modulus of Elasticity as that of the pipe, and their thicknesses were twice that of the pipe. The elastic sleeve was subsequently divided into different sections along the length of the pipe that could be added or removed during different load steps. This measure was necessary in order facilitate bending of the pipe, as plastic deformation of the pipe wall would only occur in the pipe wall elements that are not enclosed by the sleeve.

7.4.3 Cold Bending of S-B Model

The cold bending of the S-B model was comprised of 12 steps. The features of these steps are presented below, and are summarized in Figure 7.20.

1. Apply internal pressure of 10% SMYS hoop stress to the pipe in order to stabilize the solution.

2. Remove even sleeve elements.
3. Apply in-plane rotation to each end of the pipe. The magnitude of this rotation is approximately half of the desired final central bend angle. Its precise value is determined on a trial and error basis, as the total rotation of the pipe during loading consists of both the elastic and plastic deformation.
4. Remove end applied rotations. The plastic deformation caused by the application of the loads will remain in the pipe.
5. Add the even sleeve elements.
6. Remove the odd sleeve elements.
7. Apply in-plane rotation to the ends of the pipes again. This magnitude of this rotation will be the similar to that applied in Step 3.
8. Remove the end rotations. The pipe will now demonstrate the desired bend geometry.
9. Add the odd sleeve elements.
10. Remove all of the sleeve elements
11. Remove the radial cross-sectional links.
12. Remove the internal pressure. The model will now represent that of an empty cold bend pipe without any increased strengthening elements.

7.4.4 Loading of Cold Bend S-B Model

The final procedure in the S-B model was to determine the behaviour the cold bend model under combined internal pressure, axial load, and bending loads. The first step in loading the pipe was to pressurize the pipe and endplates to the internal pressure experienced by the pipe during testing. Subsequently, longitudinal displacement was applied to the loading pin. The magnitude of this displacement was sufficient to cause local buckling of the pipe wall, was well as to determine the models post buckling behaviour.

7.4.5 Comparison of S-B and T-B Model Results

The analysis of the S-B model is extremely complicated and time consuming. This is predominantly because of the numerous iterations required to determine the applied end rotations, in combination with the multiple runs required to bend the pipe and then load it. The analysis of the T-B model was relatively simple and computationally inexpensive. As the primary difference between the models was the residual stresses from cold bending were incorporated into the S-B model and were neglected for the T-B model, the sensitivity of the global and local behaviour of the model to this parameter could be understood by comparing the results from the two models.

A comparison of the moment curvature response of the S-B and T-B models is presented in Figure 7.21 for the SNAM2, TG2, and TCPL2 models. The comparison of the SNAM2 models generally demonstrated strong correlation. The peak moment for the SNAM2 T-B model was 8% less than that of the S-B model, and the global curvature corresponding to the peak moment was 13% less for the T-B model than that of the S-B model. It is also demonstrated in Figure 7.21 that the overall shape of the TG2 curves are very similar. The maximum moment of the TG2 T-B model was 2% less than that of the S-B model. Also, these curves are nearly coincidental up until the maximum moment of the T-B model is achieved. The global curvature corresponding to the peak moment of the TG2 T-B model was 16% less than that of the S-B model. In comparing the unpressurized TCPL models, it is demonstrated that the overall shape of these curves are very similar. The peak moment of the TCPL2 T-B model was 8% less than that of the S-B model, and the global curvature corresponding to the peak moment for this T-B model was 6% greater than that of the S-B model. The difference between the T-B model and the S-B model peak moment and global curvatures are provided in Table 7.2 for the SNAM2, TG2, and TCPL2 models.

In summary, the overall load deformation behaviour of the S-B and T-B models was extremely similar. Based on these results, the residual stresses due to cold bending act to increase the moment capacity of the pipes. They also increase the global deformation prior to buckling for pressurized pipes, and decrease the global deformation prior to buckling for unpressurized pipes. The peak moment and global curvature corresponding to the peak moment are very similar for both models.

7.5 Parametric Study of Test Specimens

One of the goals of this research program was to study the sensitivity of the deformational behaviour of cold bend pipes to their various parameters. This will allow for better comparison of the behaviour of cold bend pipes under field conditions to those in this testing program, as well as possibly assist in improving efficiency during the design of line pipe. Direct comparison of the influence on changing geometric, material, and loading parameters of the specimens was not possible through the experimental program because the number of required tests would become impractical. Through the use of an FEM, the effects of changing variables may be studied with far less effort than through full-scale testing. It has been shown in Section 7.2 that the T-B model demonstrates adequate predictive capabilities of both the global and local load-deformation behaviour of cold bend pipes. Additionally, it has been shown in Section 7.4 that the behaviour of this model only slightly deviates from that of the S-B model. Since the T-B model is much simpler to employ and significantly less computationally expensive than the S-B model, it will predominantly be employed to conduct this parametric study.

The moment and global curvature in the models of the parametric study were determined using the equations described in Section 7.1. The sensitivity of the global response of the models to the varying parameters will consequently be

determined by comparing their moment vs. curvature relationships. The relationship between the investigated parameters to the maximum moment will also be compared to Equation 1.4, which is the plastic moment capacity predictive equation for straight pipes that was used to predict the maximum moment of the test specimens. This will allow for the assessment of the difference in the sensitivity of the plastic moment for cold bend pipes to each parameter, in comparison to that for straight pipes.

Both the maximum moment and bilinear methods presented in Section 4.5 were used to determine the critical strain of all of the models. The critical strains from both methods are plotted against the parameters studied for all of the models when comparing the local behaviour of the models. The relationship between the studied parameters and critical strain will also be compared to the behaviour described by Equation 1.5, which is the critical strain predictive equation for a straight pipe with a rounded stress-strain curve. This will allow for the evaluation of the difference between the critical strain sensitivity to varying parameters for cold bend pipes, in comparison to that for straight pipes.

7.4.1 Investigated Parameters

There were several different parameters that influence the behaviour of the test specimens. These variables included the pipe:

1. Diameter
2. Wall Thickness
3. Material Grade
4. Internal Pressure
5. Imperfection Amplitude
6. Imperfection Period

7. Bending Degree/Diameter Length
8. Central Bend Angle
9. Initial Vertical Deflection
10. Horizontal Length

In order to reduce the number of models in the study, some of the above variables may be combined or eliminated. The diameter/thickness ratio is a common geometric descriptor for line pipe, so these variables may be combined as a single factor. The period of the imperfections was similar for all of the same-diameter specimens; accordingly this variable will be eliminated from the study. Furthermore, as it is the local behaviour that predominantly affects the load and deformation at buckling, the model will behave relatively insensitively to varying horizontal length and central bend angle, consequently these parameters may also be eliminated. Hence, the remaining variables that will be investigated in this parametric study include the pipe:

1. Diameter/thickness ratio
2. Internal Pressure
3. Material Grade
4. Initial Imperfections
5. Bending Degree / Diameter Length

The boundaries of the model parameters will mainly be limited to those studied in the experimental program, as the T-B model has only been validated with the aforementioned pipes. The values for the different variables that are compared in the models are summarized in Table 7.4.

7.4.2 Constant Variables

The horizontal length for all of the models was maintained at a constant value of 7390 mm, which corresponds to the average horizontal length of the test specimens. Also, a central bend angle of 11 degrees, which was the average central bend angle of the test specimens, was selected to define the global curvature for all of the models. The loading system employed by the models was the same as that of the test setup previously presented in Section 5.8. In order to ensure similar axial load to maximum moment ratio during the analyses, the initial maximum vertical deflection for all of the models was also maintained constant. Consequently, the average maximum deflection of 210 mm for the test specimens was incorporated for this parameter for all of the models in the parametric study.

As the majority of the test specimens were NPS 30 pipes, a diameter of 762 mm was selected for all of the models. A constant diameter for the models ensures that the moment of inertias will be relatively similar, which will allow for better comparison of their plastic moment capacities. To limit the number of cases in the parametric study, the imperfection period was maintained constant for all of the models. The average period of the initial imperfections for the seven bent test specimens ranged from between 22 to 44% of the diameter in length. Accordingly, an imperfection period of 251 mm, which corresponds to the average period of 33% of the diameter of an NPS30 pipe, was incorporated into all of the models.

7.4.3 Standard Model

To conduct the parametric study, the results from modifying each specific experimental parameter will be assessed through direct comparison with the

behaviour of a standard T-B model. This standard model will exhibit the median values of the variables selected for the parametric study. Accordingly, the parameters in the models compared in Sections 7.4.4 to 7.4.8 will be identical except for a single variable, which will allow for direct study of the affect of each specific variable on the global and local deformational behaviour of the model. To quantify the influence of each variable on cold bend pipes, the peak moment, critical curvature, and critical strains of each subsequent model will be compared to that of the standard model. The properties of the standard model are accordingly described as:

1. Diameter/Thickness Ratio = 70.
2. Internal Pressure = 40% SMYS hoop stress
3. Material Grade = X65
4. Imperfection Amplitude = 0.6 mm
5. Bending Degree / Diameter Length = 1 Degree / Diameter

The methodology undertaken for studying the influence of these parameters on the deformation behaviour of cold bend pipes will be discussed over the remainder of this section, and a summary of the results of the parametric study is provided in Table 7.4.

7.4.4 Diameter/Thickness Ratio

Increasing the diameter to thickness ratio in line pipe is one of the foremost methods exercised to minimize material costs. However, the extent of the reduction in critical strain and moment capacity with increasing diameter to thickness ratio is relatively unknown for cold bend pipes, and will accordingly be studied herein. The diameter to thickness ratio for the TG, SNAM, and TCPL specimens was 44, 63, and 93 respectively. In order to directly assess the

sensitivity of the test specimens to varying diameter to thickness ratio, diameter to thickness ratios of 45 and 95 were incorporated for the models in the parametric study for comparison with the response of the standard model to combined loading.

As demonstrated in Figure 7.22, the diameter to thickness ratio of the models demonstrates a significant effect on the global behaviour of cold bend pipes. The maximum moment in the models always increased as the diameter to thickness ratio decreased. Also, the global curvature corresponding to the peak moment always increased with decreasing diameter to thickness ratio. Moreover, this relationship behaved in a somewhat exponential manner for the modelled geometries. This relationship agrees with the plastic moment capacity equation that was presented in Equation 1.4, where the plastic moment capacity is directly proportional to the Plastic Section Modulus of the pipe, which is accordingly a function of the pipe wall thickness to the fourth degree.

In Figure 7.23 it is demonstrated that the critical strain of the models also increased with decreasing diameter to thickness ratio. This relationship agrees with that of straight pipes as presented in Equation 1.5. The rate of increase of critical strain with decreasing diameter to thickness ratio is less than that for the peak moment capacity, for the three models compared in this parametric study.

7.4.5 Internal Pressure

The internal pressure of the models was varied in order to assess the consequences of varying internal pressure of cold bend pipes under field conditions. It is specified in CSA 7662-2000 that the maximum allowable hoop stress caused by internal pressure in a line pipe is 80% of the SMYS. As this also corresponded to the internal pressure for the TCPL1 and TCPL3 specimens, this

value served as the upper bound of the internal pressure for the parametric study. During shut downs the internal pressure in a cold bend may be reduced to zero, consequently the assessment of its critical strain is very important if there are compressive strains present on the pipe wall. For this reason a zero pressure loading condition will serve as the lower bound for the parametric study, and this accordingly corresponded to the empty pipe loading condition for the SNAM3 and TCPL2 specimens. The median internal pressure of 40% SMYS hoop stress for the standard model corresponded to that of the TG specimens during testing.

The relationship between internal pressure and moment capacity is relatively complex for cold bend pipes. It is demonstrated in Figure 7.24 that the peak moment of the unpressurized model was much less than that of the standard model. This agrees with the behaviour observed during the experimental tests, however contradicts the behaviour of straight pipes in Equation 1.4, where the plastic moment capacity decreases with increasing internal pressure. This inconsistency is likely because of the increased imperfection magnitude with corresponding decrease in period for cold bend pipes in comparison to straight pipes. If the outwards stabilizing effect of internal pressure is not present, these more severe imperfections in cold bends allow for increased second order moments on the pipe wall that initiate local buckling at lower compressive loads than for straight pipes. In contrast, the peak moment of the two pressurized models were relatively similar although the peak moment of the 80% SMYS hoop stress model was less than that of the pressurized model. This decrease in moment with increasing internal pressure agrees with the relationship described by Equation 1.4, where the moment capacity decreases with increasing internal pressure. Thus it may be inferred that the peak moment in comparison to the standard model is lowered if the failure mode is either a diamond mode buckle, or if the internal pressure is increased. For all of the models the global curvature corresponding to the maximum moment increased with increasing internal pressure.

Figure 7.25 demonstrates that the critical strain of the models increased with increasing internal pressure. This relationship behaved in an exponential manner, and the magnitude of the increase in critical strain with increasing internal pressure became quite sizeable when the zero pressure and 80% SMYS pressure model critical strains were compared. This relationship agrees with the behaviour of straight pipes as described by Equations 1.5, where the critical strain increased with increasing hoop stress to SMYS ratio.

7.4.6 Material Grade

Increasing the grade of steel in a line pipe allows for increasing the allowable internal pressure with constant geometry, however sizable costs and uncertainties are often associated with modern materials. The strengthened behaviour of cold bend pipes with increased material grade may assist in justifying these costs, and will henceforth be analyzed herein. The materials modeled for this parametric study will be limited to those exhibited by the test specimens, because the tension side bend material stress-strain curve is required for input into the model and this information is not readily available for any other materials. Also, the material grades included in this research program are currently commonly found in commercial line pipe. Accordingly, the three material grades that were examined in the parametric study were Grade X60, X65, and X80. The SNAM3, TCPL3, and TG1 tension side bend materials represented the stress strain behaviours of their respective grades of steel for this study. These coupons results were empirically considered representative of the other tensions side bend materials for their same material grades. The Modulus of Elasticity ranged between 193 to 213 GPa for the material models, and they all demonstrated a rounded stress-strain curve.

It is demonstrated in Figure 7.26 that the moment capacity of the models increased with increasing material SMYS. Moreover this relationship behaved nearly linearly, which agrees with the behaviour for straight pipes described in Equation 1.4, where the plastic moment capacity is directly proportional to the yield stress of the material. The global curvature corresponding to the maximum moment for the models generally increased with increasing material grade, although this global curvature was very similar for the X60 and X65 material models.

The effect of material grade on the critical strain of cold bend pipes is more difficult to assess than its effect on the global behaviour. As demonstrated in Figure 7.27, the critical strain of both the X60 and X80 models was greater than that of the X65 model, and moreover the X60 models critical strain was nearly equivalent to that of the X80 model. This contradicts the behaviour of the critical strain of straight pipes as specified in Equation 1.5, where the critical strain increases with increasing material grade. Hence to confirm the critical strain of the models, the X60 material model was reanalyzed using the SNAM2 tension side bend material properties, and the X80 model was reanalyzed using the TG2 tension side bend material properties. Both the X60 and X80 model results became relatively unchanged with these alternate stress-strain curves, verifying the results of the parametric study models. As the magnitude of the critical strain of all three models was within 0.15%, it is inferred that the critical strain of cold bend pipes is not overly sensitive to the grade the material.

7.4.7 Imperfection Amplitude

The magnitude of the initial imperfections that are caused by field bending is largely related to the bender's experience. Discussion with the field bender of the TCPL specimens emphasized the importance of positioning the mandrel

precisely beneath the die in the cold bending machine in order to minimize the magnitude of the ripples that are caused by cold bending. The criterion employed at this cold bending yard to limit the initial imperfections in a cold bend was achieved by resting a straight edge on two peaks of the imperfection ripples, and attempting to slide a dime between the pipe and straight edge anywhere between the two peaks. Consequently, if the dime is able to pass through the gap the cold bend is considered inadequate. This criterion is extremely empirical, and for this reason the response of the models to varying imperfection amplitude was previously examined in Section 5.5, and will be further studied herein for comparison with the standard model.

The imperfection measurements obtained by the IMD demonstrated that the minimum and maximum average imperfection amplitudes of the test specimens were approximately 0.3 and 1.3 mm respectively. Accordingly, these imperfection amplitudes will be modelled in the parametric study to determine their effect on the behaviour of the test specimens. The imperfection amplitude of 0.6 mm that was incorporated for the standard model was the average imperfection amplitude of the seven bend specimens. Also in order to examine the effects of very large imperfections, an imperfection amplitude of 1.8 mm, which corresponds to the maximum measured imperfection amplitude of all of the test specimens, will also be modelled. The imperfection amplitude at the 45-degree circumferential position of the test specimens averaged 70% of that at the compression line, consequently this ratio will be assigned for the imperfections at this position for the models in order to define their circumferential distribution.

It is demonstrated in Figure 7.28 that the maximum moment of the models always reduced with increasing imperfection amplitude. In addition, the global curvature corresponding to the peak moment always decreased with increasing amplitudes of imperfections. This parameter is not included plastic moment capacity derived by Mohareb, however the observed imperfection effect on the models global response is logical from an engineering judgement standpoint.

As shown in Figure 7.29, the critical strains of both the 0.3 and 1.8 mm initial imperfections models were greater than that of the standard model. This contradicts the behaviour of straight pipes presented in Equation 1.5, where the critical strain decreases with increasing imperfection magnitude. The magnitudes of the critical strains of the models in the parametric study were always within 0.14% of that of the standard model. This range is extremely small when considering that the largest modelled imperfection was six times that of the smallest modelled imperfection. This information, in combination with that of the sensitivity analysis described in Section 6.11, suggests that the critical strain of cold bend pipes is not very sensitive to the initial imperfection amplitude.

7.4.8 Bending Degree / Diameter Length

It was previously discussed in Chapter 1 that CSA Z662 –2003 limits the bending degree per interval length for cold bend pipes to 1.5 degrees per diameter. This was also the specified bending degree / interval length for the TCPL2 and TCPL3 test specimens. Consequently this value will represent the upper limit of the bending degree / interval length in the parametric study. Through finite element analysis it is possible to analytically assess the effects of any level of cold bending on the behaviour of line pipe under combined load. Accordingly, a straight pipe was selected to represent the lower bound of the bending degree / diameter length in the parametric study. A bending degree per diameter of length of 1.0 was selected as the intermediate bend degree / interval length that was inputted into the standard model. This was the lowest specified bend degree / diameter of the test specimens in the experimental program.

It is not possible to model the bending degree / diameter length with the T-B model, however it can be modelled using the S-B model. As it was previously

demonstrated in Section 7.3.5 that the behaviour of the two models are relatively similar, the latter model will be used to determine the effects of this parameter. A typical X65 pipe material was incorporated for this model because the S-B model requires the virgin material properties for the steel, and all of these models consisted of X65 material. Accordingly, the stress-strain curve for the S-B model demonstrated its proportional limit at 0.2% strain, its yield stress at 0.5% strain, and its ultimate stress at a strain of 12%. In order to modify the bending degree per diameter length during modelling, the sleeve length was maintained constant and the magnitude of the applied end rotation was adjusted during the cold bending load steps for the model. A blister shaped initial imperfection of 15% of the wall thickness over a length of 762 mm was incorporated as the initial imperfection for the straight specimen. Only the maximum moment critical strain was readily available from the output files for the S-B model.

The maximum moment and corresponding global curvature always both decreased as bending degree / diameter length increased. As shown in Figure 7.30, the decrease in maximum moment is minor, while the decrease in global curvature corresponding to the maximum moment is relatively significant. This decrease in critical curvature is greatest when comparing the straight model to the 1 degree / diameter bend model.

There was also a sizeable decrease in critical strain with increasing bending degree / diameter length, as shown in Figure 7.31. The critical strain of the straight model was 45% greater than that of the 1 degree / diameter bend model, and the critical strain of the 1.5 degree/diameter bend model was 16% less than that of the 1.0 degree / diameter bend model. This information demonstrates that the critical strain is very sensitive to the bending degree / interval length parameter.

7.5 Summary of FEA Results and Parametric Study

A comparison of the test results to the FEA using the model described in Chapter 6 was presented in the first portion of this Chapter. The model performed remarkably when simulating the initial stiffness and post-buckling region of the load-deformation responses both globally, and at the buckle location. Also, the model was able to replicate the bulge shaped buckle that occurred for the pressurized test specimens, as well as the diamond shaped buckle that formed during the unpressurized specimen tests.

The average percent difference between the test and model peak moment, and global curvature corresponding to the peak moment, were 7 and 19% respectively. This demonstrates that the model demonstrated a reasonable predictive capability for the moment-curvature relationships of the test specimens. When considering the critical strain of the models using the maximum moment methods, the percent differences between the model and test results were 18 and 66% for the pressurized and unpressurized specimens respectively. The percent differences of the model and test results for the critical strain when using the bilinear method were 30 and 63% for the pressurized and unpressurized specimens respectively. The magnitude of the difference between model and test critical strains for the unpressurized specimens was always less than 0.3% when using either critical strain determination methods, which is relatively small for design purposes. Thus it may be concluded that the model described in Chapter 6 demonstrates a reasonable capability to simulate the global and local buckle load-deformation behaviour, however there is some room for improvement in the FEM. This will be further discussed in the following chapter.

The FEM described in Chapter 6 neglected the residual stresses in the pipe that are induced by the cold bending machine during field bending. As including this parameter may improve the load-deformation predictive capabilities of the model, a supplementary model that incorporated residual stresses was created at

the University of Alberta. This model began as straight, was then cold bent, and was subsequently loaded in a similar manner as the specimens experienced during testing. In order to prevent local buckling during cold bending of the model, radial direction links that connected all locations of the pipe wall, as well as elastic sleeves that stiffened the pipe wall, were incorporated into the model. Permanent bending of the pipe could only occur when the elastic sleeves were removed. The model was cold bent by removing half of the sleeve sections from the model, rotating the ends of the pipe, reapplying the former sleeves and removing the other half of the sleeves, and rotating the ends of the pipes again. This model was called the Straight-Bend (S-B) model, while the model described in Chapter 6 was denoted as the Test-Bend (T-B) model.

When comparing the global behaviours of the T-B and S-B models, it was observed that the overall behaviours of the two models were extremely similar. The maximum moments of the two models were always within 8% for the SNAM2, TG2, and TCPL2 models, and the global curvature corresponding to the maximum moment was always within 16% for these models. As the S-B model was considerably more time consuming and complicated to model, while the results of the two models were relatively similar, the T-B model was predominantly used for the parametric study.

A parametric study was conducted to evaluate the sensitivity of the behaviour of cold bend pipes to the variables compared in the testing program. The variables investigated were the pipe: diameter to thickness ratio, internal pressure, material grade, imperfection amplitude, and bending degree / diameter length. The T-B model was used to evaluate the first four of these parameters, while the S-B model was used to evaluate the bending degree / diameter length parameter.

The results of the study demonstrated that the model was considerably more sensitive to some parameters than others. It was established that increasing

either the diameter to thickness ratio, or bending degree / diameter length, resulted in a substantial reduction in the critical strain of the pipes and a moderate reduction in moment capacity. It was also revealed that increasing the material grade significantly increased the moment capacity, but was inconclusive in its effect on the critical strain of cold bend pipes. It was also established that increasing internal pressure increased the pipes critical strain, however both the zero pressure and 80% SMYS hoop stress models demonstrated lower maximum moments than the 40% SMYS hoop stress model. Finally, it was found that varying the imperfection amplitude between 0.3 to 1.8 mm demonstrated very little influence on either the maximum moment or critical strain of the modelled pipes.

Table 7.1 – Summary of Difference between Model and Test Results

| Model | Maximum Moment % Difference | Critical Curvature % Difference | Maximum Moment Critical Strain % Difference | Bilinear Critical Strain % Difference |
|-------|--------------------------------|------------------------------------|---|---|
| SNAM1 | -7 | 37 | 11 | 8 |
| SNAM2 | -7 | -12 | 5 | -6 |
| SNAM3 | 1 | -8 | 56 | 45 |
| TG1 | -8 | -11 | 2 | 41 |
| TG2 | -9 | -16 | 23 | -17 |
| TCPL1 | -2 | -30 | -29 | -46 |
| TCPL2 | -9 | -15 | 79 | 80 |
| TCPL3 | -9 | -22 | 37 | -60 |

Table 7.2 – Summary of Difference between T-B and S-B Model Results

| Model | Maximum Moment % Difference | Critical Curvature % Difference |
|-------|--------------------------------|------------------------------------|
| SNAM2 | -8 | -13 |
| TG2 | -2 | -16 |
| TCPL2 | -8 | 6 |

Table 7.3 – Parametric Study Model Matrix

| Model | Diameter / Thickness Ratio | Internal Pressure (% SMYS Hoop Stress) | Material Grade | Imperfection Amplitude (mm) | Bending Degree / Diameter Length |
|-----------------------|----------------------------|--|----------------|-----------------------------|----------------------------------|
| T-B Standard | 70 | 40 | X65 | 0.6 | 1.0 |
| D/t = 45 | 45 | 40 | X65 | 0.6 | 1.0 |
| D/t = 95 | 95 | 40 | X65 | 0.6 | 1.0 |
| p/p _y = 0 | 70 | 0 | X65 | 0.6 | 1.0 |
| p/p _y = 80 | 70 | 80 | X65 | 0.6 | 1.0 |
| Grade X60 | 70 | 40 | X60 | 0.6 | 1.0 |
| Grade X80 | 70 | 40 | X80 | 0.6 | 1.0 |
| Imp = 0.3 | 70 | 40 | X65 | 0.3 | 1.0 |
| Imp = 1.3 | 70 | 40 | X65 | 1.3 | 1.0 |
| Imp = 1.8 | 70 | 40 | X65 | 1.8 | 1.0 |
| 0 deg/diam | 70 | 40 | X65 | - | 0.0 |
| S-B Standard | 70 | 40 | X65 | - | 1.0 |
| 1.5 deg/diam | 70 | 40 | X65 | - | 1.5 |

Table 7.4 – Parametric Study Results

| Name | Maximum Moment (kNm) | Critical Curvature (rad/m) | Maximum Moment Critical Strain (%) | Bilinear Critical Strain (%) |
|-----------------------|----------------------|----------------------------|------------------------------------|------------------------------|
| T-B Standard | 2536 | 0.0080 | 0.715 | 0.562 |
| D/t = 45 | 4326 | 0.0118 | 1.373 | 0.911 |
| D/t = 95 | 1763 | 0.0069 | 0.519 | 0.441 |
| p/p _y = 0 | 2253 | 0.0074 | 0.665 | 0.508 |
| p/p _y = 80 | 2480 | 0.0099 | 1.196 | 0.734 |
| Grade X60 | 2175 | 0.0082 | 0.860 | 0.602 |
| Grade X80 | 3017 | 0.0095 | 0.832 | 0.650 |
| Imp = 0.3 | 2597 | 0.0085 | 0.738 | 0.602 |
| Imp = 1.3 | 2445 | 0.0077 | 0.843 | 0.559 |
| Imp = 1.8 | 2397 | 0.0076 | 0.855 | 0.567 |
| 0 deg/diam | 2348 | 0.0161 | 1.230 | |
| S-B Standard | 2311 | 0.0094 | 0.846 | |
| 1.5 deg/diam | 2290 | 0.0080 | 0.710 | |

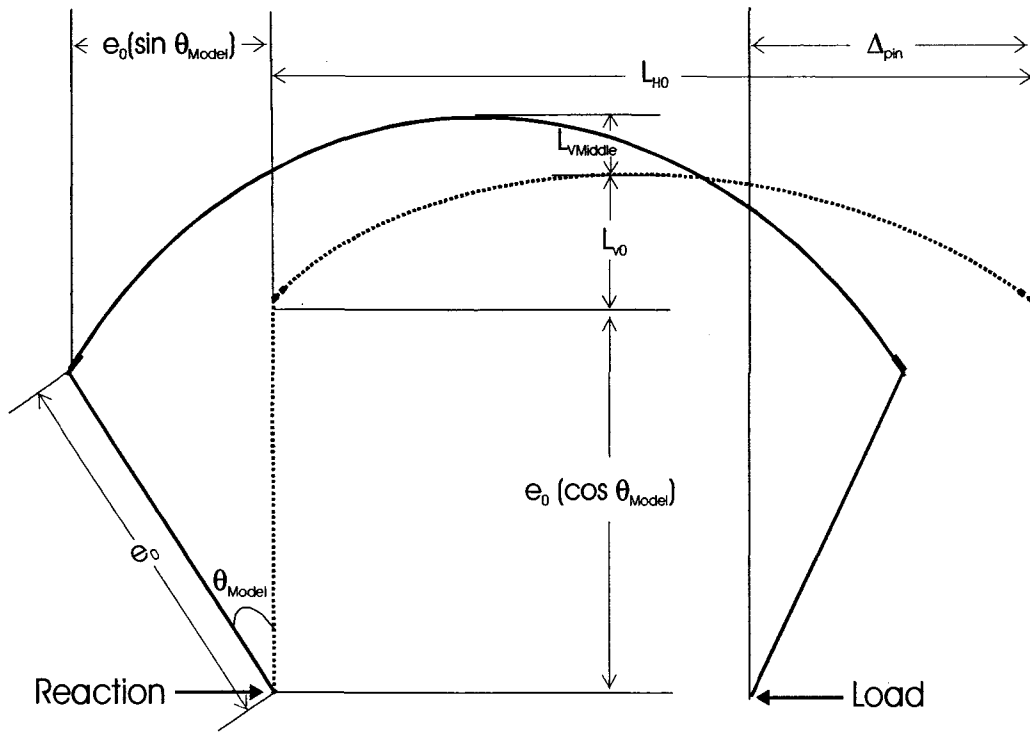


Figure 7.1 – Schematic of Model Deformation During Loading

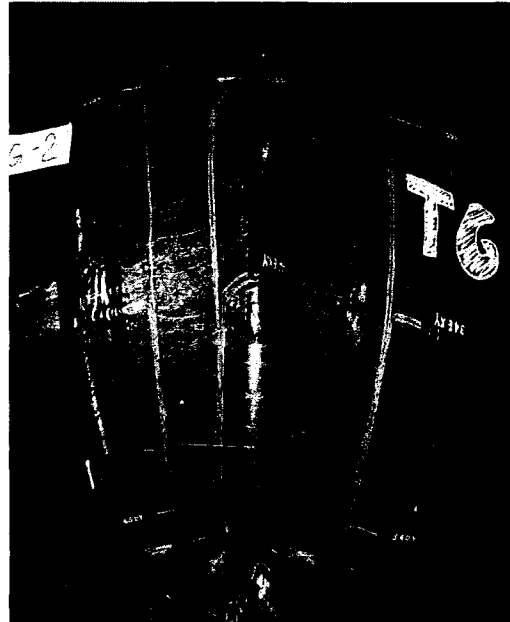
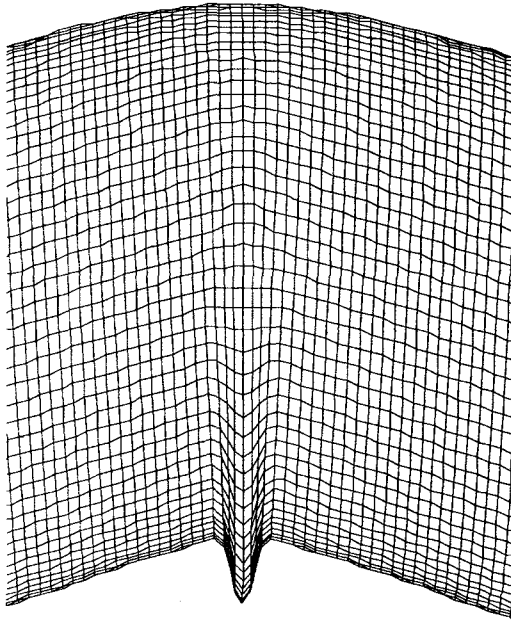


Figure 7.2 – Comparison of Pressurized Model and Specimen Buckle Shape

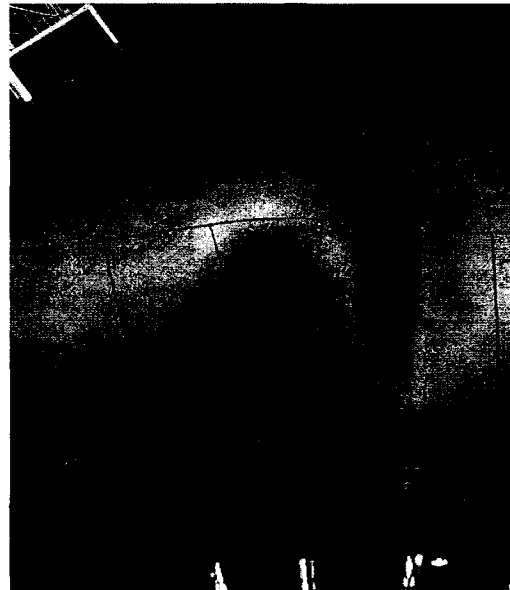
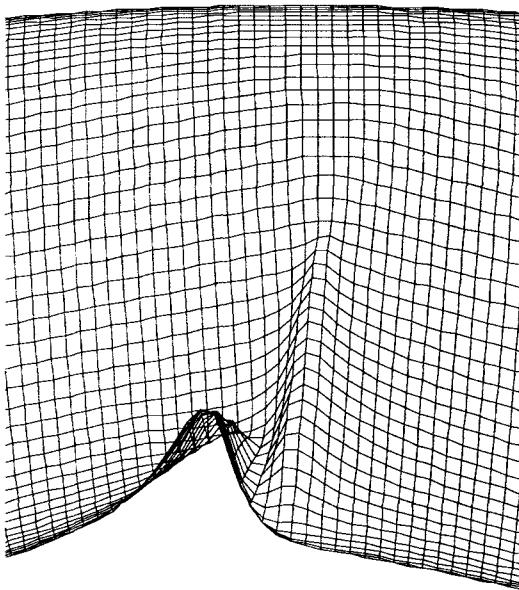


Figure 7.3 – Comparison of Unpressurized Model and Specimen Buckle Shape

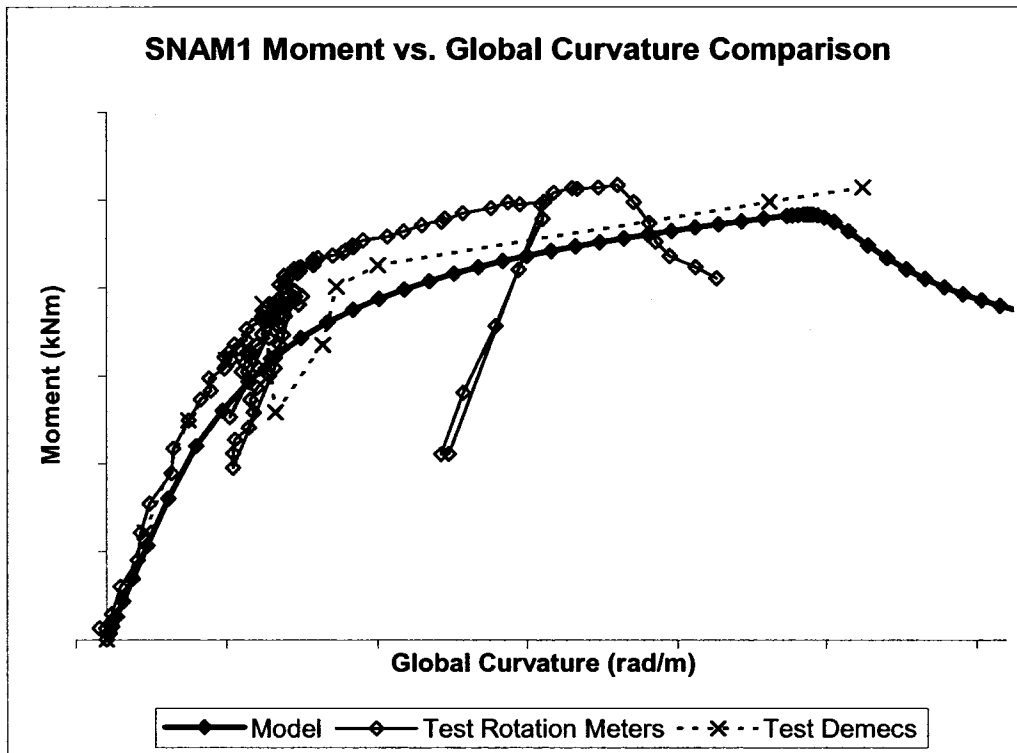


Figure 7.4 – SNAM1 Model and Test Moment vs. Global Curvature

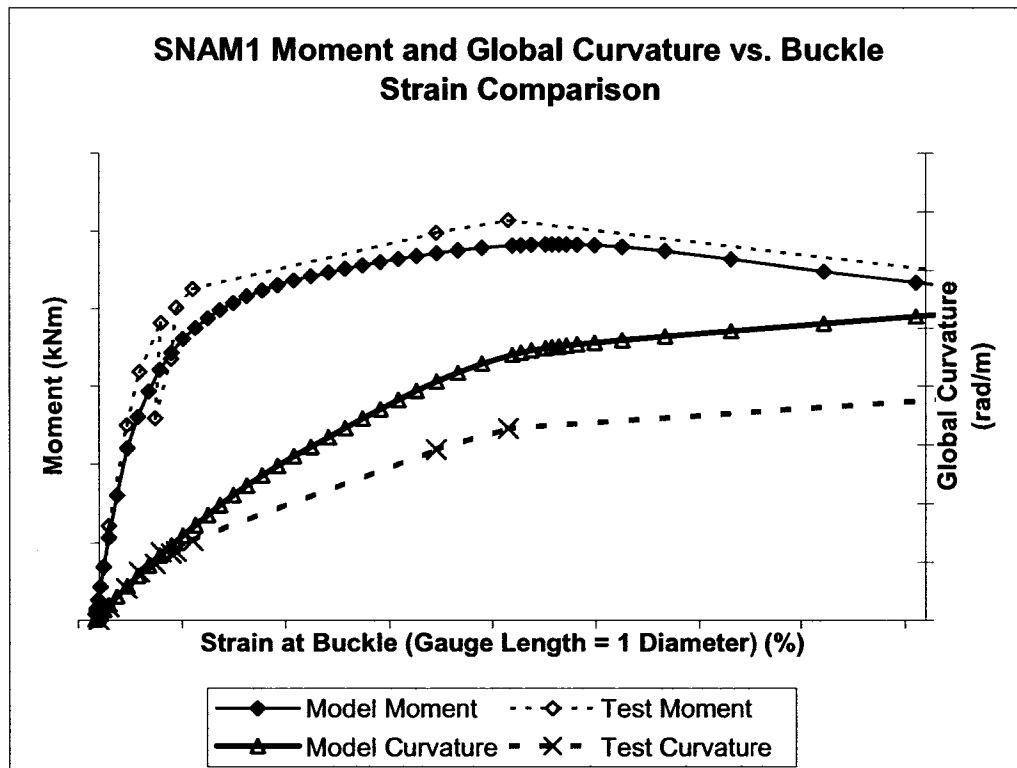


Figure 7.5 – SNAM1 Model and Test Moment and Curvature vs. Buckle Strain

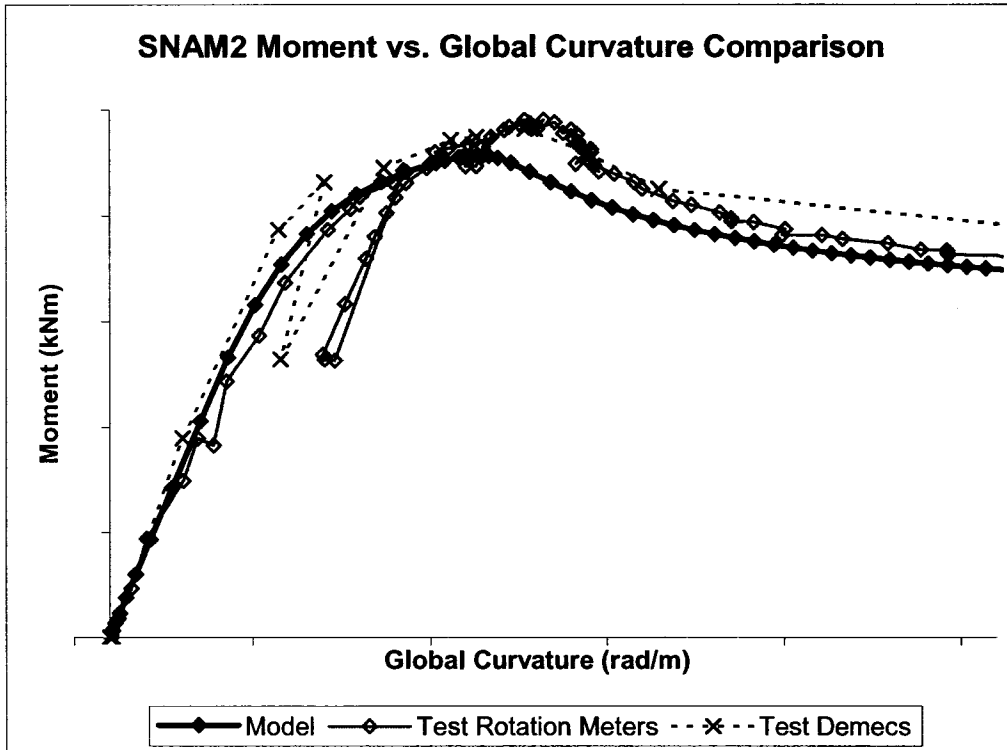


Figure 7.6 – SNAM2 Model and Test Moment vs. Global Curvature

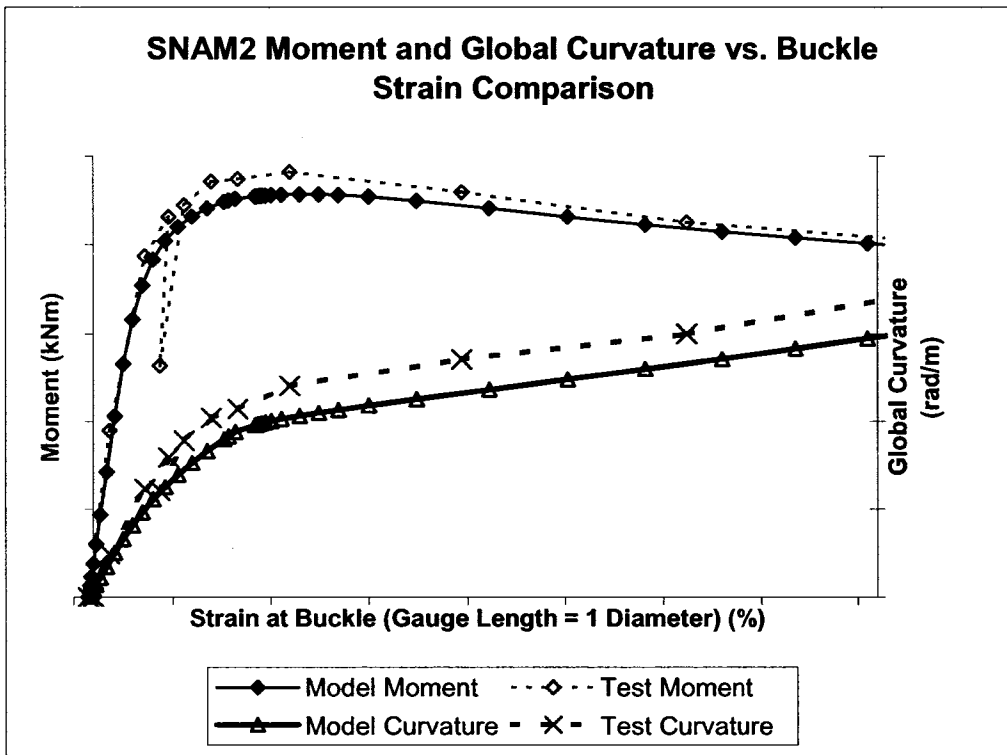


Figure 7.7 – SNAM2 Model and Test Moment and Curvature vs. Buckle Strain

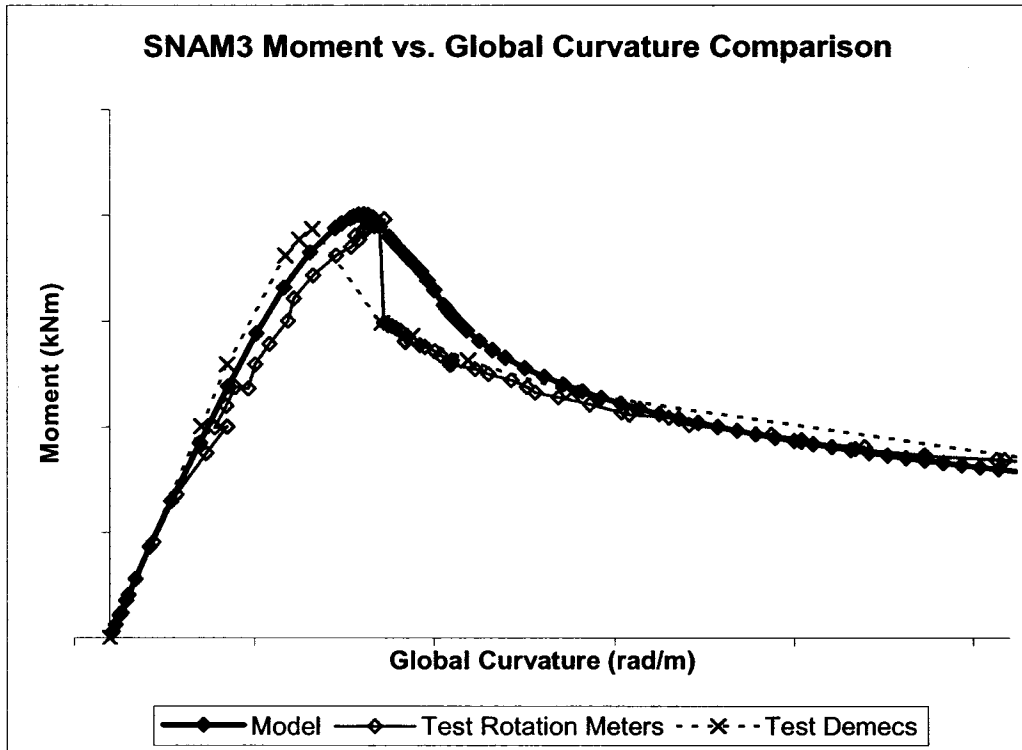


Figure 7.8 – SNAM3 Model and Test Moment vs. Global Curvature

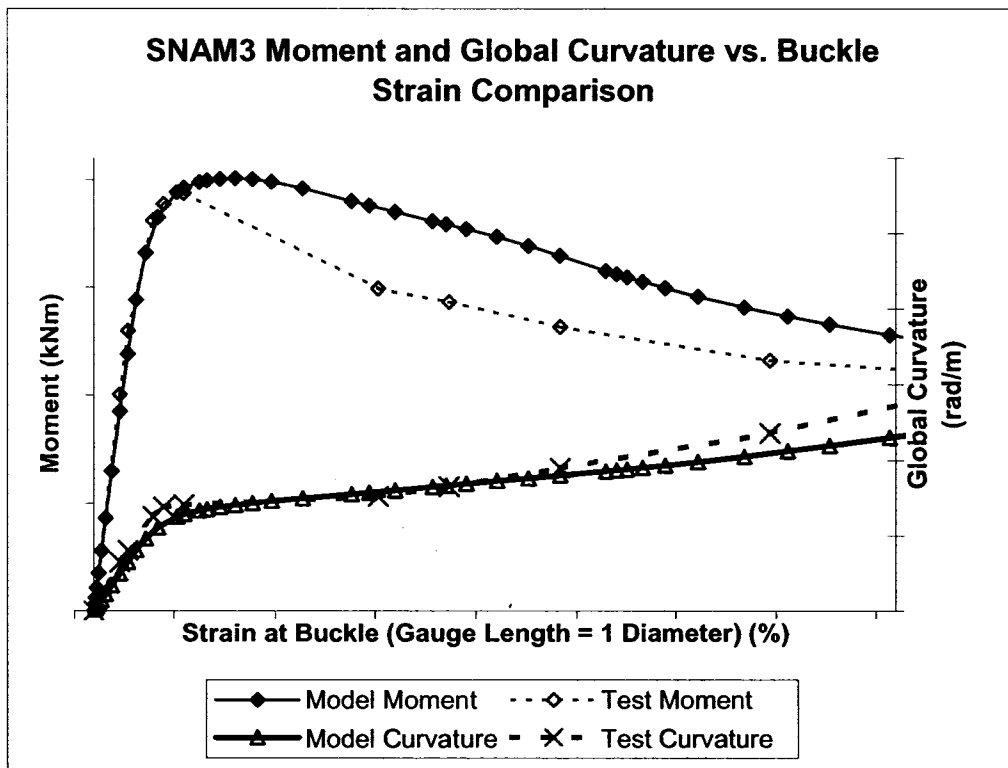


Figure 7.9 – SNAM3 Model and Test Moment and Curvature vs. Buckle Strain

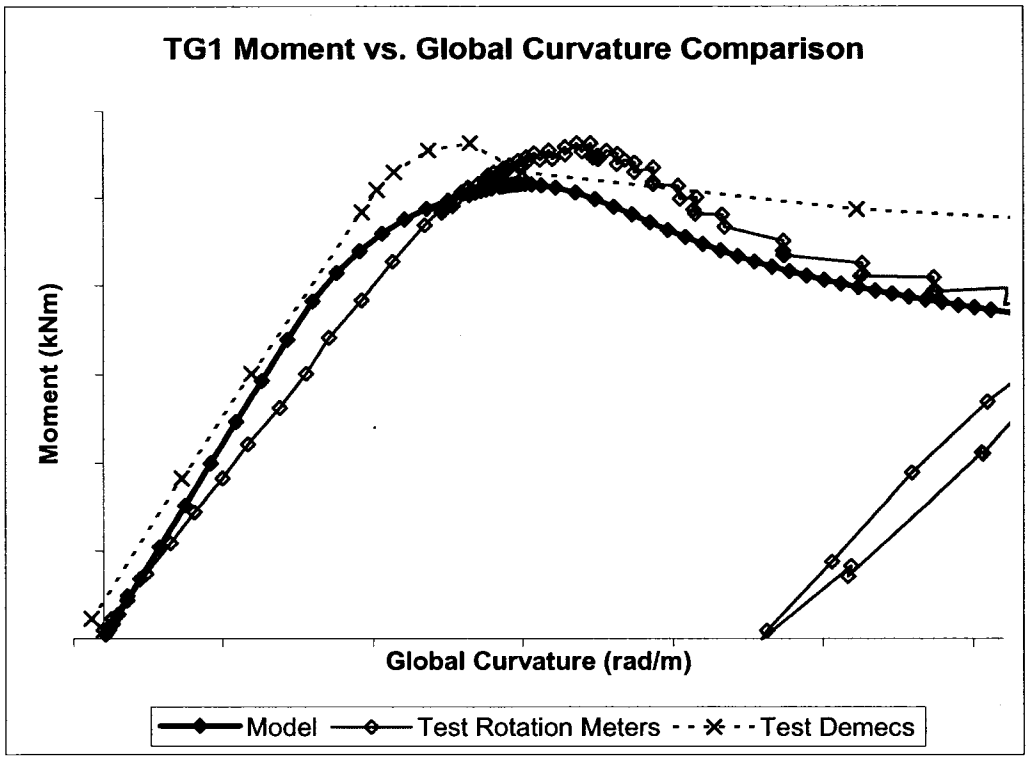


Figure 7.10 – TG1 Model and Test Moment vs. Global Curvature

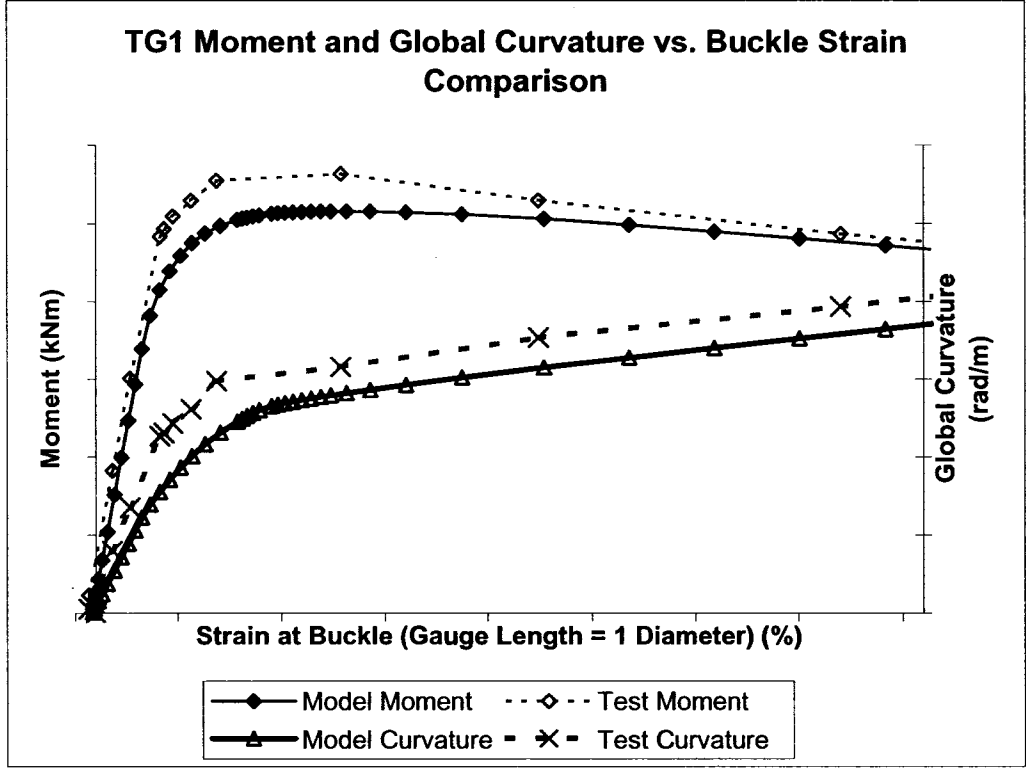


Figure 7.11 – TG1 Model and Test Moment and Curvature vs. Buckle Strain

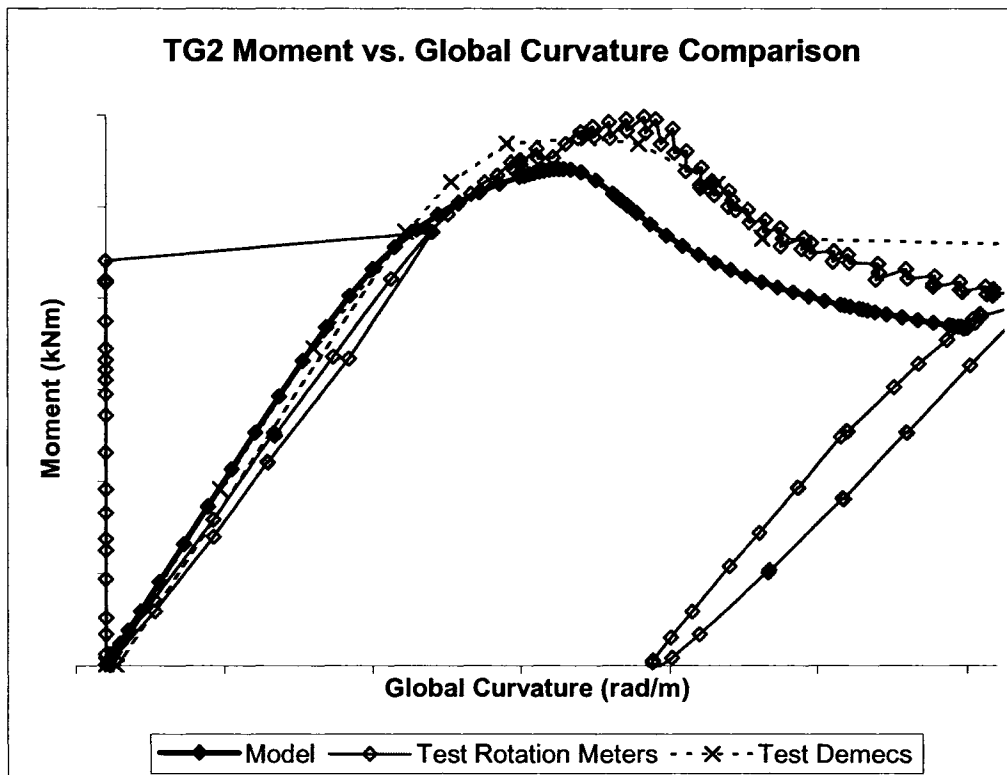


Figure 7.12 – TG2 Model and Test Moment vs. Global Curvature

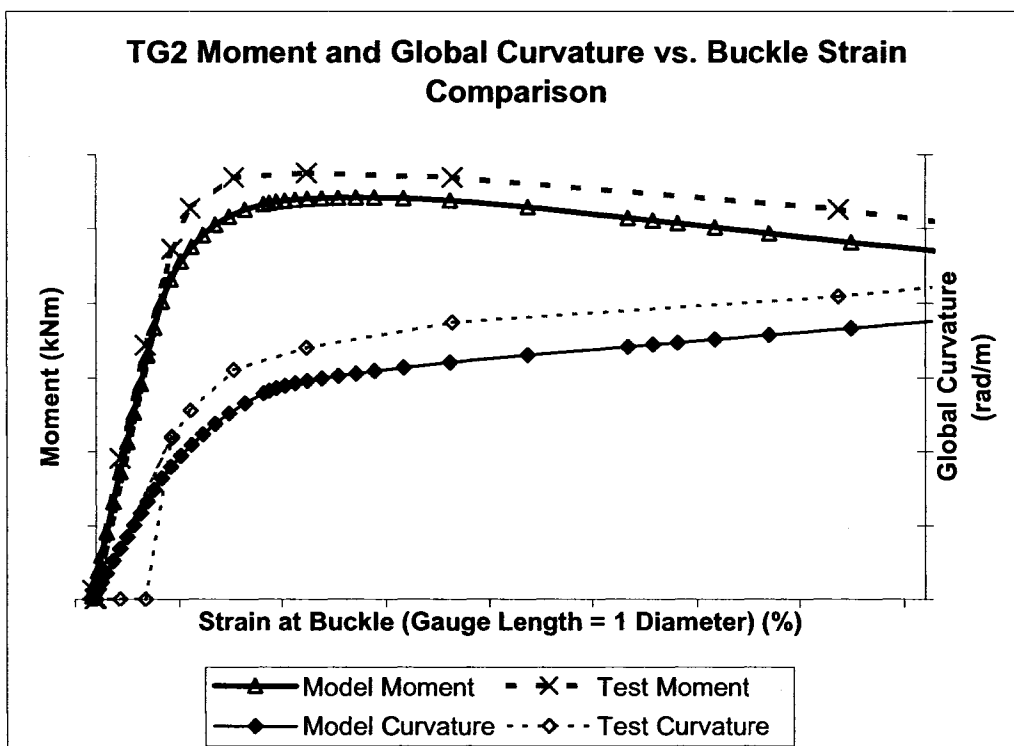


Figure 7.13 – TG2 Model and Test Moment and Curvature vs. Buckle Strain

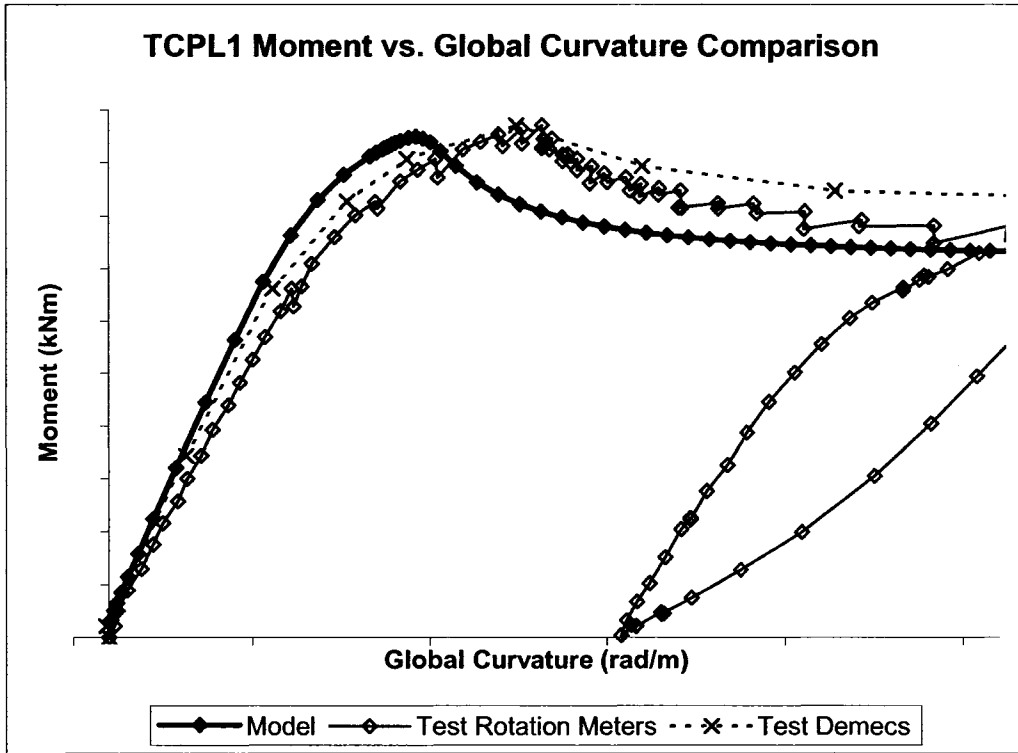


Figure 7.14 – TCPL1 Model and Test Moment vs. Global Curvature

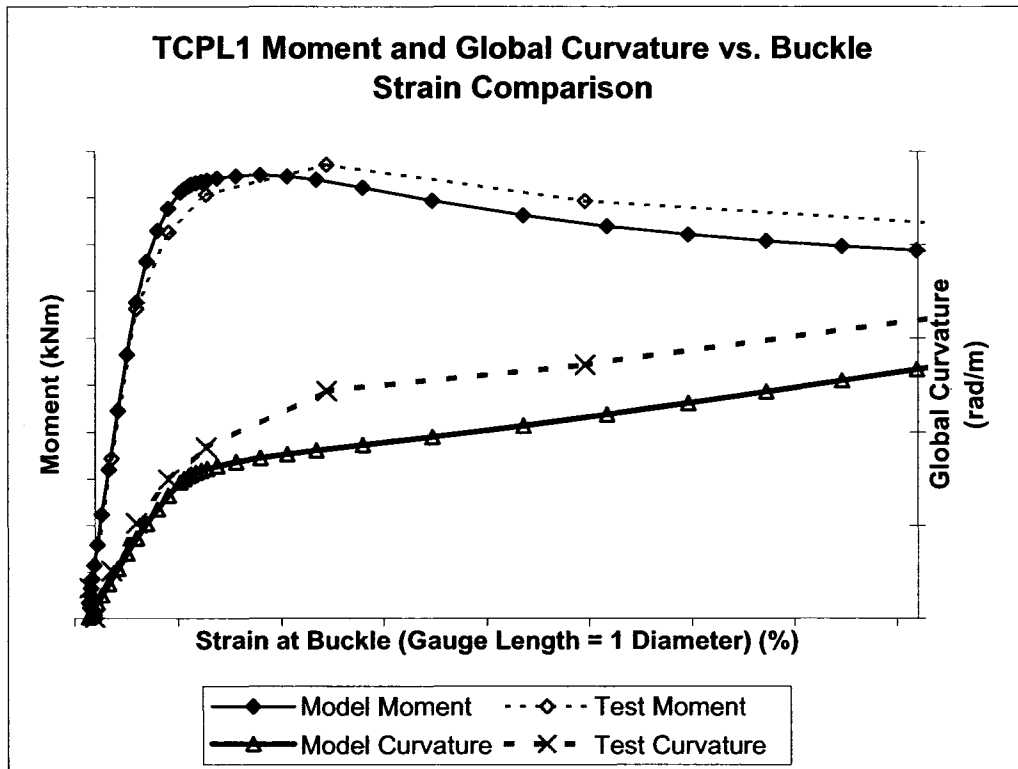


Figure 7.15 – TCPL1 Model and Test Moment and Curvature vs. Buckle Strain

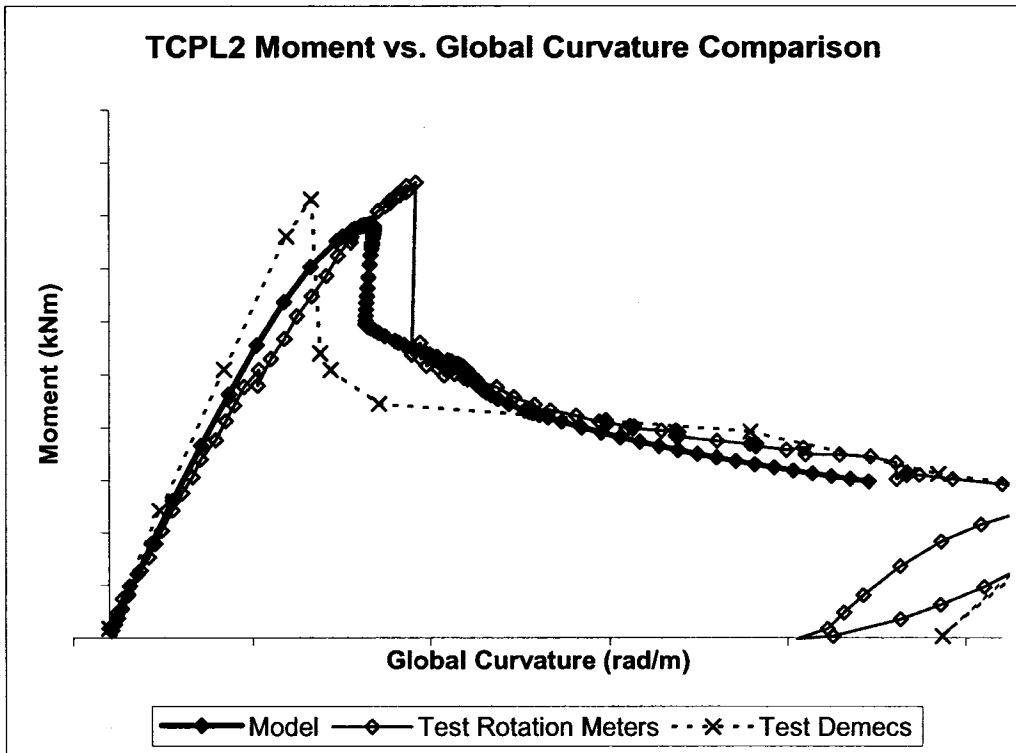


Figure 7.16 – TCPL2 Model and Test Moment vs. Global Curvature

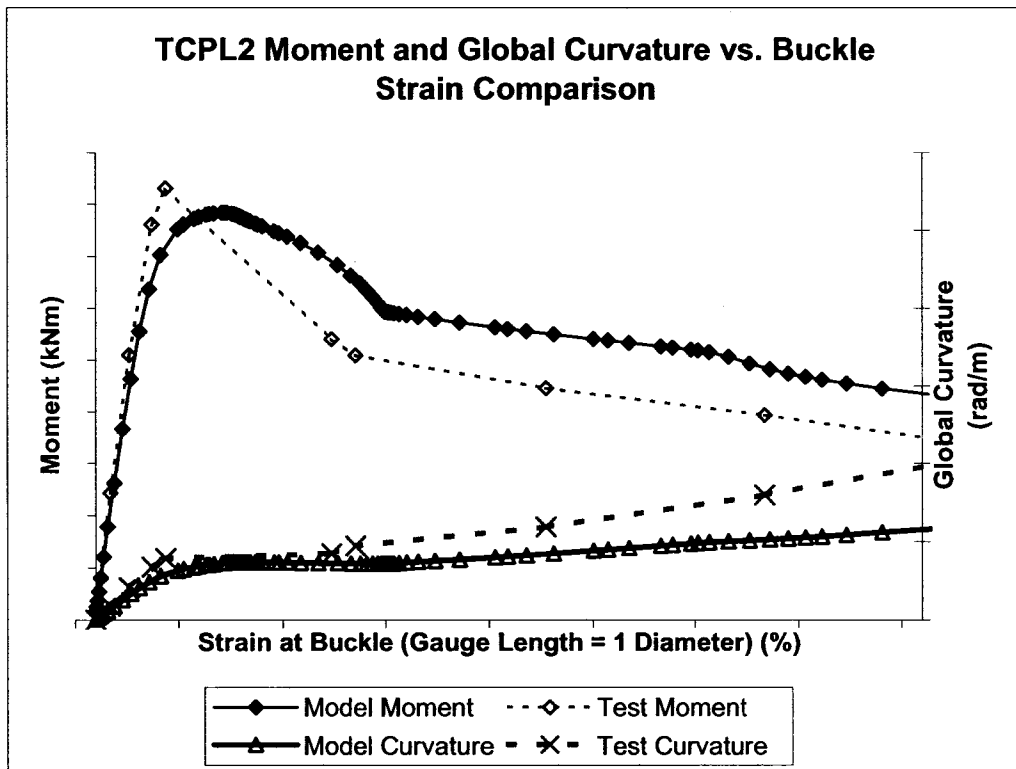


Figure 7.17 – TCPL2 Model and Test Moment and Curvature vs. Buckle Strain

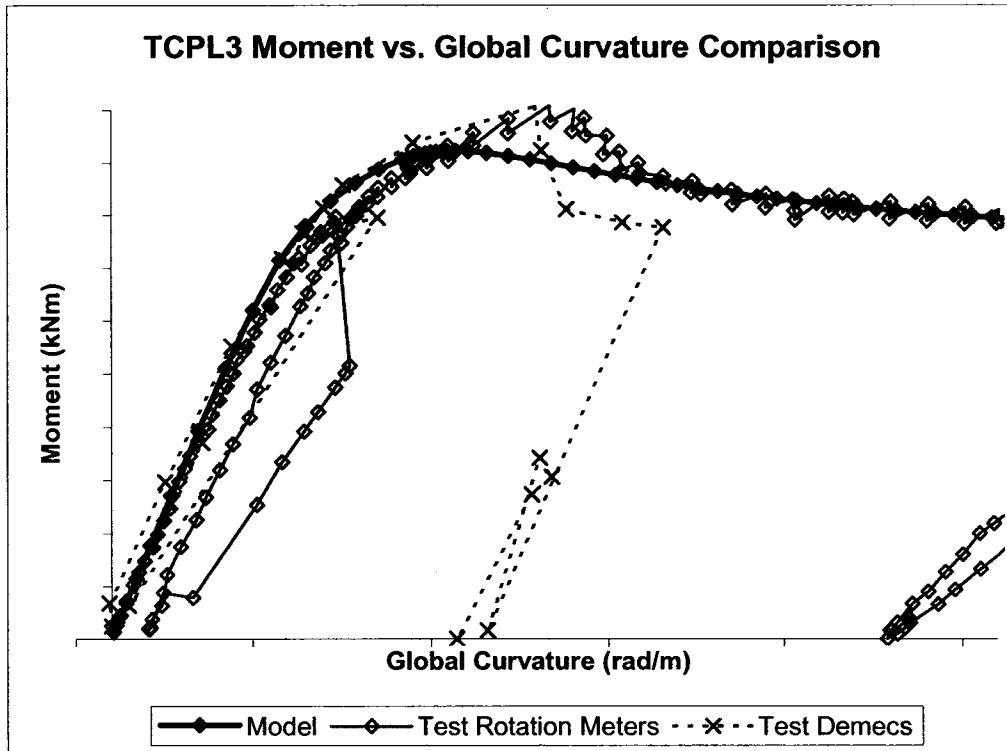


Figure 7.18 – TCPL3 Model and Test Moment vs. Global Curvature

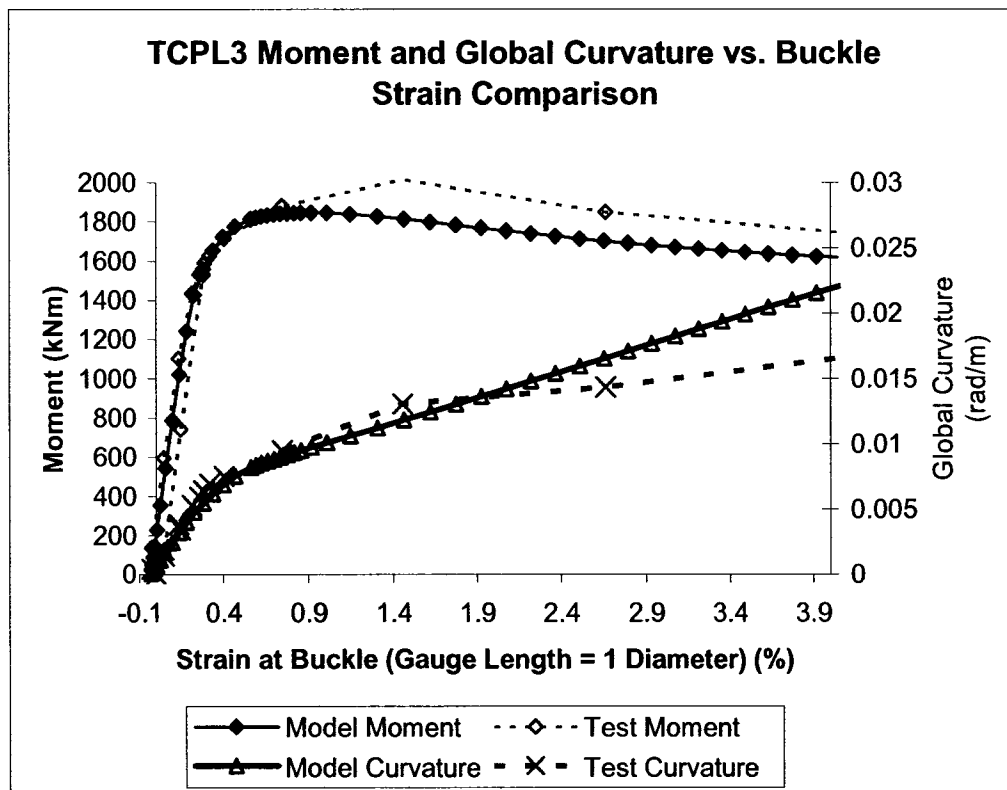
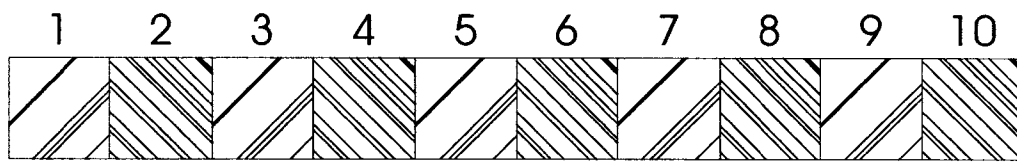
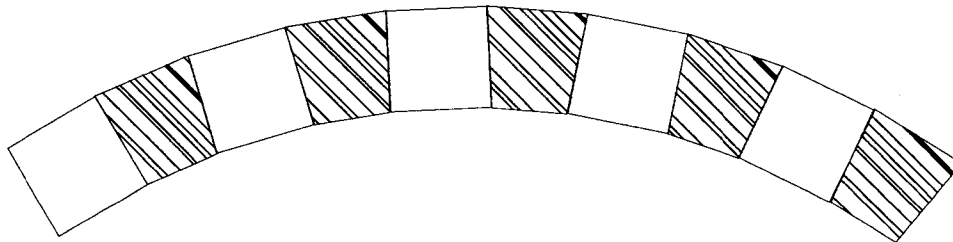


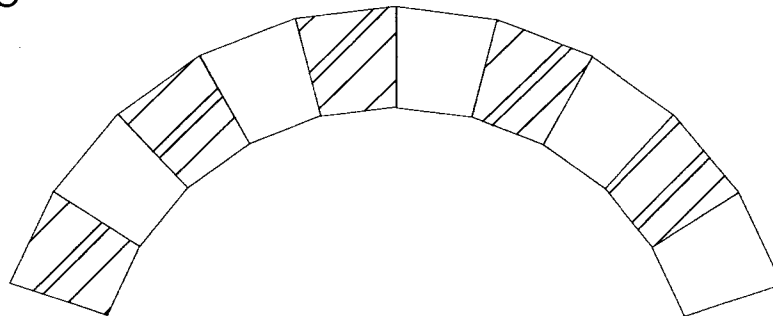
Figure 7.19 – TCPL3 Model and Test Moment and Curvature vs. Buckle Strain



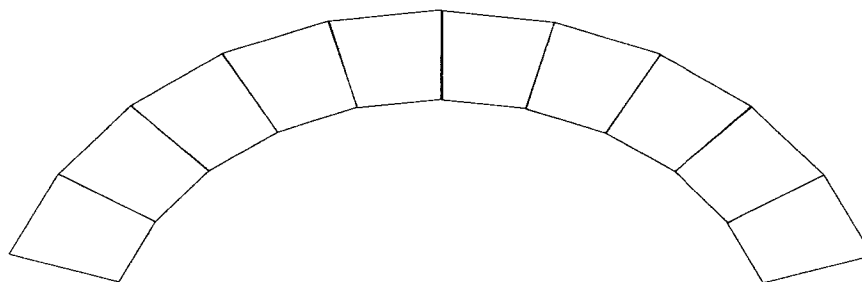
Pipe straight with radial links and elastic sleeves



Even sleeves removed and rotation applied to ends of pipe



Rotation released, even sleeves inserted, odd sleeves removed, rotation applied to ends of pipe



Rotation released, all sleeves and radial links removed from pipe

Figure 7.20 – Cold Bending Procedure for S-B Model

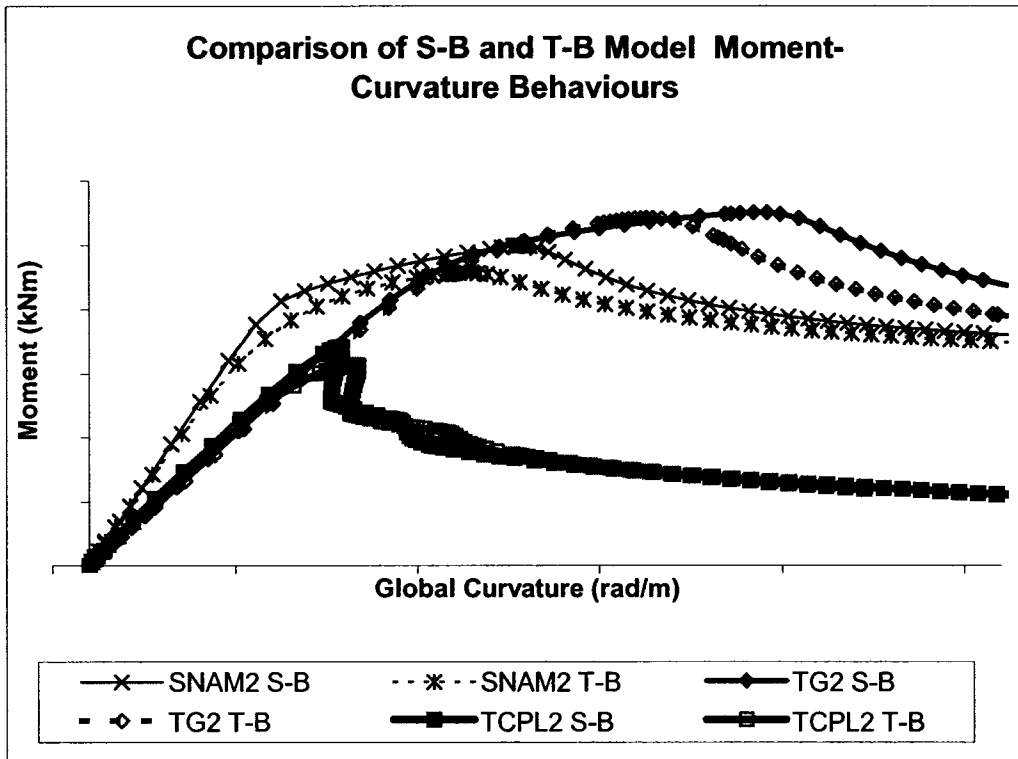


Figure 7.21 – Comparison of S-B and T-B Models Global Behaviours

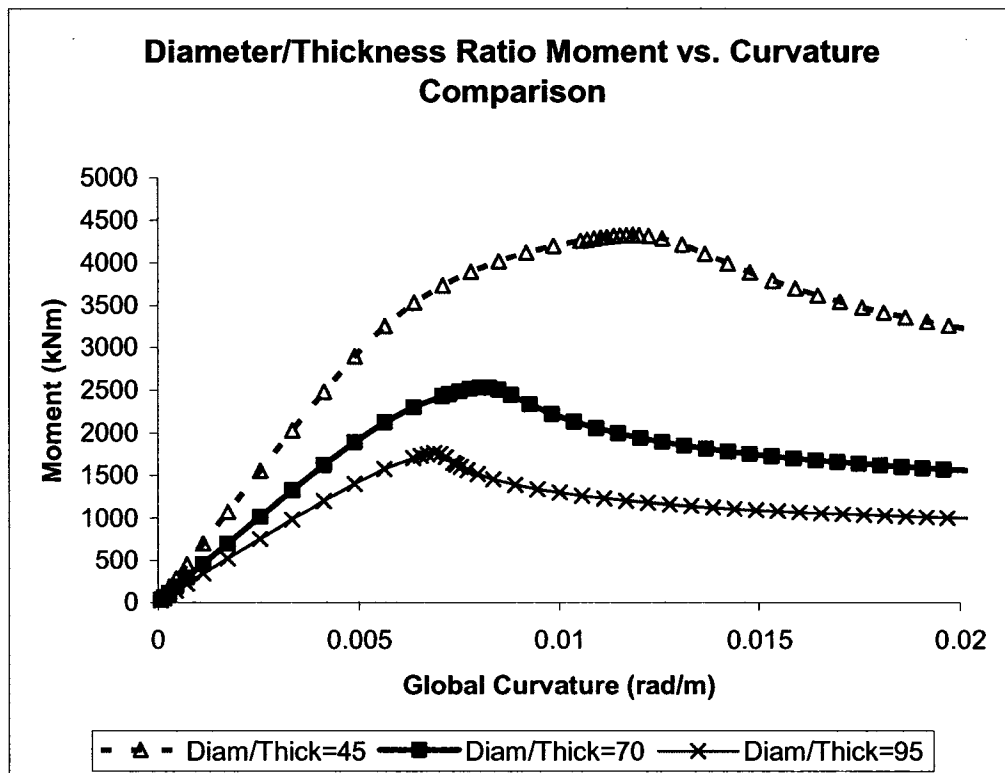


Figure 7.22 – Diameter/Thickness Ratio Global Behaviour Comparison

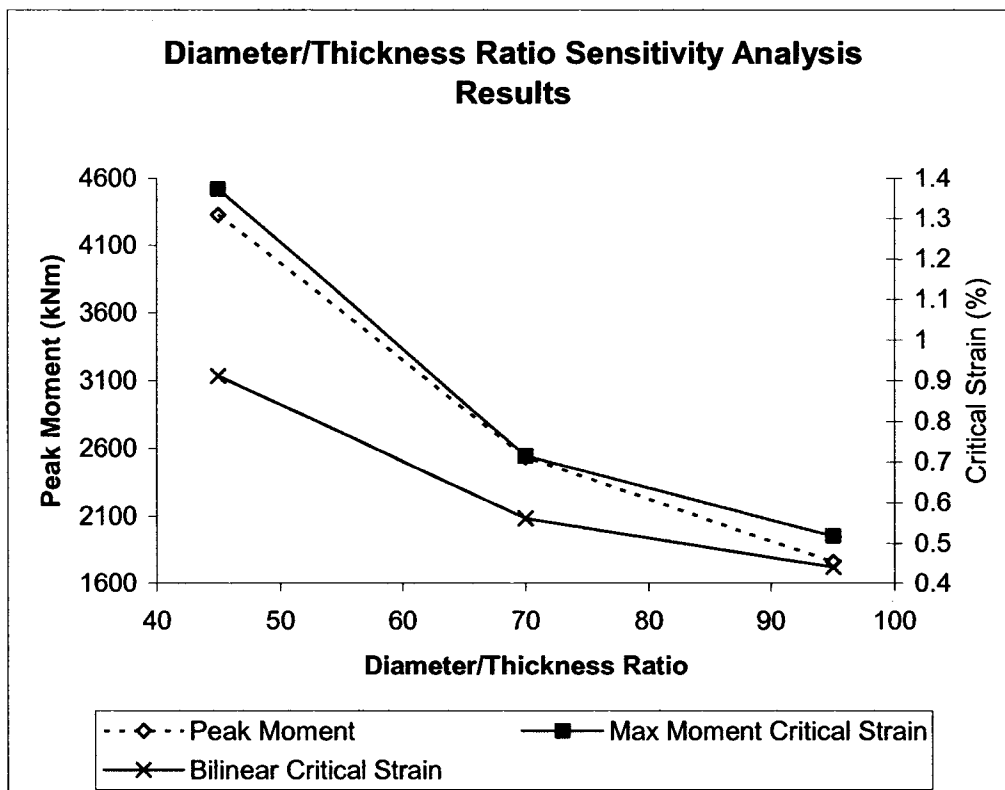


Figure 7.23 – Diameter/Thickness Ratio Moment and Critical Strain Comparison

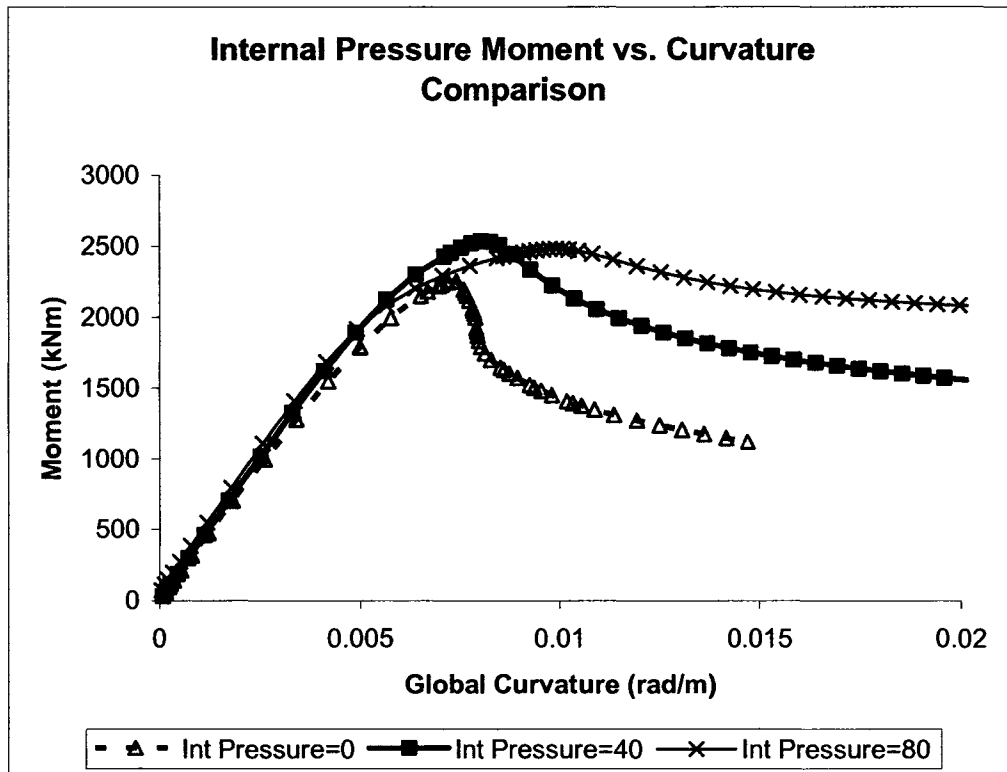


Figure 7.24 – Internal Pressure Global Behaviour Comparison

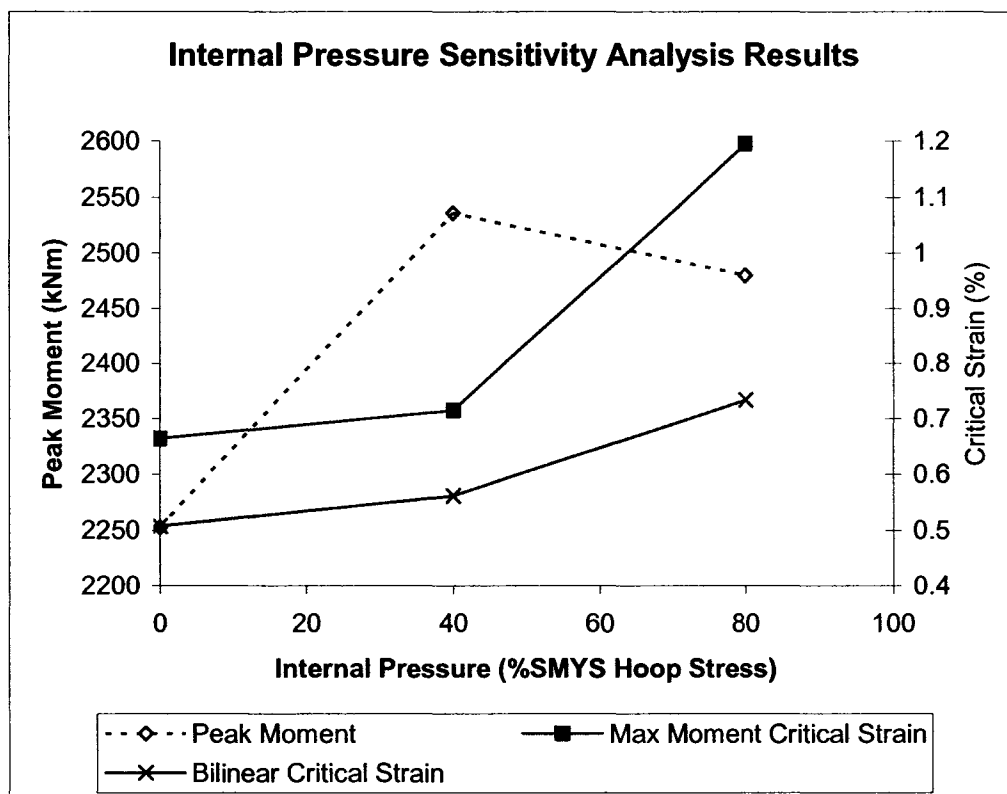


Figure 7.25 – Internal Pressure Moment and Critical Strain Comparison

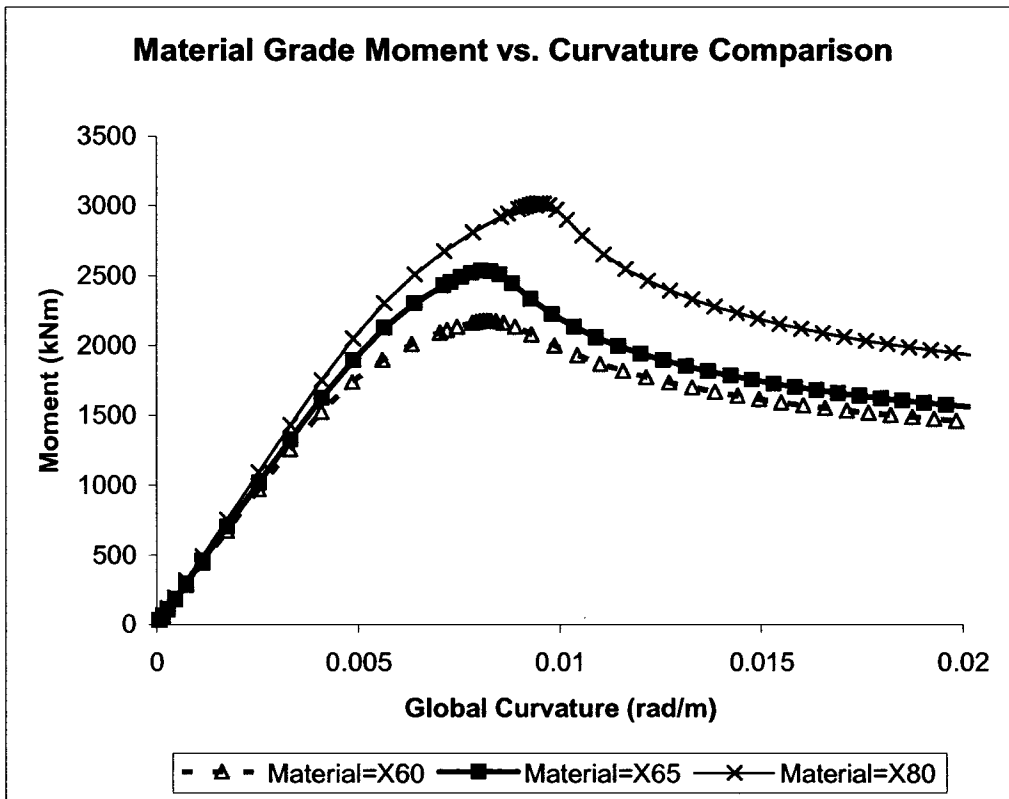


Figure 7.26 – Material Grade Global Behaviour Comparison

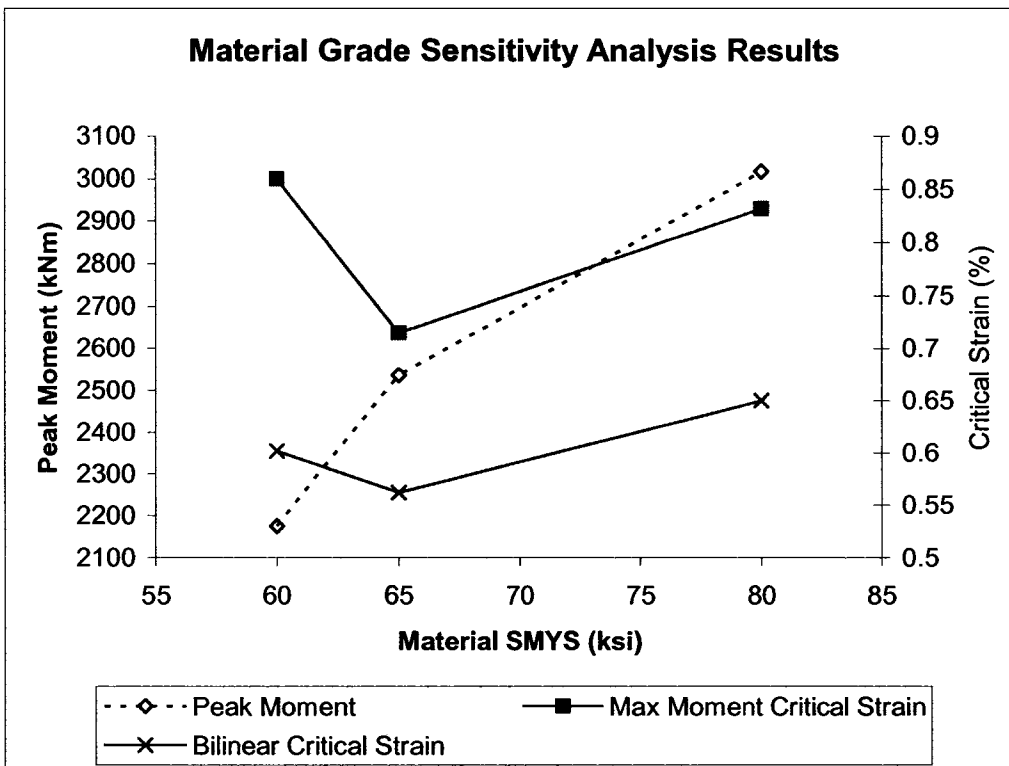


Figure 7.27 – Material Grade Moment and Critical Strain Comparison

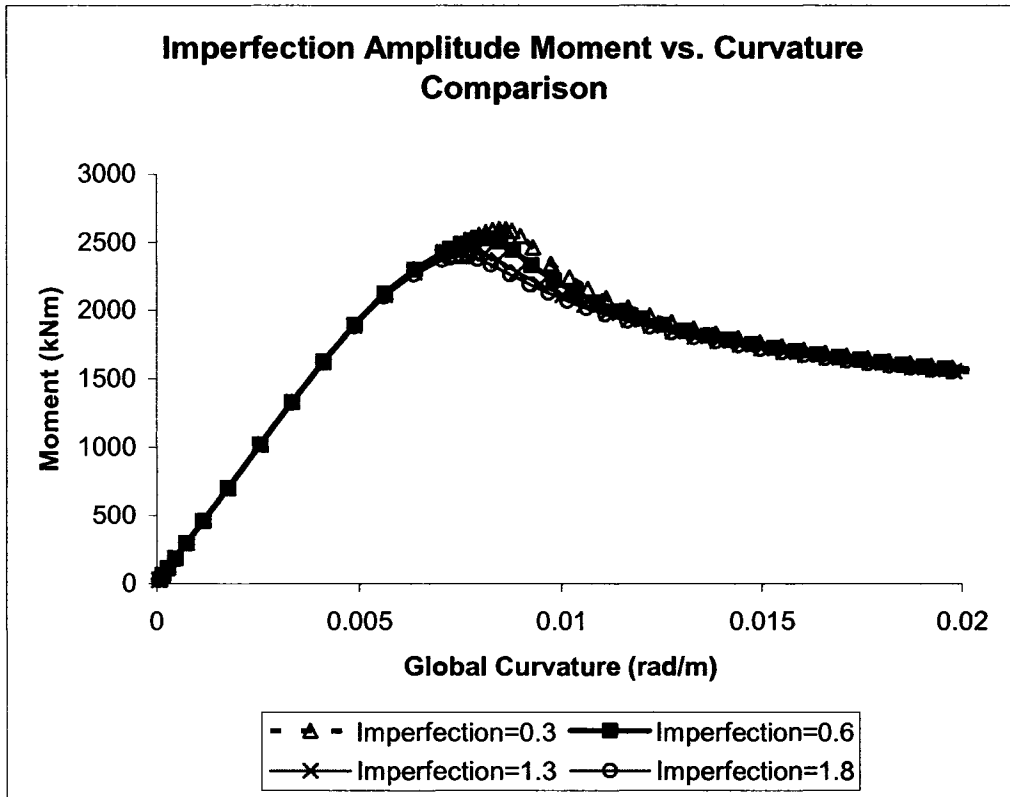


Figure 7.28 – Imperfection Amplitude Global Behaviour Comparison

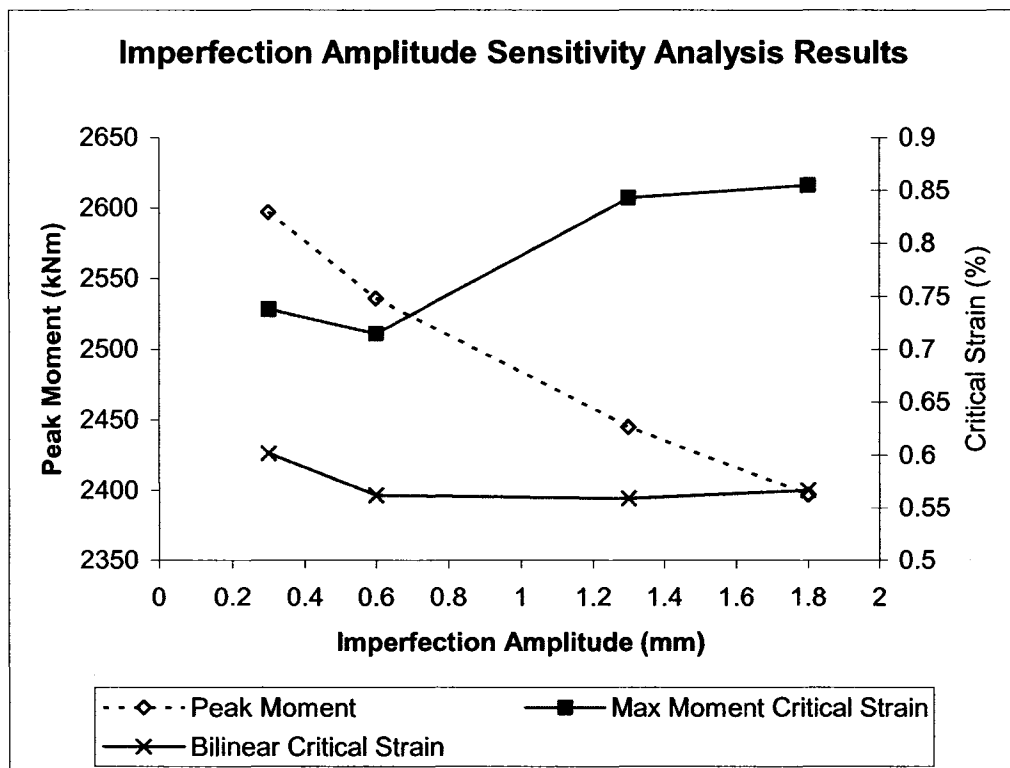


Figure 7.29 – Imperfection Amplitude Moment and Critical Strain Comparison

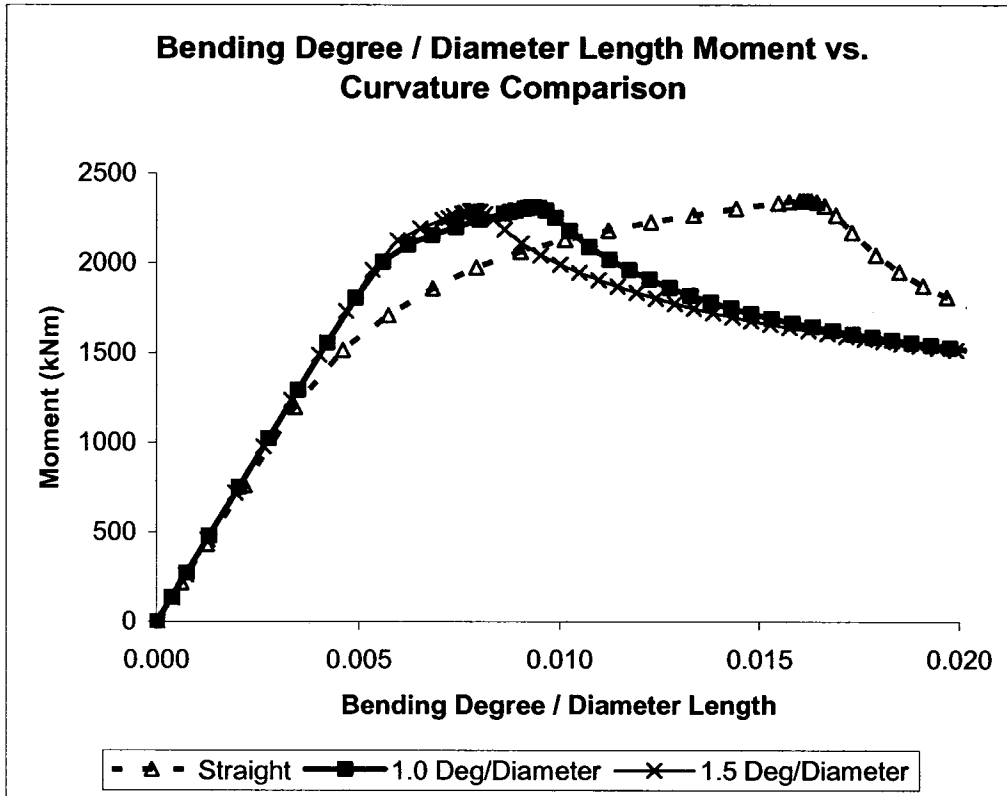


Figure 7.30 – Bending Degree / Diameter Length Global Behaviour Comparison

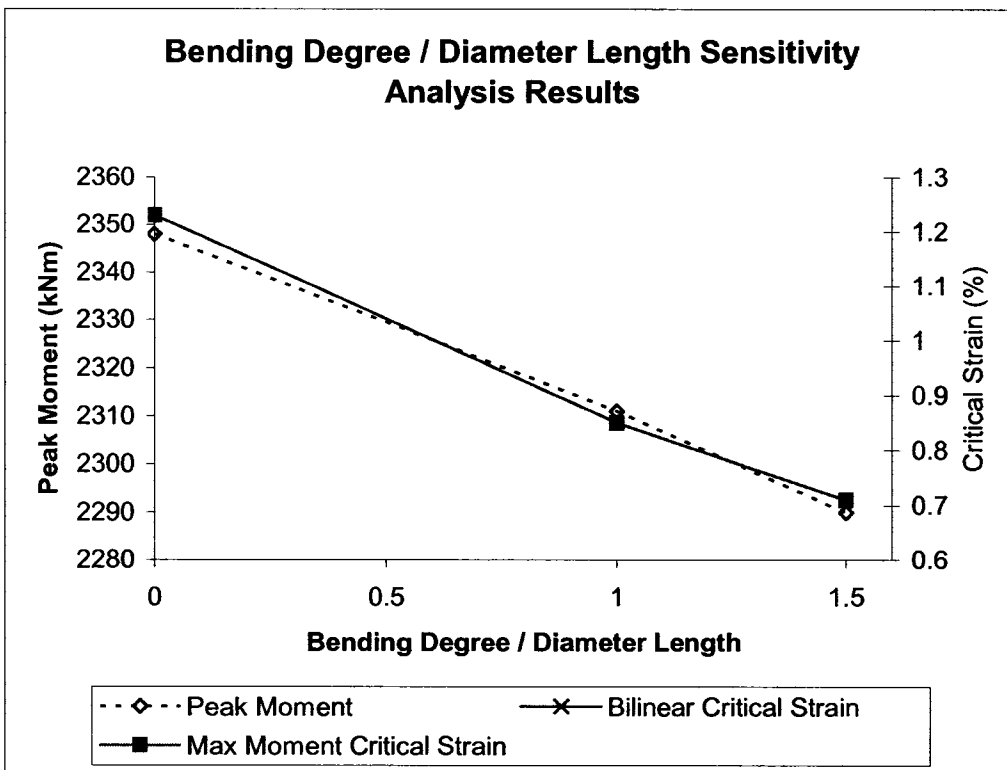


Figure 7.31 – Bending Degree/Diameter Moment and Critical Strain Comparison

8.0 SUMMARY, CONCLUSIONS, AND RECOMMENDATIONS

This chapter summarizes the work presented in the previous chapters, presents the main conclusions that have previously been reported, and provides recommendations for future research pertaining to cold bend pipes.

8.1 Summary

Cold bends are often installed in pipelines in order to change the vertical and horizontal direction of the pipeline route. They are created by loading a pipe into three-point bending, with of a cold bending machine. Due to the considerable plastic strain induced on the pipe, geometric and material property transformations accompany its cold bending. During slope movement, earthquake, and thermal expansion, deformations tend to accumulate at the site of cold bends. Because of the corresponding accumulation of strain, local buckles are often found at these locations. As little is currently known about the allowable strain that may accumulate in a cold bend pipe prior to its local buckling, the main objective of this research program was to investigate the critical strain of cold bend pipes. Another objective was to examine the allowable deformation a cold bend pipe might experience prior to fracture in order to evaluate an ultimate state for a cold bend during an earthquake. The final objective of this research program was to develop a finite element model that can simulate the load-deformation behaviour of cold bend pipes.

Eight full-scale tests were conducted on seven cold bend pipes and one straight pipe in order to achieve the objectives of this research. These specimens were NPS 24 and NPS 30 pipes with diameter to thickness ratios between 44 and 93. The material grades ranged from X60 to X80, and the bending degree /

diameter length varied from straight to 1.5 degrees / diameter. The internal pressure applied during testing of the pipes caused hoop stresses between 0 to 80% SMYS.

The geometric changes caused by cold bending were measured for the test specimens in this research program. The residual strains were measured by mounting strain gauges on the pipes while straight and subsequently recording their measurements upon completion of cold bending, as well as by punching hole into the pipes while straight and comparing the distance between these holes before and after cold bending. The wall thickness was measured at numerous locations over the specimens' circumference and length in order to investigate the extent of wall thinning / thickening that is caused by cold bending. The diameters were measured at four locations at each end to examine the degree of ovalization at the ends of the pipes. A special measuring device was constructed in order to measure the initial imperfections of the specimens that were caused by cold bending. This device measured the radial direction profile of the pipe, the vertical deflection, and the angle of the pipe centreline at all locations along its length. Through these measurements the magnitude and distribution of the initial imperfections, the vertical profile, and the end angles were obtained for the seven bend specimens.

The experimental testing of the pipes was conducted by applying bending loads, axial loads, and internal pressure to the specimens. A self-equilibrating testing frame was constructed to facilitate this procedure. This frame consisted of two bending beams that were connected at each end to tension members, and had a 600 mm moment arm that was connected to the middle of these beams. The bending and axial loads during testing was provided by the same 4000 kN hydraulic jack, and collars were installed at the ends of the pipes to prevent end failure. The jack stroke was increased during testing until a local buckle formed near the middle of the pipes. For several of the specimens the central bend angle of the specimens was further increased until fracture occurred. This was

accomplished by resetting the jack stroke during testing, however the specimens experienced large tensile loads during this process because of the internal pressure acting against the end plates.

An extensive material testing program was carried out to investigate the pipe material property changes that accompany cold bending. Tension coupon tests were conducted on stubs removed from the ends of the specimens prior to testing to determine the virgin material properties. Coupon tests were also conducted on material cut from the tension side of the bends to examine the effects of work hardening. They were also conducted on material cut from the compression side of the bends to examine the Bauschinger Effect in the pipe material that would be demonstrated during opening mode deformation. Finally, coupon tests were conducted on material from the ends of the pipes after testing to examine the effects of testing on the pipe material.

A finite element model was created in order to simulate the behaviour of the specimens during testing. Half of the pipe was modeled in the out of plane direction, and a uniform mesh with an aspect ratio of approximately 1.5 was selected to define the node distribution. Shell elements capable of modeling both thick and thin wall behaviour were incorporated to define the pipe wall, and the boundary conditions applied at the loading and reaction pins of the model replicated those in the test setup. The geometry of the model was based on the vertical deflection measurements obtained during imperfection measuring, and the model end angles were the average of the test specimen end angles. The initial imperfections in the model were incorporated using a uniform amplitude and period. These values were selected as the average amplitude and period of each test specimen, as determined during imperfection measuring. The tension side bend material stress-strain behaviour of the specimens was used to define the material properties for the model.

A short parametric study was conducted to evaluate the sensitivity of the test specimens to the different variables that were investigated. This will allow for better comparison of the behaviour of in-situ cold bends to that of the specimens during testing. The parameters studied were the pipe diameter to thickness ratio, internal pressure, material grade, imperfection amplitude, and bending degree / diameter length. The ranges of the parameters were similar to those demonstrated by the test specimens. A total of 12 cases were analyzed, and the effect of each parameter was assessed against the behaviour of a standard model.

8.2 Conclusions

Several conclusions may be drawn from the results of the initial measurements, experimental tests, material tests, finite element model, and parametric study that were conducted for this research.

1. The extent of wall thinning / thickening, as well as ovalization, was insignificant for the cold bend specimens.
2. The residual strains in the specimens demonstrated a fairly regular distribution. Their magnitude generally increased towards the extreme fibres of the bend, and they also increased as the bending degree / diameter length of the pipe increased. The maximum and minimum residual strains were similar to calculated values that were based on the geometry of the bend.
3. The initial imperfections of the pipes demonstrated a distribution that was extremely different from that of a straight pipe. The distribution of imperfections was relatively similar for the pipes within each set of

specimens. This demonstrates the bending degree / degree length of the specimens does not generate a significant influence on the initial imperfection distribution.

4. Under applied bending loads, pressurized cold bend specimens will develop a bulge shaped buckle, while unpressurized specimens will form a diamond shaped buckle. This behaviour is similar to that observed for straight pipes.
5. The critical strain of the test specimens ranged from between 25 to 85% of that of a similar straight pipe as predicted by equation, with an average reduction in critical strain of 48%. Also, the maximum moment and critical strains of unpressurized cold bends are significantly less than those of similar pressurized cold bend. It was also observed that the bending degree / diameter length does not appreciably change either the peak moment or critical strains of similar cold bends. The moment capacity of the test specimens generally increased with decreasing diameter to thickness ratio and increasing material grade.
6. Cold bends are susceptible to very low cycle fatigue, as two of the specimens fractured at the wrinkle location after 3 and 6 compression – tension cycles. However, considerable deformation prior to fracture is attainable as these fractures occurred only after a central bend angle of 35 degrees was achieved. Tension side fracture may occur for pipes experiencing large curvatures with high internal pressures. This phenomenon may occur because of the brittleness that is introduced to the pipe material when it experiences large biaxial stresses. The behaviour of low pressure cold bends may be extremely ductile, as a central bend angle of 49 degrees was achieved without fracture for one of the test specimens.

7. Work hardening in the tension side bend material of the cold bends caused an increase in yield stress between 1 to 19% in comparison to that of the virgin material. The Bauschinger Effect caused between a 10 – 20% reduction in the compression side bend materials yield stress when loaded in tension. The effect of testing is minor at the ends of the pipe. The ultimate stress of the material is nearly unchanged during cold bending. The fracture strain of cold bend material decreases with increasing residual strain.

8. The finite element model that was developed in this research program was able to reasonably simulate both the global and local response of the specimens during testing. The average percent error for the model peak moment and critical curvature was 7 and 19% respectively. The average percent error for the model maximum moment critical strain was 18 and 66% for the pressurized and unpressurized specimens respectively, while that for the bilinear critical strain was 30 and 63% for the pressurized and unpressurized specimens respectively. The magnitude of the difference between the unpressurized model and test critical strains was always less than 0.27%, which is relatively small for design purposes. The global behaviour of the model developed for this research was relatively similar to that of a model that incorporated the cold bending procedure. This demonstrates that residual stresses from cold bending do not significantly affect the pipes global load-deformation response.

9. The parametric study revealed that some variables affect the load deformation behaviour of cold bends more than others. Decreasing the diameter to thickness ratio significantly increases the moment capacity and critical strain of the model. The moment capacity of the model also increases with increasing internal pressure and material grade. Varying the imperfection amplitude between 0.3 to 1.8 mm does not significantly affect either the moment capacity or critical strain of cold bends. Finally,

increasing bending degree / diameter length decreases the critical strain of cold bend pipes.

8.3 Recommendations

To the author's knowledge, this research work has been the first of its kind concerning cold bend pipes. The experimental program has significantly increased the available information about the behaviour of cold bend pipes under combined loads. Also, the model that was created is able to reasonably simulate the behaviour of the test specimens. However, there are several areas pertaining to cold bends that require additional study.

1. The degree of springback during cold bending was not assessed in this research. Increased knowledge of this factor may aid fabricators of field bends produce more consistent kinks. Also, future study into methods during cold bending that may be employed to reduce imperfection magnitudes would also generate cost savings.
2. The imperfection-measuring device demonstrated difficulty in measuring the ovality of the specimens because of the non-uniform in plane diameter of the pipes. A new imperfection-measuring device with an independent datum would improve these measurements.
3. There was significant variation between the critical strains based on the maximum moment and bilinear methods for both the test specimens and models. Further study of a more consistent critical strain determination method would be advantageous for future research.

4. Additional full-scale testing should be conducted to confirm the results of the parametric study. Furthermore, it is unexpected that the moment capacity and critical strain are unaffected by the bending degree / diameter length, consequently additional tests with pipes from the same material heat with different bending profiles could reinforce this conclusion. Any future testing should include multiple methods for accurately assessing the global curvature of the specimens.
5. Investigation of the effect of axial load on the behaviour of cold bend test specimens would assist in understanding the behavior of in-situ field bends with thermal loads.
6. Additional tests to determine the allowable curvature prior to fracture should be conducted on pressurized specimens. These tests should eliminate the tension loads during the jack resets so that the specimens do not fail under fatigue. This information will greatly contribute to the implementation of an ultimate limit state for earthquake design.
7. Further research involving tension side fracture should also be conducted in order to better understand this seldom observed phenomenon. This research should include a more in depth study of what the root causes for this type of failure may be.
8. Experimental evaluation of the residual stresses caused by cold bending would be advantageous to confirm any calculated residual stress distribution and magnitudes.
9. Compressive coupon tests on the compression side bend material would be beneficial to more accurately assess the behaviour at the buckle of cold bends. Also, circumferential direction coupon testing would help assess the changes caused by cold bending to the hoop

direction material properties. Also, longitudinal direction coupon tests at different locations around the circumference of the bend would generate a better understanding of the variation in material properties throughout the depth of the pipe.

10. Implementing the above material properties into the finite element model may improve the accuracy of its load deformation behaviour. In addition, replicating the precise imperfection pattern and residual stresses would improve the predictive capabilities of the finite element model.
11. An additional model that replicates the step-by-step bending procedure during field bending may best simulate the behaviour of cold bend pipes. This model should implement the die, mandrel, pin up shoe, and stiffback dimensions of the cold bending machine.
12. The number of models analyzed in the parametric study should be significantly increased. The range of the parameters should be extended, and the effect from modifying several parameters coincidentally should be assessed. This would allow for the development of a design equation that could be employed to predict the critical strain of cold bend pipes, for implementation into industry.

REFERENCES

Abel, A., 1987. "Historical Perspectives and some of the Main Features of the Bauschinger Effect", *Material Forum*, Institution of Engineers, Australia, Vol. 10, No. 1, p. 11-26.

American Society for Testing and Materials, 1994. "Standard Test Methods and Definitions for Mechanical Testing of Steel Products", ASTM Designation A370-94.

American Society of Mechanical Engineers, 1999. "Process Piping - ASME Code for Pressure Piping", B31.3-1999, ASME, New York, New York.

American Water Works Association, 1987. "Steel Pipe – A Guide for Design and Installation", AWWA M11, 2nd Edition, American Water Works Association, Denver, CO.

Bathe, K-J., 1996. "Finite Element Procedures", Prentice-Hall Inc., Englewood Cliffs, New Jersey.

Beer, F.P., and Johnston, E.R., 1992. "Mechanics of Materials – Second Edition in SI Units", McGraw-Hill Book company, New York, New York.

Behbahanifard, M., Cheng, J.J.R., Murray, D.W., Zhou, Z., Adams, K., Yoshizaki, K., Fukada, N., Como, M., Cerelli, E., 2004. "Simulation of Cold Bends by Finite Element Method", *Proceedings of the 5th Biennial International Pipeline Conference*, American Society of Mechanical Engineers, Calgary, Alberta, p. 427-435.

Bilston, P., and Murray, N., 1993. "The Role of Cold Field Bending in Pipeline Construction", 8th Symposium on Line Pipe Research, American Gas Association, Paper No. 27.

Boresi, A.P., Sidebottom, O.M., 1985. "Advanced Mechanics of Materials", 4th Edition, John Wiley & Sons, Inc.

Bouwkamp, G., and Stephen, R.M. 1973, "Large Diameter Pipe under Combined Loading", *Transportation Engineering Journal*, Vol. 99, No. TE3, pp. 521-536.

Boyle, J.T., and Spence, J., 1981. "A Simple Stress Analysis for Oval, Pressurized Pipe Bends Under External Bending", *Proceedings of the 4th International Conference on Pressure Vessel Technology*, I. Mech. E., London, 1980.

- Boyle, J.T., and Spence, J., 1981. "A Simple Stress Analysis for Out-of-Round Pressurized Pipe Bends", *International Journal of Pressure Vessels and Piping*, No. 9, p. 251-261.
- Brazier, L.G. (1927). "On the Flexure of Thin Cylindrical Shells and other 'Thin' Sections", Series A, Vol. CXVI, *Proceedings of the Royal Society of London*
- Callister, W.D., 1994, "Materials Science and Engineering – An Introduction", 3rd Edition, John Wiley & Sons, Inc.
- Canadian Standards Association, 2003. "Z662-03 Oil and Gas Pipeline Systems", Canadian Standards Association, Etobicoke, Ontario.
- Cheng, J.J.R., Sen, M., Behbahanifard, M., and Murray, D.W., 2004, Local Buckling Behaviour and Design of Cold Bend Pipes, Pipeline Technology Report No. 2004-1, Department of Civil Engineering, University of Alberta, Edmonton, Alberta, Canada.
- Das, S., Cheng, J.J.R., and Murray, D.W., 2003. "Fracture of Wrinkled Energy Pipelines", PhD. Thesis, Department of Civil Engineering, University of Alberta, Edmonton, Alberta, Canada.
- Davis, E.A., 1945. "Yielding and Fracture of Medium-Carbon Steel Under Combined Stress", *Journal of Applied Mechanics*, Trans. A.S.M.E., No. 67, March 1945, p. A13-A24.
- Davis, H.E., and Parker, E.R., 1948. "Behaviour of Steel Under Biaxial Stress as Determined by Tests on Tubes", *Journal of Applied Mechanics*, Trans. A.S.M.E., No. 67, September 1945, p. 201-215.
- Del Col, P.R., Grondin, G.Y., Cheng, J.J.R., and Murray, D.W., 1998. "Behaviour of Large Diameter Line Pipe Under Combined Loads", Structural Engineering Report No. 224, Department of Civil Engineering, University of Alberta, Edmonton, Alberta, Canada.
- DiBattista, J.D., Cheng, J.J.R., and Murray, D.W., 2000. "Behaviour of Sleeper Supported Line Pipe", Structural Engineering Report No. 230, Department of Civil Engineering, University of Alberta, Edmonton, Alberta, Canada.
- Dieter, G.E., 1978. "Mechanical Metallurgy", 3rd edition, International Edition. McGraw-Hill Book Co., Singapore.
- DNV-OS-F101, 2000. "Offshore Standard OS-F101, Submarine Pipeline Systems", Det Norske Veritas, Veritasveien 1, N-13222, Hovik, Norway.

Dorey, A.B., Cheng, J.J.R., and Murray, D.W., 2001. "Critical Buckling Strains for Energy Pipelines", Structural Engineering Report No. 237, Department of Civil Engineering, University of Alberta, Edmonton, Alberta, Canada.

Fukada, N., Yatabe, H., Masuda, T., Toyoda, M., 2002. "Changes in Tensile Properties due to Cold Bending of Line Pipes", Proceedings of OMAE'02 21st International Conference on Offshore Mechanics and Arctic Engineering, American Society of Mechanical Engineers, Oslo, Norway.

Fukada, N., Yatabe, H., Masuda, T., Toyoda, M., 2002. "Effect of Changes in Tensile Properties due to Cold Bending on Large Deformation Behaviour of High-Grade Cold Bend Pipe", Proceedings of IPC2002 4th International Pipeline Conference, American Society of Mechanical Engineers, Calgary, Alberta.

Fukada, N., Yatabe, H., Watanabe, T., Kawaguchi, S., Masuda, T., 2001. "Experimental and Analytical Study of Cold Bending Process for Pipelines", Proceedings of OMAE'01 20th International Conference on Offshore Mechanics and Arctic Engineering, American Society of Mechanical Engineers, Rio de Janeiro, Brazil.

Gillanders, J., 1984. "Pipe and Tube Bending Manual", Gulf Publishing Company, Houston, Texas.

Gresnigt, A.M., 1986. "Plastic Design of Buried Steel Pipelines in Settlement Areas", *Heron*, vol. 31, no. 4.

Hibbit, Karlsson, & Sorenson, Inc., 2002. ABAQUS Standard, Version 6.3 software manuals. Hibbit, Karlsson, & Sorenson, Inc., Pawtucket, Rhode Island.

Jayadevan, K.R., Ostby, E., and Thaulow, C., 2004. "Fracture Response of Pipelines Subjected to Large Plastic Deformation Under Tension", *International Journal of Pressure Vessels and Piping*, No. 81, p. 771-783.

MacGregor, C.W., and Coffin, L.F., 1946. "Yielding and Fracture of Medium-Carbon Steel Under Combined Stress - Discussion", *Journal of Applied Mechanics*, Trans. A.S.M.E., March 1946, p. A71-A73.

Microsoft Corporation, 2000. Microsoft Office 2000 Standard (software package).

Mohareb, M.E., Elwi, A.E., Kulak, G.L., and Murray, D.W., 1994. "Deformational Behaviour of Line Pipe", Structural Engineering Report No. 202, Department of Civil Engineering, University of Alberta, Edmonton, Alberta, Canada.

- Mohareb, M., Kulak, G.L., Elwi, A., and Murray, D.W., 2001. "Testing and Analysis of Steel Pipe Segments", *Journal of Transportation Engineering*, A.S.C.E., September/October 2001, p. 408-417.
- Murray, N.W., and Bilston, P., 1992. "Local Buckling of Thin-Walled Pipes being Bent in the Plastic Range", *Thin-Walled Structures*, No. 14, p. 411-434.
- Murray, N.W., and Bilston, P., 1992. "Rational Acceptance Limits for Field Bends in Oil or Gas Pipelines", *International Conference on Pipeline Reliability*, Paper V-2, June 2-5, 1992.
- Murray, N.W., and Bilston, P., 1992. "Elasto-Plastic and Strain-Hardening Bending of Thin Steel Pipes in the Pre-Buckling Region", *Transactions of the Institution of Engineers, Australia Civil Engineering*, Vol. CE34, No. 3, September 1992, P. 247-253.
- Olson, R., Clark, T., 1995. "Evaluation of the Structural Integrity of Cold Field Bent Line Pipe", *EPRG/PRC 10th Biennial Joint Technical Meeting on Line Pipe Research*, Paper 6, April 18-21, 1995.
- Olson, R., Clark, T., and Odom, T. "Evaluation of the Structural Integrity of Cold Field Bent Line Pipe", *9th Symposium on Pipeline Research*, Paper 33, Sept 30, 1996.
- Palynchuk, A., 1983. "Strains Caused by Field Bending of 42-inch Pipe", *Pipe Line Industry*, March 1983, p. 23-26.
- Rao, S.S., 2005. "The Finite Element Method in Engineering", 4th Edition, Elsevier Butterworth Heinemann, Boston, Massachusetts.
- Rosenfeld, M.J., Hart, J.D., Zulfiqar, N., Gailing, R.W., 2002. "Development of Acceptance Criteria for Mild Ripples in Pipeline Field Bends", *Proceedings of IPC2002 4th International Pipeline Conference*, American Society of Mechanical Engineers, Calgary, Alberta.
- Sen, M., Cheng, J.J.R., Murray, D.W., Zhou, Z., Adams, K., Yoshizaki, K., Fukada, N., Como, M., Cerelli, E., 2004. "Full Scale Tests of Cold Bend Pipes", *Proceedings of the 5th Biennial International Pipeline Conference*, American Society of Mechanical Engineers, Calgary, Alberta, p. 419-426.
- Sen, M., Cheng, J.J.R, and Murray, D.W., 2005, *Behaviour of Cold Bend Pipes Under Combined Loads*, Pipeline Technology Report No. 2005-1, Department of Civil Engineering, University of Alberta, Edmonton, Alberta, Canada.
- Sherman, D., 1976. "Tests of Circular Steel Tubes in Bending", *ASCE Journal of Structural Division*, vol. 102, ST11.

Shibli, I.A., 1986. "Investigation of a Failure Problem in Cold-bent Boiler Riser and Supply Pipes", *International Journal of Pressure Vessels and Piping*, No. 24, p. 303-336.

Shim, D., Choi, J., and Kim, Y., 2004. "Failure Strength Assessment of Pipes with Local Wall Thinning Under Combined Loading Based on Finite Element Analysis", *Journal of Pressure Vessel Technology*, Vol. 126, p. 179-183.

Smallman, R.E., 1985. "Modern Physical Metallurgy", 4th Edition, Butterworth & Co, Ltd.

Timoshenko, S., 1956. "Strength of Materials – Part II – Advanced Theory and Problems", 3rd Edition, D. Van Nostrand Company, Inc.

Wassermann, D.R., 1983. "Experimental Investigation of Stresses in Cold-Bent Pipes Due to Internal Pressure and In-Plane Bending", *International Journal of Pressure Vessels and Piping*, No. 14, p. 135-151.

Yatabe, H., Fukada, N., Kawaguchi, S., Masuda, T., 2001. "Effects of Mechanical Properties on the Deformability of High Grade Line Pipe", *Proceedings of OMAE'01 20th International Conference on Offshore Mechanics and Arctic Engineering*, American Society of Mechanical Engineers, Rio de Janeiro, Brazil.

Yatabe, H., Fukada, N., Toyoda, M., 200. "Analytical Study of Appropriate Design for the High-Grade Induction Bend Pipes Subjected to Large Ground Deformation", *Proceedings of OMAE'02 21st International Conference on Offshore Mechanics and Arctic Engineering*, American Society of Mechanical Engineers, Oslo, Norway.

Yoosef-Ghodsii, N., and Murray, D.W., 2002. "Analysis of Buried Pipelines with Thermal Applications", *Structural Engineering Report No. 246*, Department of Civil Engineering, University of Alberta, Edmonton, Alberta, Canada.

Yoshizaki, K., Ando, H., and Oguchi, N., 1998. "Large Deformation Behaviour of Pipe Bends Subjected to In-Plane Bending", *Proceedings of the International Pipeline Conference*, American Society of Mechanical Engineers, Calgary, Alberta.

Yoshizaki, K., 2002. "Strain Measurements and Investigation of Changes in Tensile Properties due to Cold Bending", Tokyo Gas Co., Ltd.